JPL D–26280

Earth Observing System (EOS)
Microwave Limb Sounder (MLS)

EOS MLS
Instrument Calibration Report
Volume 2

Appendixes A – F

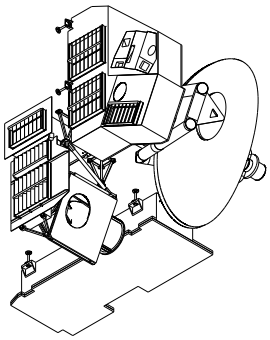

$$\dot{\mathbf{P}}_{\mathbf{i}}^{\mathbf{L}} = \frac{\mathbf{1}}{\eta_{\mathbf{r}}^{\mathbf{ML}}}\left(\frac{\mathbf{C}_{\mathbf{i}}^{\mathbf{L}} - \widehat{\mathbf{C}}_{\mathbf{i}}^{\mathbf{S}}(\mathbf{L})}{\hat{\mathbf{g}}_{\mathbf{i}}(\mathbf{L})} + \eta_{\mathbf{r}}^{\mathbf{MS}}\dot{\mathbf{P}}_{\mathbf{r}}^{\mathbf{S}} - (\mathbf{1} - \eta_{\mathbf{r}}^{\mathbf{ML}})\dot{\mathbf{P}}_{\mathbf{r}}^{\mathbf{BL}} + (\mathbf{1} - \eta_{\mathbf{r}}^{\mathbf{MS}})\dot{\mathbf{P}}_{\mathbf{r}}^{\mathbf{BS}}\right)$$

Robert F. Jarnot, Richard E. Cofield, Herbert M. Pickett, Paul C. Stek

28 March 2005

Jet Propulsion Laboratory
California Institute of Technology
Pasadena, CA 91109-8099

The research was carried out at the Jet Propulsion Laboratory, California Institute of Technology, under a contract with the National Aeronautics and Space Administration (80NM0018D004).

Release Record

Version	Date	Comments
draft	12 Feb 2003	Start of working/draft version
	30 Mar 2004	Initial release for review
Public	11 Feb 2025	URS wording added to cover

/users/jarnot/texinput/calrep/EOS/CalRepVol2.TEX

Contents

A Introduction **1**

B Radiometric Calibration and Characterization **3**
B.1 Sensitivity Data . . . 3
B.2 Linearity Data . . . 96
B.3 Blue Sky Measurement Data . . . 143
B.3.1 A comment on data quality . . . 143

C Relative Sideband Calibration **157**
C.1 GHz Relative Sideband Data and Analysis Results . . . 157
C.2 THz Sideband Calibration . . . 185

D FOV Calibration for the GHz Module **187**
D.1 Near Field Range Concepts . . . 187
D.2 Interferometer Design . . . 188
D.2.1 Radiometers R1A and R1B . . . 188
D.2.2 Radiometers R2 and R3 . . . 189
D.2.3 Radiometer R4 . . . 191
D.3 Near Field Scanner . . . 195
D.3.1 Planarity Verification . . . 196
D.3.2 Scan Pattern . . . 196
D.3.3 Cables . . . 196
D.4 Scan Plane/Instrument Angle Measurement . . . 196
D.5 Testing Procedure . . . 196
D.6 FOV Analysis Models . . . 197
D.6.1 Scattered Power Fraction . . . 197
D.6.2 Diffraction and Spillover . . . 198
D.7 Analysis of Measured Patterns . . . 199
D.7.1 Definitive FOV direction (dFOV) . . . 199
D.7.2 Definitive FOVs for L2PC . . . 204
D.7.3 FOV Variability due to Scan Angle and Frequency Dependence of FOVs 220
D.7.4 Conclusions . . . 221
D.8 Measured Reflectivity of Witness Specimens . . . 221
D.9 Radiometer FOV patterns . . . 223

E Calibration Files and Programs **231**
E.1 GHz Radiometric data files . . . 231
E.2 GHz Spectral data files . . . 231
E.3 GHz FOV data files . . . 231
E.4 THz data files . . . 231

F Bus Sniffing Calibration Controllers **233**
F.1 Calibration Controller . . . 233
F.2 Controller Software . . . 235
F.2.1 Atmel Software . . . 236
F.2.2 Rabbit Software . . . 240
References . . . 253

Appendix A

Introduction

In this volume of the EOS MLS Calibration Report we expand on the data presented in Volume 1, covering the following:

- ❏ Radiometric performance and calibrations,
- ❏ relative sideband response,
- ❏ FOV calibrations, and
- ❏ additional details of the controllers used in radiometric and spectral calibrations.

We also include additional information on the locations of the calibration data files, and some of the software used to create them.

Volume 3 of this report is devoted to presentation of the voluminous high-resolution spectral sweep data, and Volume 4 to post-launch updates to instrument performance and calibrations.

Appendix B

Radiometric Calibration and Characterization

In this Appendix we expand upon the sensitivity, linearity and 'Blue Sky' data presented in Volume 1.

B.1 Sensitivity Data

A full sensitivity characterization data set is presented below for all GHz filter channels. Several similar data sets were taken during the course of instrument Integration and Testing, and analyzed with the same software tools. No significant differences exist between any of the data runs taken on the Flight Model version of the instrument. The data below were taken on 3 November 2002, except for the Band 12 data which was taken on 2 December 2002.

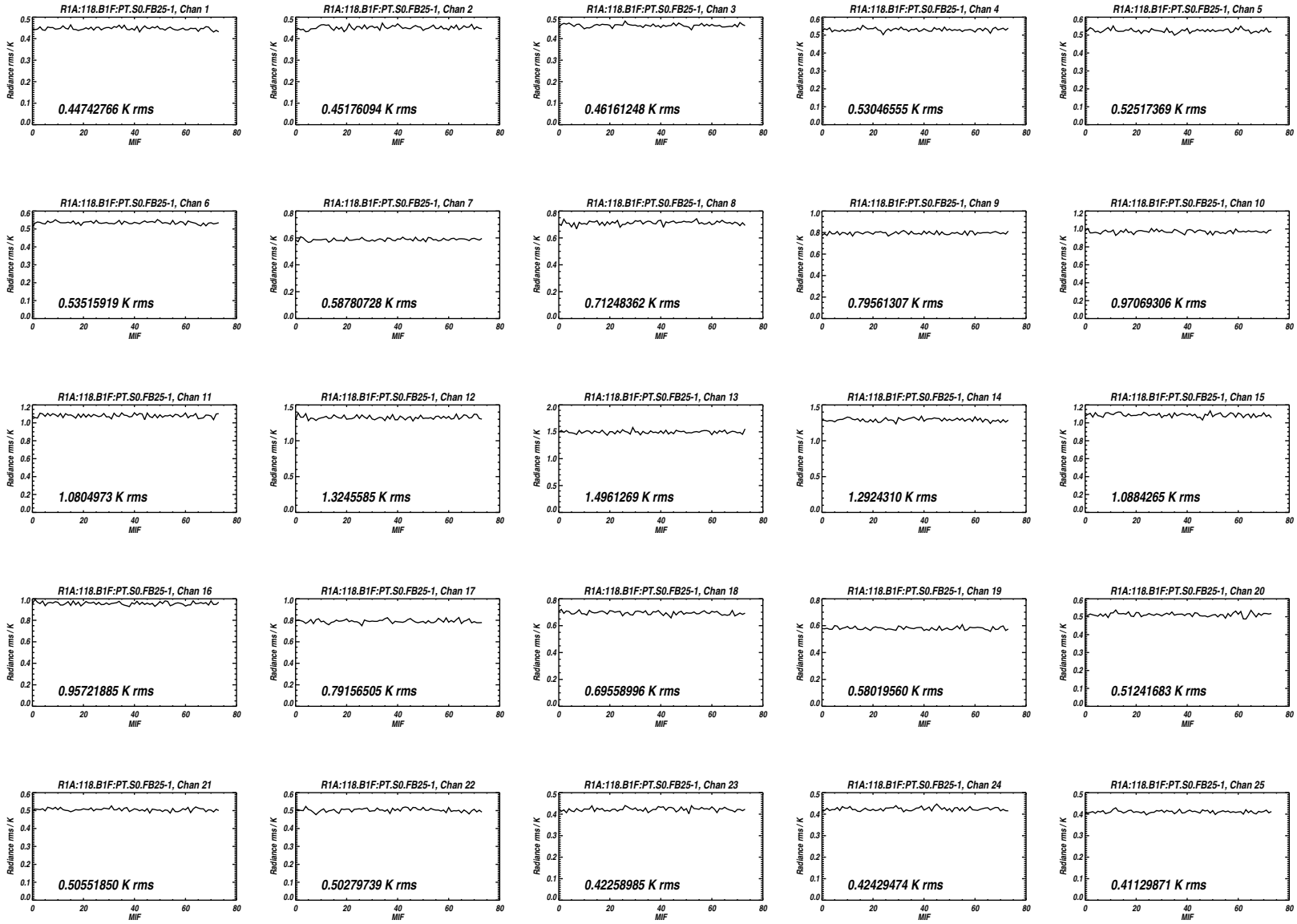

Figure B.1: Measured *rms* noise for all 25 channels of Band 1 for the MIFs treated as Limb views in Level 1 processing.

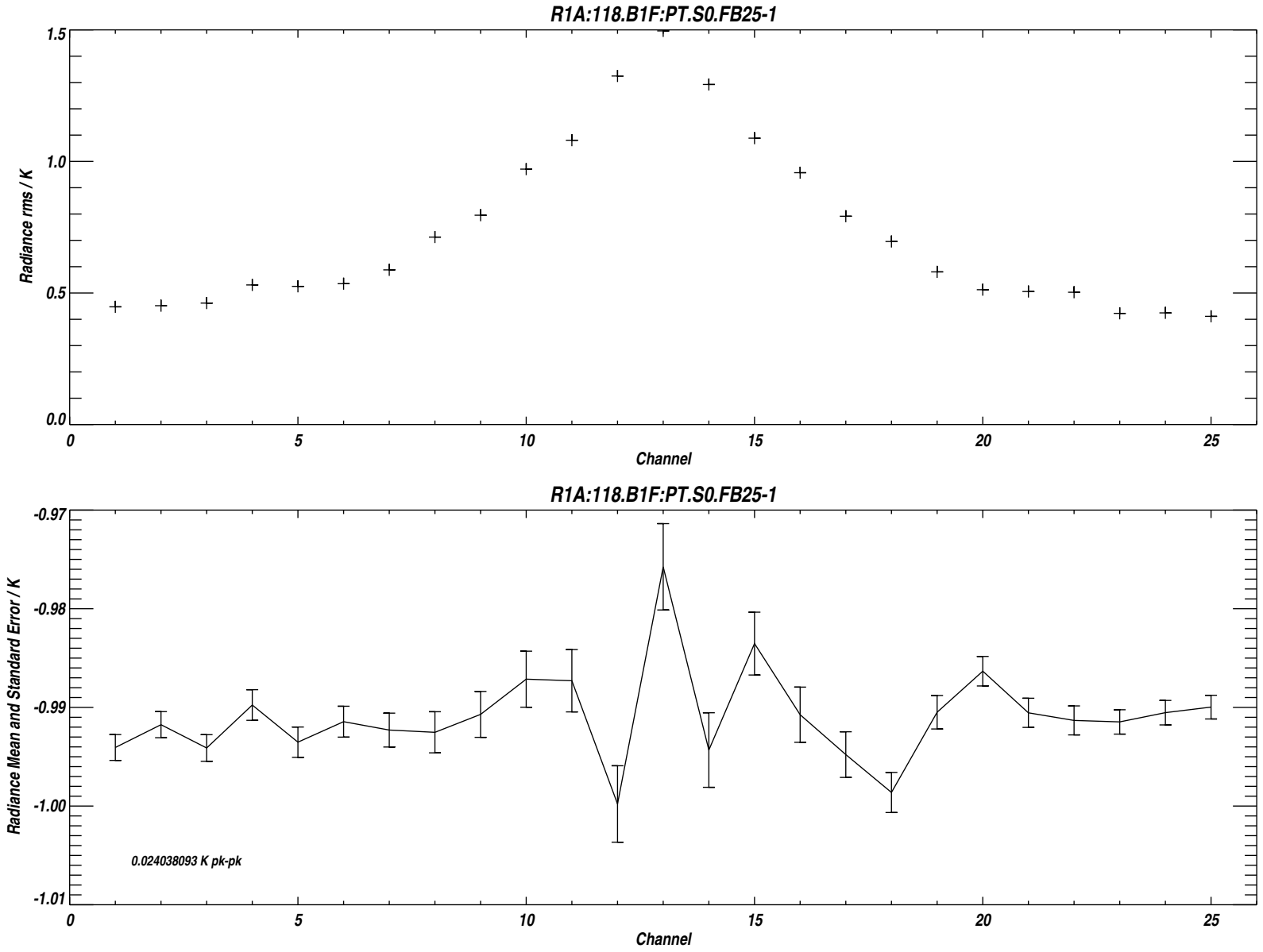

Figure B.2: Measured *rms* noise for each channel of Band 1 (upper panel). The lower panel plots the difference between the mean 'Limb' and reference radiances, the vertical bars indicating the *rms* uncertainty due to noise.

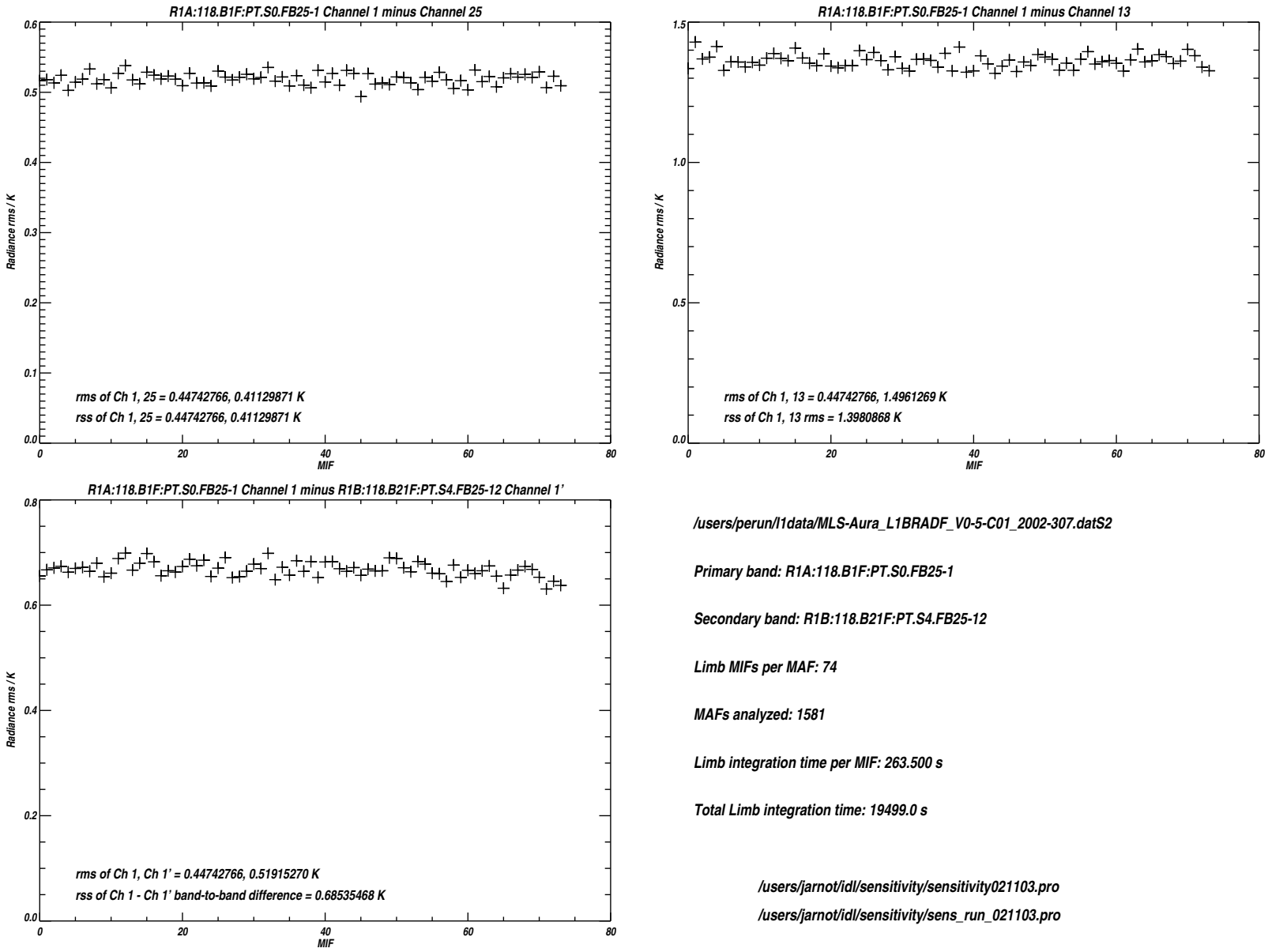

Figure B.3: Measured *rms* noise on the radiance differences between Channels 1 and 25 of Band 1 (upper left panel), Channels 1 and 13 of B1 (upper right panel), and between Channel 1 of Band 1 and Channel 1 of Band 21 (R1B).

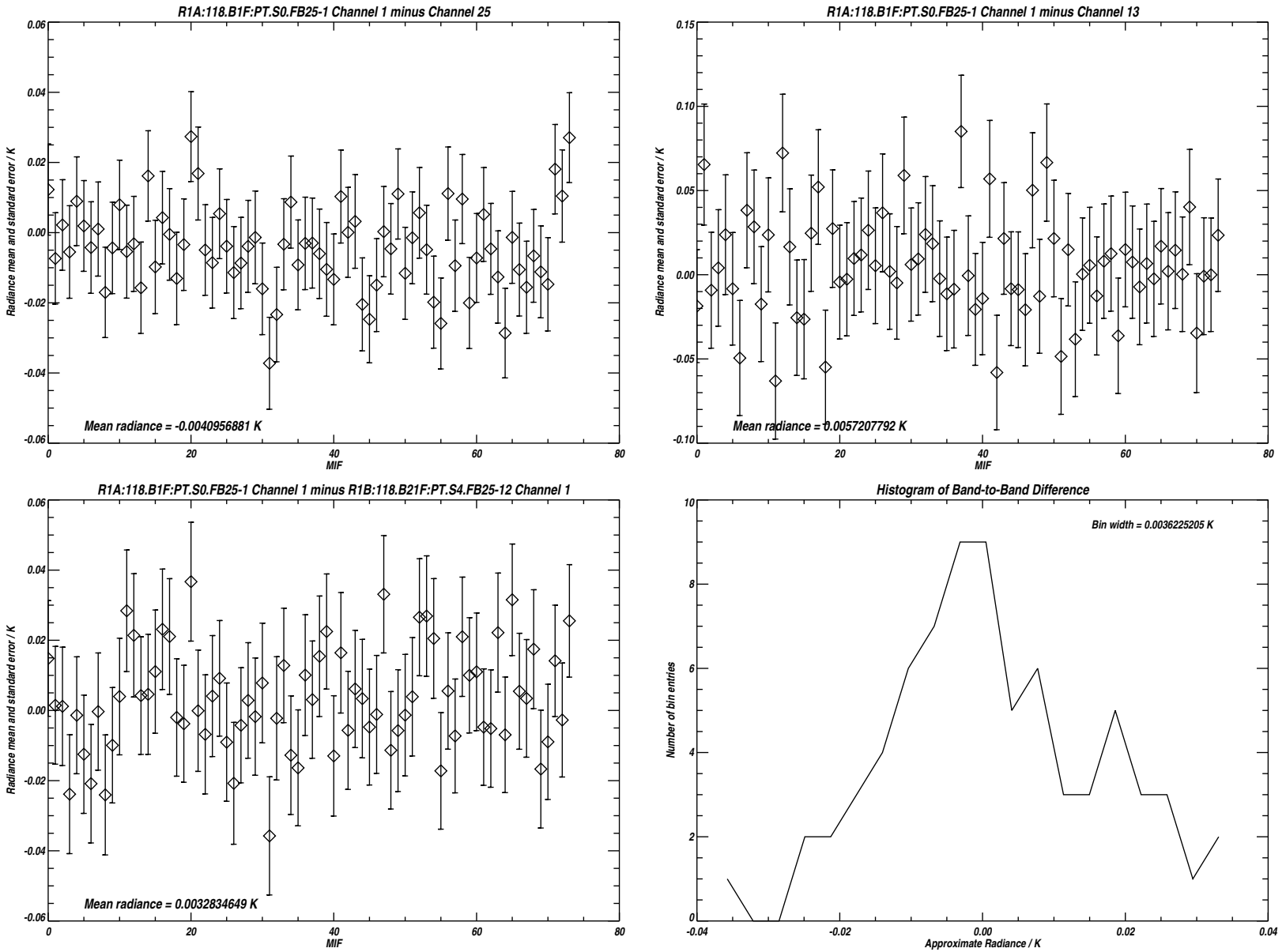

Figure B.4: Radiance differences between the 3 channel pairs plotted in Figure B.3. The vertical bars indicating the *rms* uncertainty due to noise. The lower right hand panel is a histogram of the data in the panel to its left. See text for additional details.

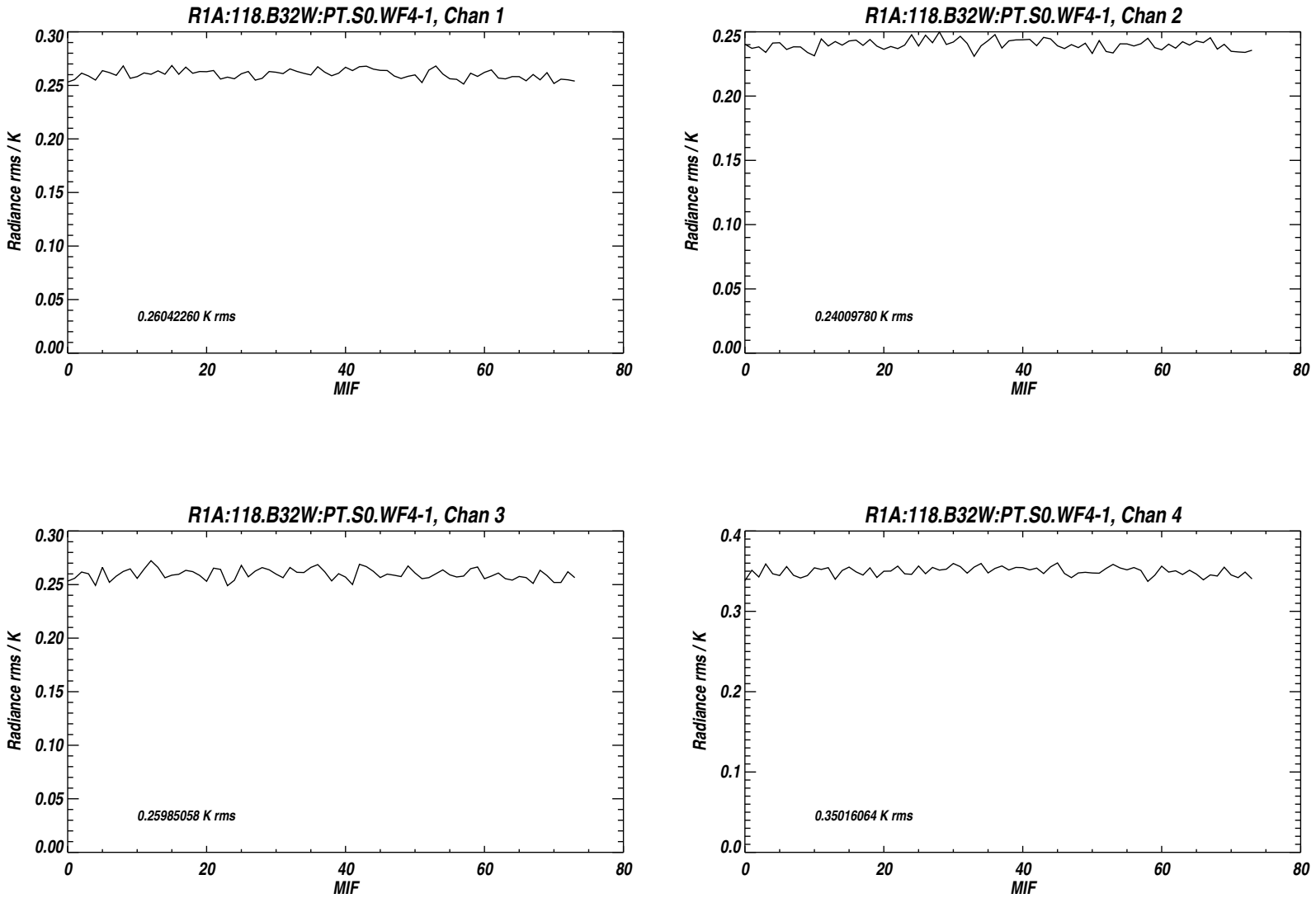

Figure B.5: Measured *rms* noise for the 4 Wide Filter channels of Band 32 (R1B) for the MIFs treated as Limb views in Level 1 processing.

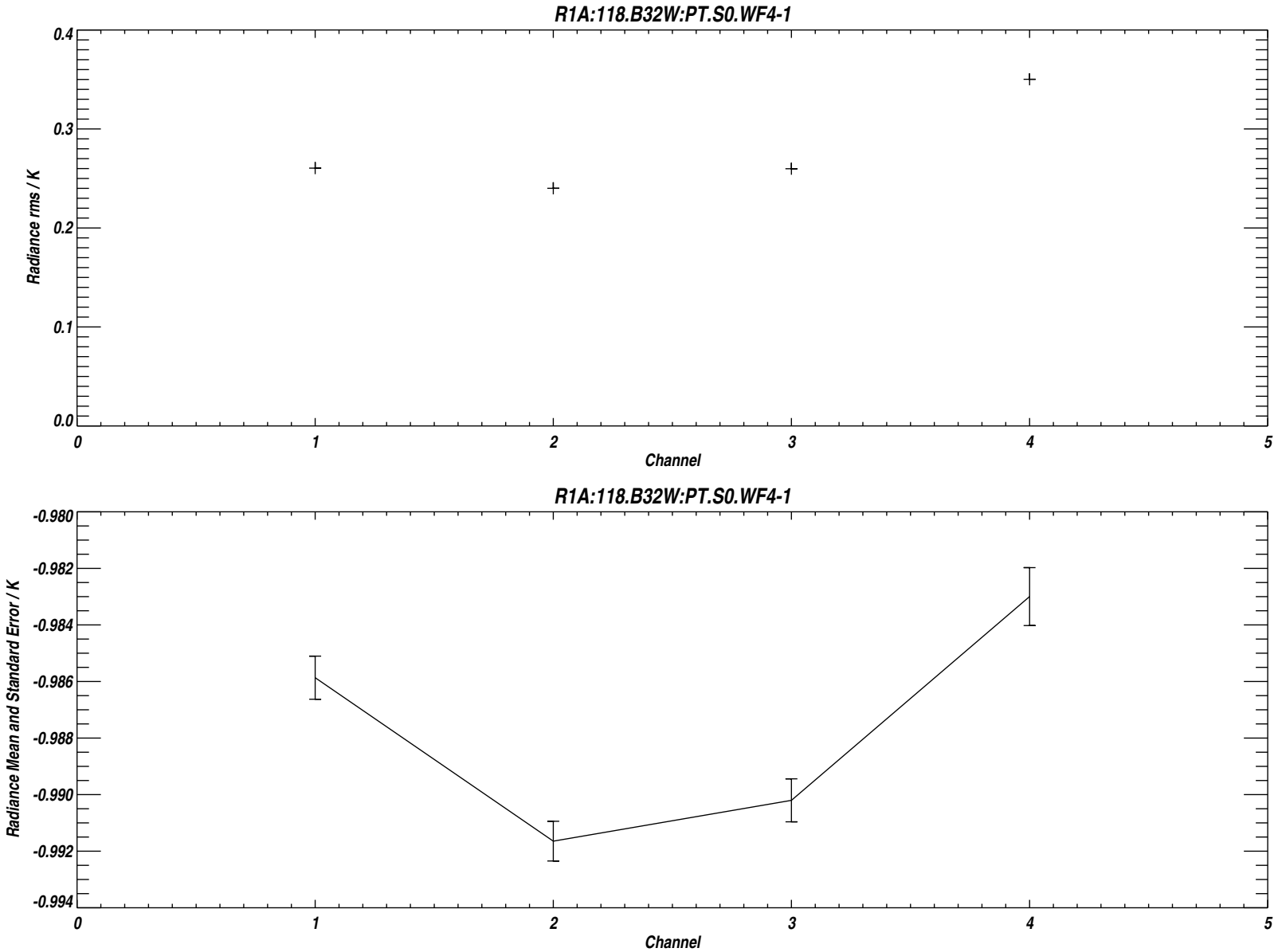

Figure B.6: Measured *rms* noise for the Wide Filter channels of Band 32. (upper panel). The lower panel plots the difference between the mean 'Limb' and reference radiances, the vertical bars indicating the *rms* uncertainty due to noise.

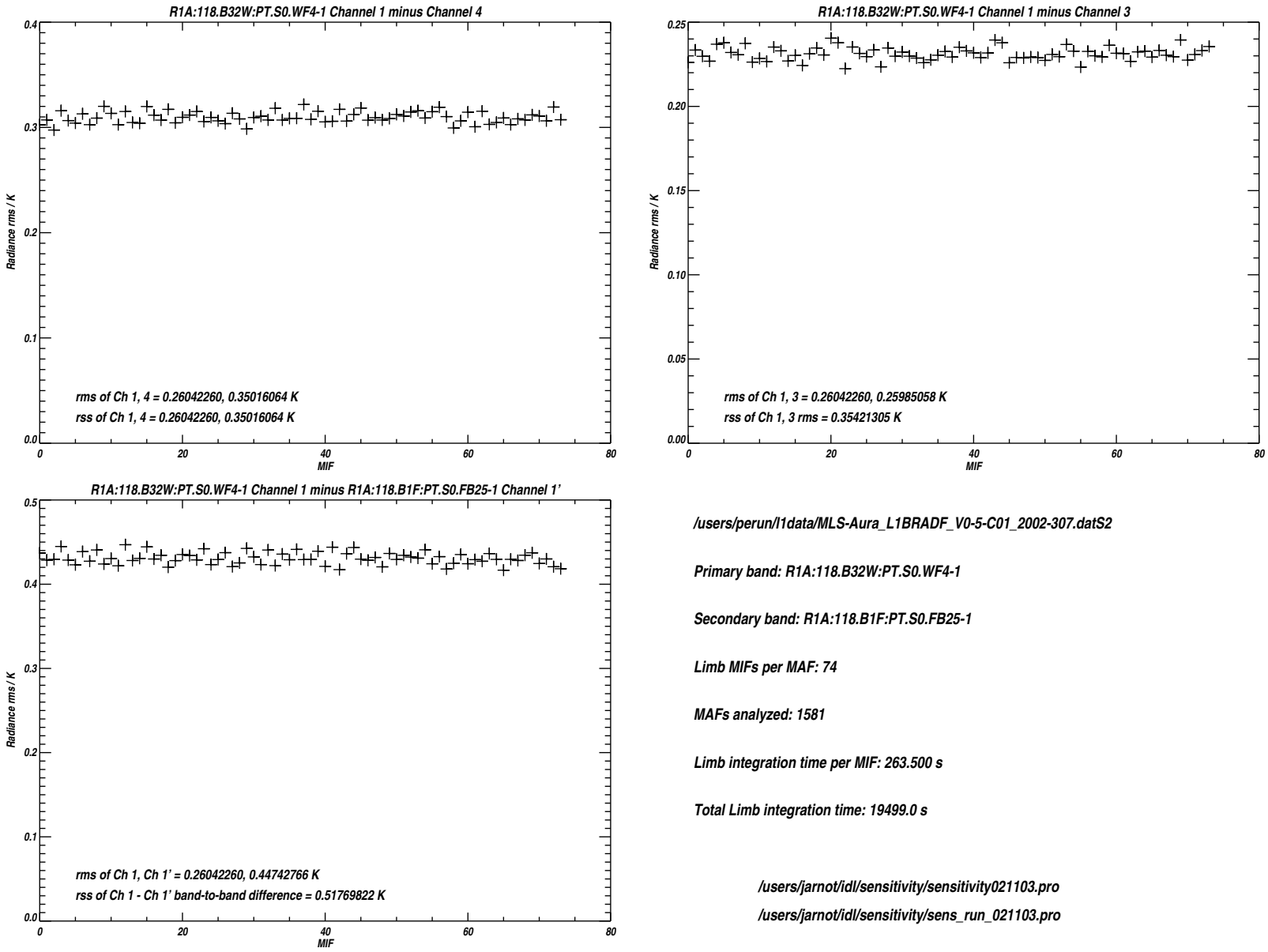

Figure B.7: Measured *rms* noise on the radiance differences between Wide Filter channels 1 and 4 of Band 32 (upper left panel), Wide Filter channels 1 and 3 of Band 32 (upper right panel), and between Wide Filter channel 1 of Band 32 and Channel 1 of Band 21 (FB25, R1B).

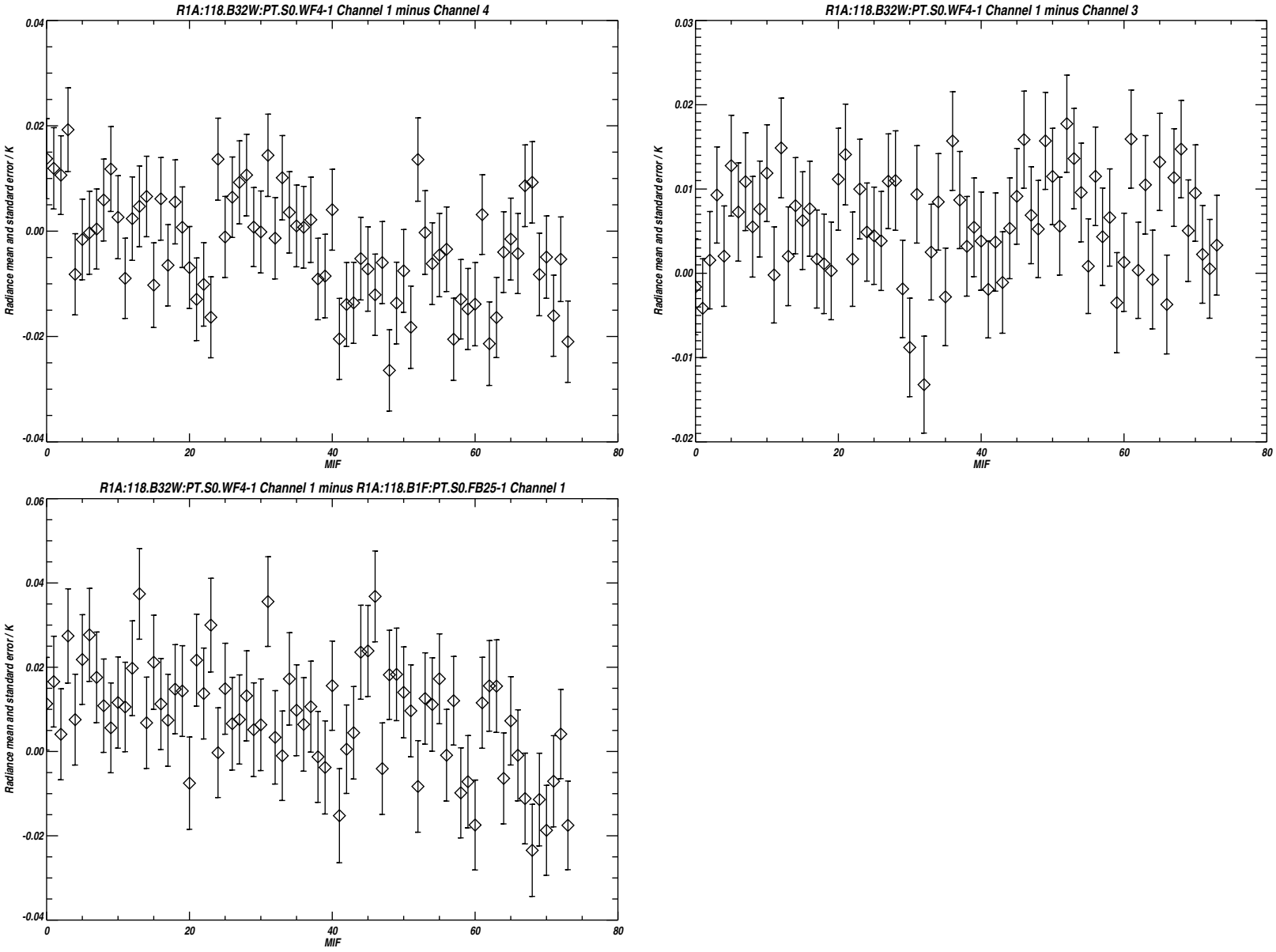

Figure B.8: Radiance differences between the 3 channel pairs plotted in Figure B.7. The vertical bars indicating the *rms* uncertainty due to noise. See text for additional details.

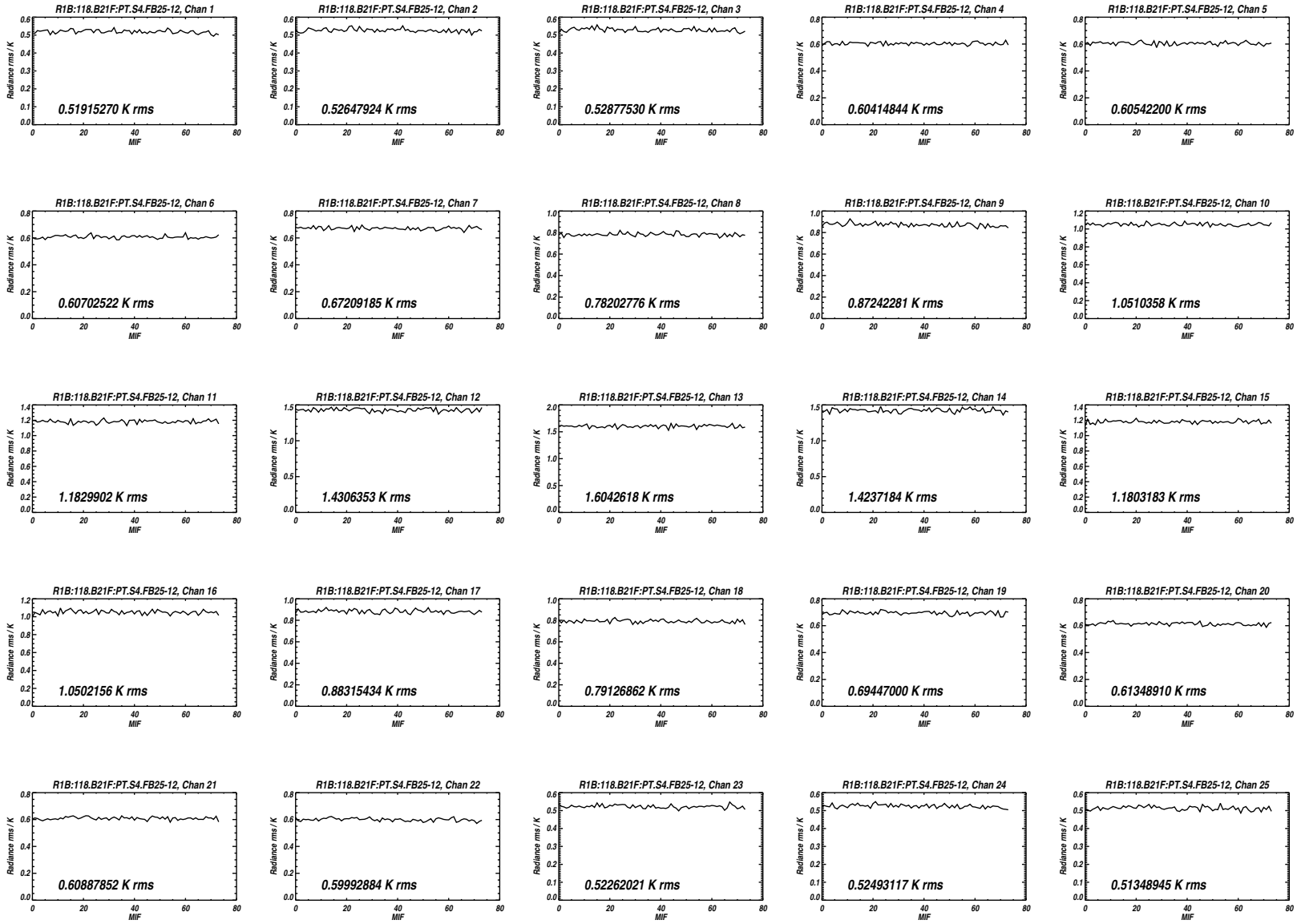

Figure B.9: Measured *rms* noise for all 25 channels of Band 21 for the MIFs treated as Limb views in Level 1 processing.

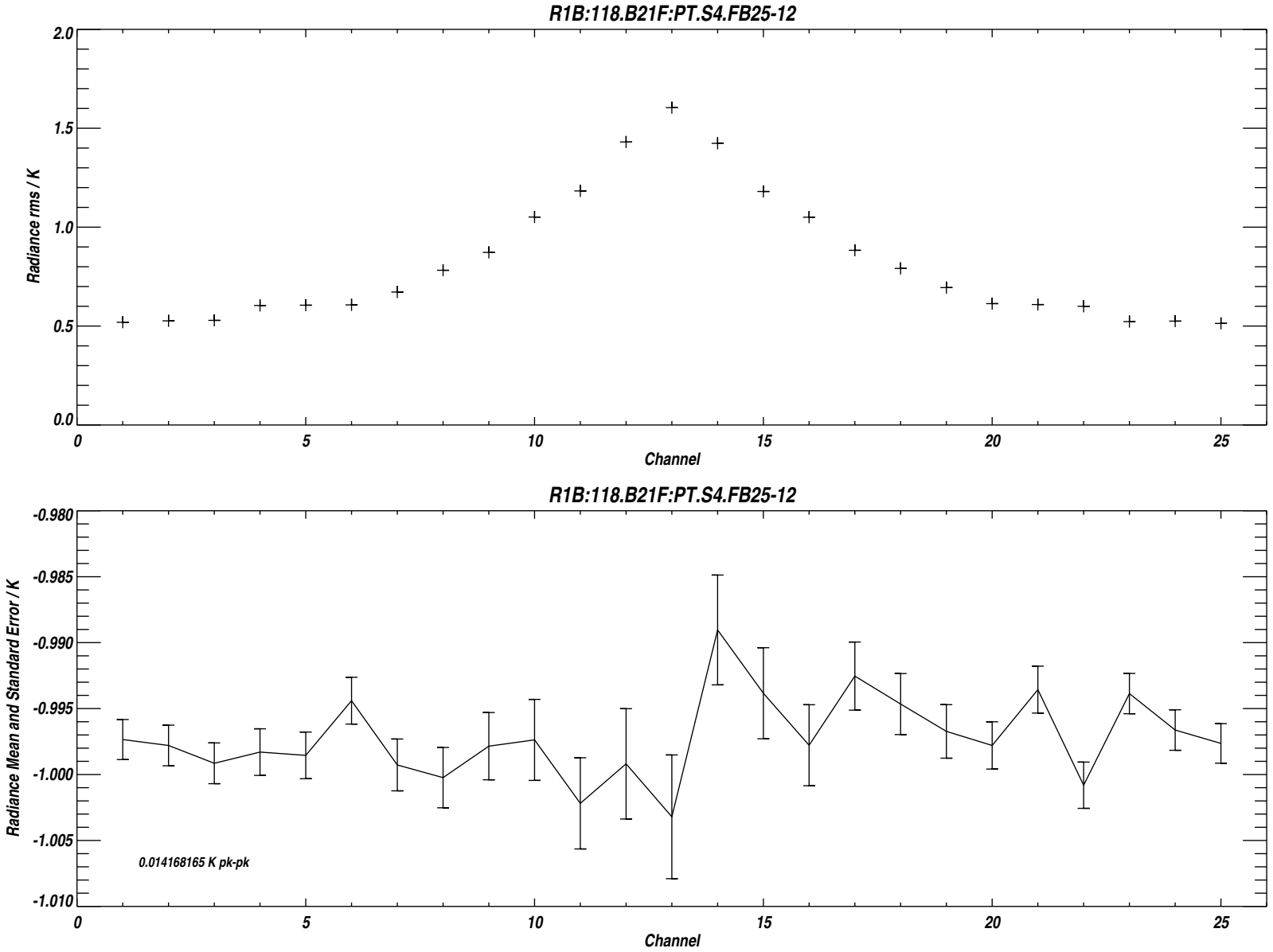

Figure B.10: Measured *rms* noise for each channel of Band 21 (upper panel). The lower panel plots the difference between the mean 'Limb' and reference radiances, the vertical bars indicating the *rms* uncertainty due to noise.

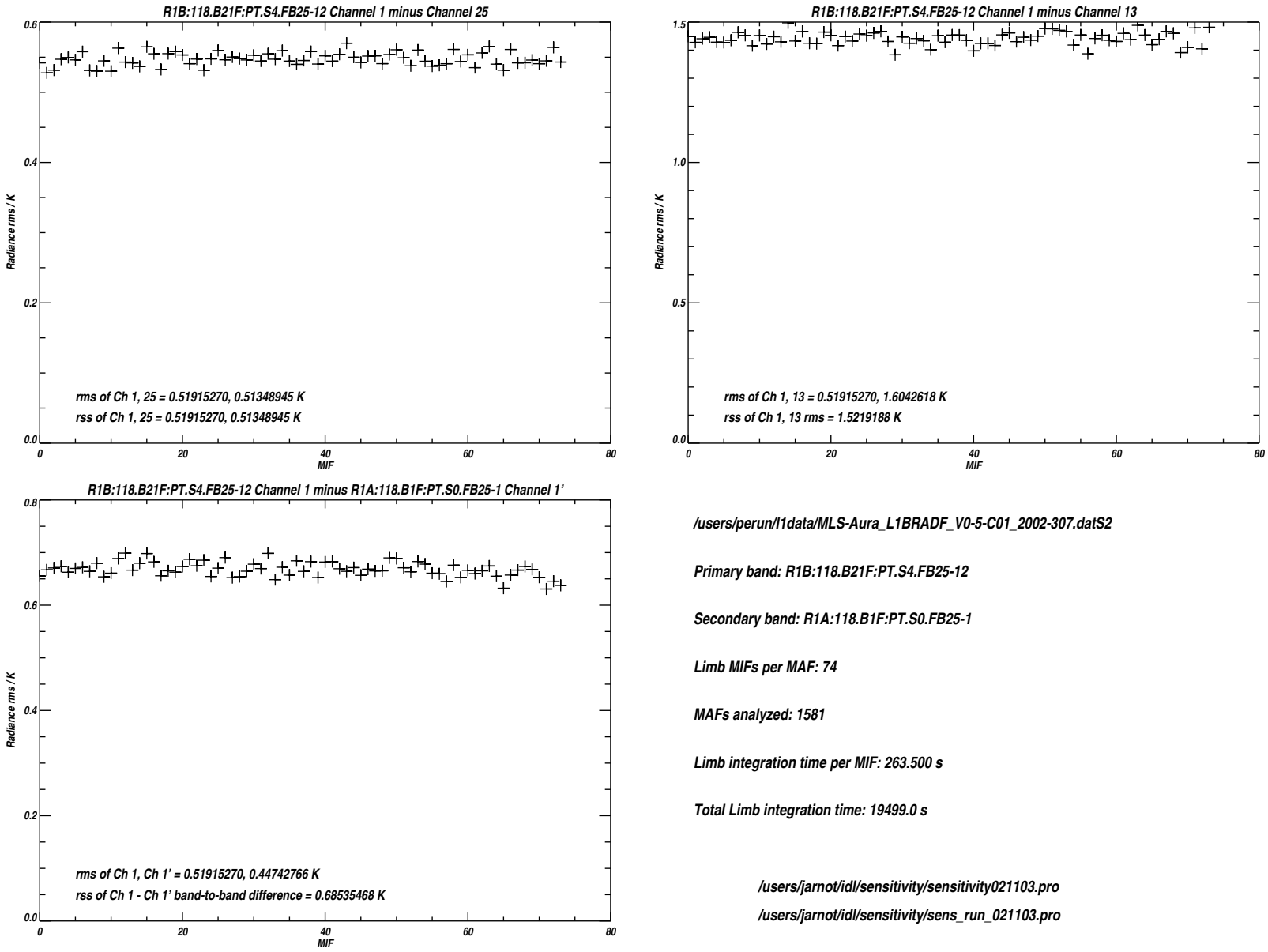

Figure B.11: Measured *rms* noise on the radiance differences between Channels 1 and 25 of Band 21 (upper left panel), Channels 1 and 13 of Band 21 (upper right panel), and between Channel 1 of Band 21 and Channel 1 of Band 1 (R1A).

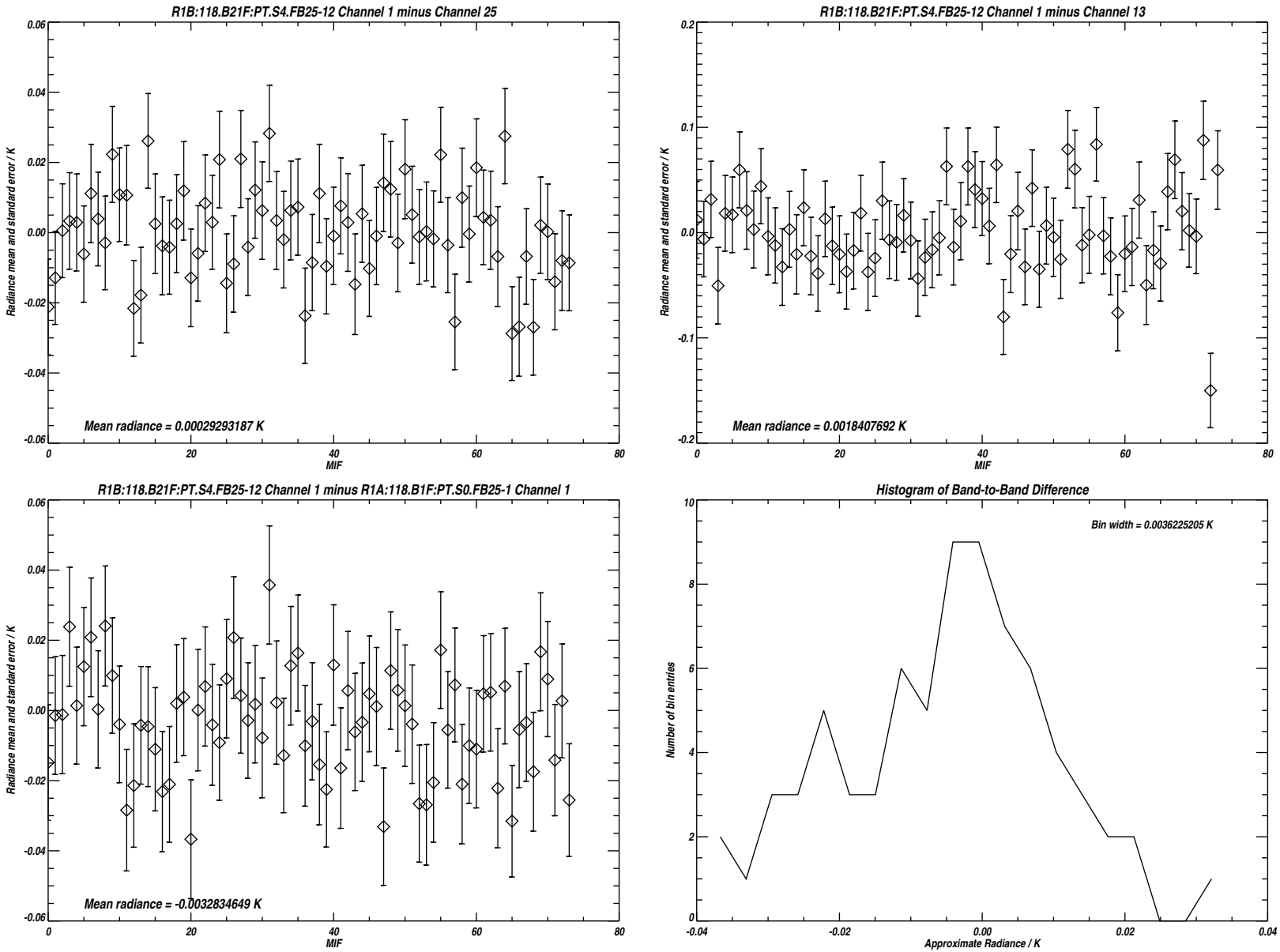

Figure B.12: Radiance differences between the 3 channel pairs plotted in Figure B.11. The vertical bars indicating the *rms* uncertainty due to noise. The lower right hand panel is a histogram of the data in the panel to its left. See text for additional details.

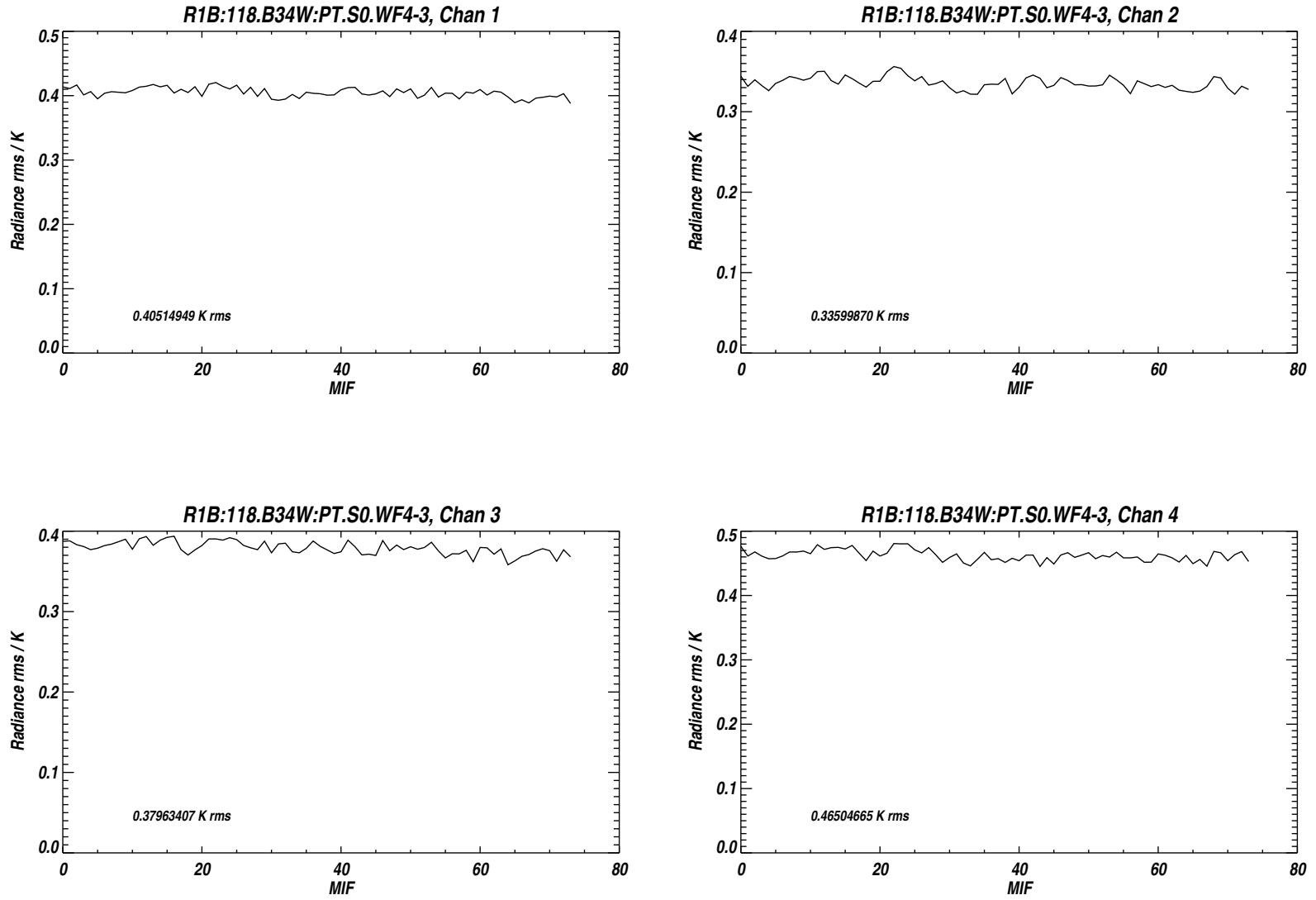

Figure B.13: Measured *rms* noise for the 4 Wide Filter channels of Band 34 (R1B) for the MIFs treated as Limb views in Level 1 processing.

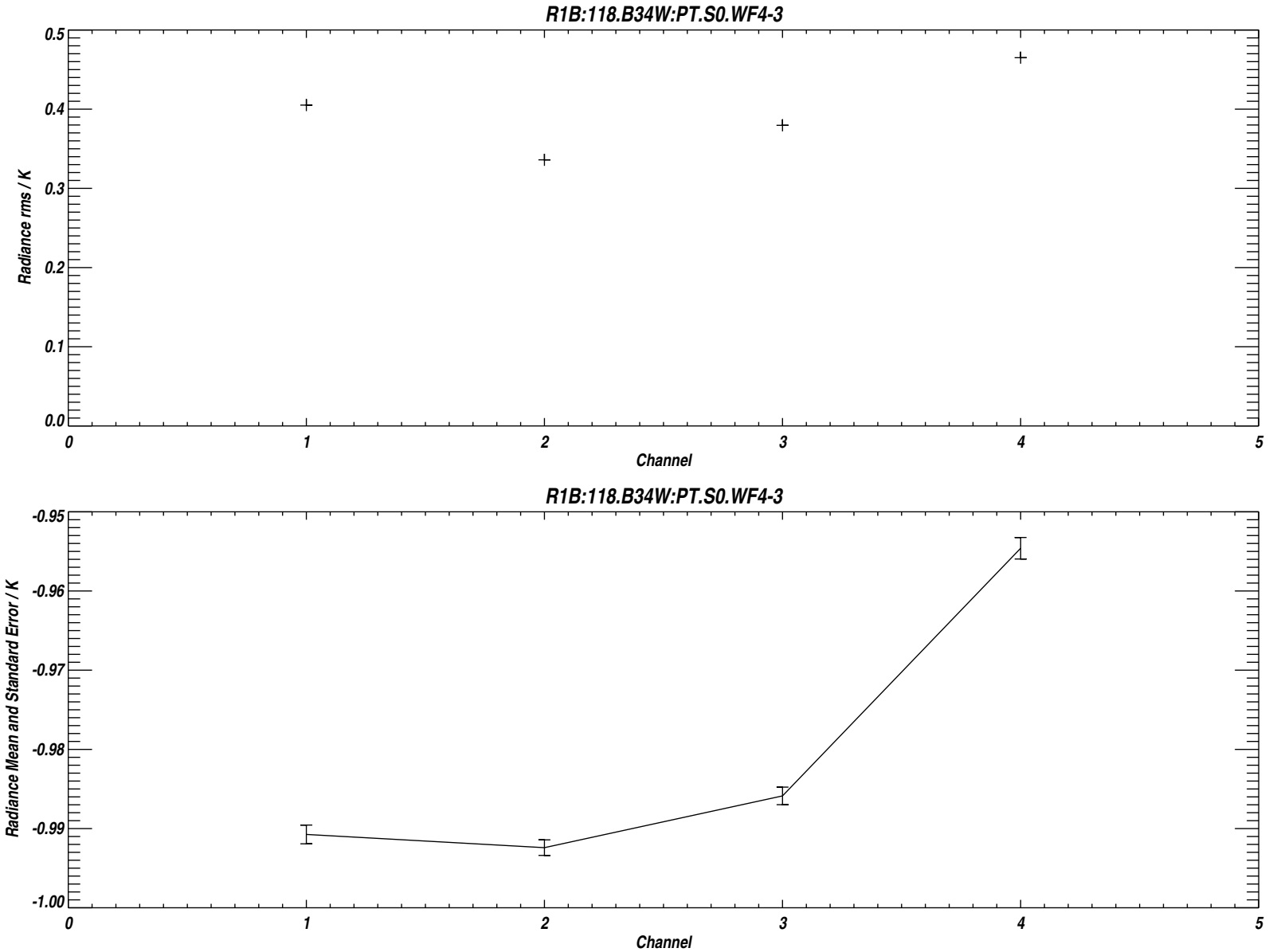

Figure B.14: Measured *rms* noise for the Wide Filter channels of Band 34. (upper panel). The lower panel plots the difference between the mean 'Limb' and reference radiances, the vertical bars indicating the *rms* uncertainty due to noise.

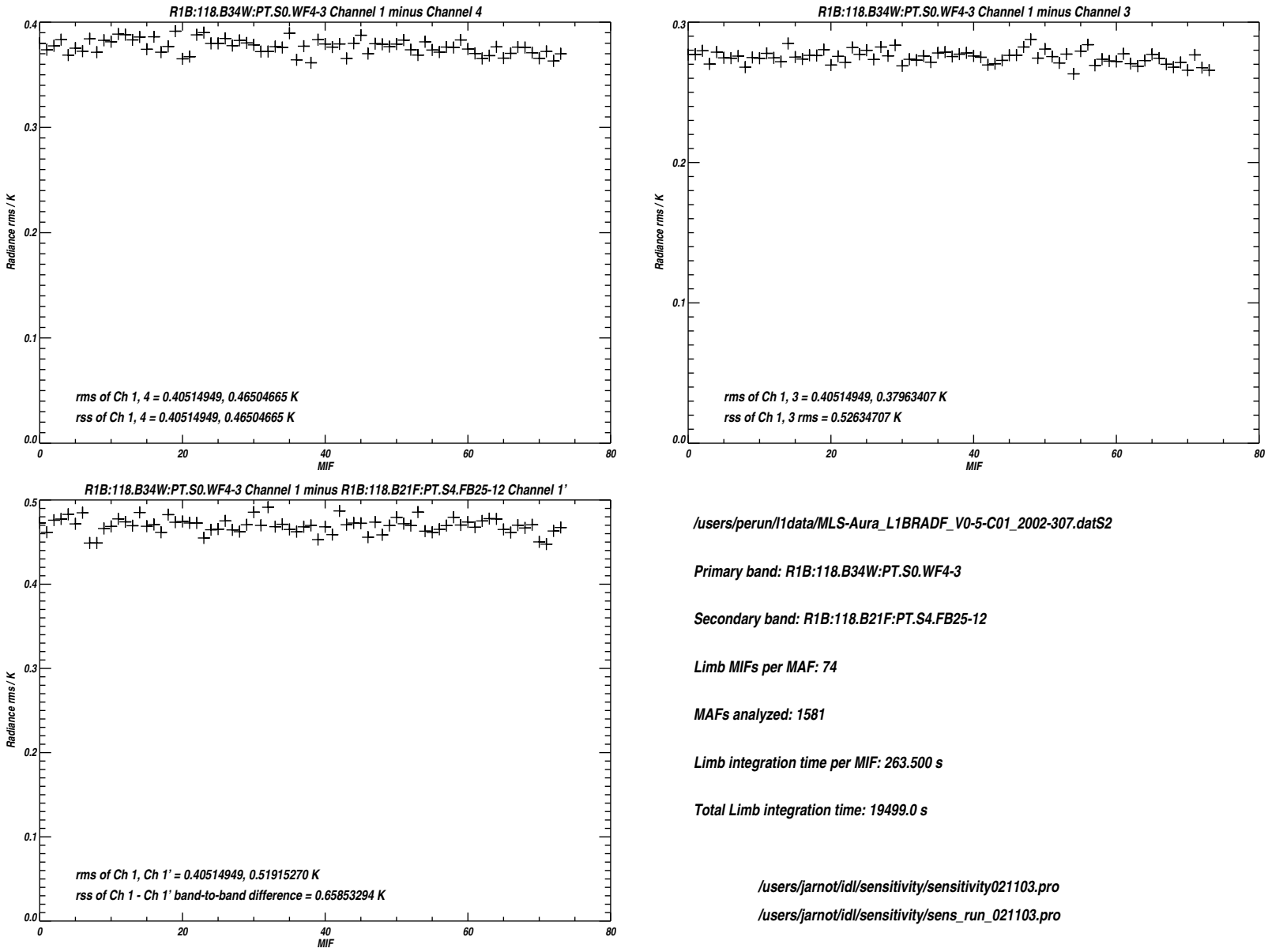

Figure B.15: Measured *rms* noise on the radiance differences between Wide Filter channels 1 and 4 of Band 34 (upper left panel), Wide Filter channels 1 and 3 of Band 34 (upper right panel), and between Wide Filter channel 1 of Band 34 and Channel 1 of Band 21 (FB25, R1B).

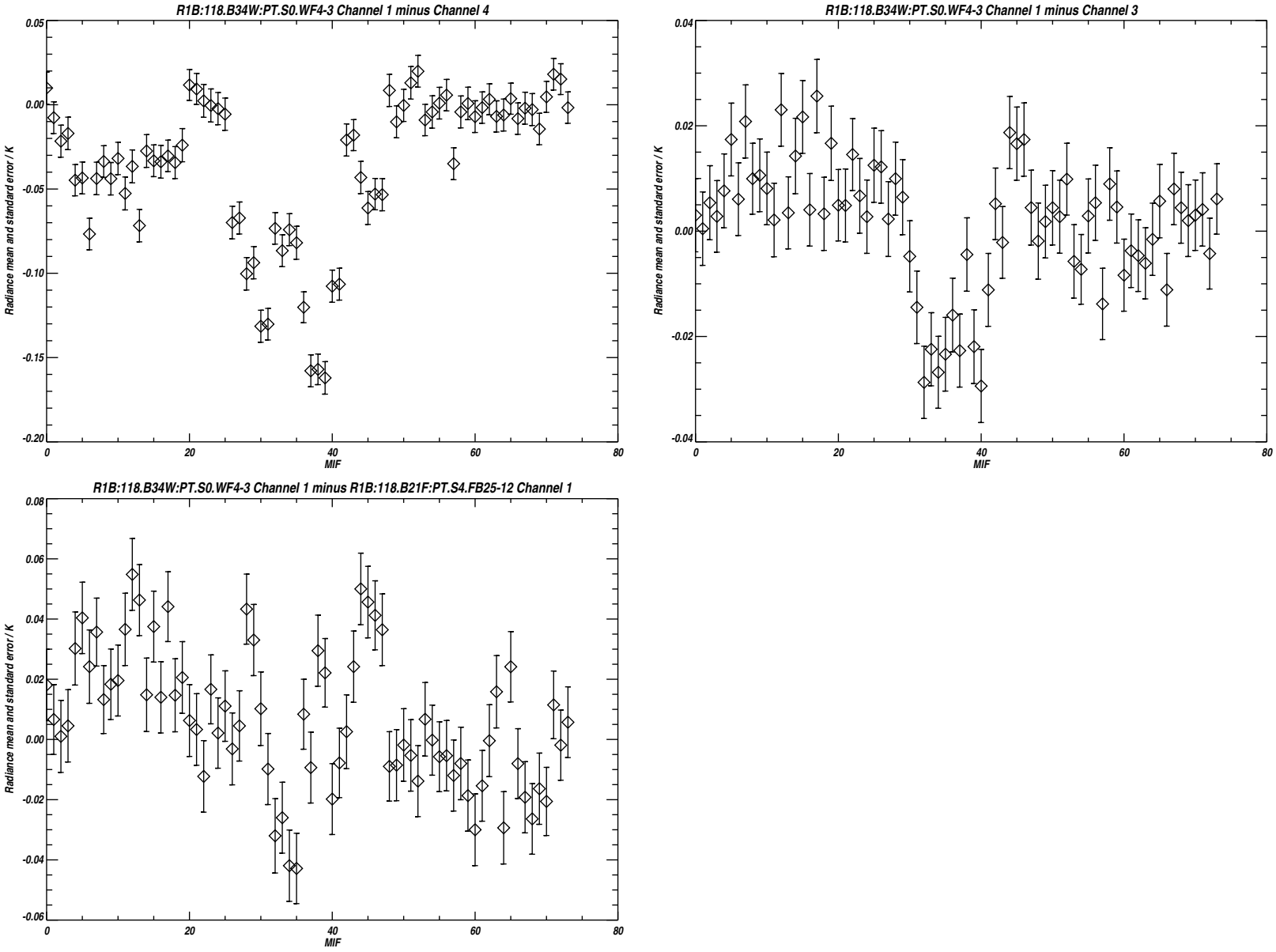

Figure B.16: Radiance differences between the 3 channel pairs plotted in Figure B.15. The vertical bars indicating the *rms* uncertainty due to noise. See text for additional details.

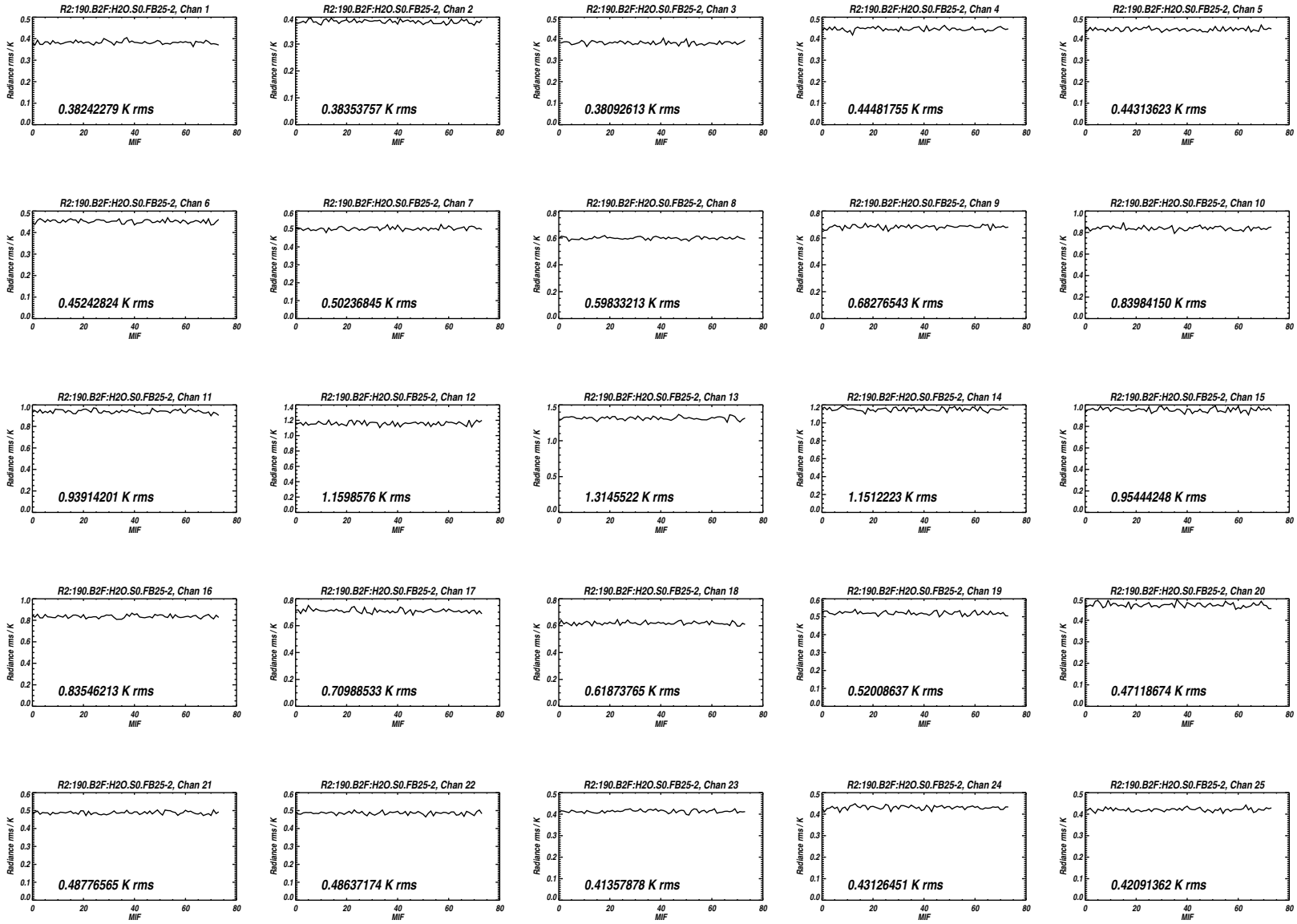

Figure B.17: Measured *rms* noise for all 25 channels of Band 2 for the MIFs treated as Limb views in Level 1 processing.

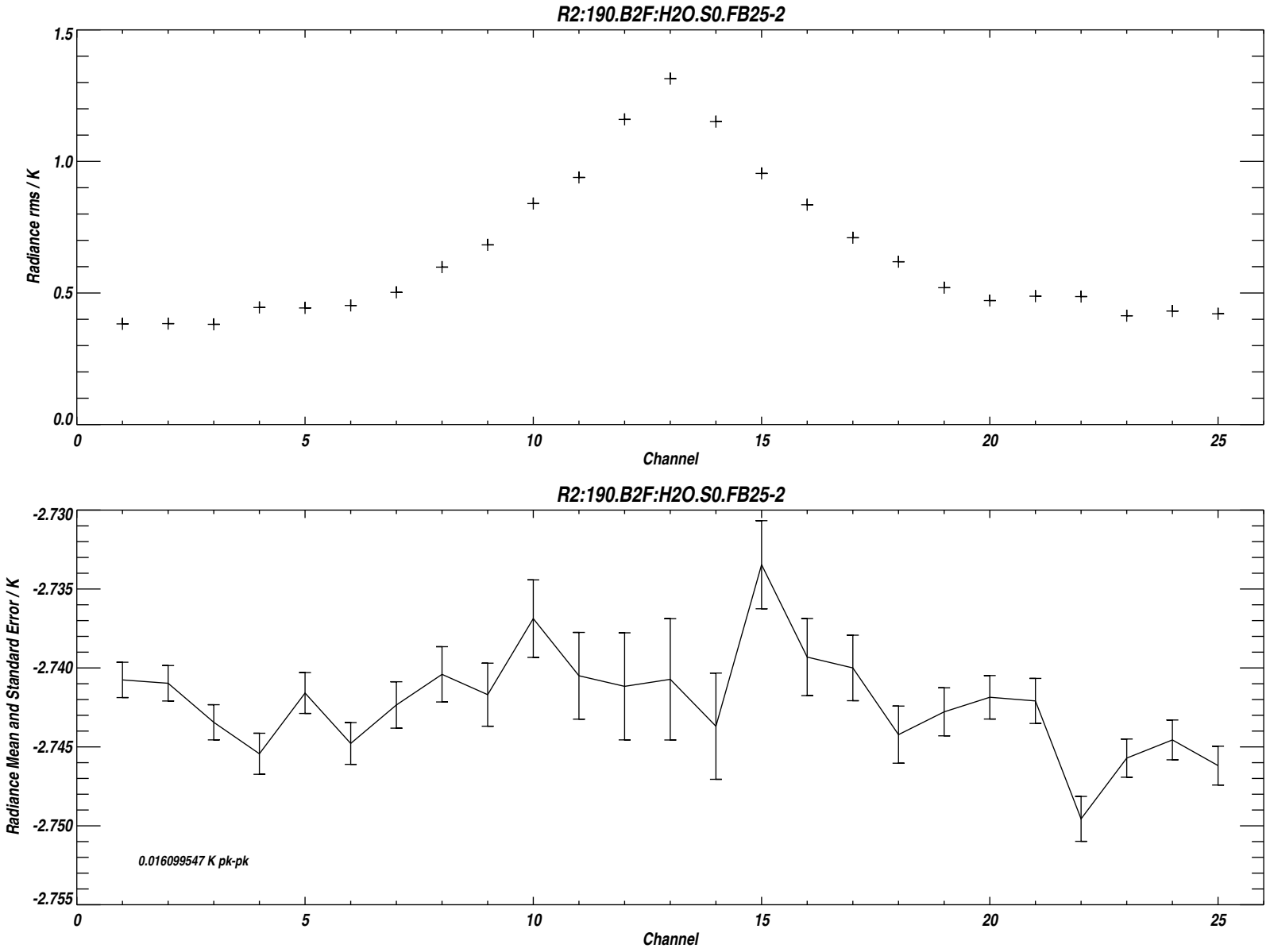

Figure B.18: Measured *rms* noise for each channel of Band 2 (upper panel). The lower panel plots the difference between the mean 'Limb' and reference radiances, the vertical bars indicating the *rms* uncertainty due to noise.

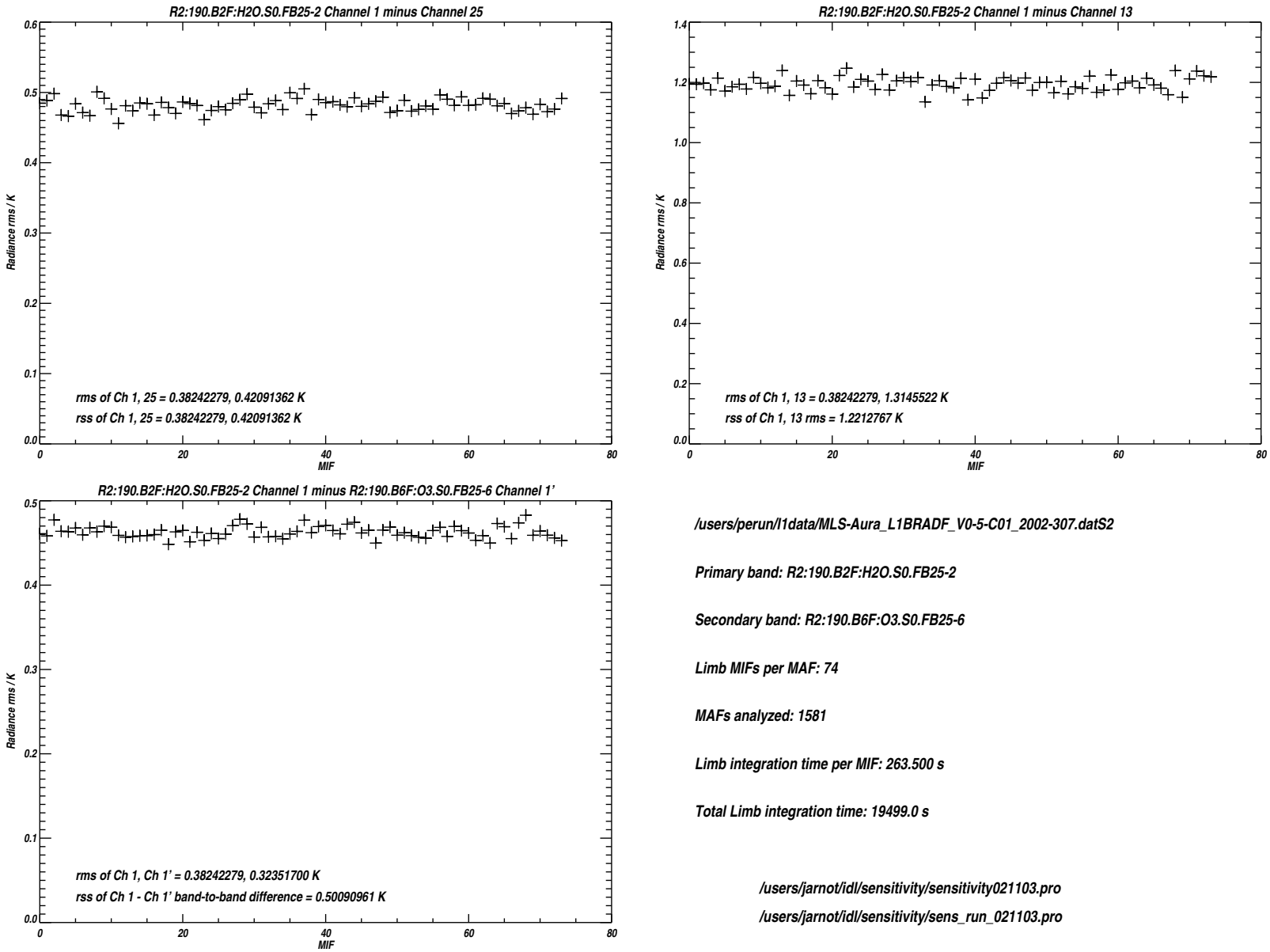

Figure B.19: Measured *rms* noise on the radiance differences between Channels 1 and 25 of Band 2 (upper left panel), Channels 1 and 13 of Band 2 (upper right panel), and between Channel 1 of Band 2 and Channel 1 of Band 6.

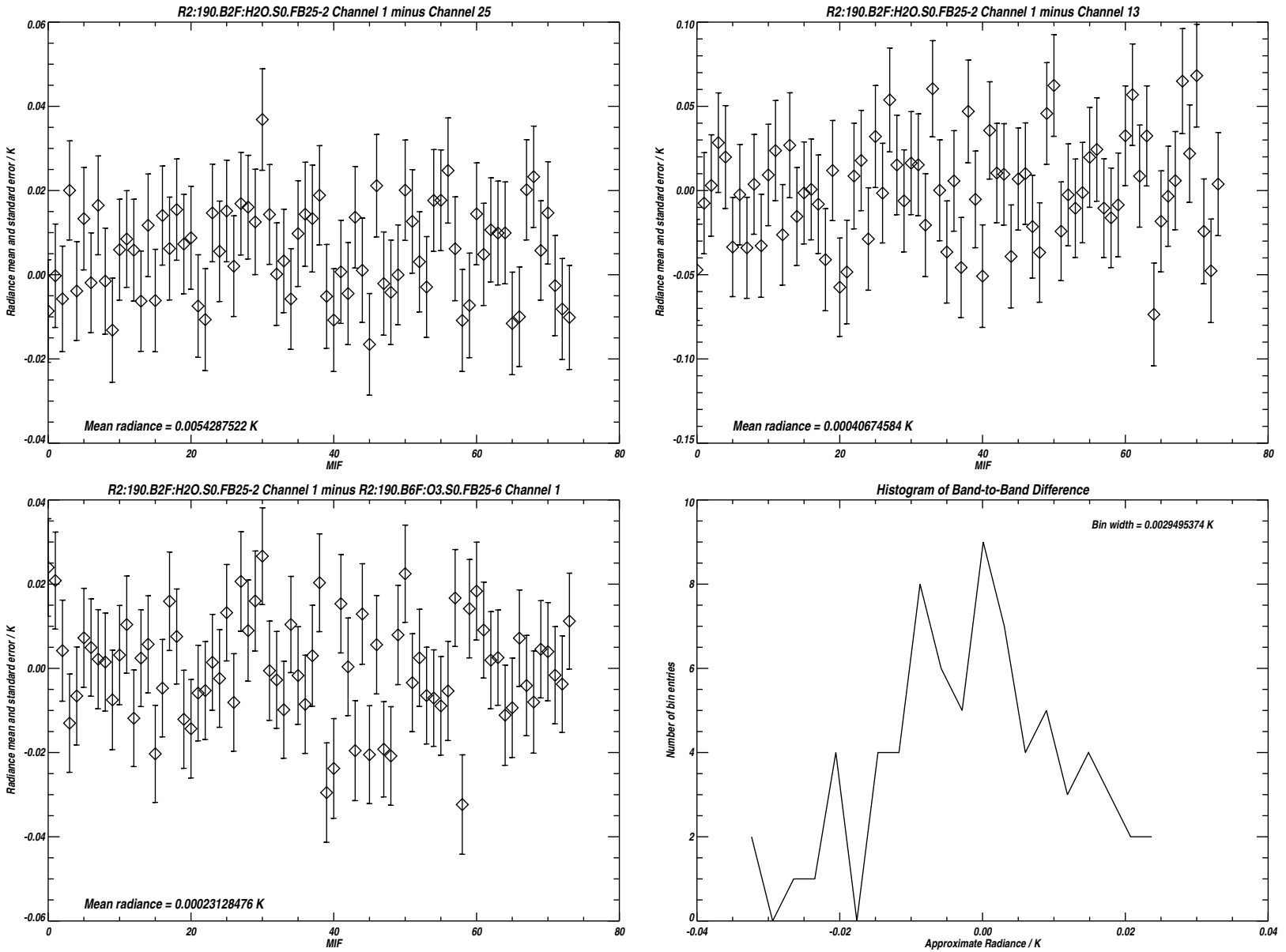

Figure B.20: Radiance differences between the 3 channel pairs plotted in Figure B.19. The vertical bars indicating the *rms* uncertainty due to noise. The lower right hand panel is a histogram of the data in the panel to its left. See text for additional details.

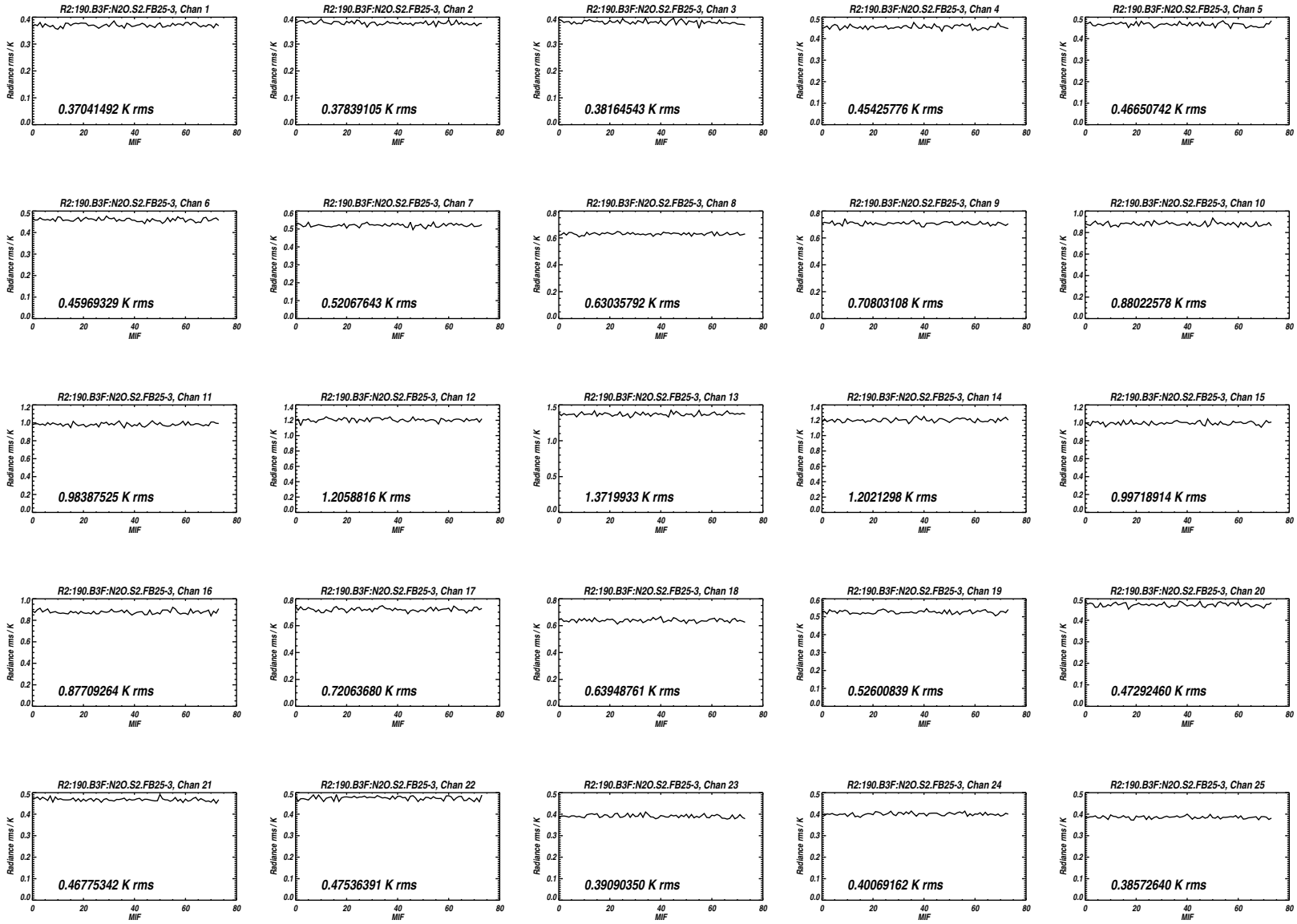

Figure B.21: Measured *rms* noise for all 25 channels of Band 3 for the MIFs treated as Limb views in Level 1 processing.

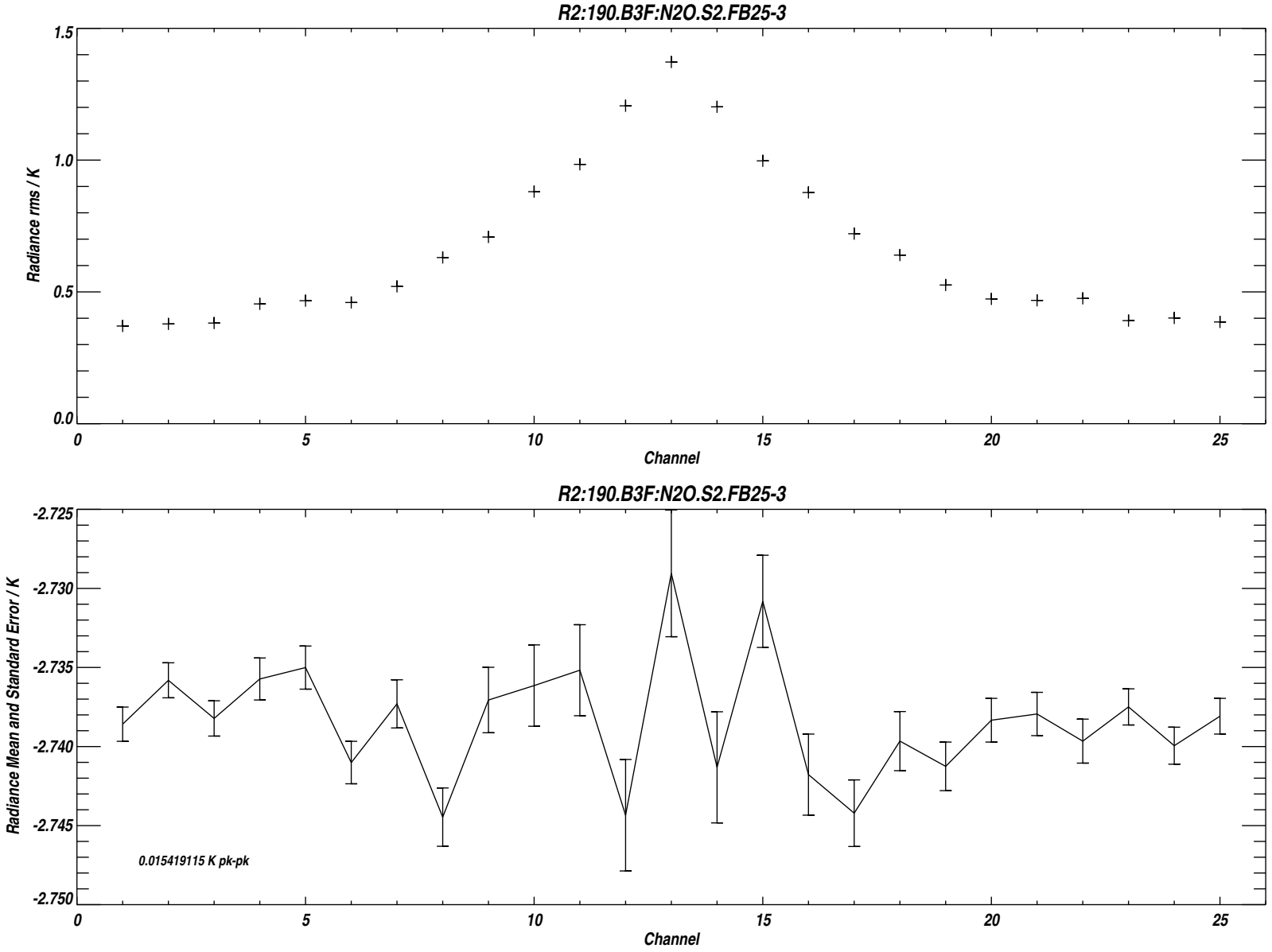

Figure B.22: Measured *rms* noise for each channel of Band 3 (upper panel). The lower panel plots the difference between the mean 'Limb' and reference radiances, the vertical bars indicating the *rms* uncertainty due to noise.

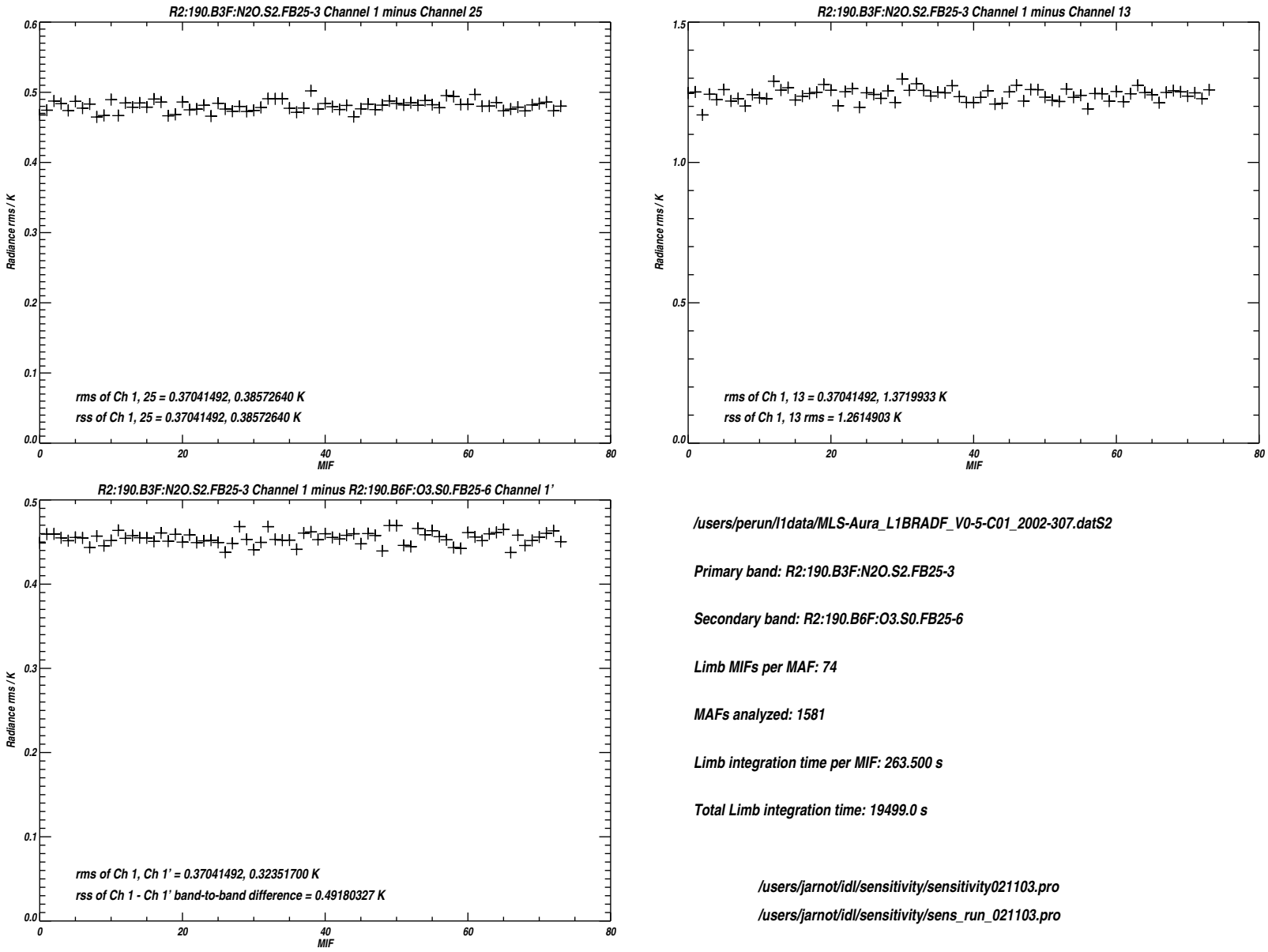

Figure B.23: Measured *rms* noise on the radiance differences between Channels 1 and 25 of Band 3 (upper left panel), Channels 1 and 13 of Band 3 (upper right panel), and between Channel 1 of Band 3 and Channel 1 of Band 6.

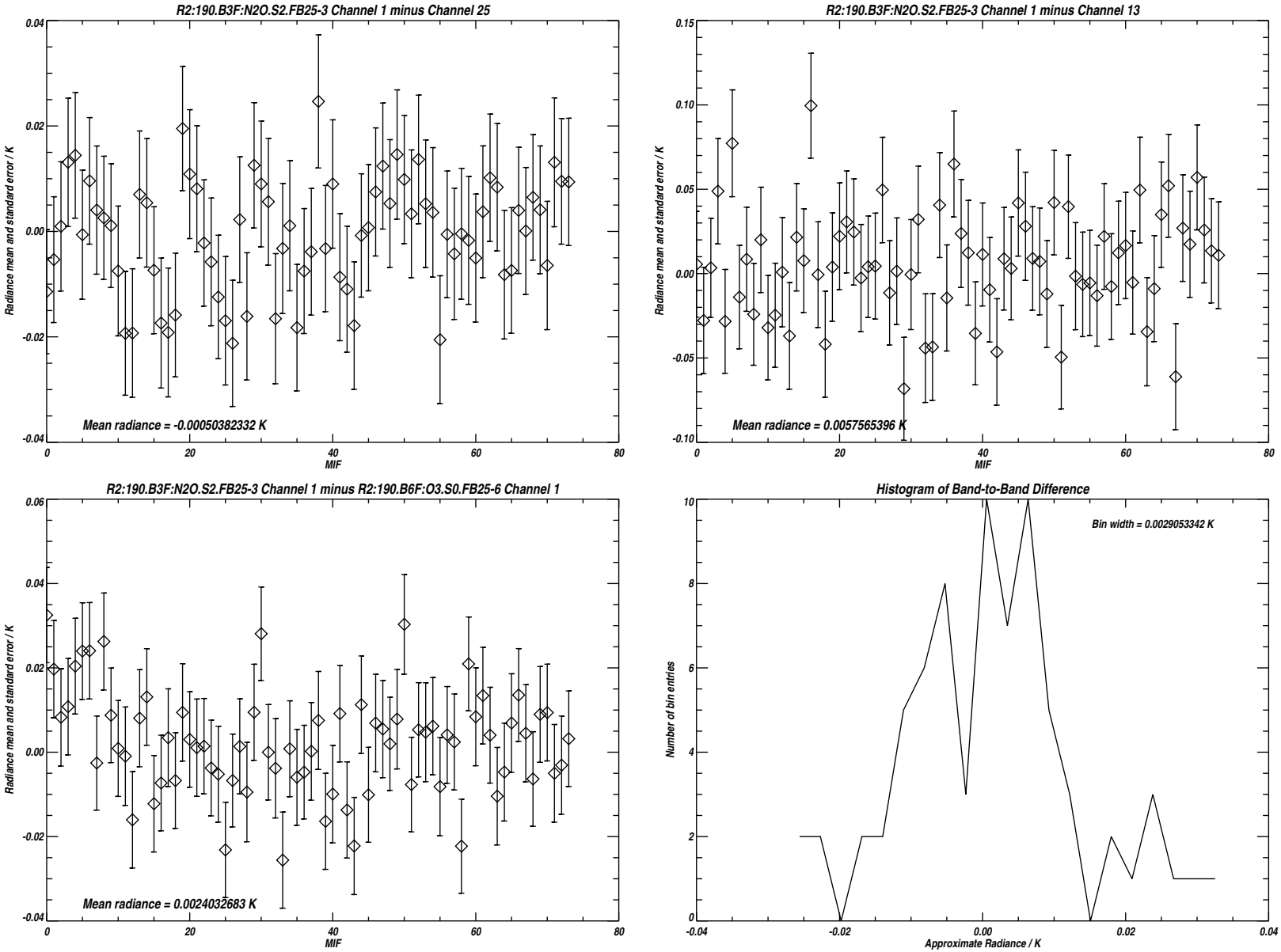

Figure B.24: Radiance differences between the 3 channel pairs plotted in Figure B.23. The vertical bars indicating the *rms* uncertainty due to noise. The lower right hand panel is a histogram of the data in the panel to its left. See text for additional details.

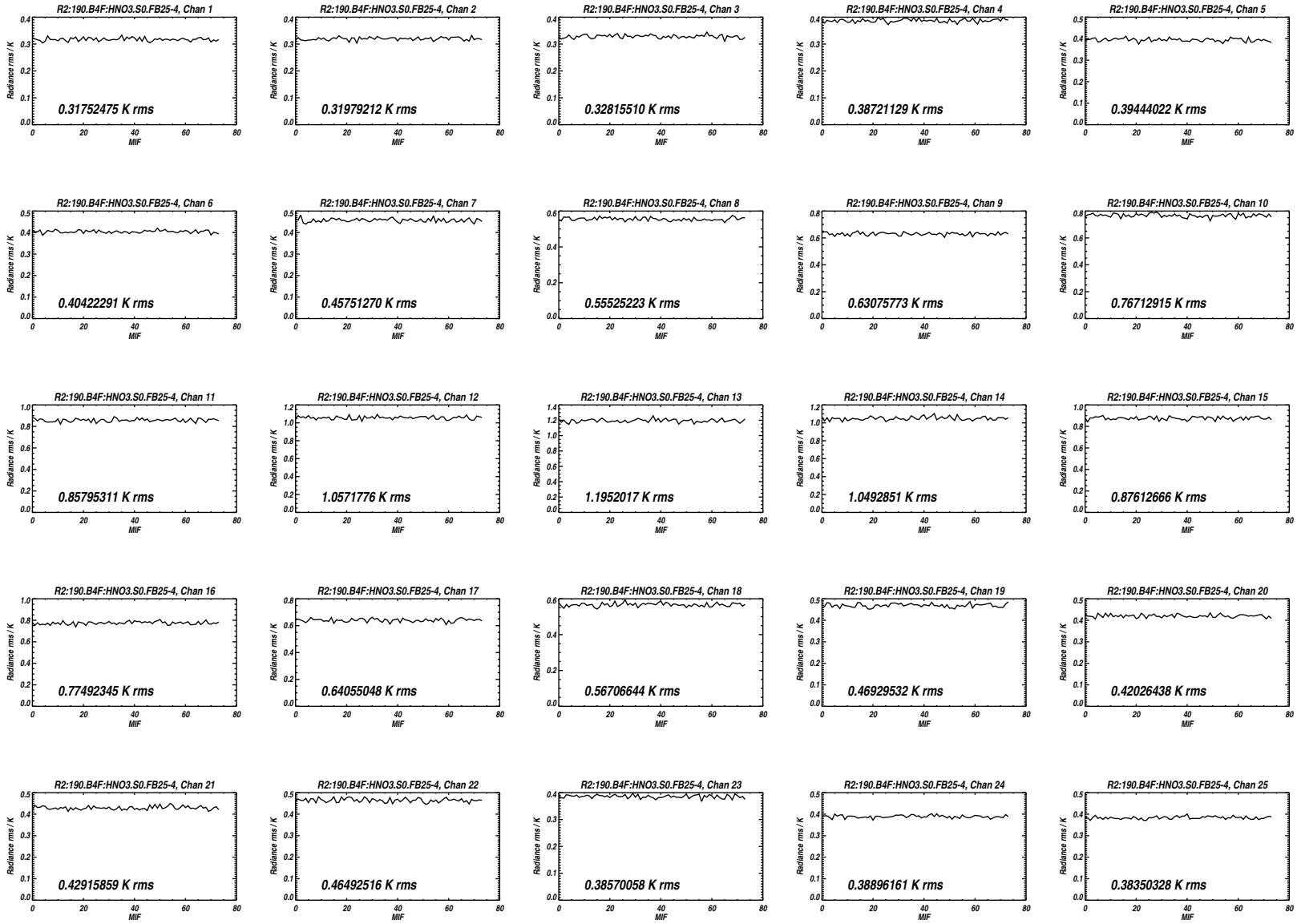

Figure B.25: Measured *rms* noise for all 25 channels of Band 4 for the MIFs treated as Limb views in Level 1 processing.

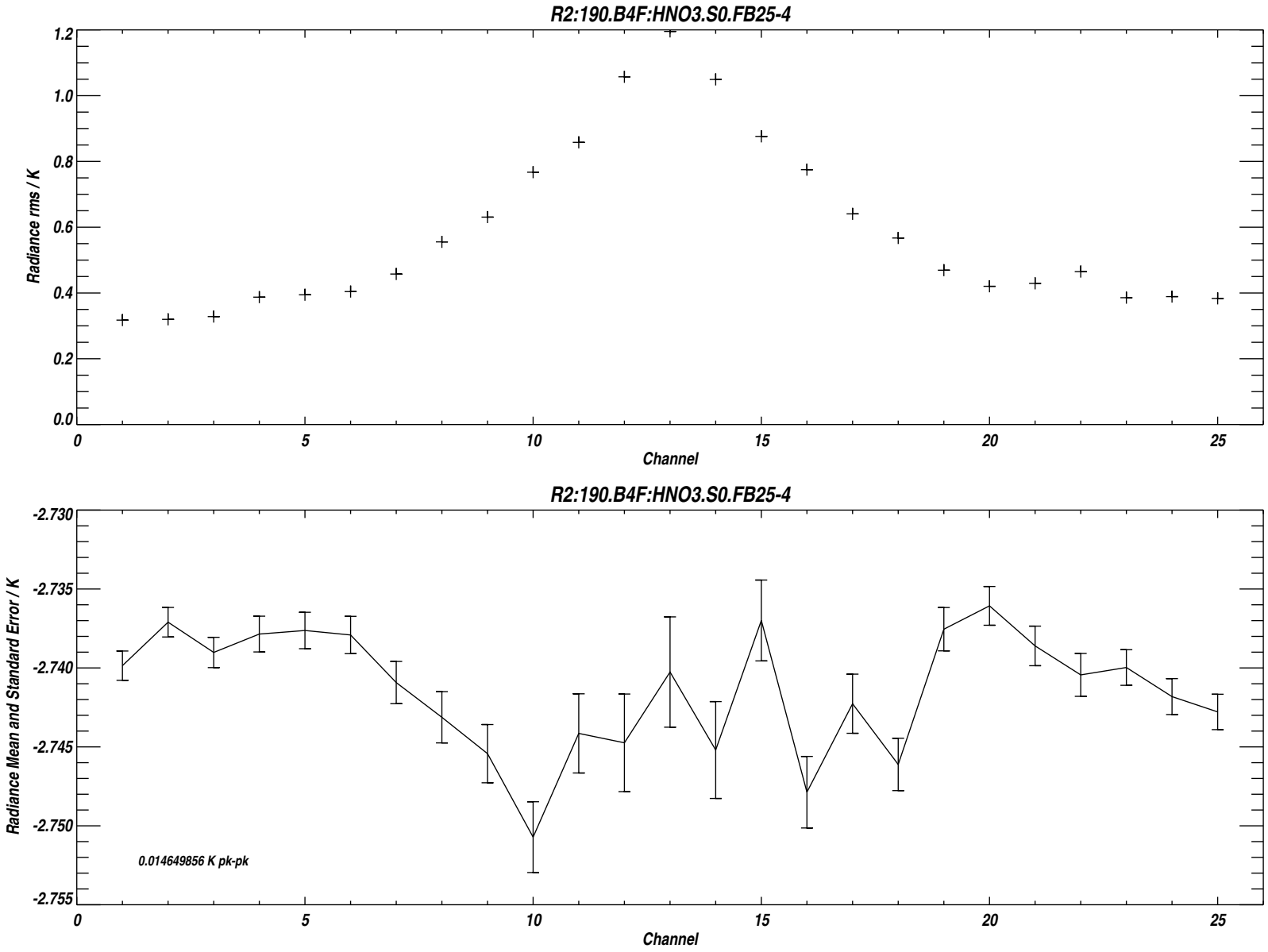

Figure B.26: Measured *rms* noise for each channel of Band 4 (upper panel). The lower panel plots the difference between the mean 'Limb' and reference radiances, the vertical bars indicating the *rms* uncertainty due to noise.

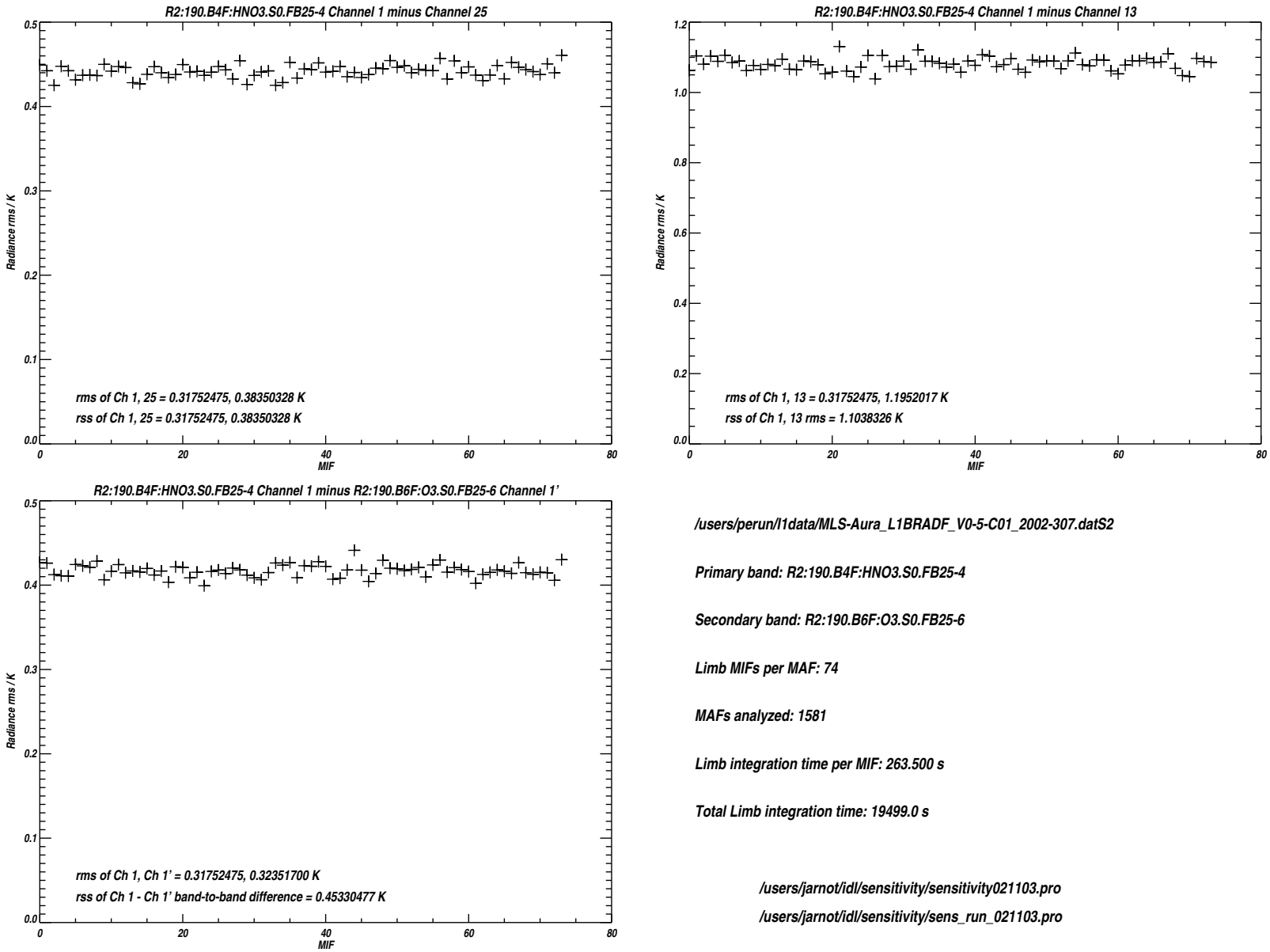

Figure B.27: Measured *rms* noise on the radiance differences between Channels 1 and 25 of Band 4 (upper left panel), Channels 1 and 13 of Band 4 (upper right panel), and between Channel 1 of Band 4 and Channel 1 of Band 6.

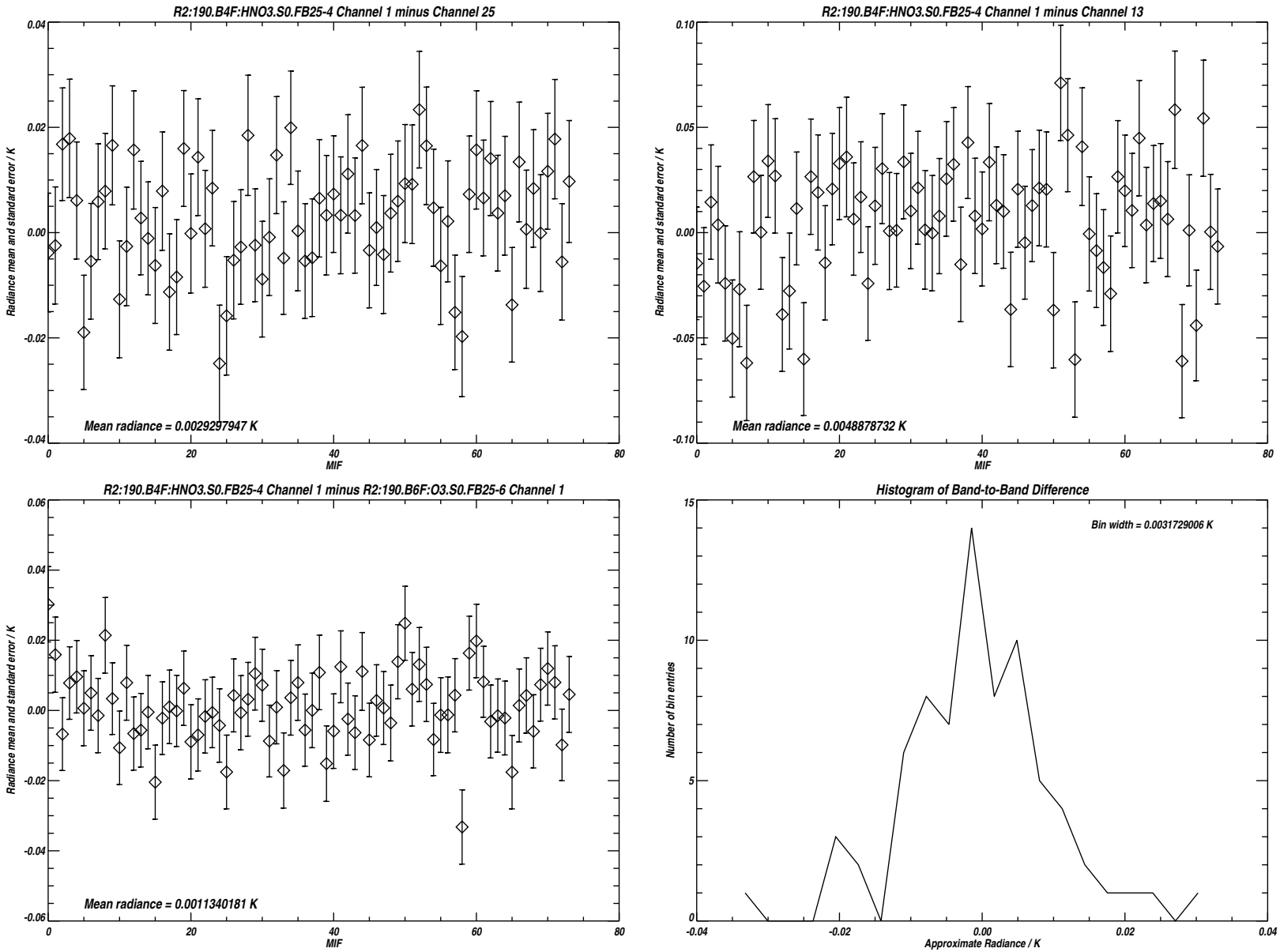

Figure B.28: Radiance differences between the 3 channel pairs plotted in Figure B.27. The vertical bars indicating the *rms* uncertainty due to noise. The lower right hand panel is a histogram of the data in the panel to its left. See text for additional details.

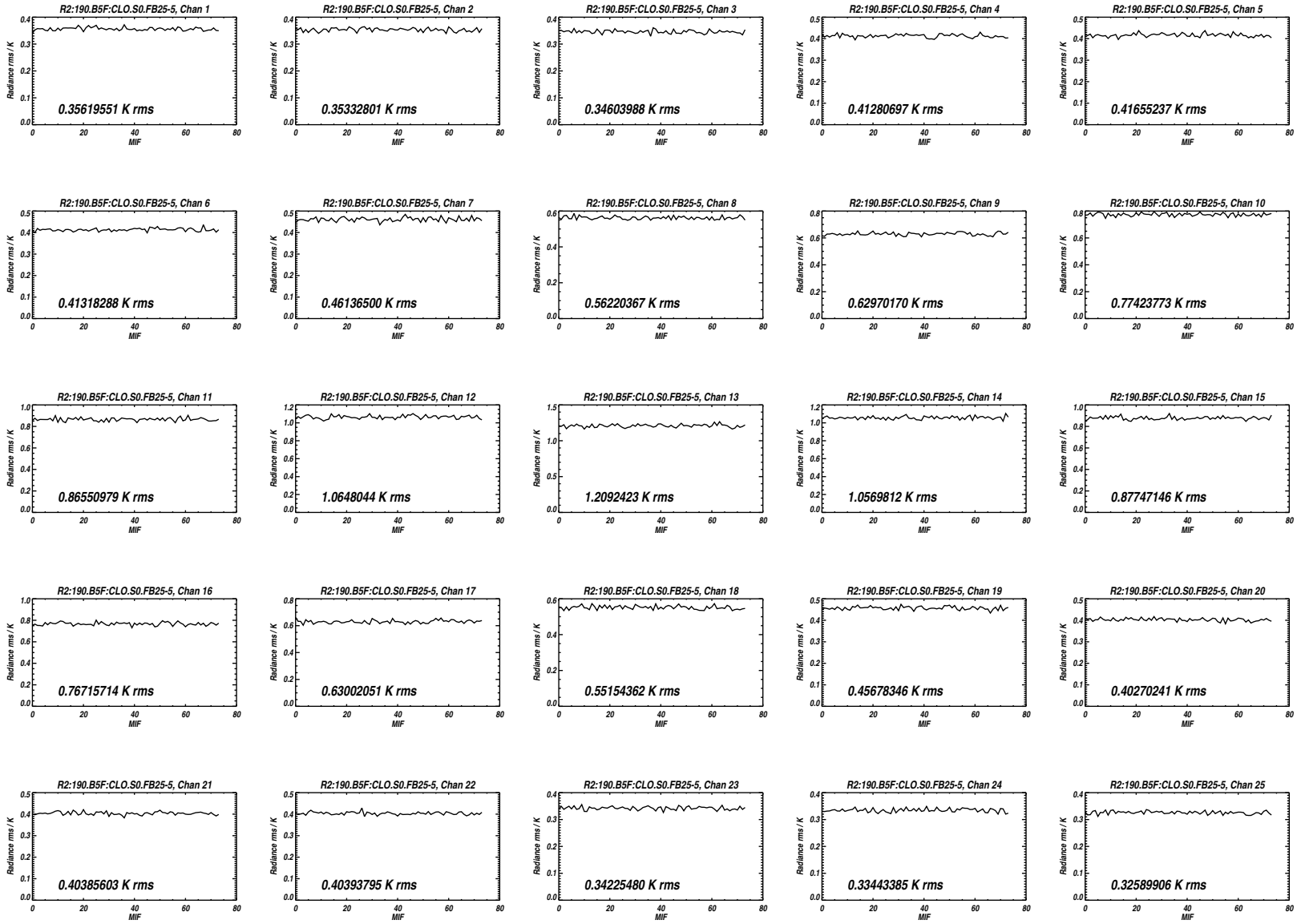

Figure B.29: Measured *rms* noise for all 25 channels of Band 5 for the MIFs treated as Limb views in Level 1 processing.

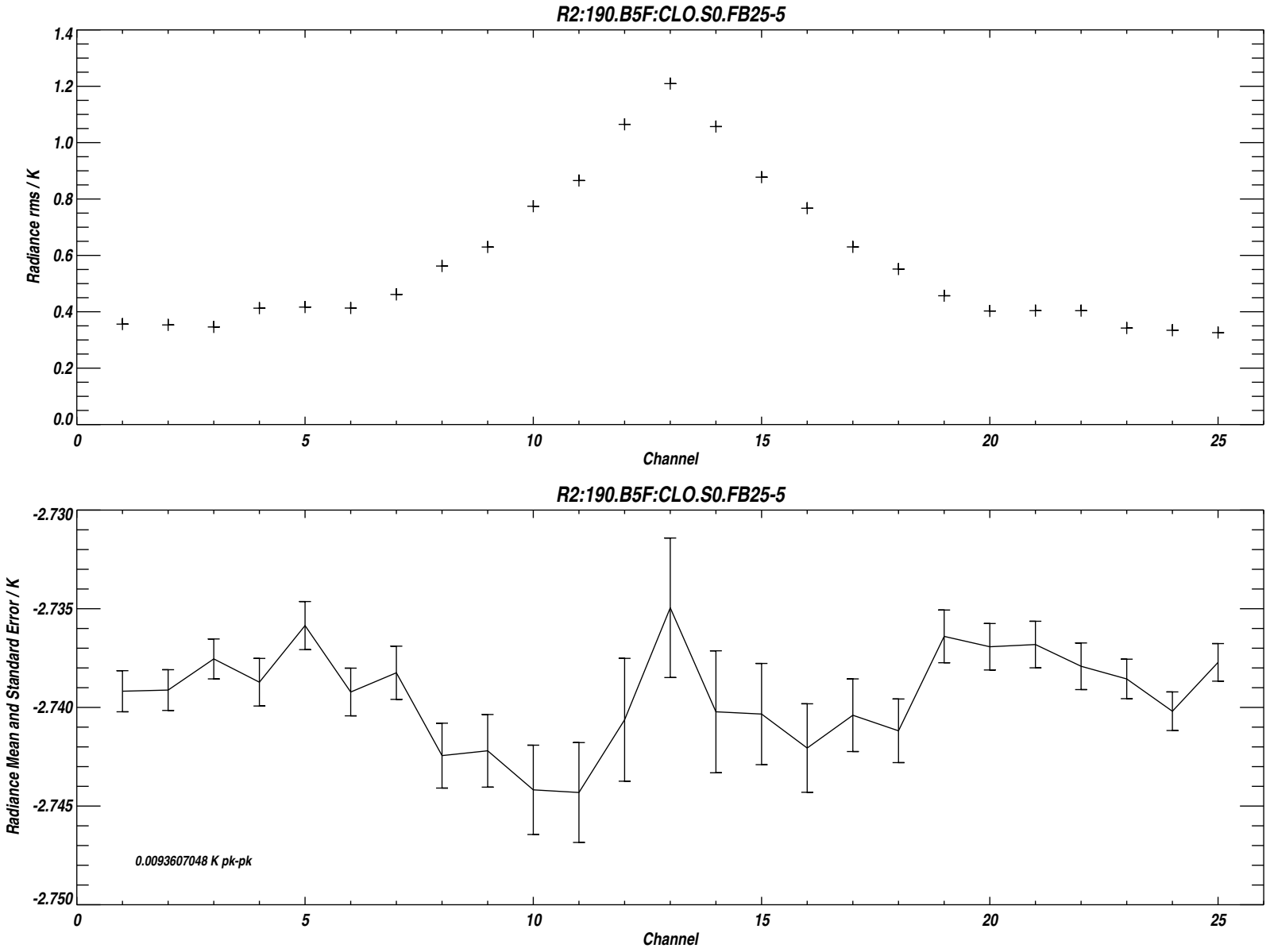

Figure B.30: Measured *rms* noise for each channel of Band 5 (upper panel). The lower panel plots the difference between the mean 'Limb' and reference radiances, the vertical bars indicating the *rms* uncertainty due to noise.

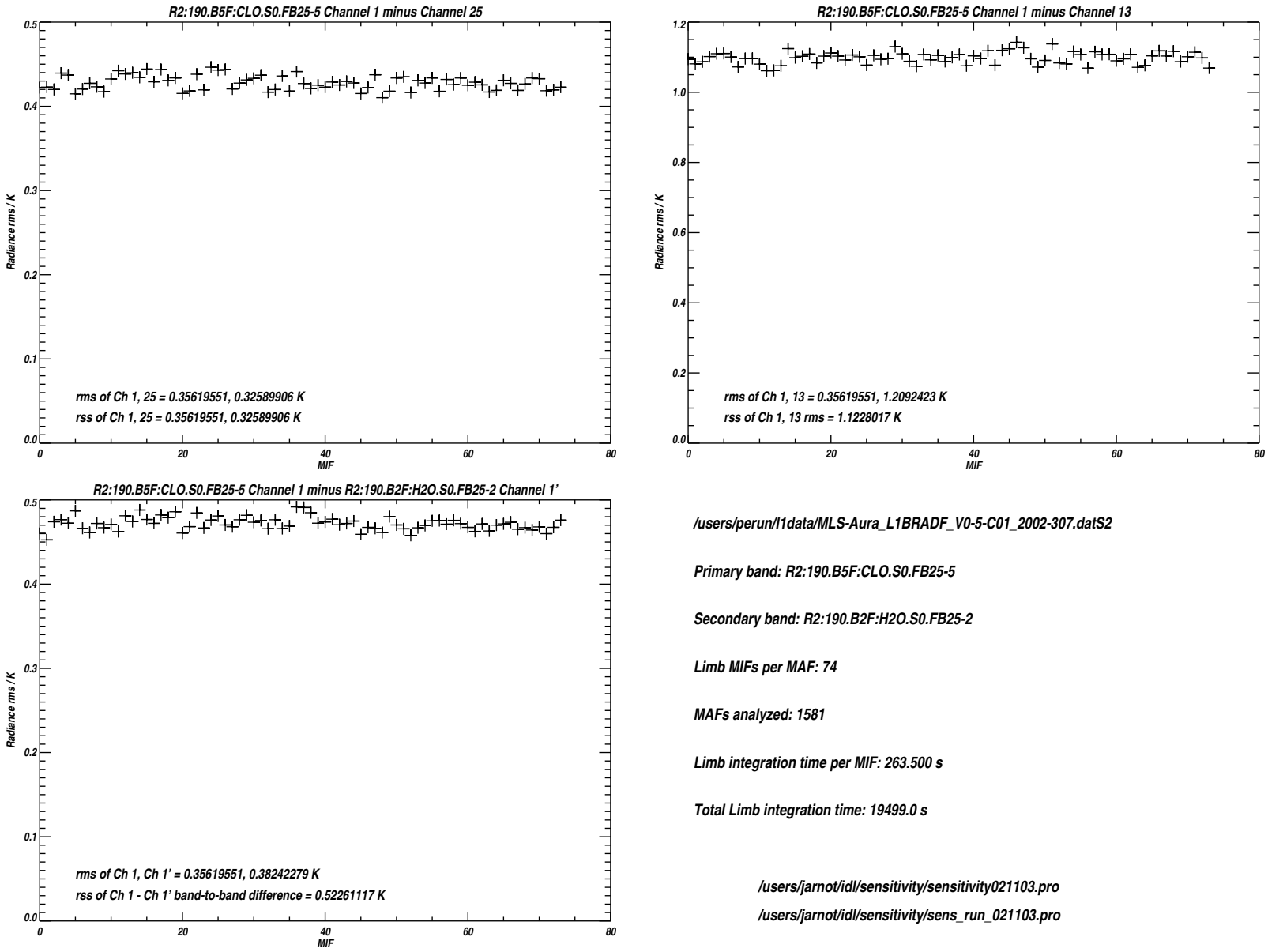

Figure B.31: Measured *rms* noise on the radiance differences between Channels 1 and 25 of Band 5 (upper left panel), Channels 1 and 13 of Band 5 (upper right panel), and between Channel 1 of Band 5 and Channel 1 of Band 2.

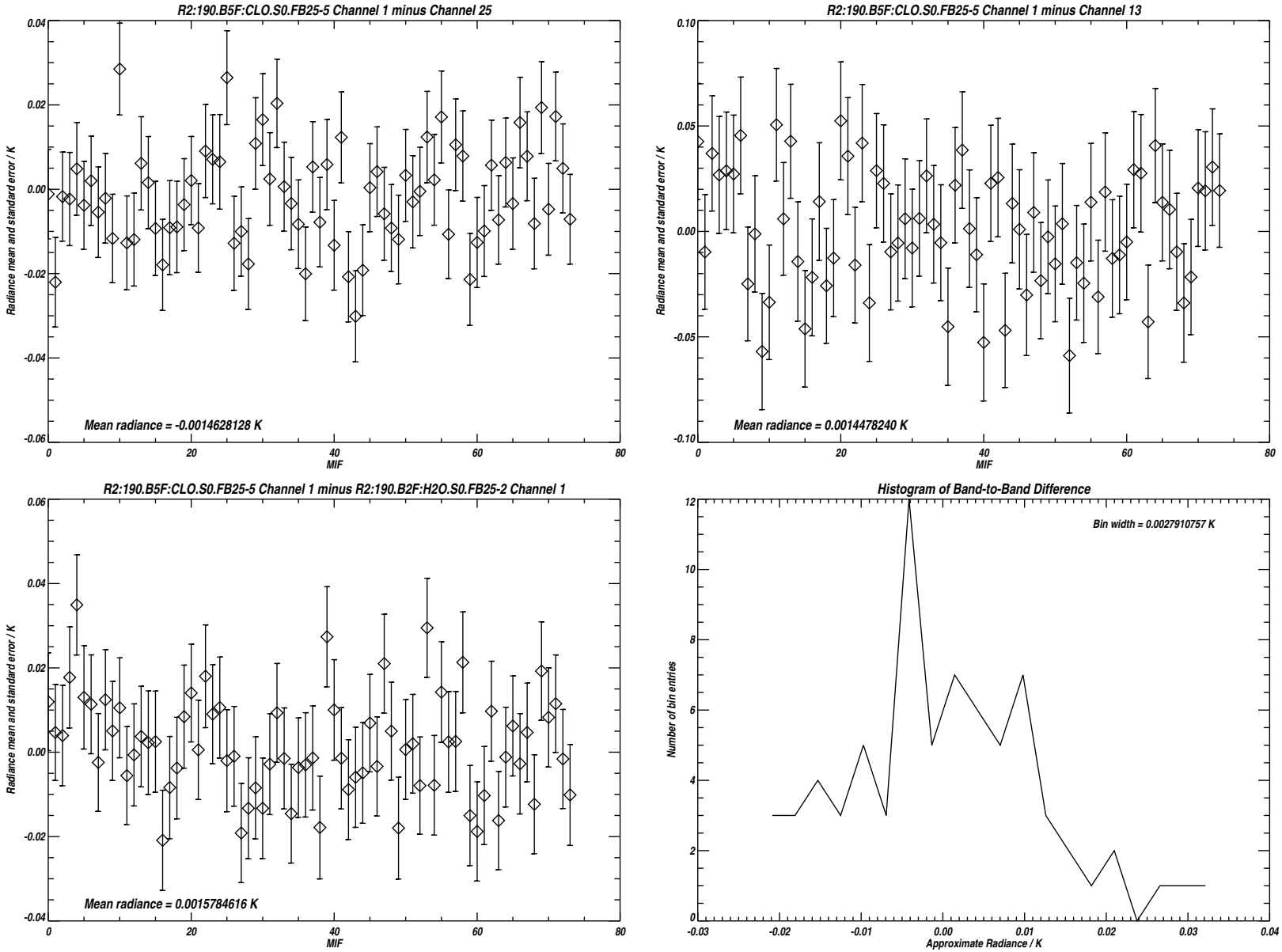

Figure B.32: Radiance differences between the 3 channel pairs plotted in Figure B.31. The vertical bars indicating the *rms* uncertainty due to noise. The lower right hand panel is a histogram of the data in the panel to its left. See text for additional details.

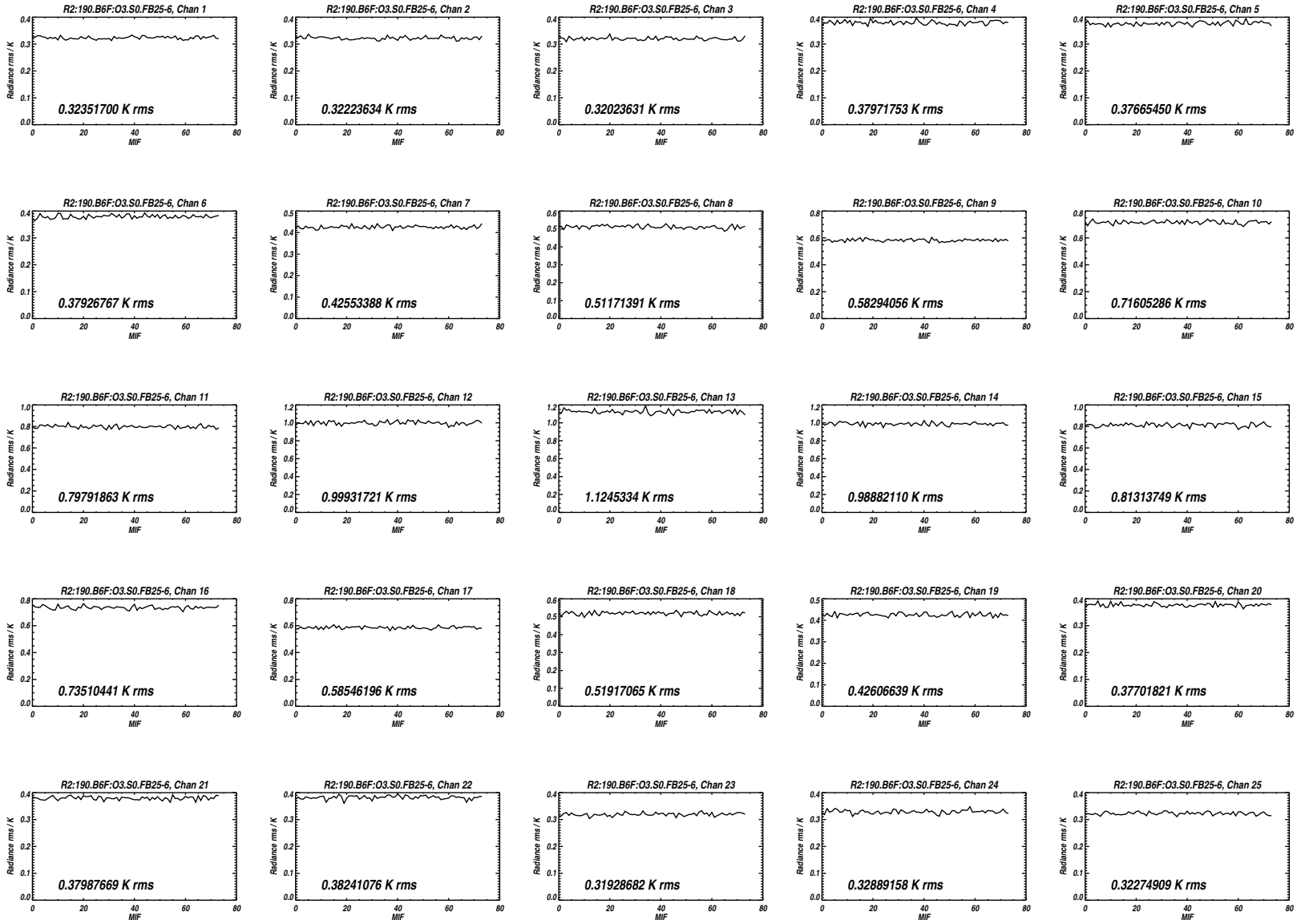

Figure B.33: Measured *rms* noise for all 25 channels of Band 6 for the MIFs treated as Limb views in Level 1 processing.

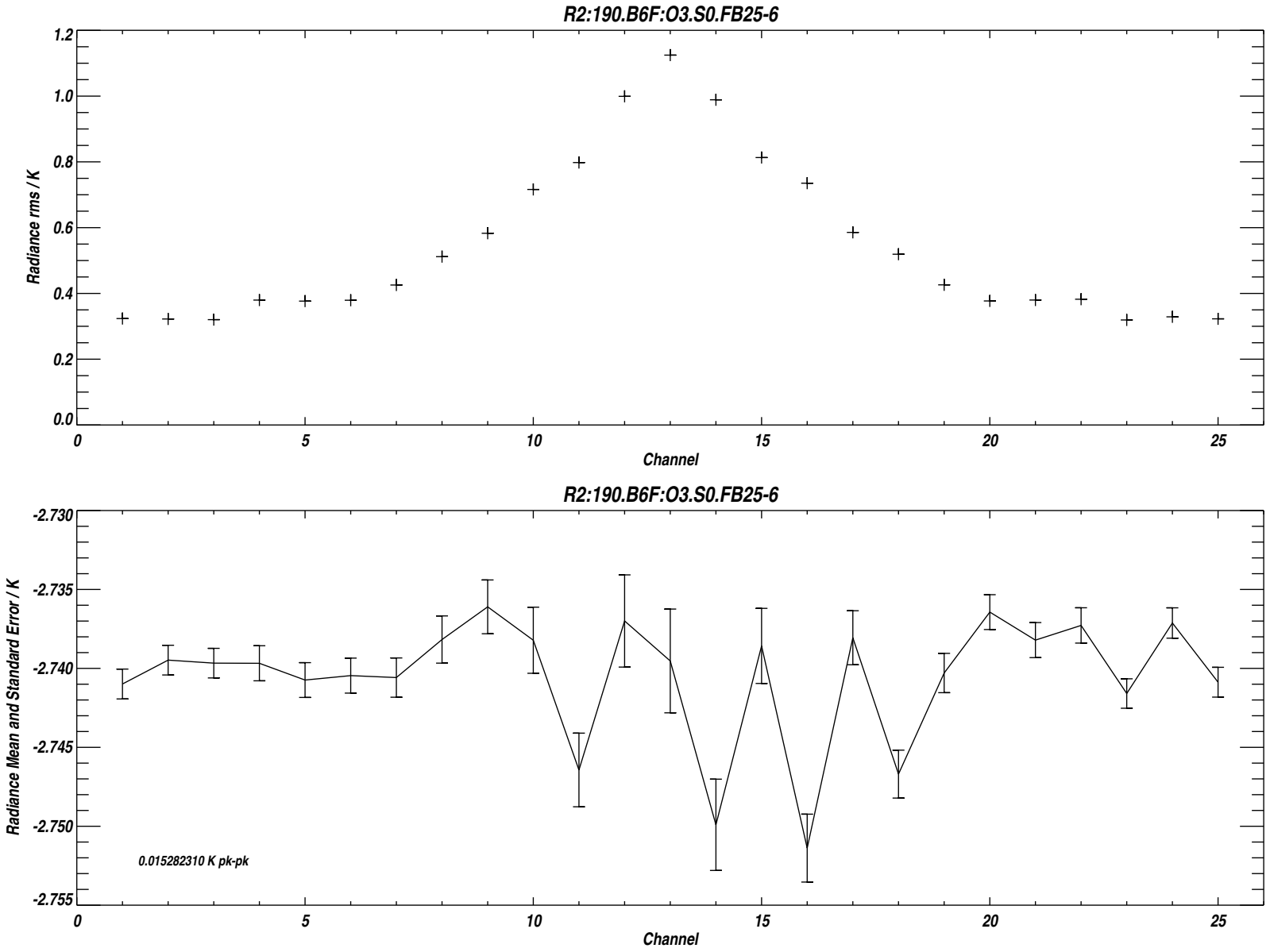

Figure B.34: Measured *rms* noise for each channel of Band 6 (upper panel). The lower panel plots the difference between the mean 'Limb' and reference radiances, the vertical bars indicating the *rms* uncertainty due to noise.

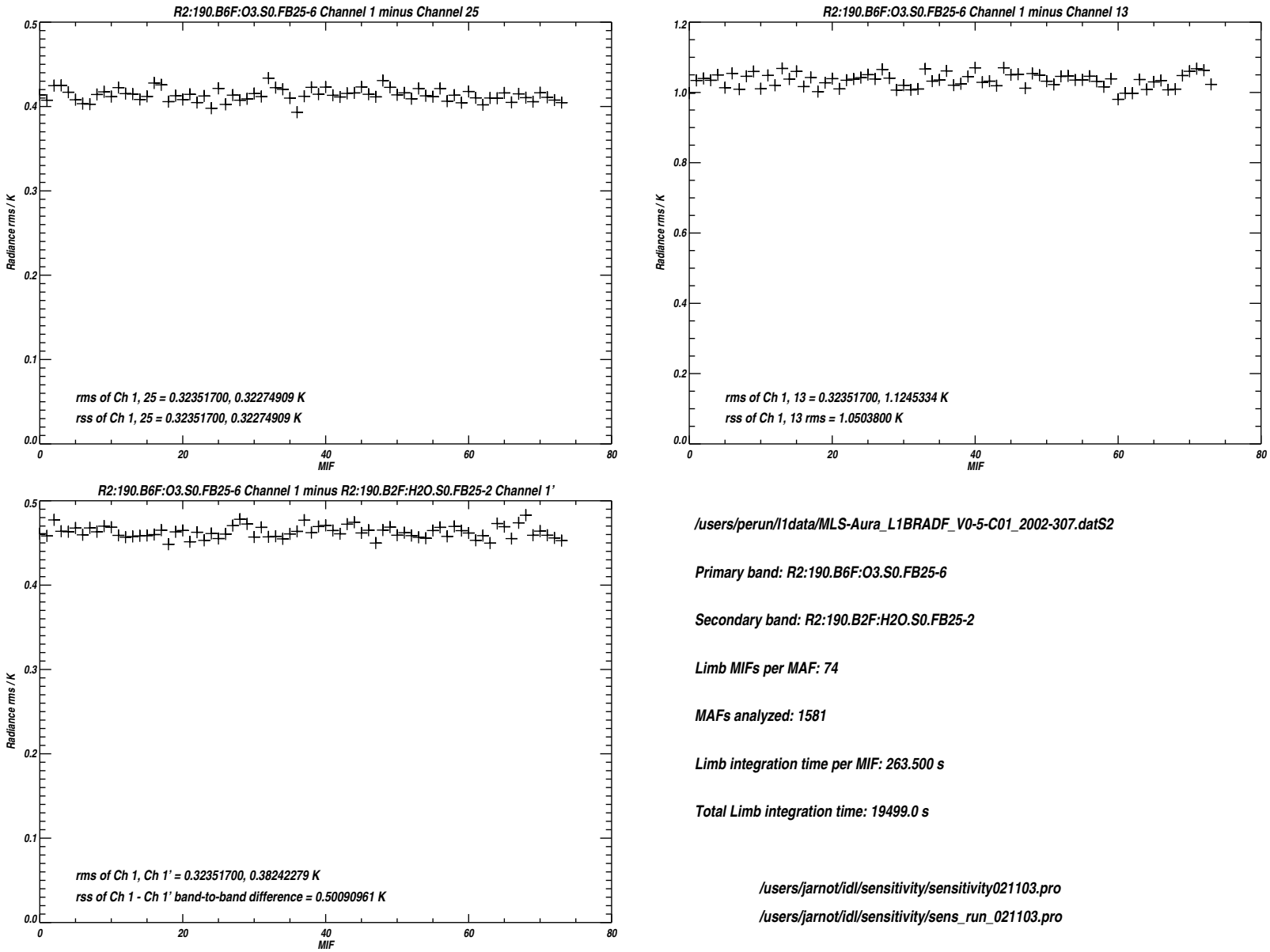

Figure B.35: Measured *rms* noise on the radiance differences between Channels 1 and 25 of Band 6 (upper left panel), Channels 1 and 13 of Band 6 (upper right panel), and between Channel 1 of Band 6 and Channel 1 of Band 2.

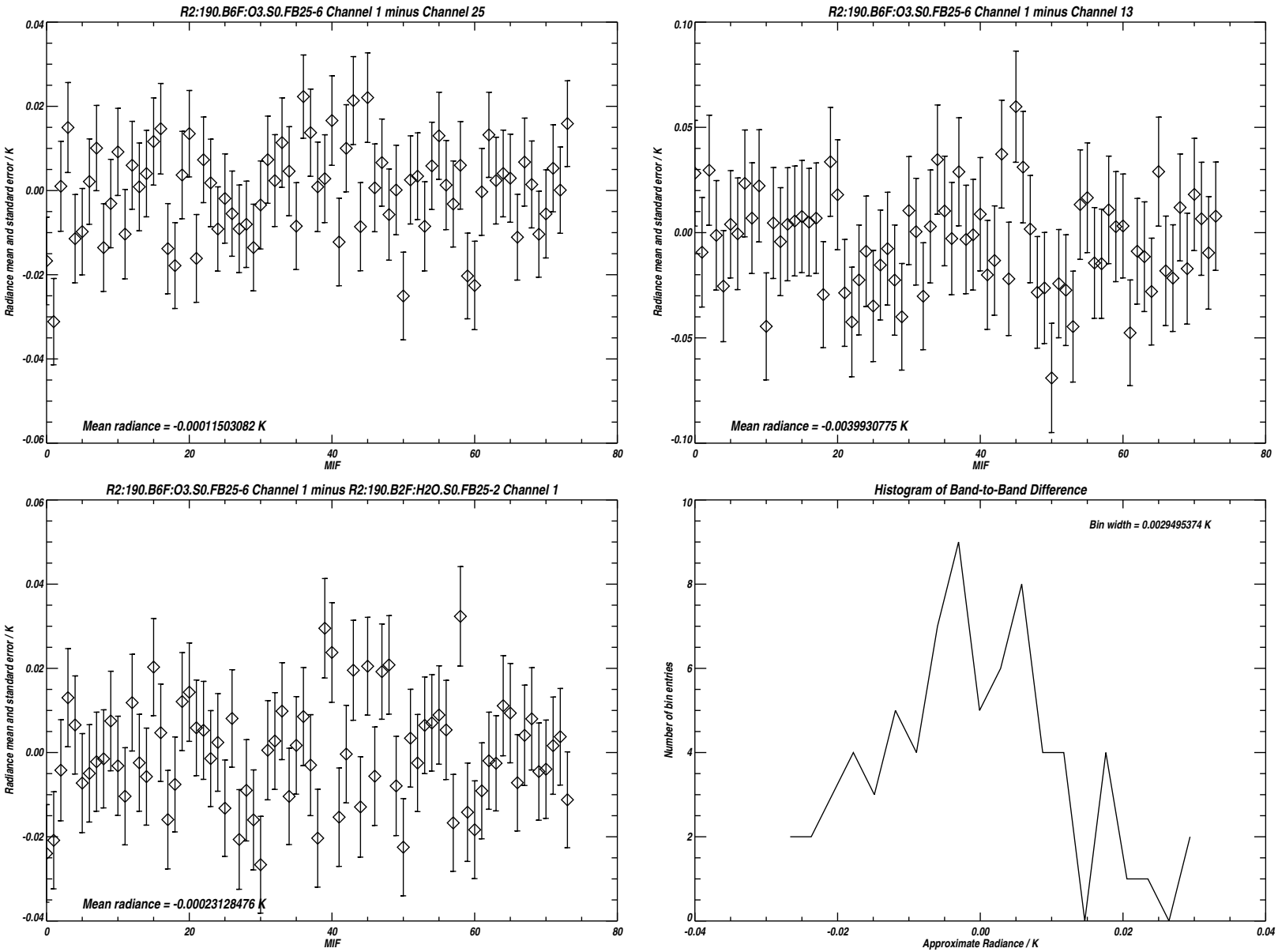

Figure B.36: Radiance differences between the 3 channel pairs plotted in Figure B.35. The vertical bars indicating the *rms* uncertainty due to noise. The lower right hand panel is a histogram of the data in the panel to its left. See text for additional details.

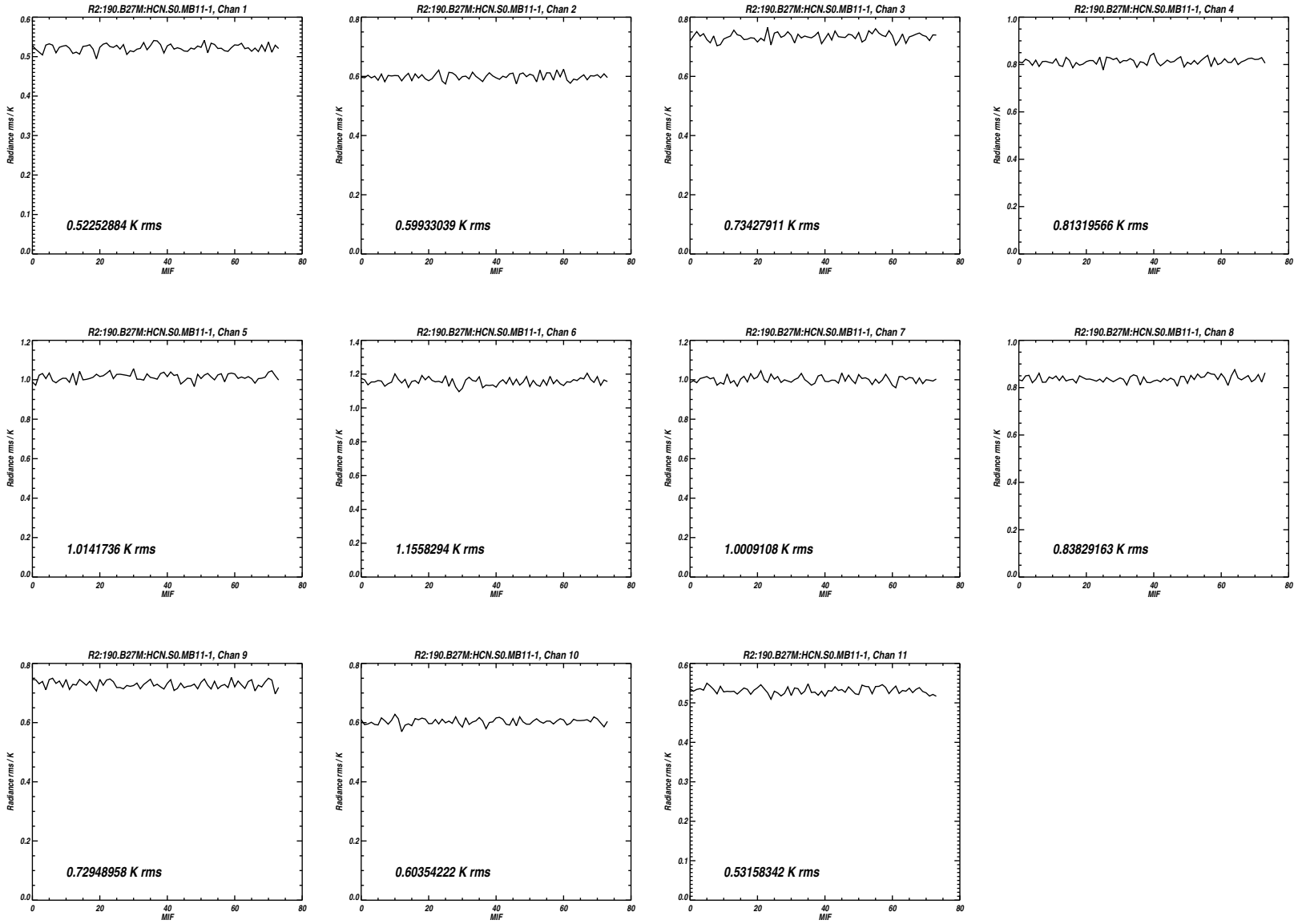

Figure B.37: Measured *rms* noise for all 11 channels of Mid-band 27 for the MIFs treated as Limb views in Level 1 processing.

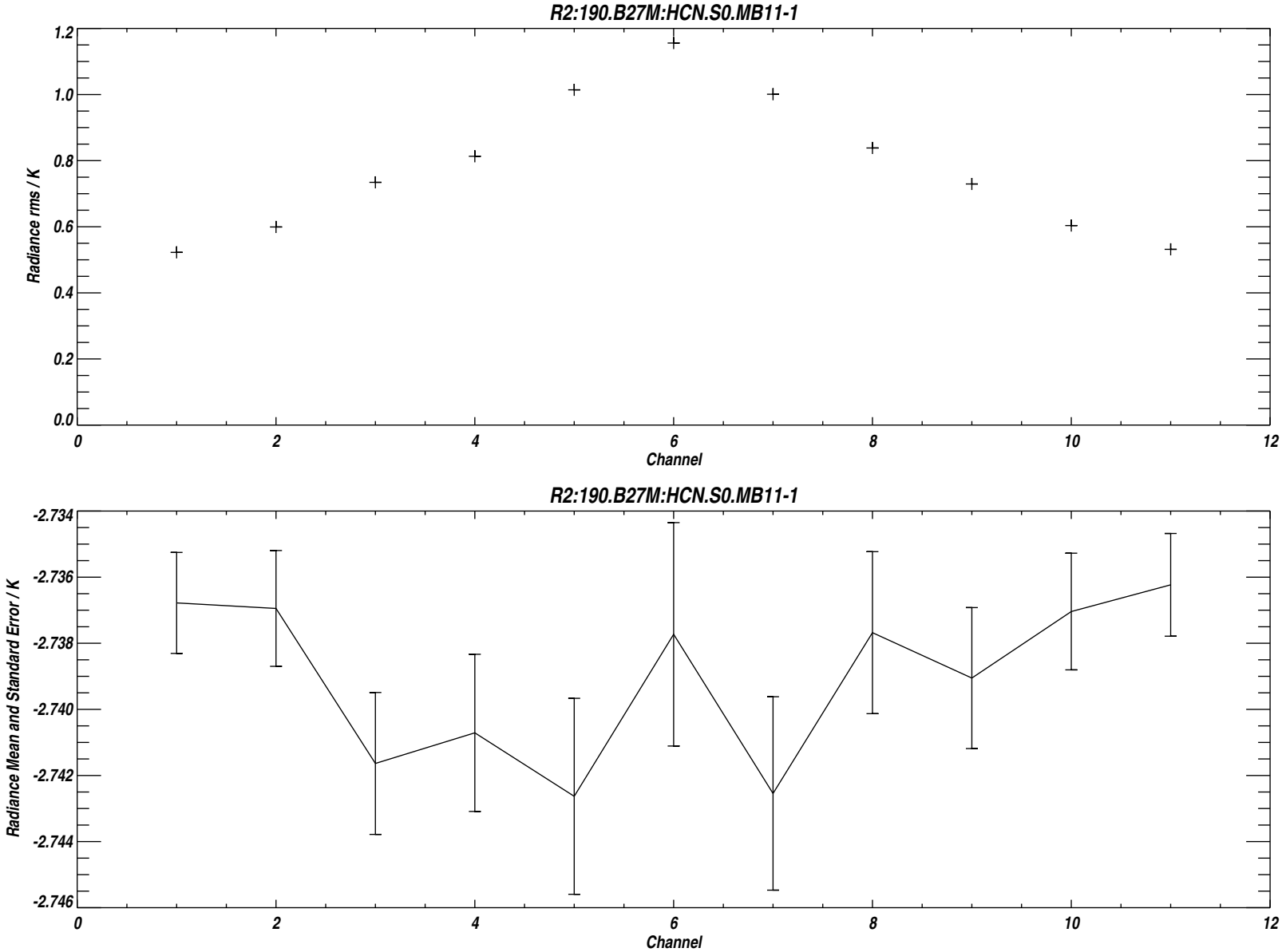

Figure B.38: Measured *rms* noise for each channel of Mid-band 27 (upper panel). The lower panel plots the difference between the mean 'Limb' and reference radiances, the vertical bars indicating the *rms* uncertainty due to noise.

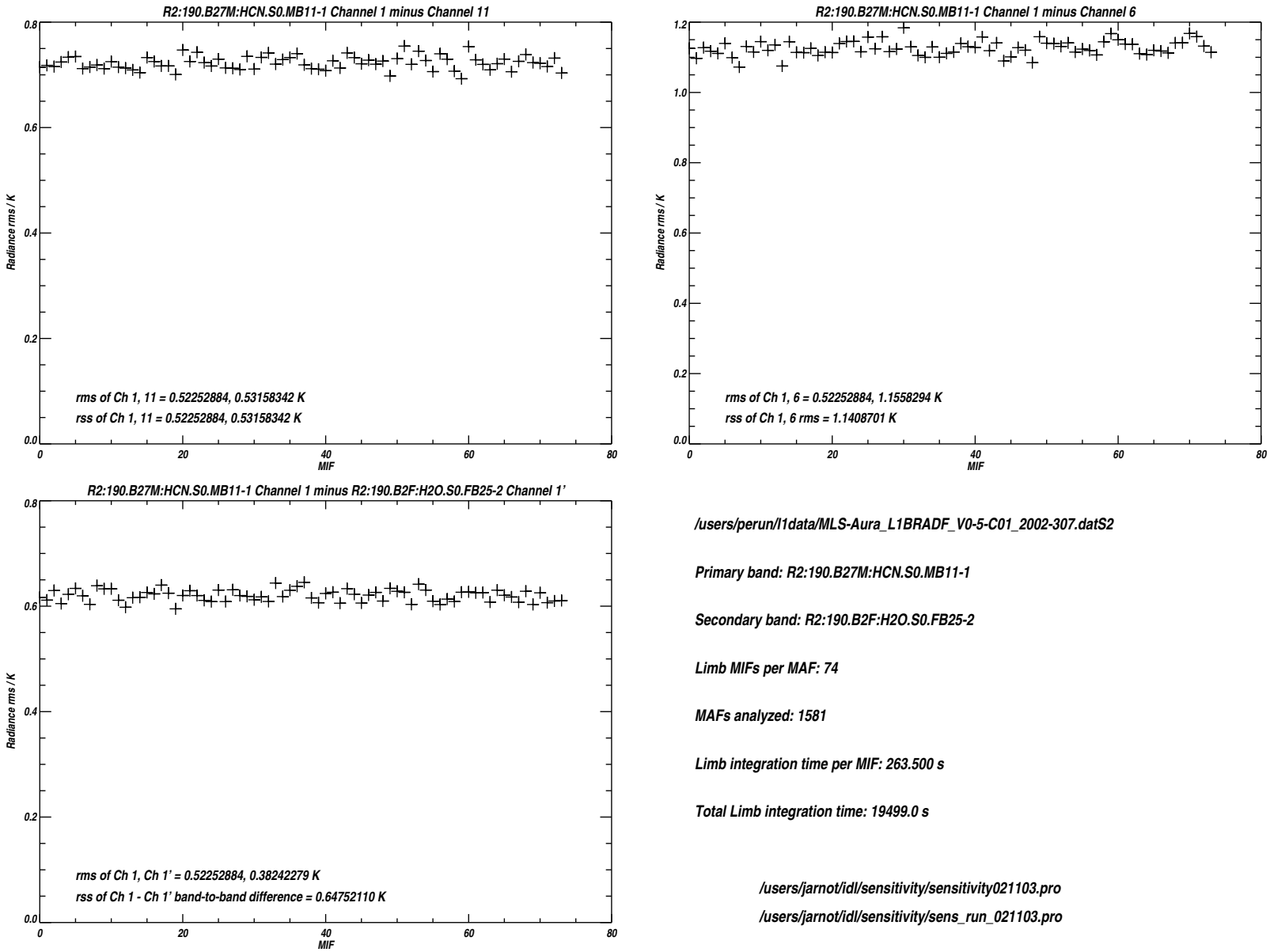

Figure B.39: Measured *rms* noise on the radiance differences between Channels 1 and 11 of Mid-band 27 (upper left panel), Channels 1 and 6 of Mid-band 27 (upper right panel), and between Channel 1 of Mid-band 27 and Channel 1 of Band 2.

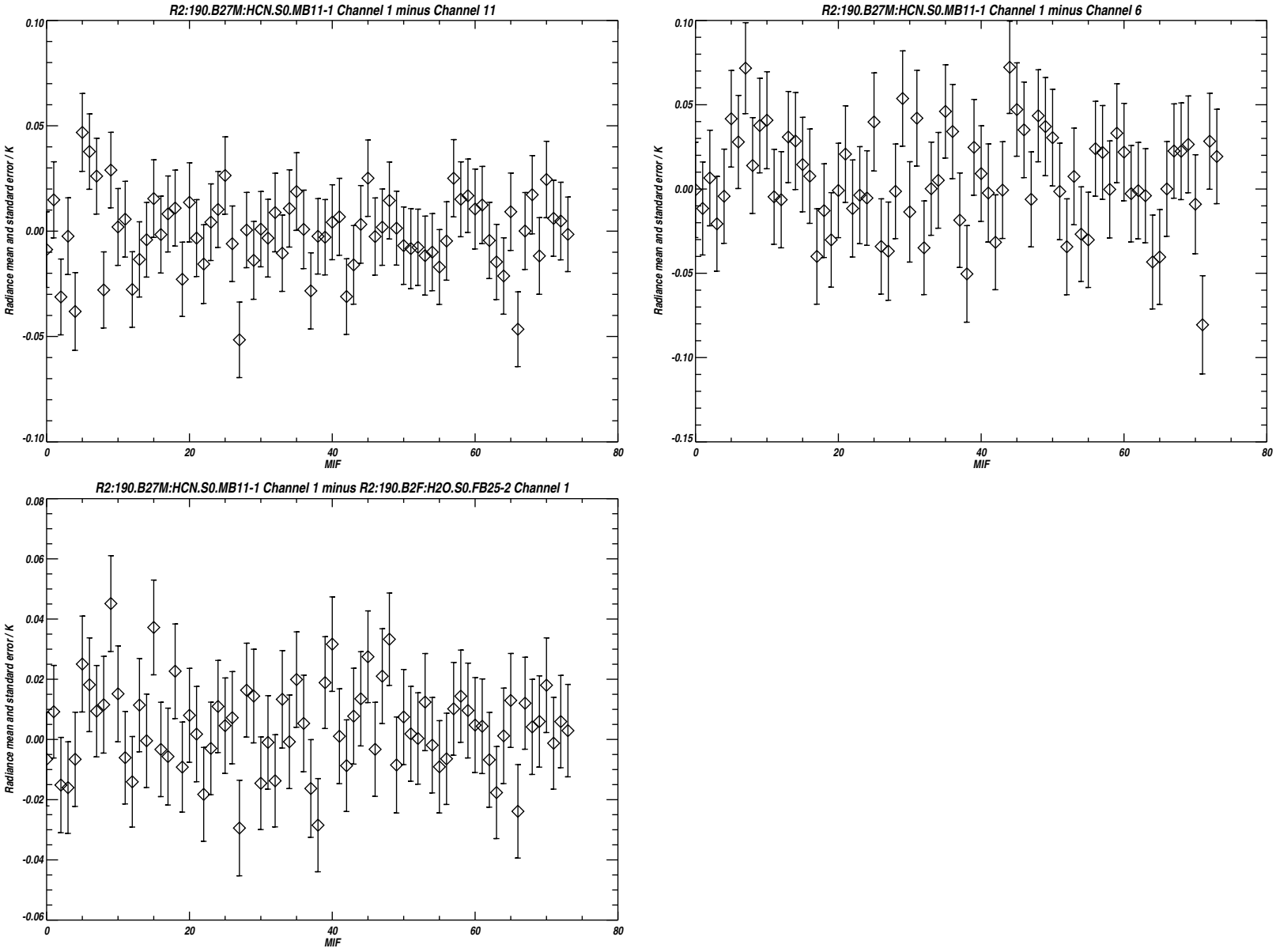

Figure B.40: Radiance differences between the 3 channel pairs plotted in Figure B.39. The vertical bars indicating the *rms* uncertainty due to noise. See text for additional details.

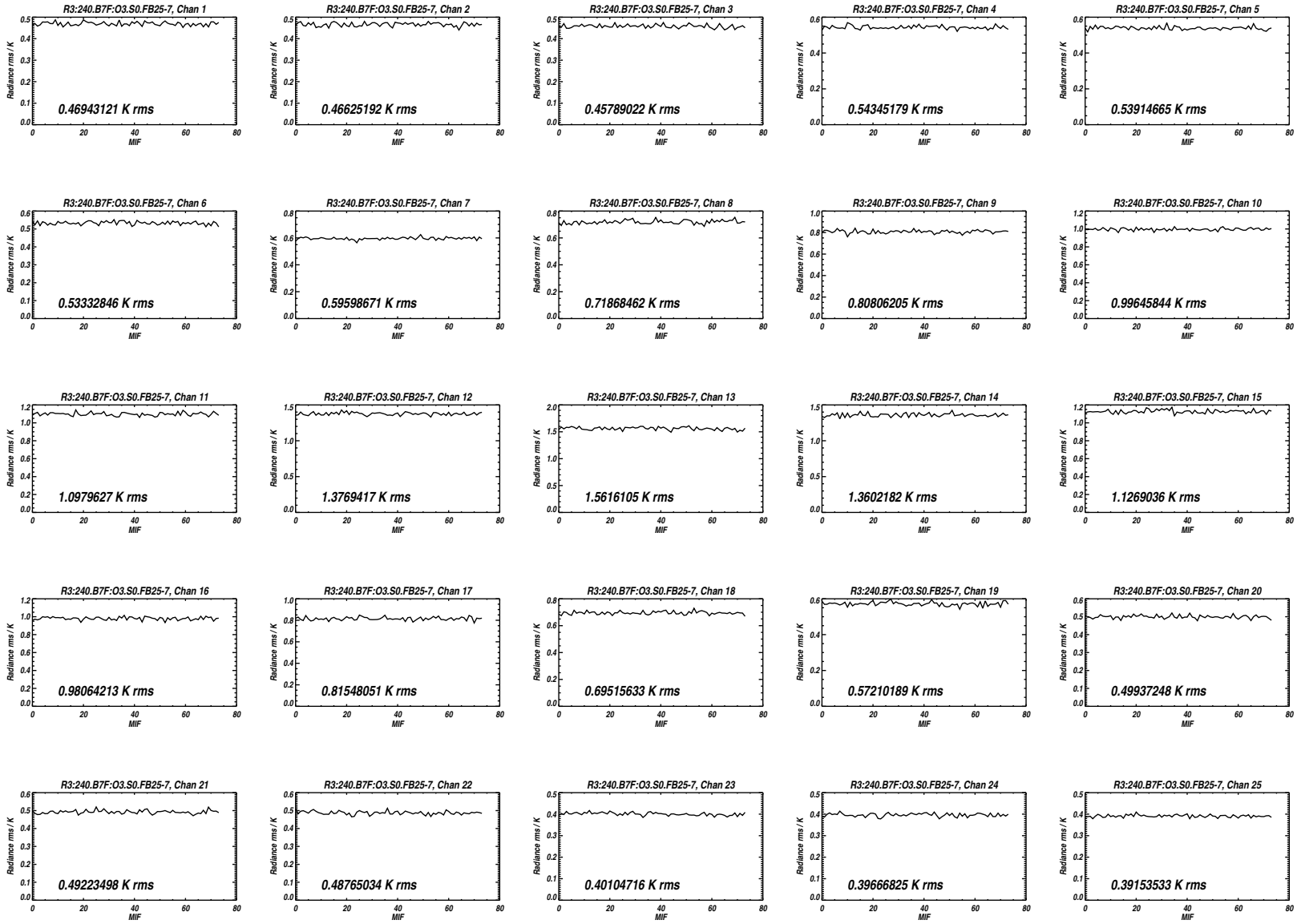

Figure B.41: Measured *rms* noise for all 25 channels of Band 7 for the MIFs treated as Limb views in Level 1 processing.

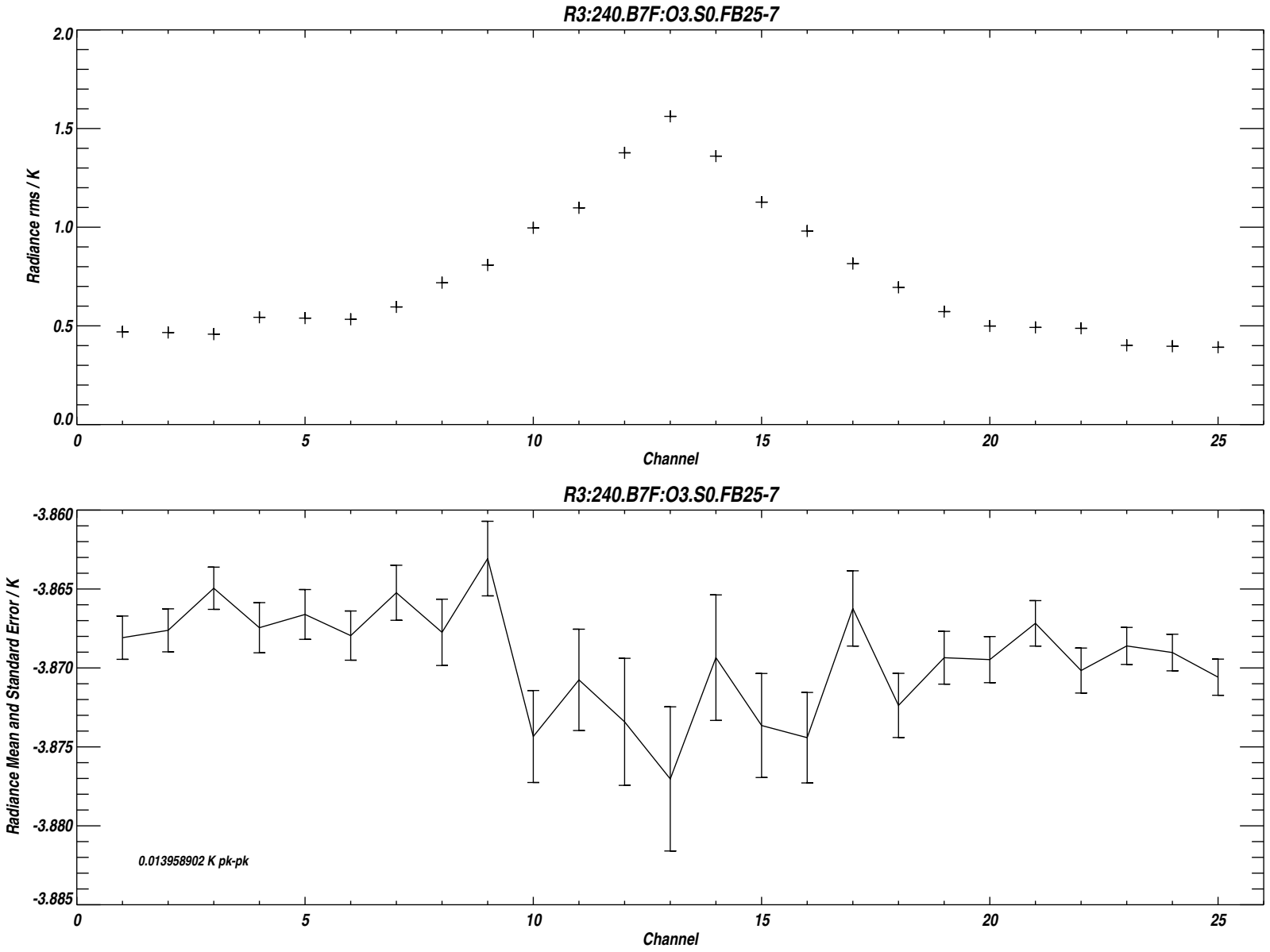

Figure B.42: Measured *rms* noise for each channel of Band 7 (upper panel). The lower panel plots the difference between the mean 'Limb' and reference radiances, the vertical bars indicating the *rms* uncertainty due to noise.

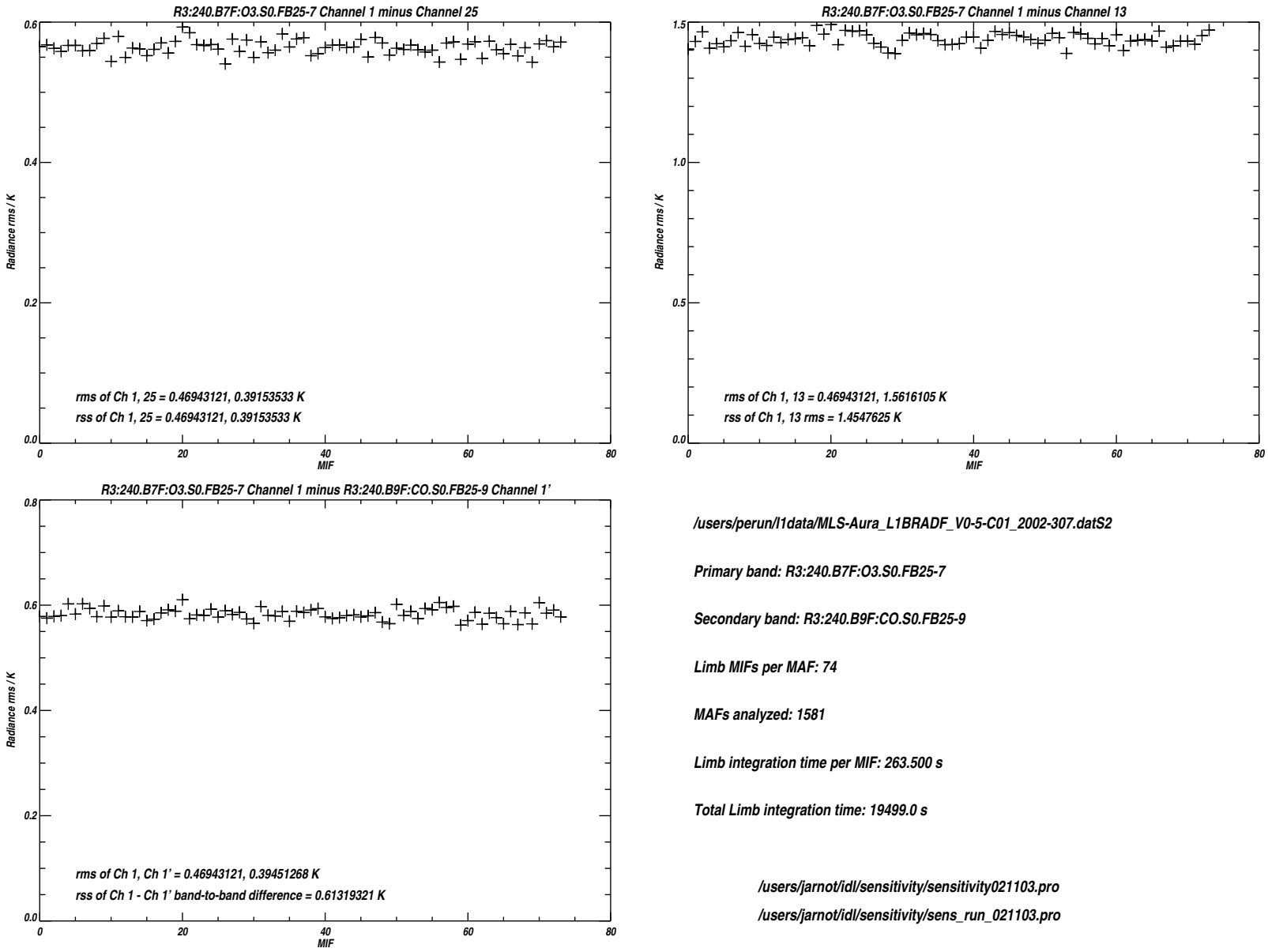

Figure B.43: Measured *rms* noise on the radiance differences between Channels 1 and 25 of Band 7 (upper left panel), Channels 1 and 13 of Band 7 (upper right panel), and between Channel 1 of Band 7 and Channel 1 of Band 9.

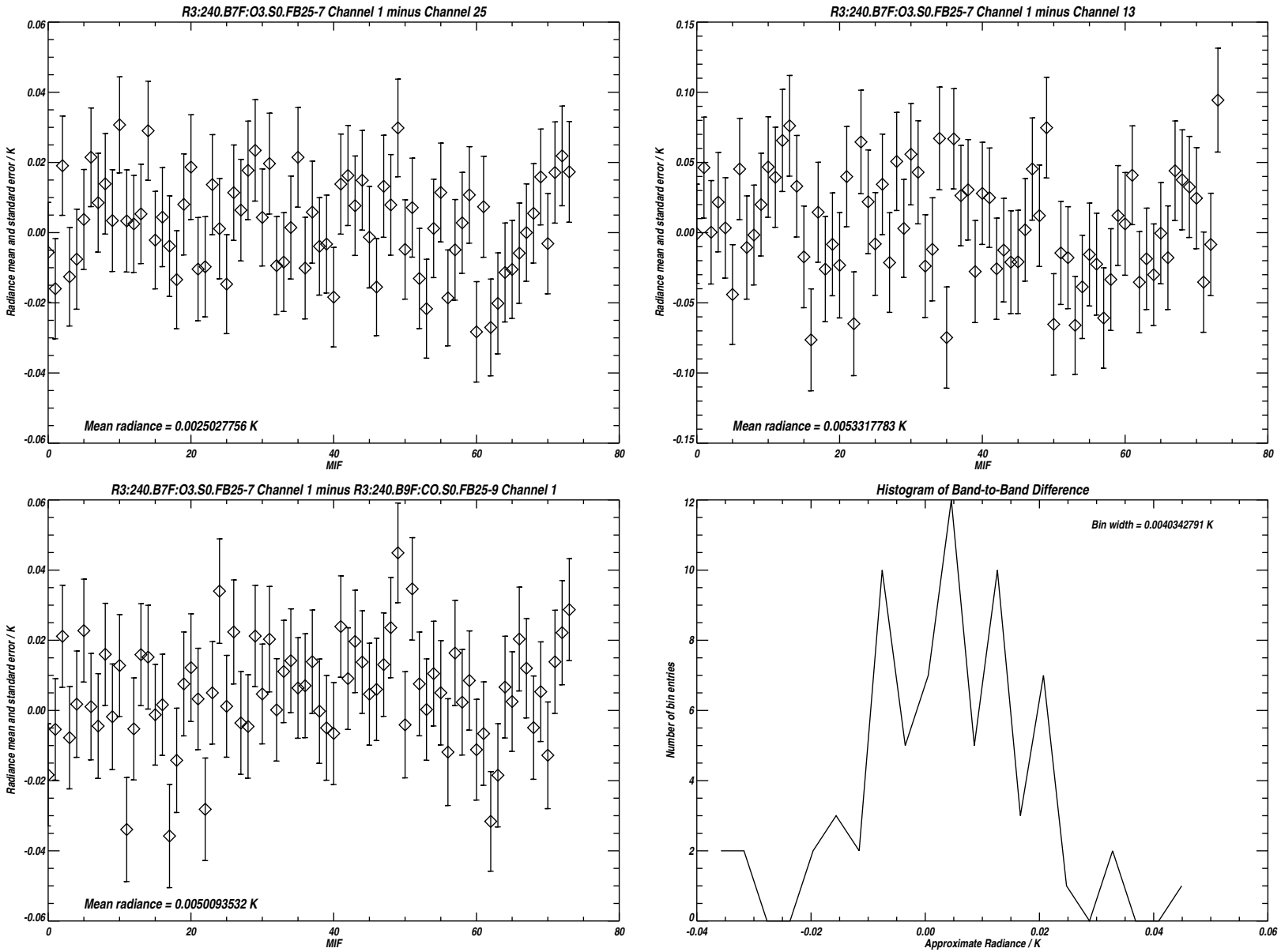

Figure B.44: Radiance differences between the 3 channel pairs plotted in Figure B.43. The vertical bars indicating the *rms* uncertainty due to noise. The lower right hand panel is a histogram of the data in the panel to its left. See text for additional details.

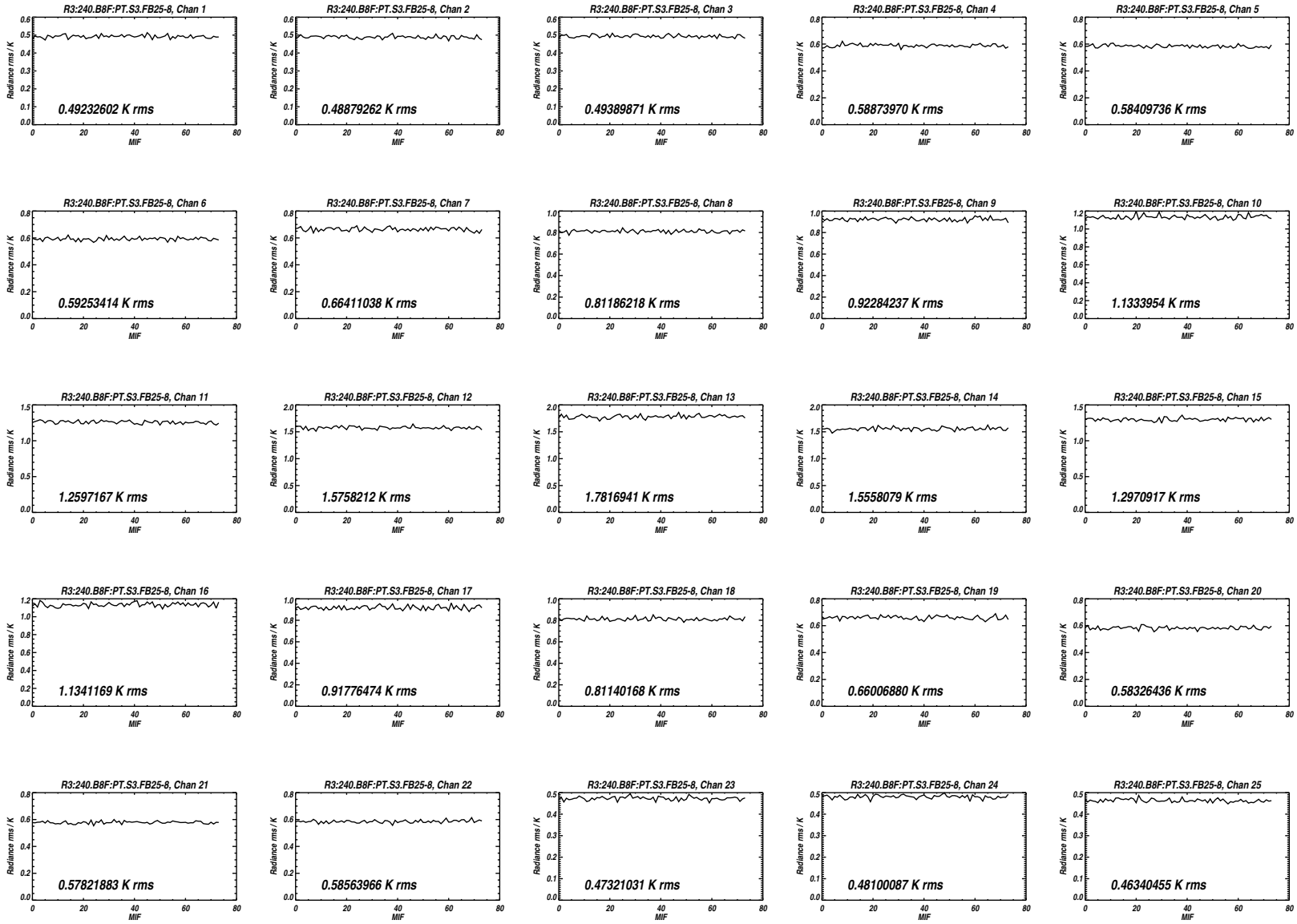

Figure B.45: Measured *rms* noise for all 25 channels of Band 8 for the MIFs treated as Limb views in Level 1 processing.

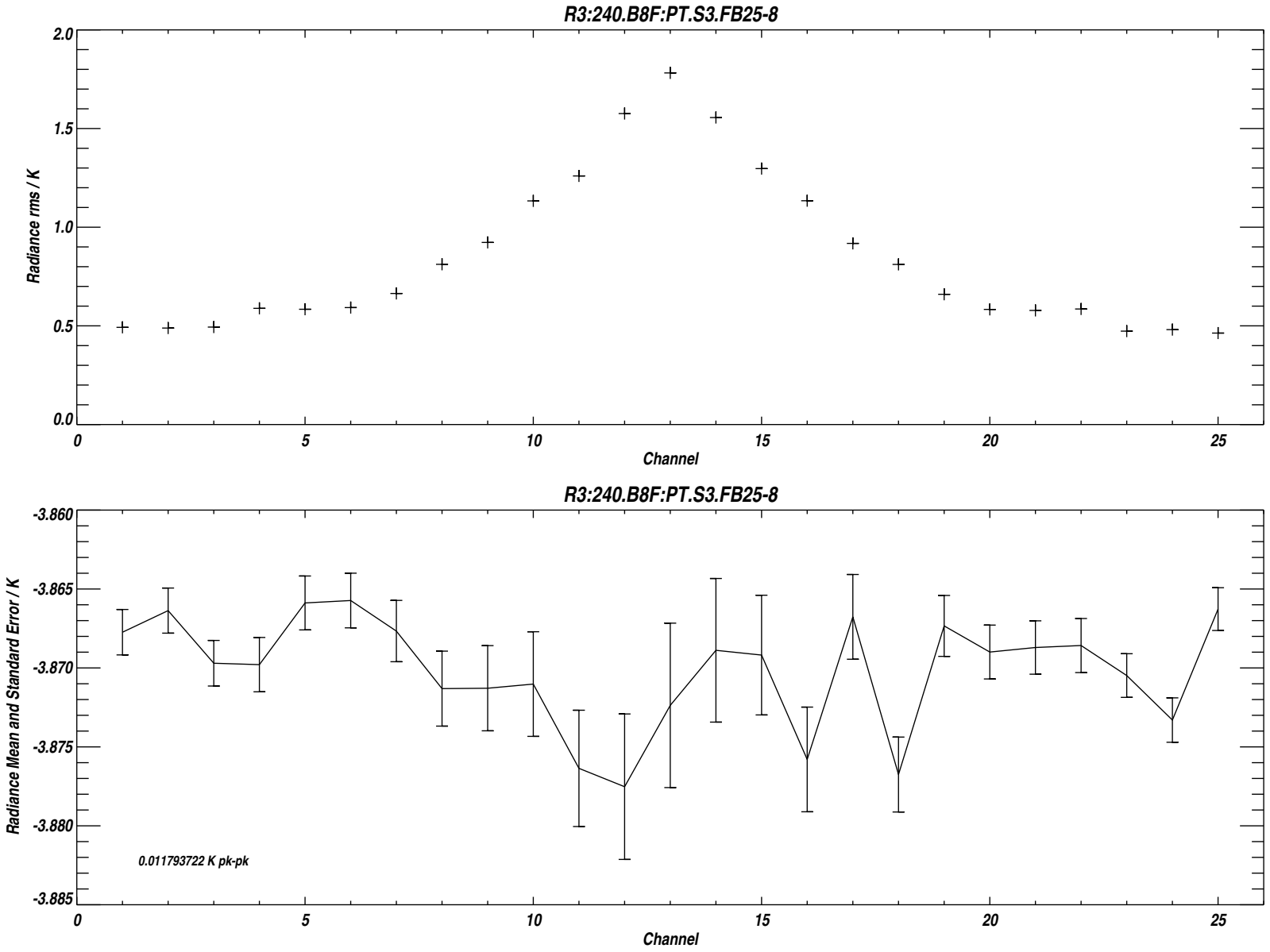

Figure B.46: Measured *rms* noise for each channel of Band 8 (upper panel). The lower panel plots the difference between the mean 'Limb' and reference radiances, the vertical bars indicating the *rms* uncertainty due to noise.

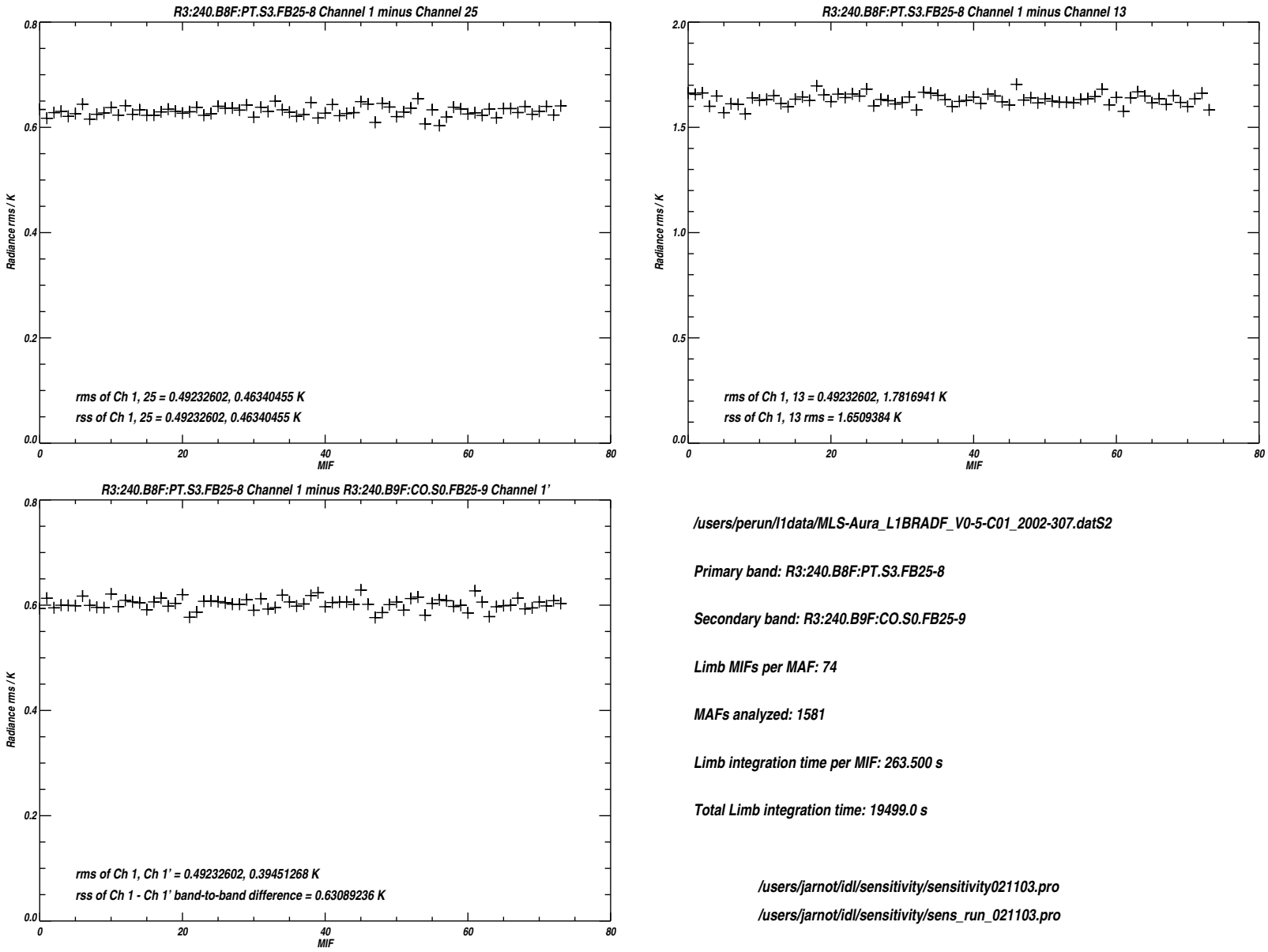

Figure B.47: Measured *rms* noise on the radiance differences between Channels 1 and 25 of Band 8 (upper left panel), Channels 1 and 13 of Band 8 (upper right panel), and between Channel 1 of Band 8 and Channel 1 of Band 9.

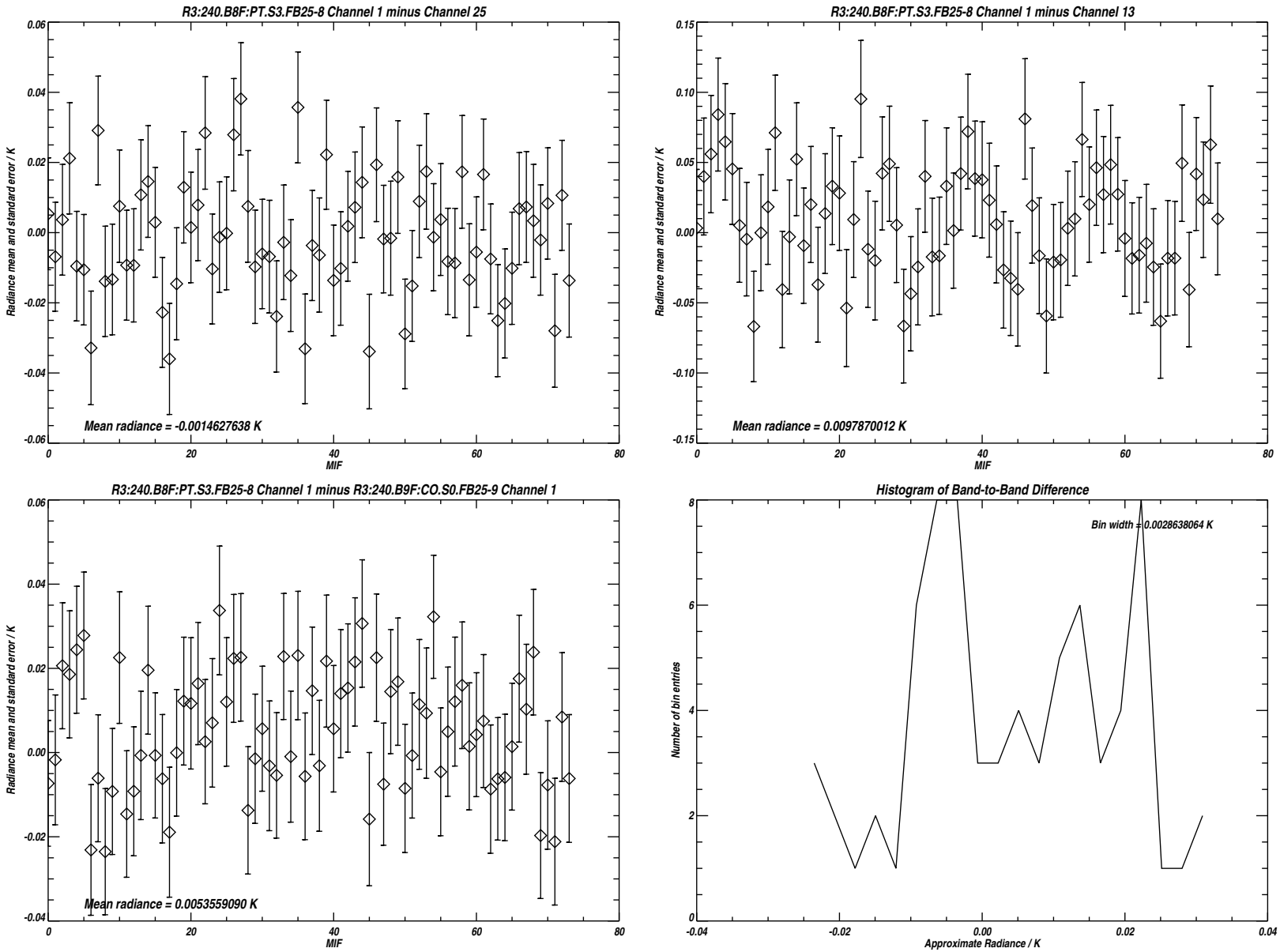

Figure B.48: Radiance differences between the 3 channel pairs plotted in Figure B.47. The vertical bars indicating the *rms* uncertainty due to noise. The lower right hand panel is a histogram of the data in the panel to its left. See text for additional details.

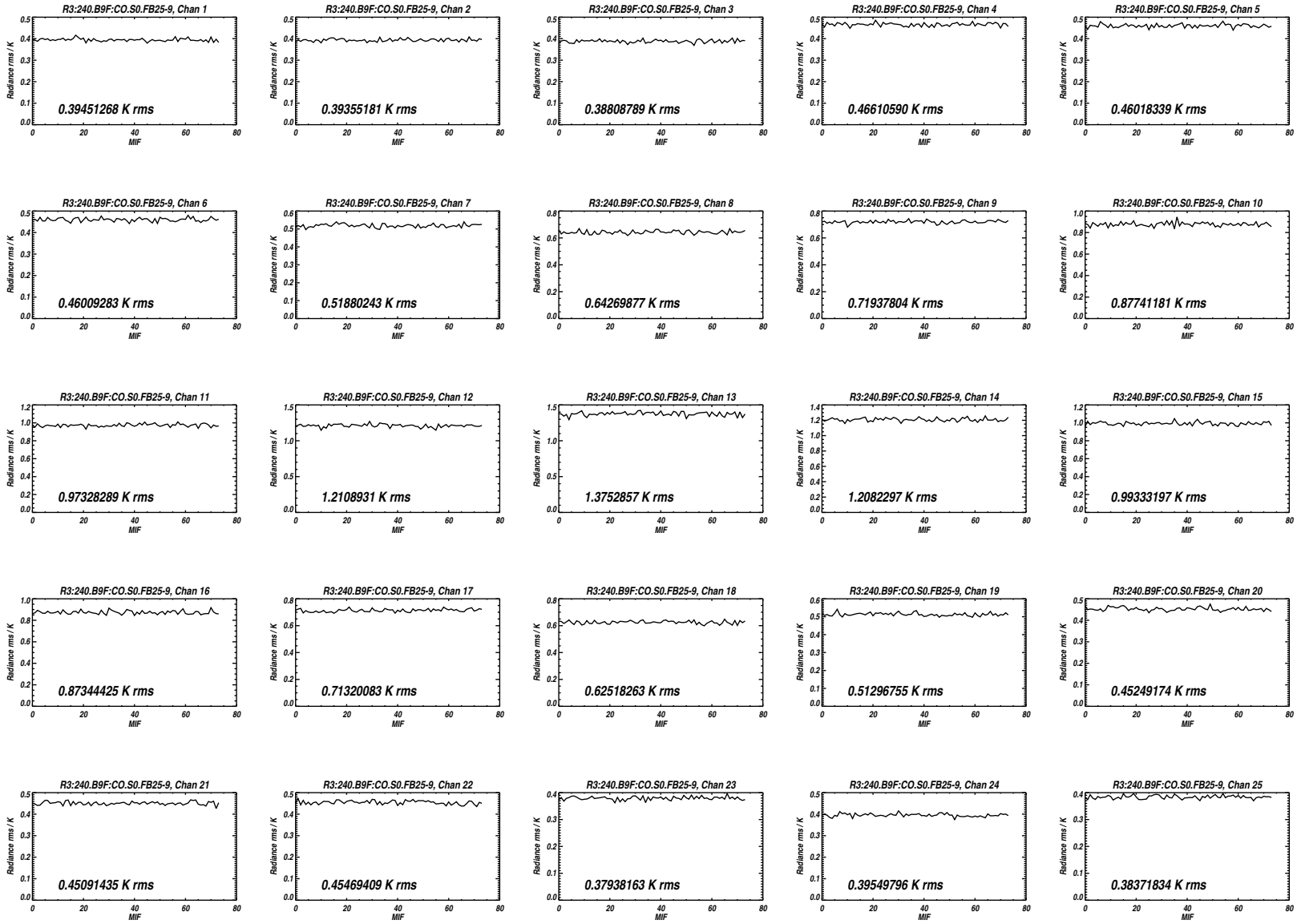

Figure B.49: Measured *rms* noise for all 25 channels of Band 9 for the MIFs treated as Limb views in Level 1 processing.

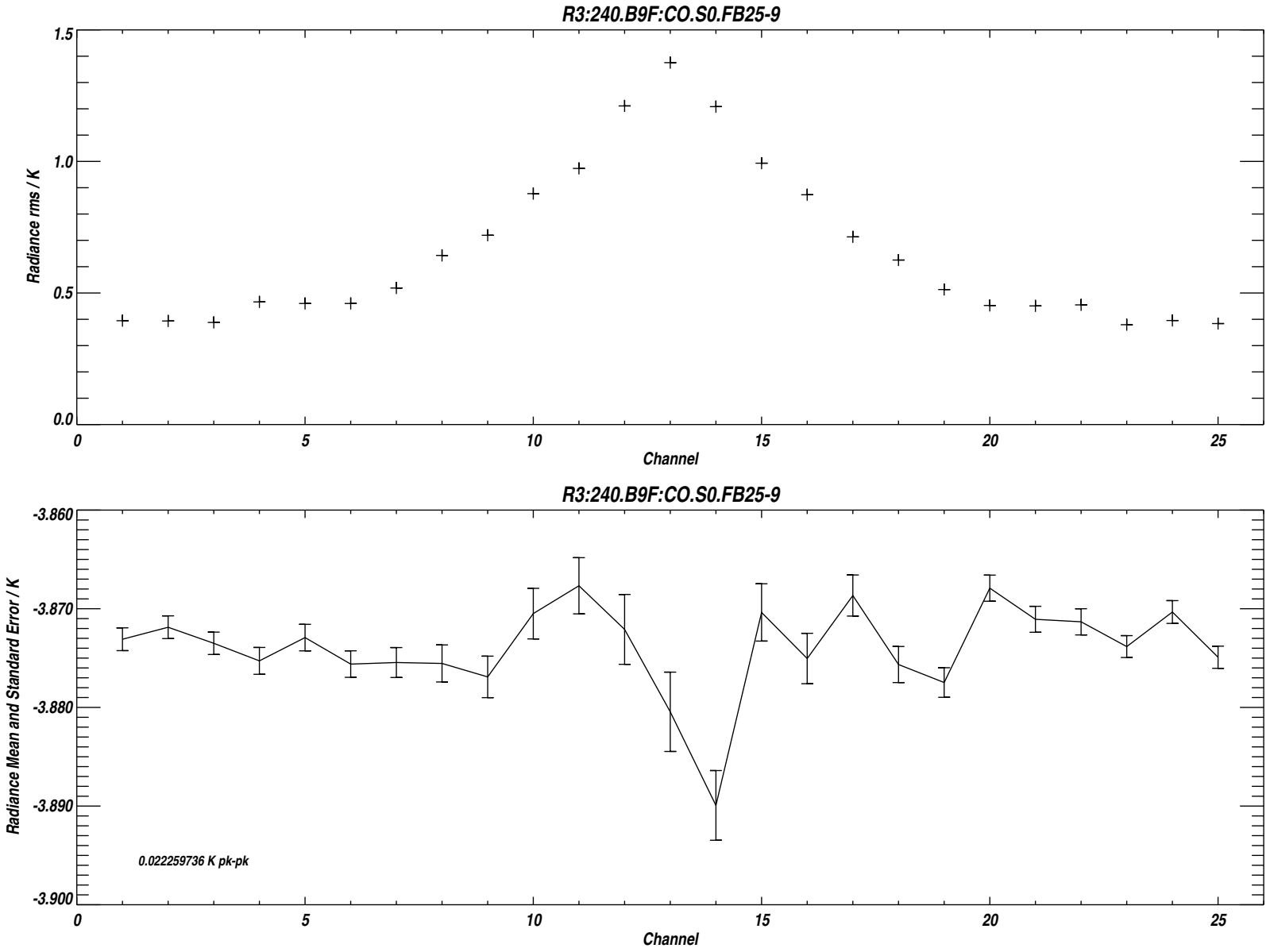

Figure B.50: Measured *rms* noise for each channel of Band 9 (upper panel). The lower panel plots the difference between the mean 'Limb' and reference radiances, the vertical bars indicating the *rms* uncertainty due to noise.

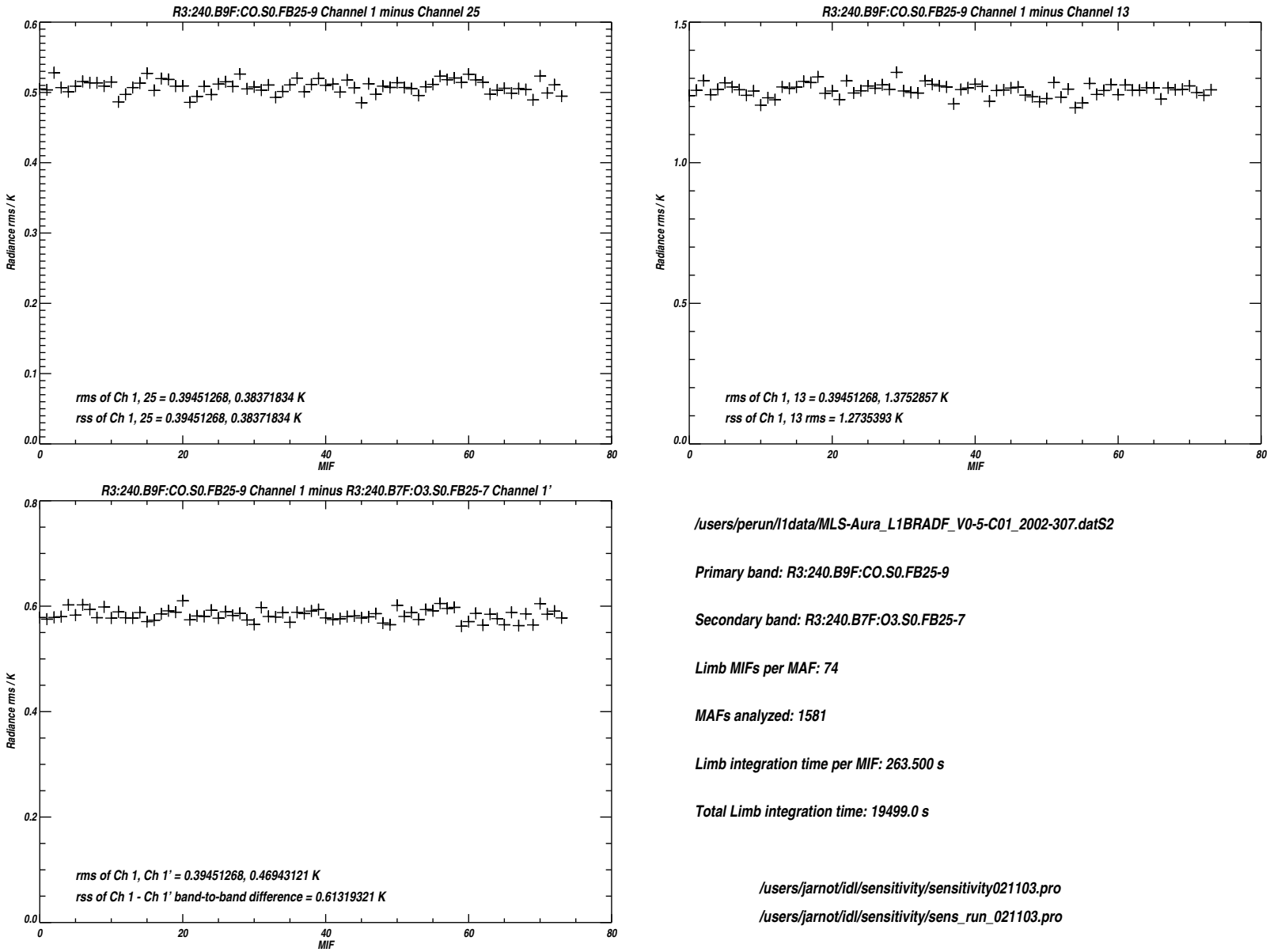

Figure B.51: Measured *rms* noise on the radiance differences between Channels 1 and 25 of Band 9 (upper left panel), Channels 1 and 13 of Band 9 (upper right panel), and between Channel 1 of Band 9 and Channel 1 of Band 7.

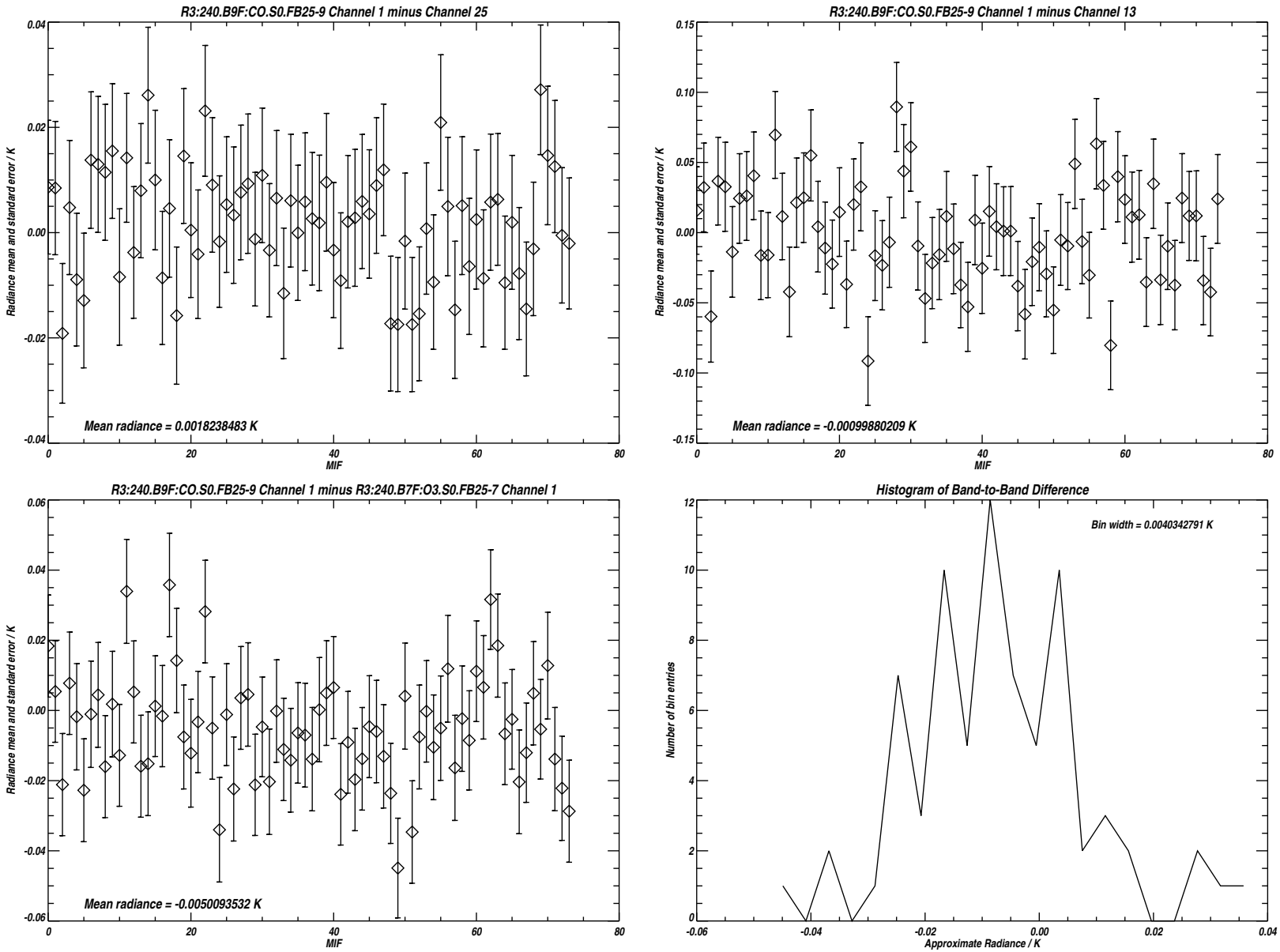

Figure B.52: Radiance differences between the 3 channel pairs plotted in Figure B.51. The vertical bars indicating the *rms* uncertainty due to noise. The lower right hand panel is a histogram of the data in the panel to its left. See text for additional details.

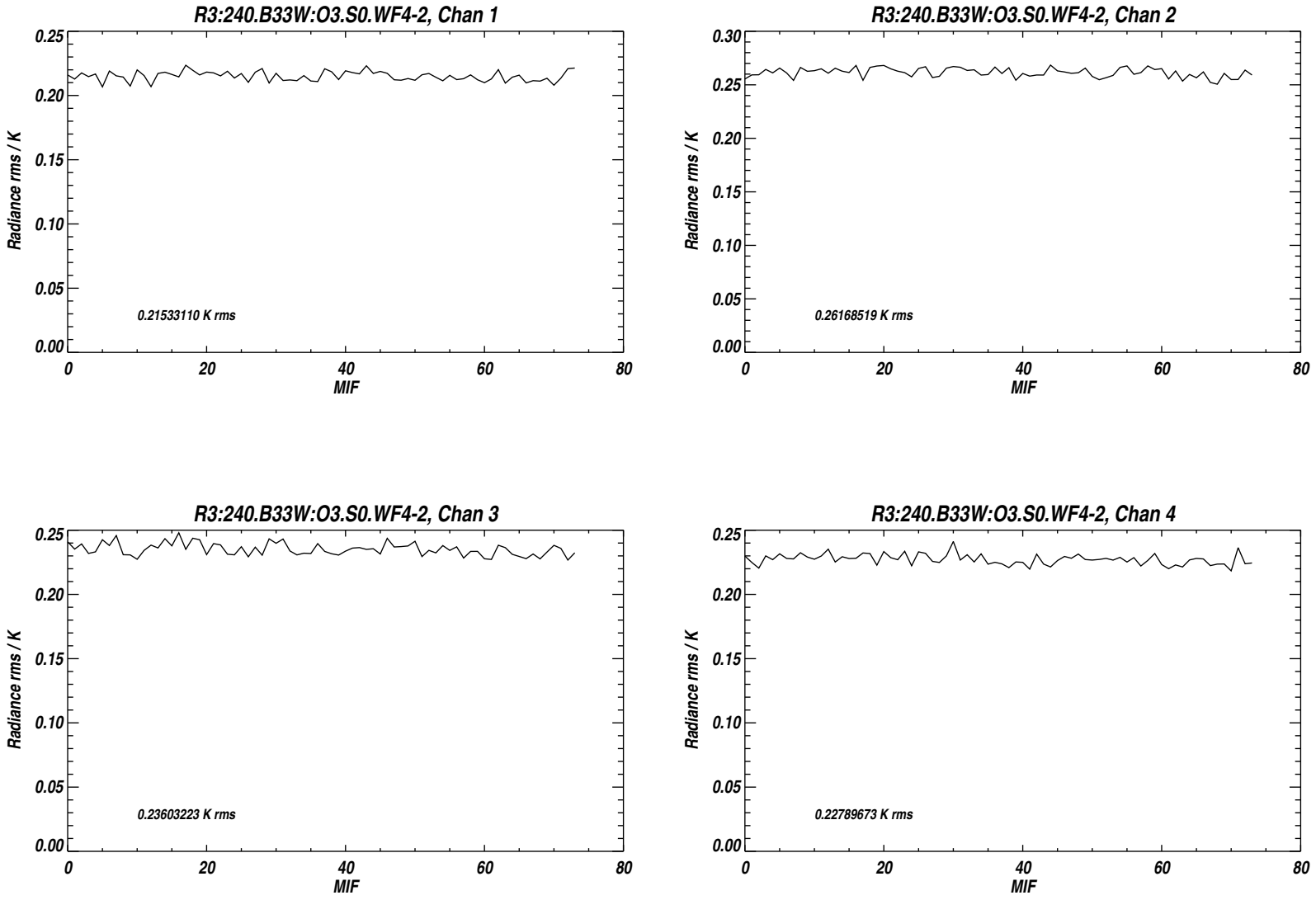

Figure B.53: Measured *rms* noise for the 4 Wide Filter channels of Band 33 (R3) for the MIFs treated as Limb views in Level 1 processing.

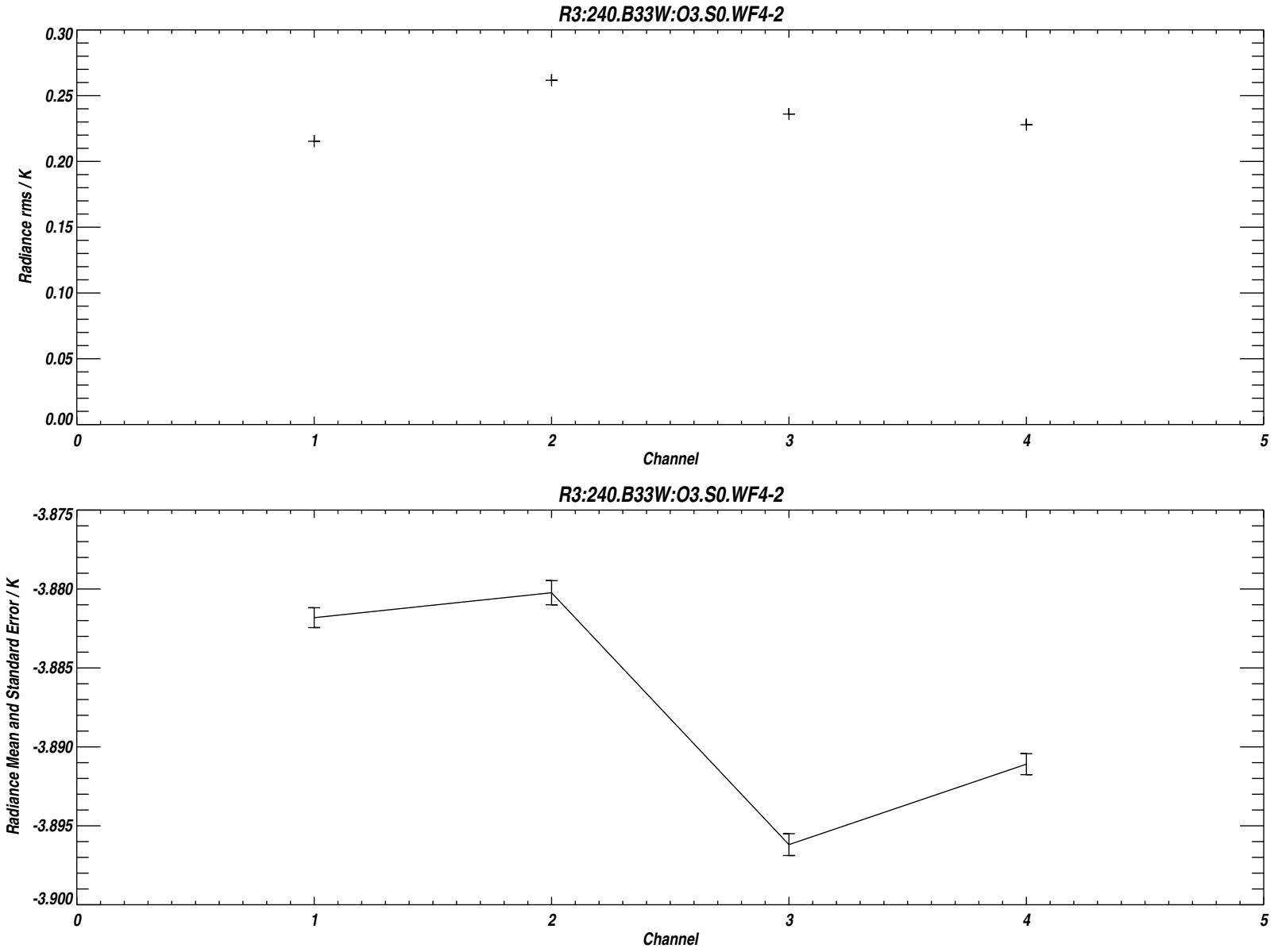

Figure B.54: Measured *rms* noise for the Wide Filter channels of Band 33. (upper panel). The lower panel plots the difference between the mean 'Limb' and reference radiances, the vertical bars indicating the *rms* uncertainty due to noise.

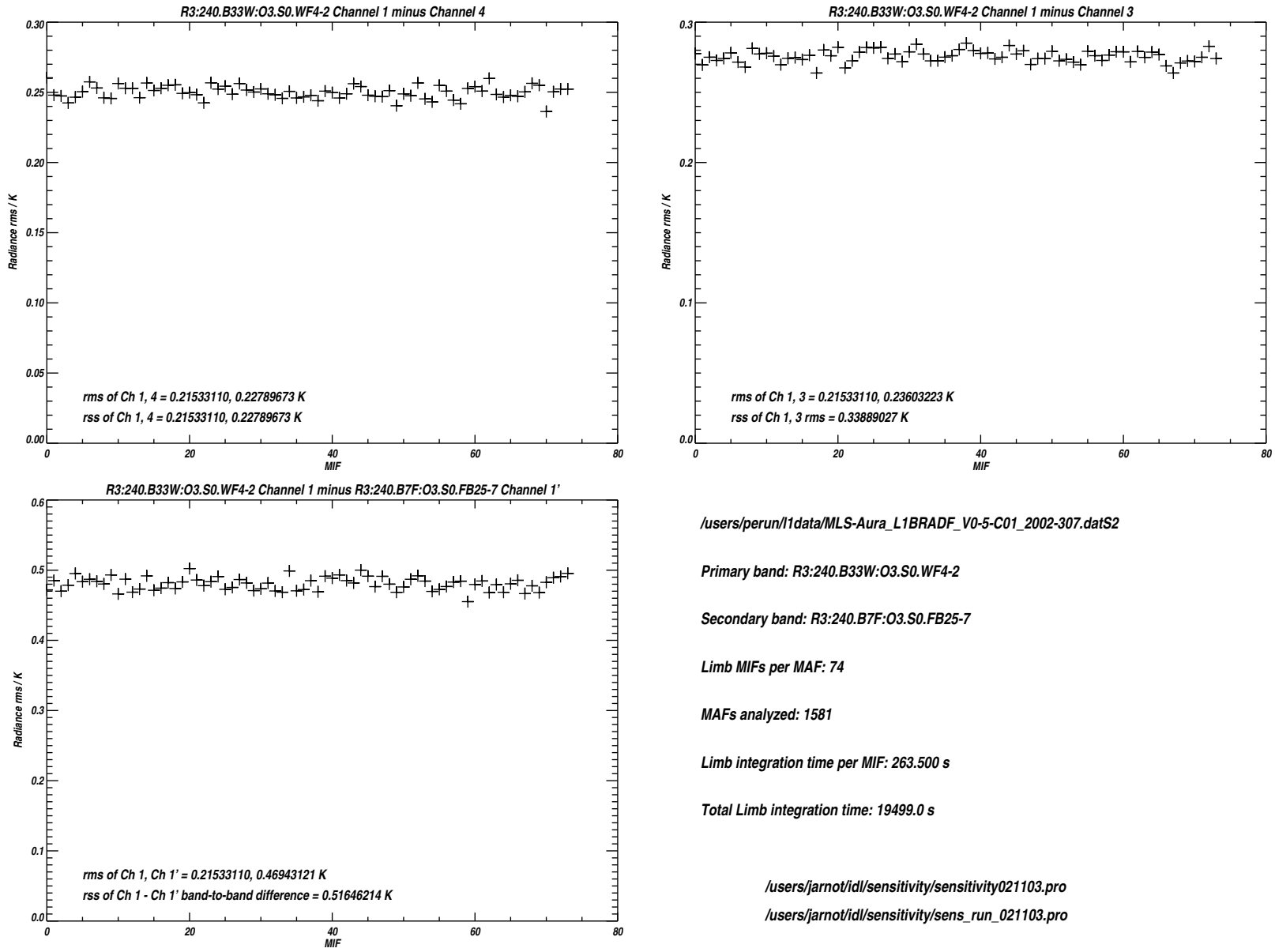

Figure B.55: Measured *rms* noise on the radiance differences between Wide Filter channels 1 and 4 of Band 33 (upper left panel), Wide Filter channels 1 and 3 of Band 33 (upper right panel), and between Wide Filter channel 1 of Band 33 and Channel 1 of Band 7 (FB25, R1B).

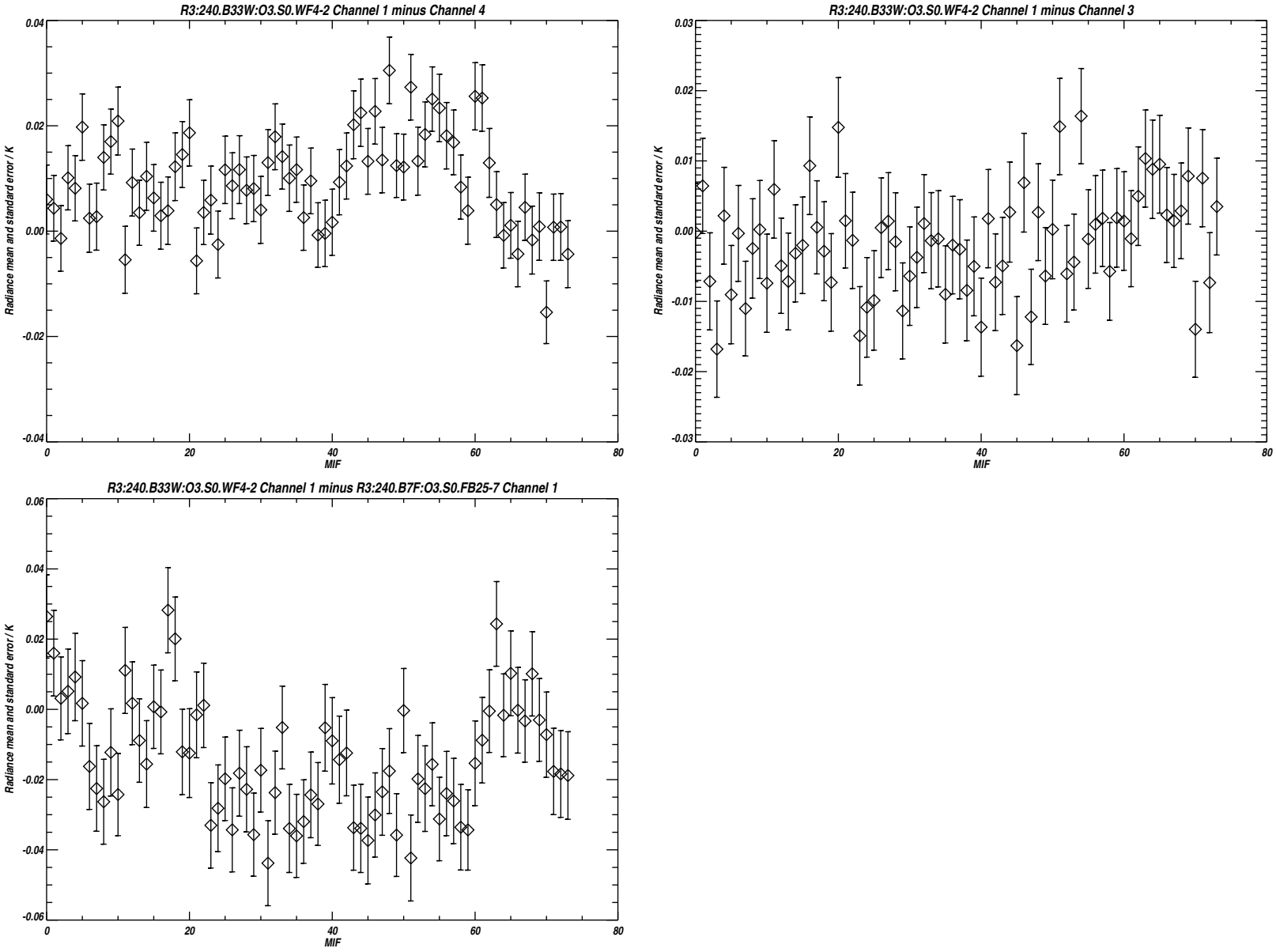

Figure B.56: Radiance differences between the 3 channel pairs plotted in Figure B.55. The vertical bars indicating the *rms* uncertainty due to noise. See text for additional details.

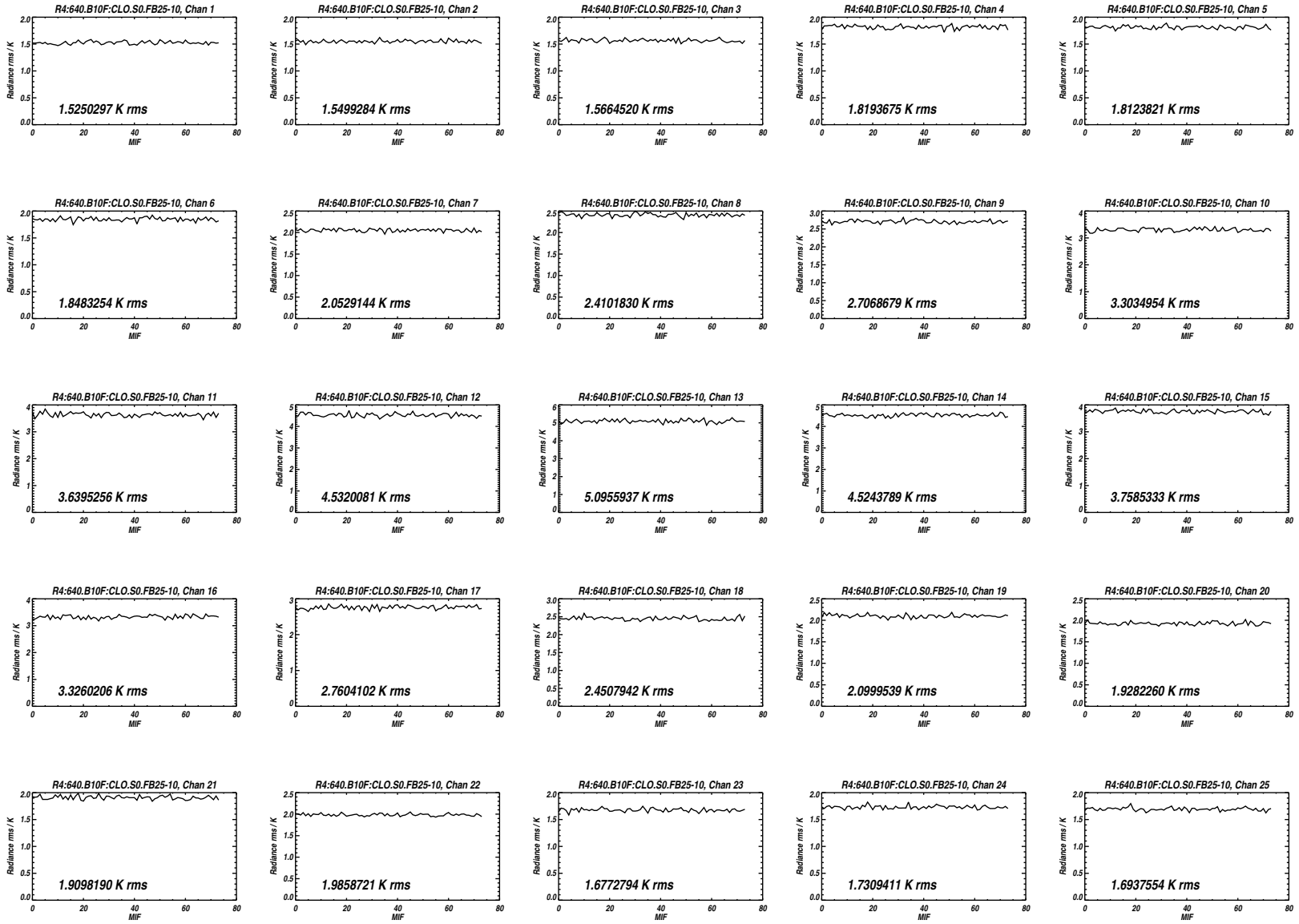

Figure B.57: Measured *rms* noise for all 25 channels of Band 10 for the MIFs treated as Limb views in Level 1 processing.

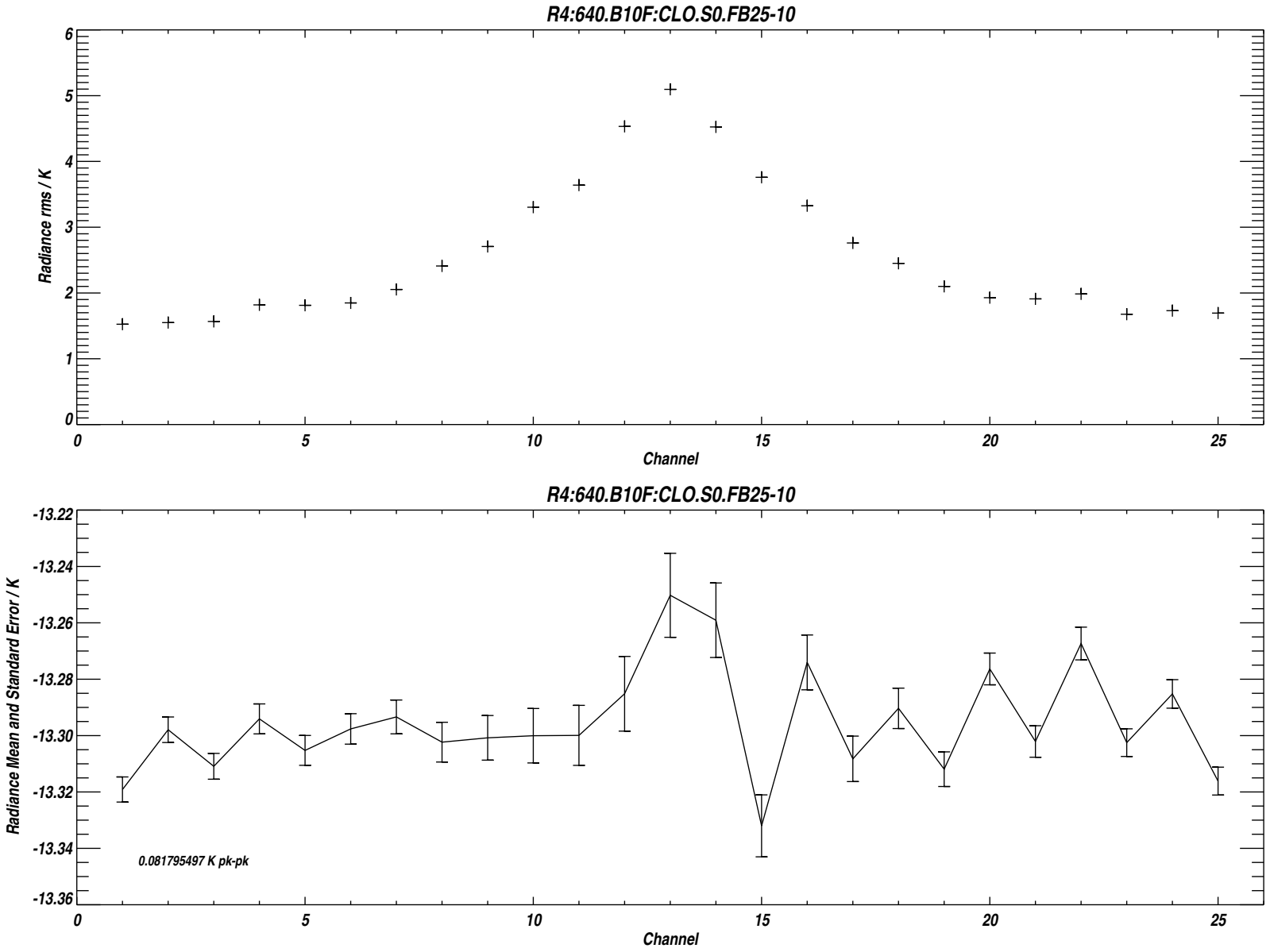

Figure B.58: Measured *rms* noise for each channel of Band 10 (upper panel). The lower panel plots the difference between the mean 'Limb' and reference radiances, the vertical bars indicating the *rms* uncertainty due to noise.

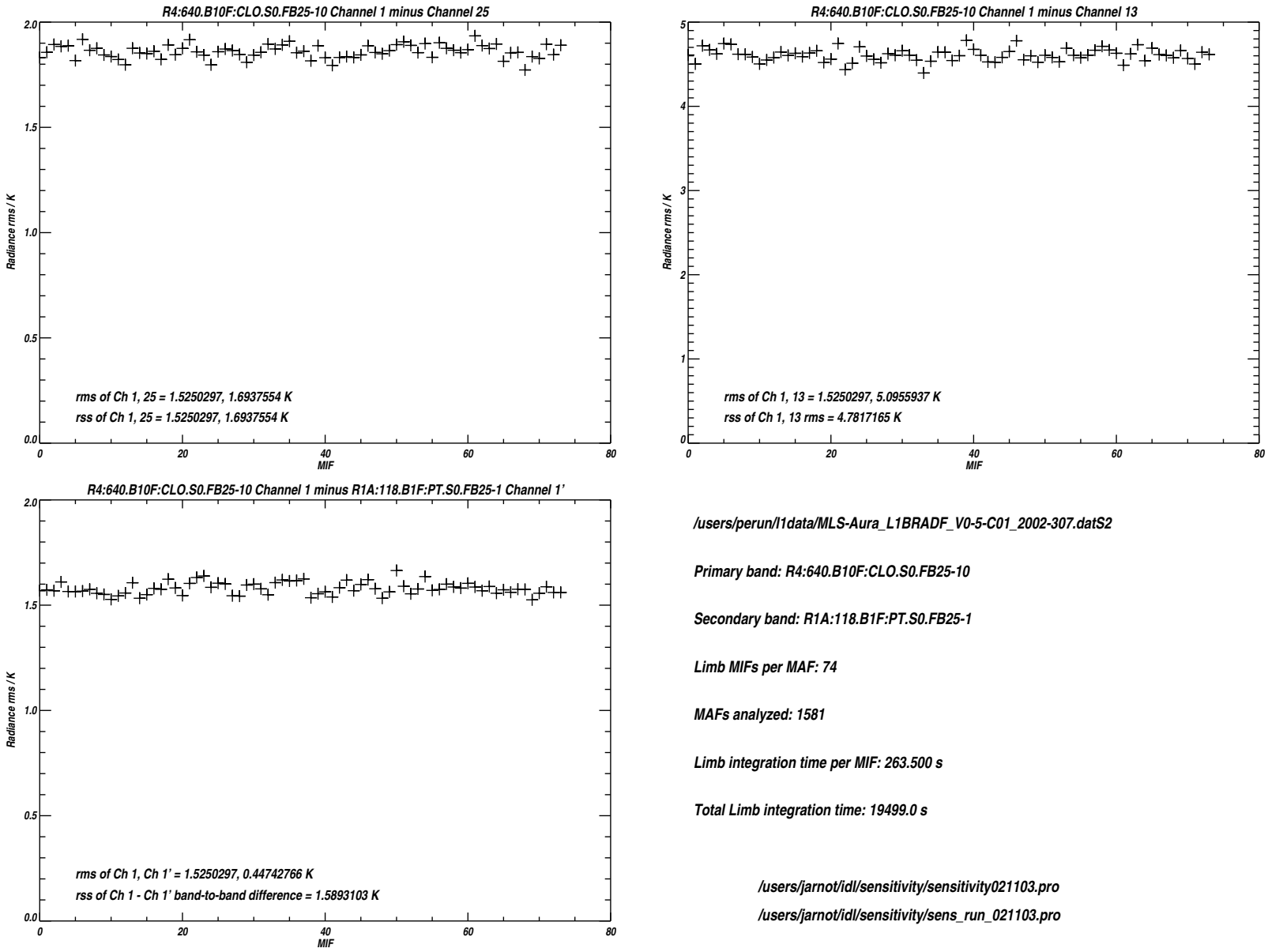

Figure B.59: Measured *rms* noise on the radiance differences between Channels 1 and 25 of Band 10 (upper left panel), Channels 1 and 13 of Band 10 (upper right panel), and between Channel 1 of Band 10 and Channel 1 of Band 14.

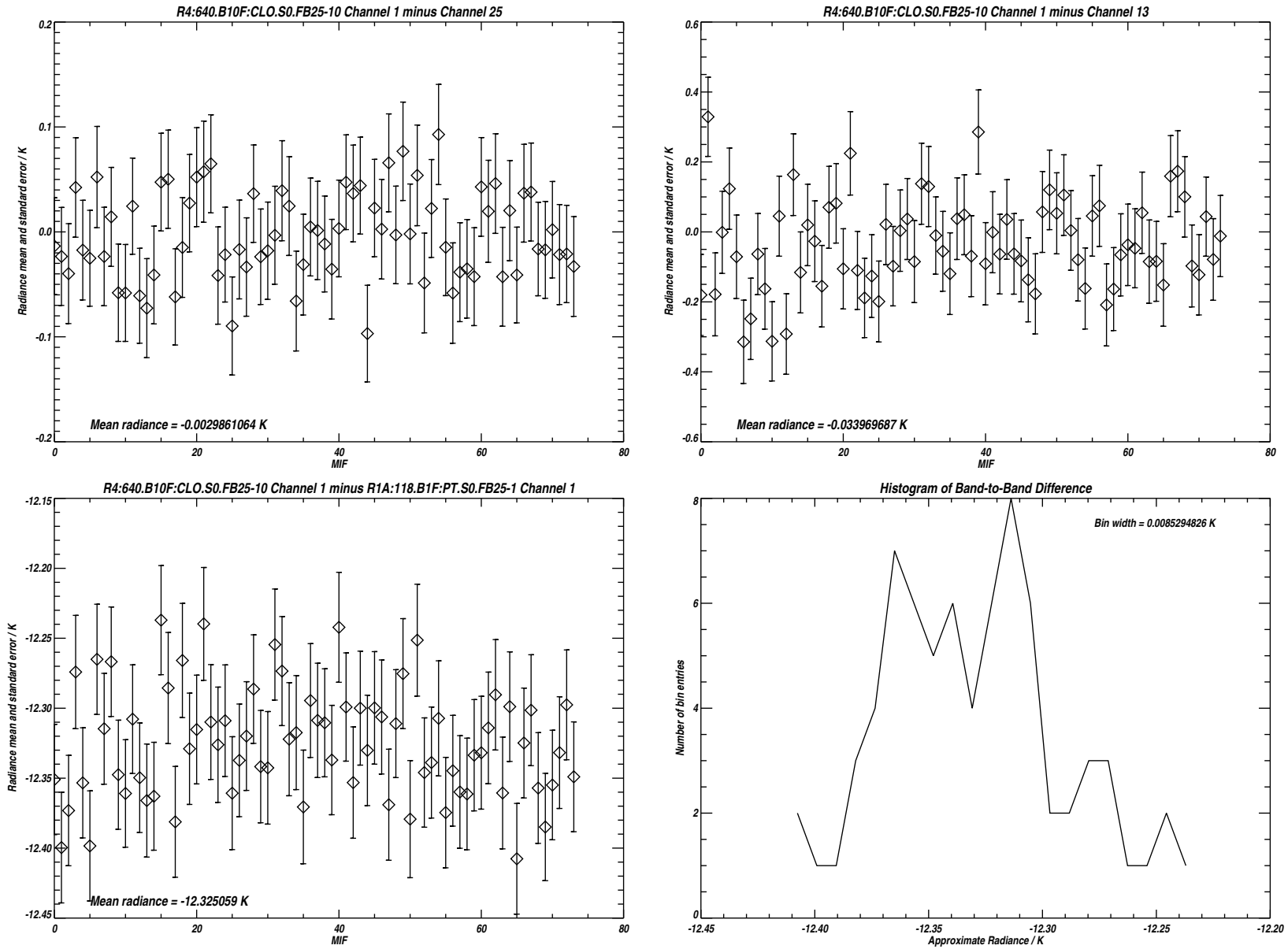

Figure B.60: Radiance differences between the 3 channel pairs plotted in Figure B.59. The vertical bars indicating the *rms* uncertainty due to noise. The lower right hand panel is a histogram of the data in the panel to its left. See text for additional details.

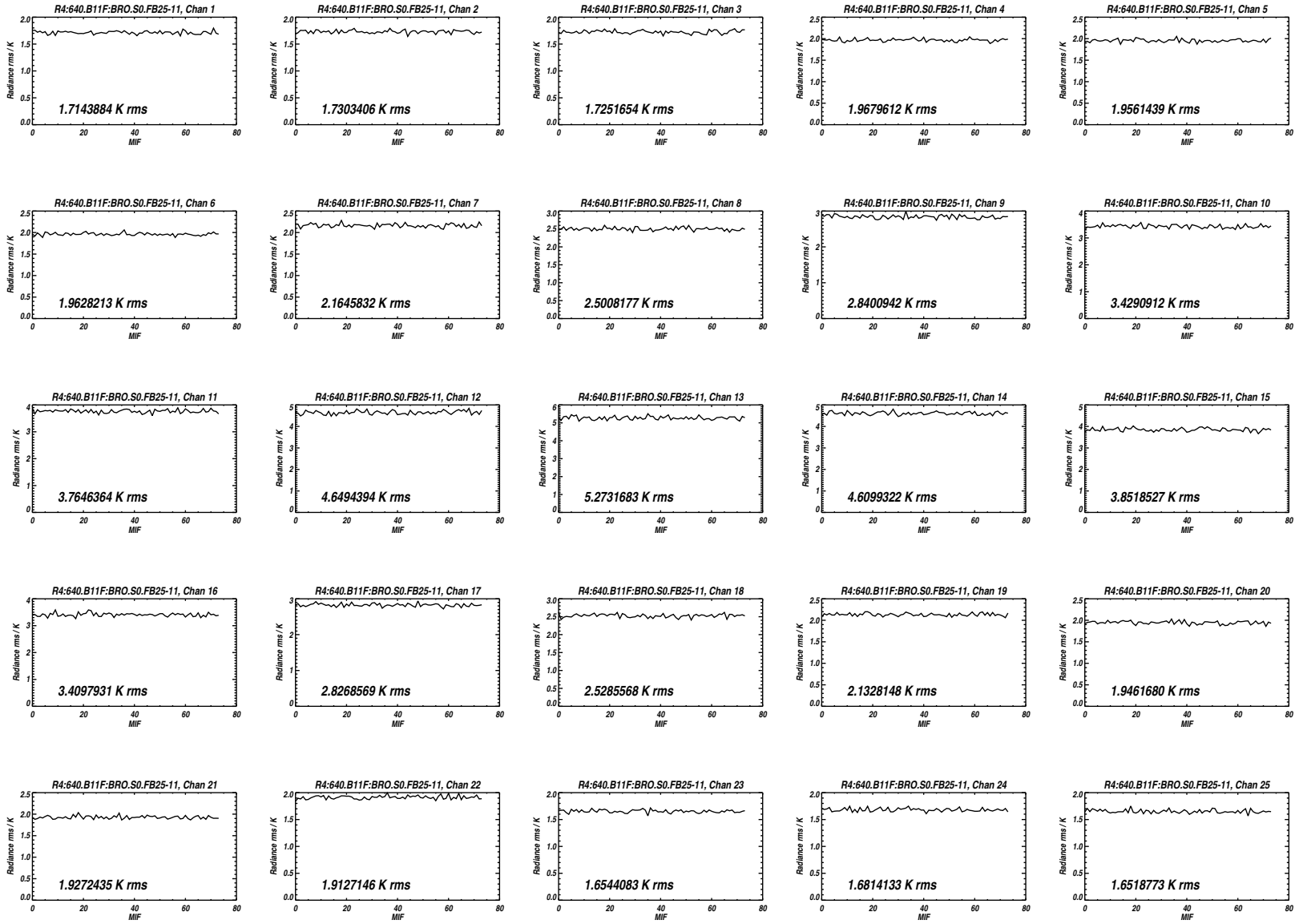

Figure B.61: Measured *rms* noise for all 25 channels of Band 11 for the MIFs treated as Limb views in Level 1 processing.

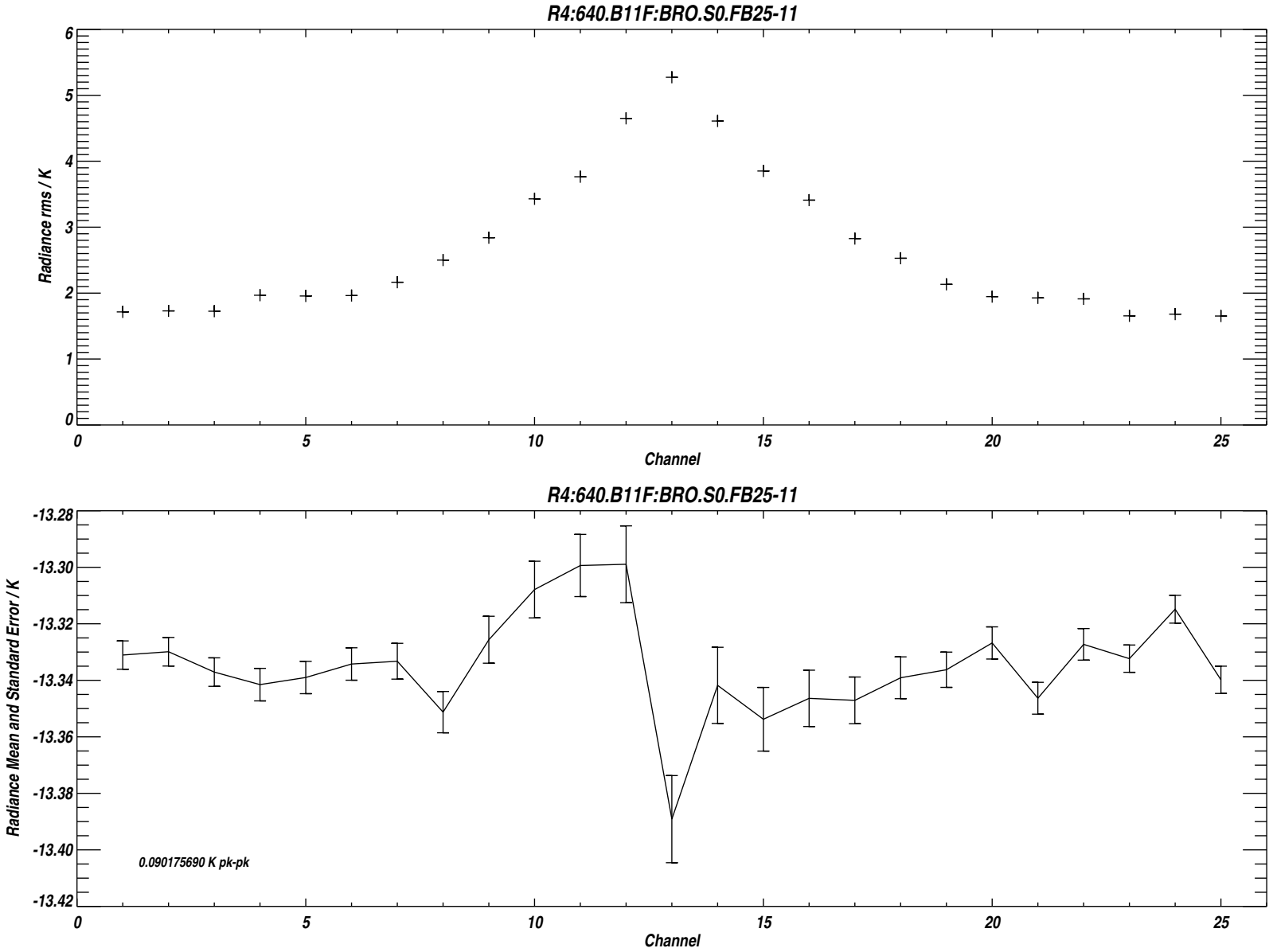

Figure B.62: Measured *rms* noise for each channel of Band 11 (upper panel). The lower panel plots the difference between the mean 'Limb' and reference radiances, the vertical bars indicating the *rms* uncertainty due to noise.

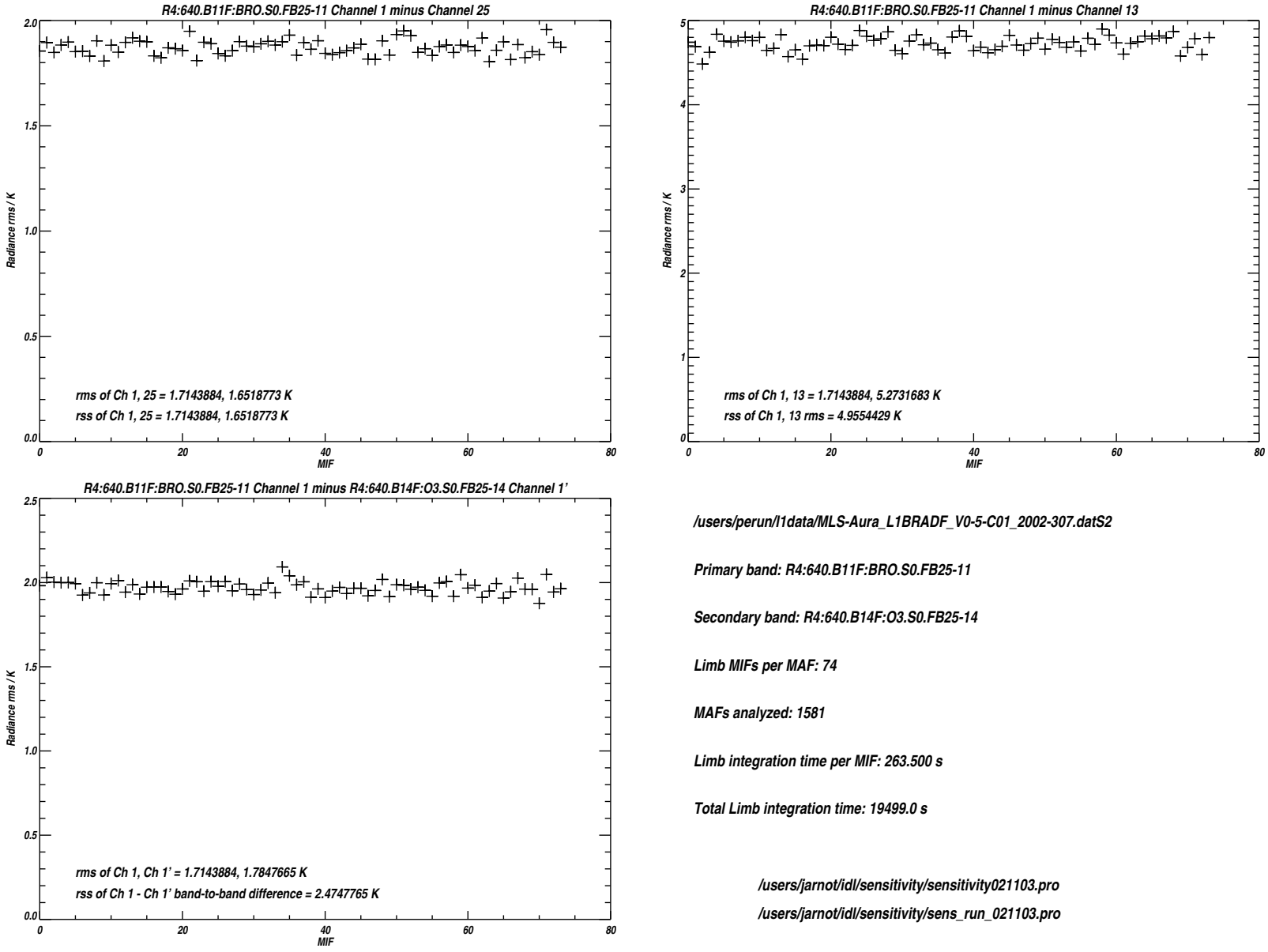

Figure B.63: Measured *rms* noise on the radiance differences between Channels 1 and 25 of Band 11 (upper left panel), Channels 1 and 13 of Band 11 (upper right panel), and between Channel 1 of Band 11 and Channel 1 of Band 14.

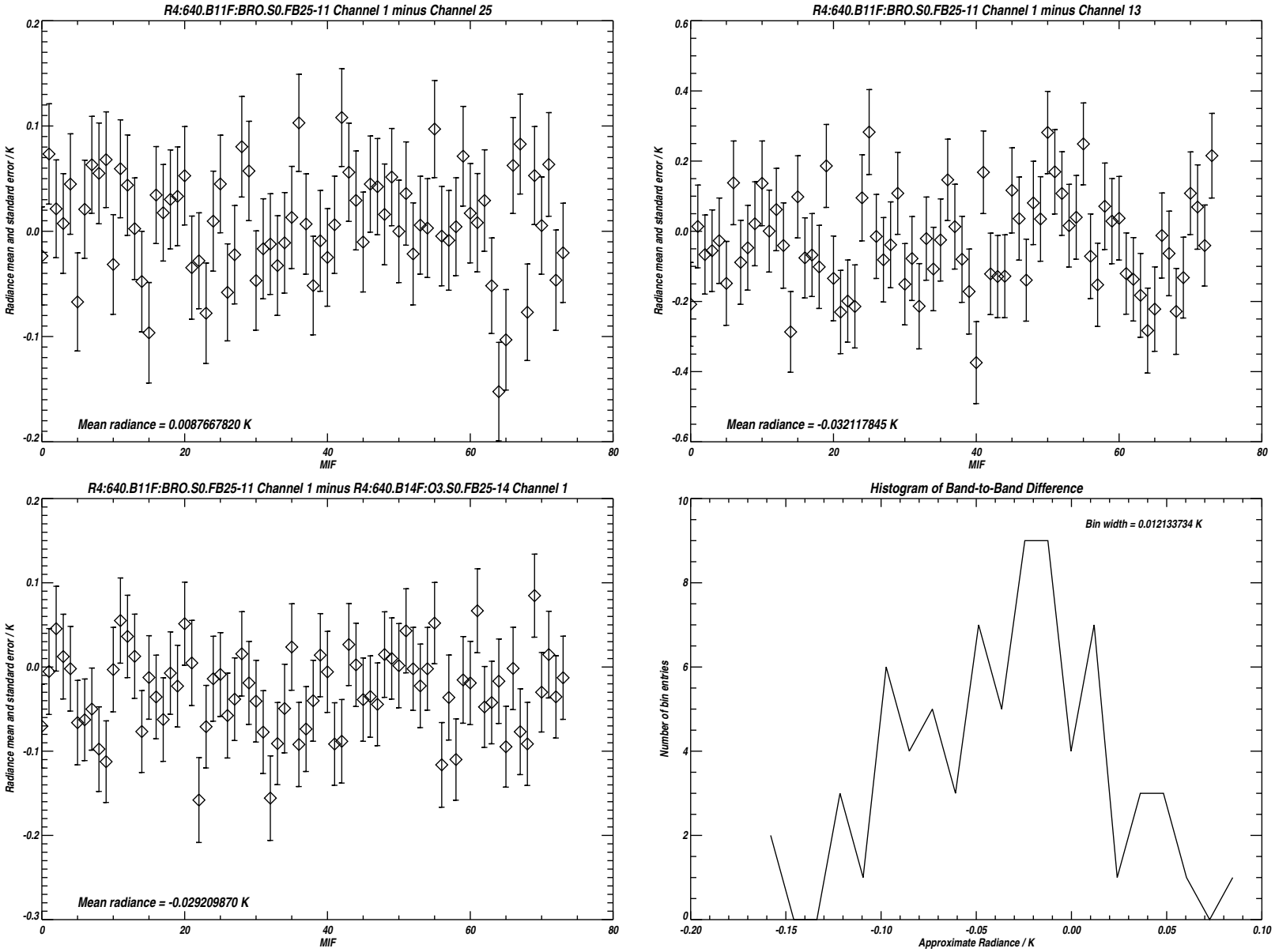

Figure B.64: Radiance differences between the 3 channel pairs plotted in Figure B.63. The vertical bars indicating the *rms* uncertainty due to noise. The lower right hand panel is a histogram of the data in the panel to its left. See text for additional details.

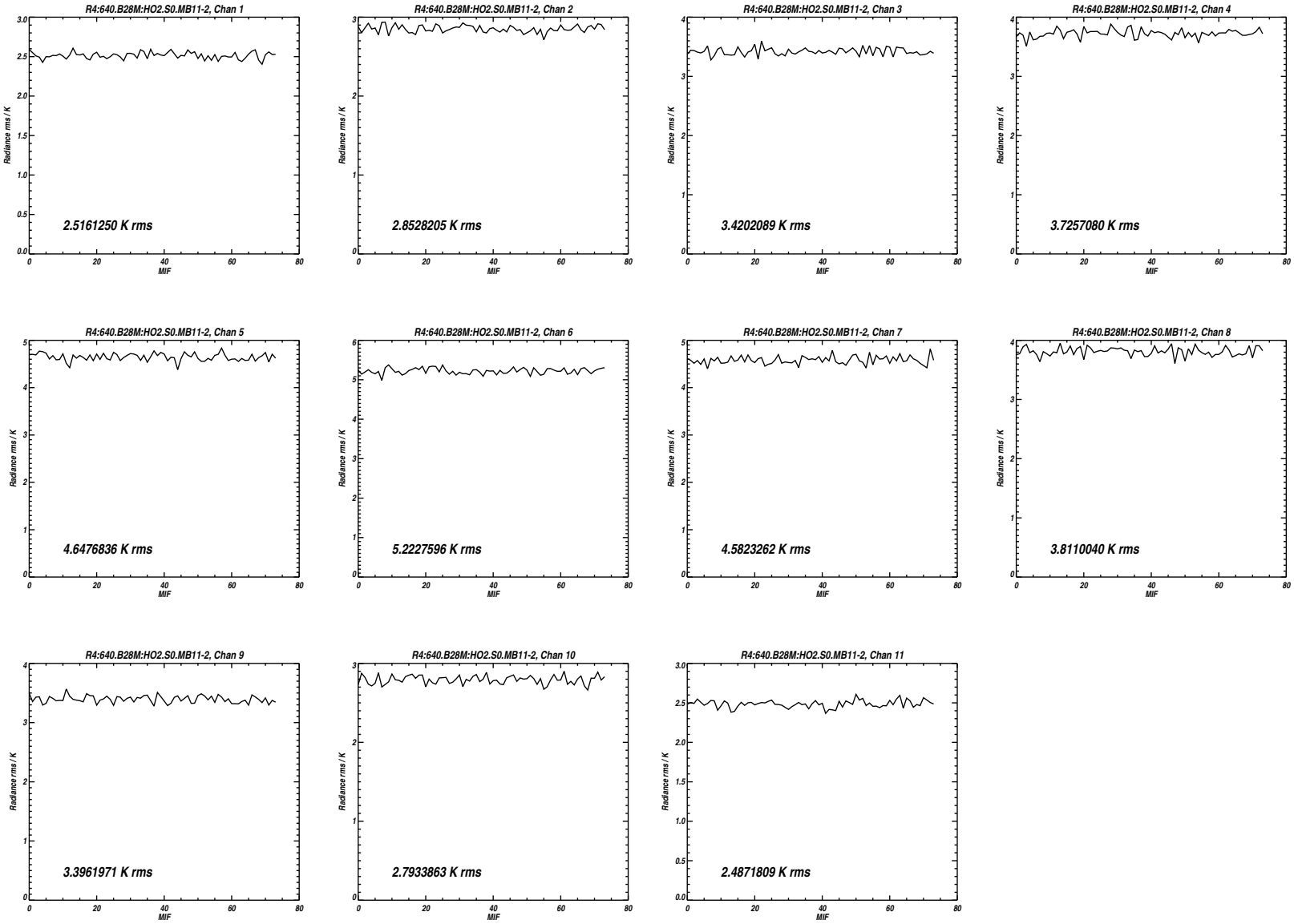

Figure B.65: Measured *rms* noise for all 11 channels of Mid-band 28 for the MIFs treated as Limb views in Level 1 processing.

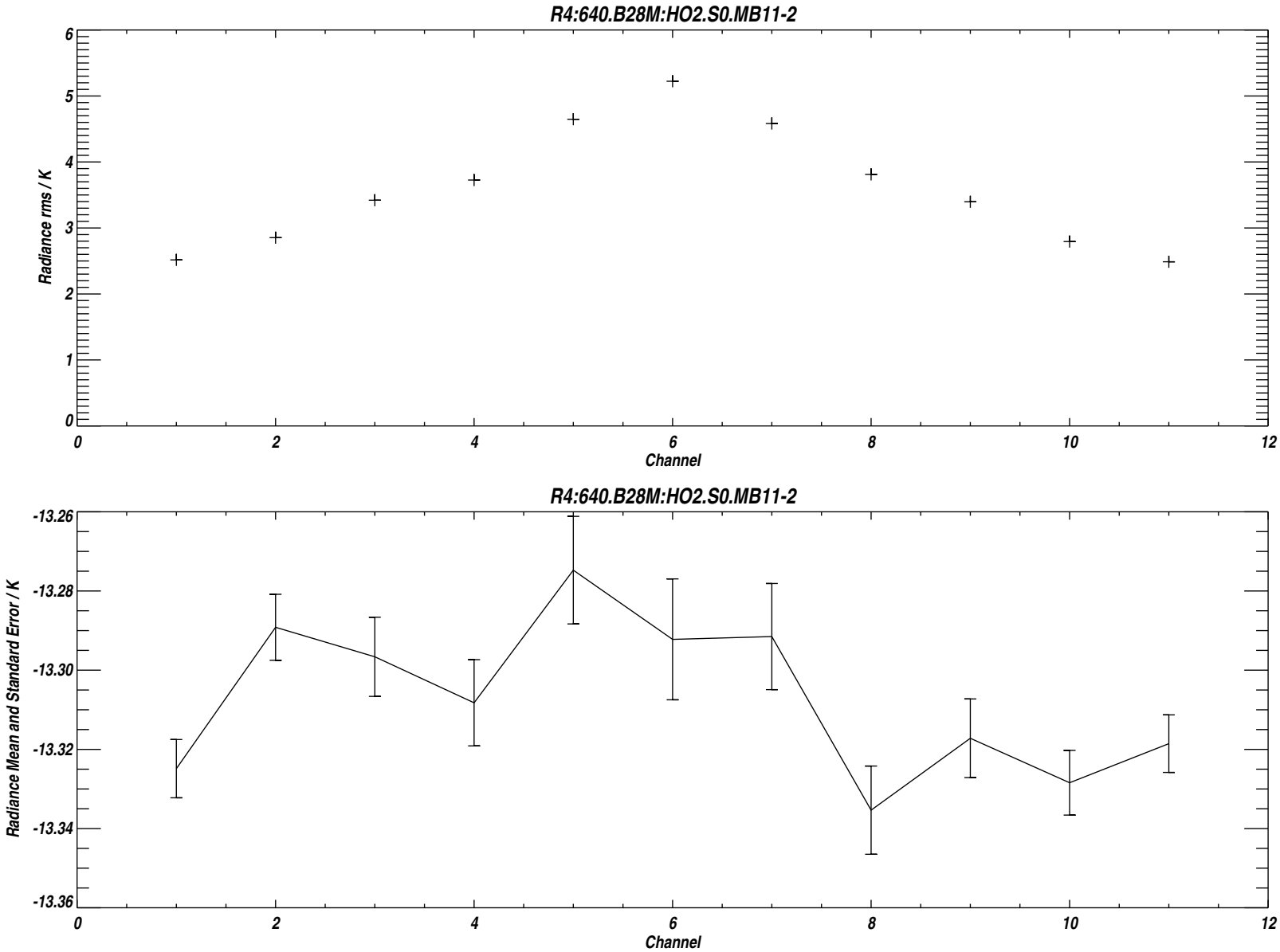

Figure B.66: Measured *rms* noise for each channel of Mid-band 28 (upper panel). The lower panel plots the difference between the mean 'Limb' and reference radiances, the vertical bars indicating the *rms* uncertainty due to noise.

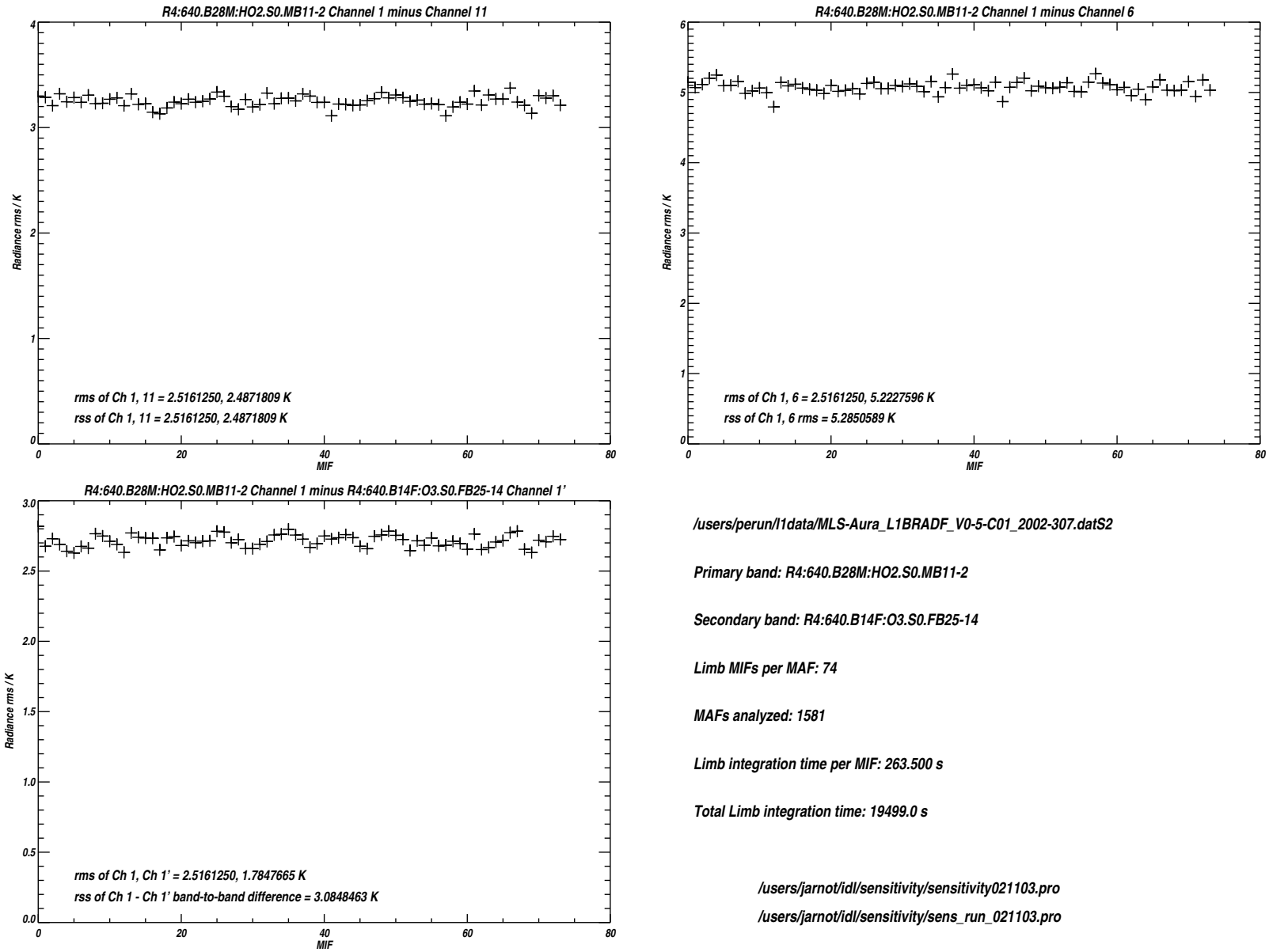

Figure B.67: Measured *rms* noise on the radiance differences between Channels 1 and 11 of Mid-band 28 (upper left panel), Channels 1 and 6 of Mid-band 28 (upper right panel), and between Channel 1 of Mid-band 28 and Channel 1 of Band 14.

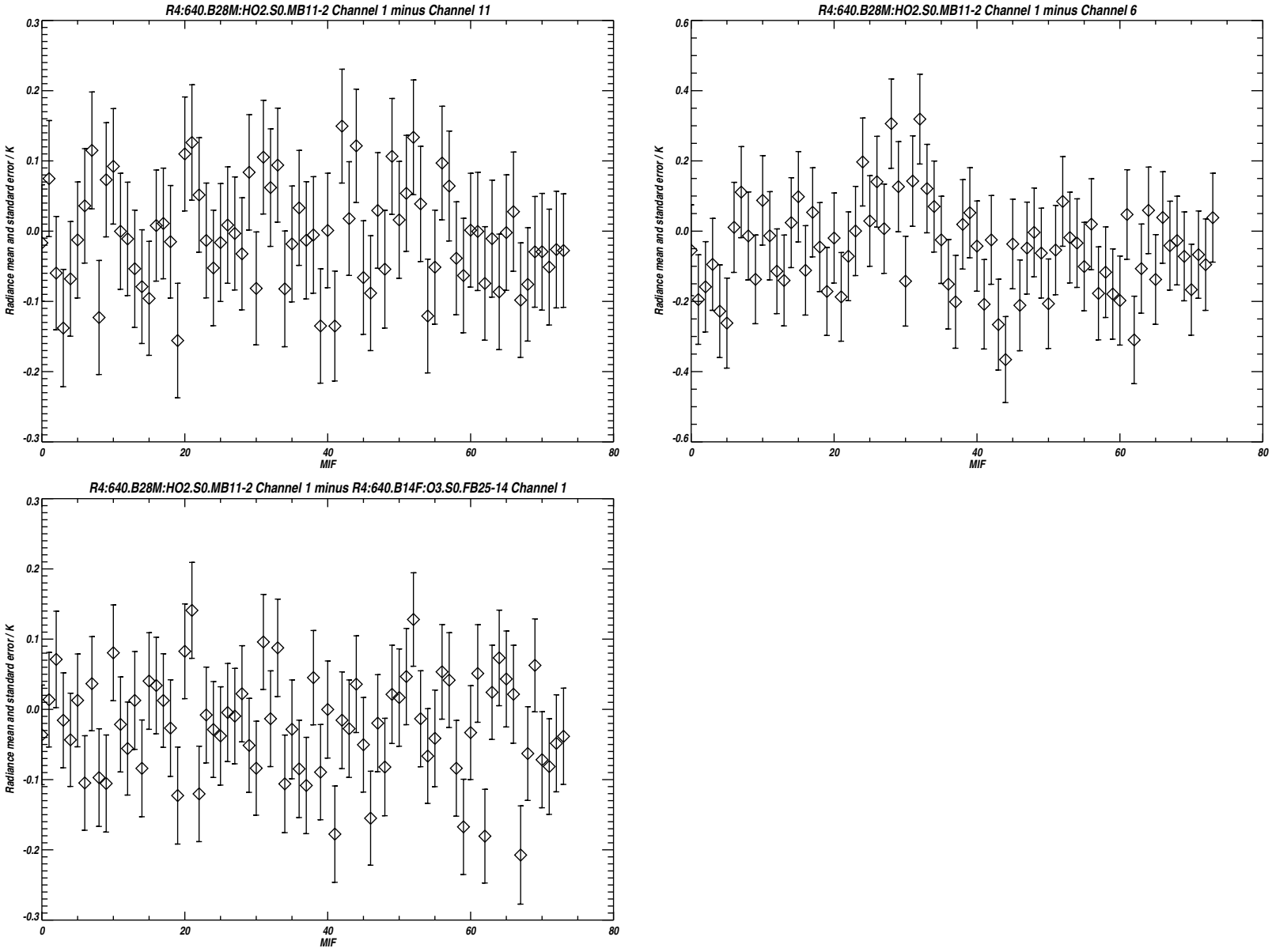

Figure B.68: Radiance differences between the 3 channel pairs plotted in Figure B.67. The vertical bars indicating the *rms* uncertainty due to noise. See text for additional details.

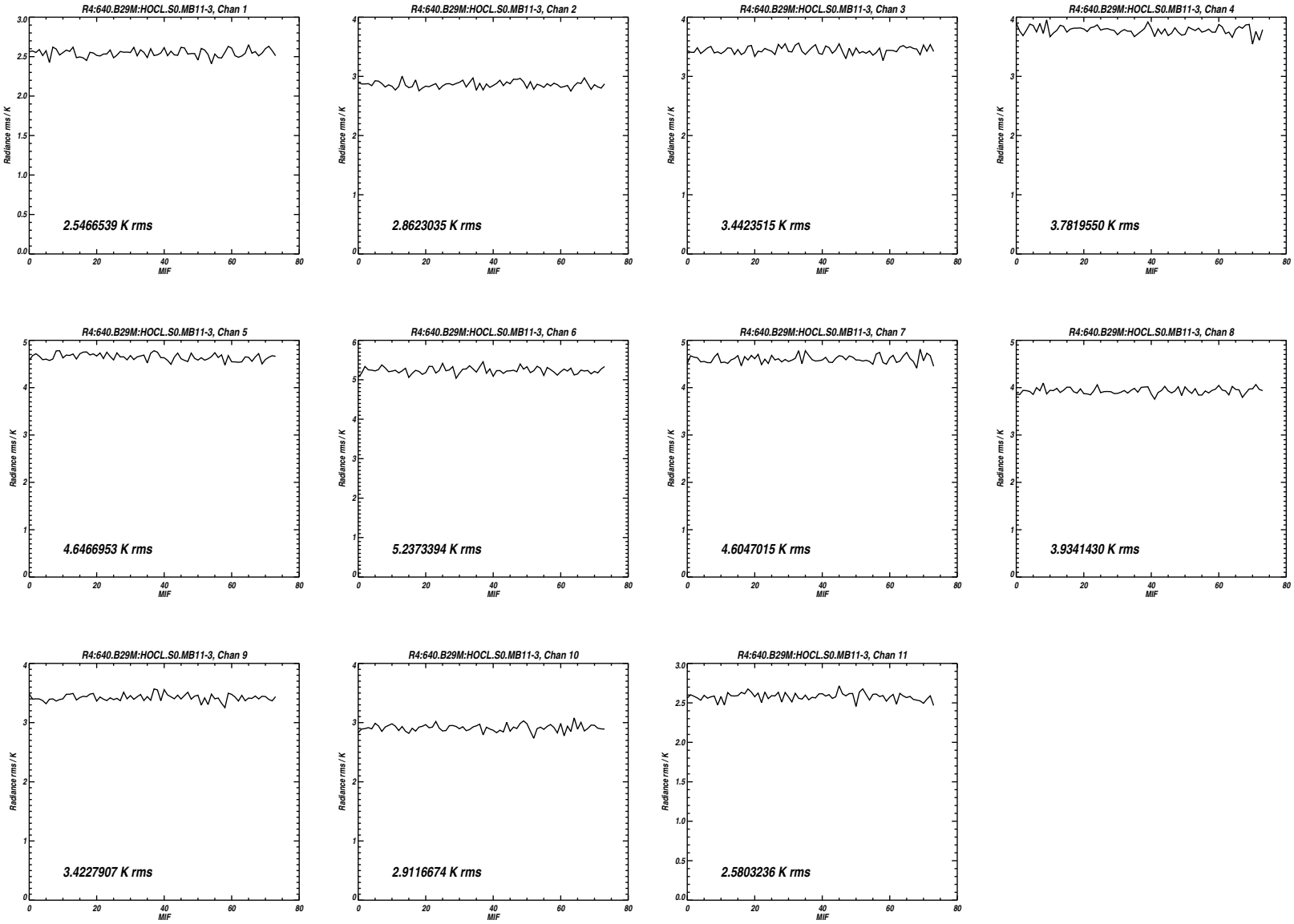

Figure B.69: Measured *rms* noise for all 11 channels of Mid-band 29 for the MIFs treated as Limb views in Level 1 processing.

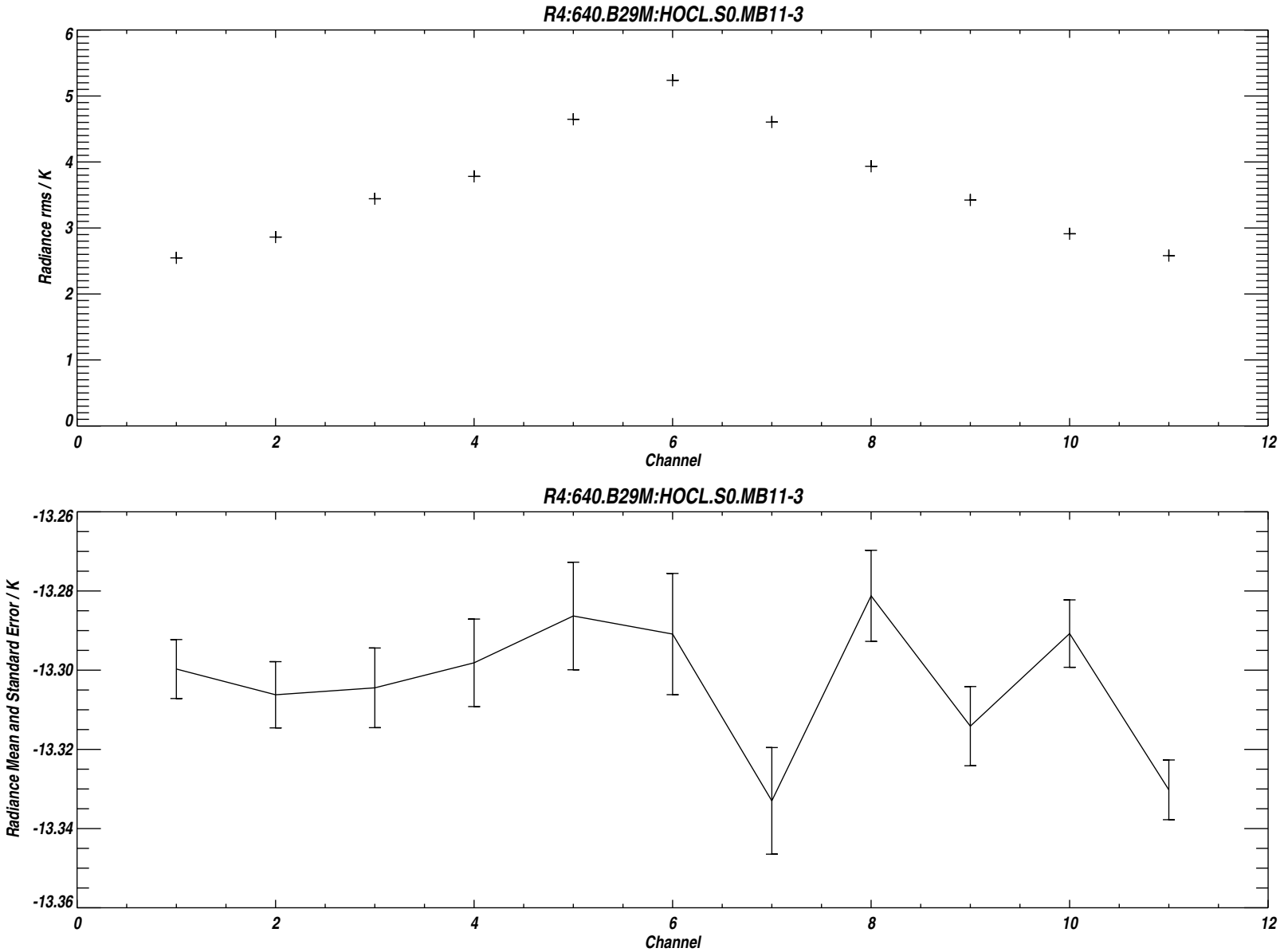

Figure B.70: Measured *rms* noise for each channel of Mid-band 29 (upper panel). The lower panel plots the difference between the mean 'Limb' and reference radiances, the vertical bars indicating the *rms* uncertainty due to noise.

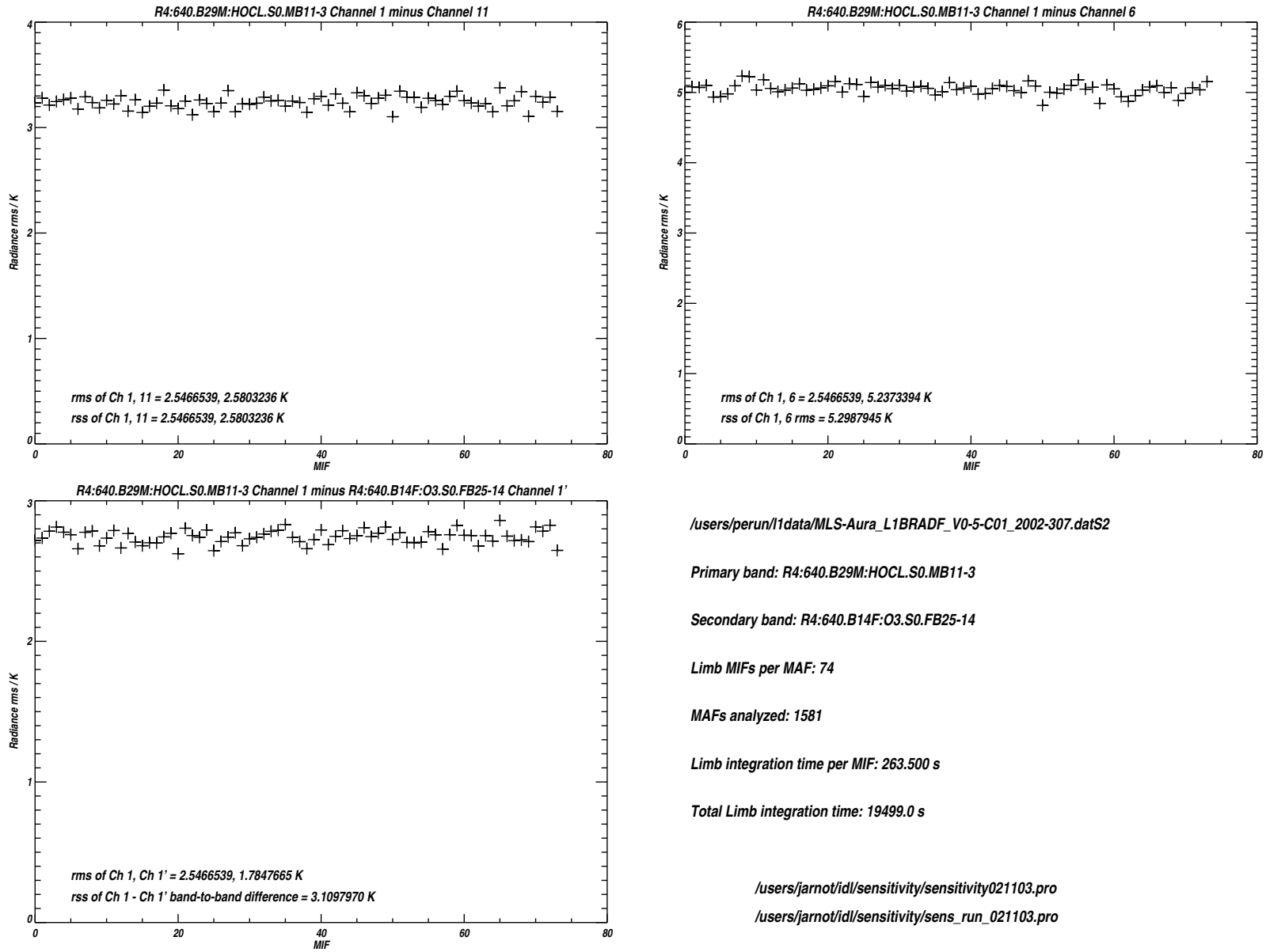

Figure B.71: Measured *rms* noise on the radiance differences between Channels 1 and 11 of Mid-band 29 (upper left panel), Channels 1 and 6 of Mid-band 29 (upper right panel), and between Channel 1 of Mid-band 29 and Channel 1 of Band 14.

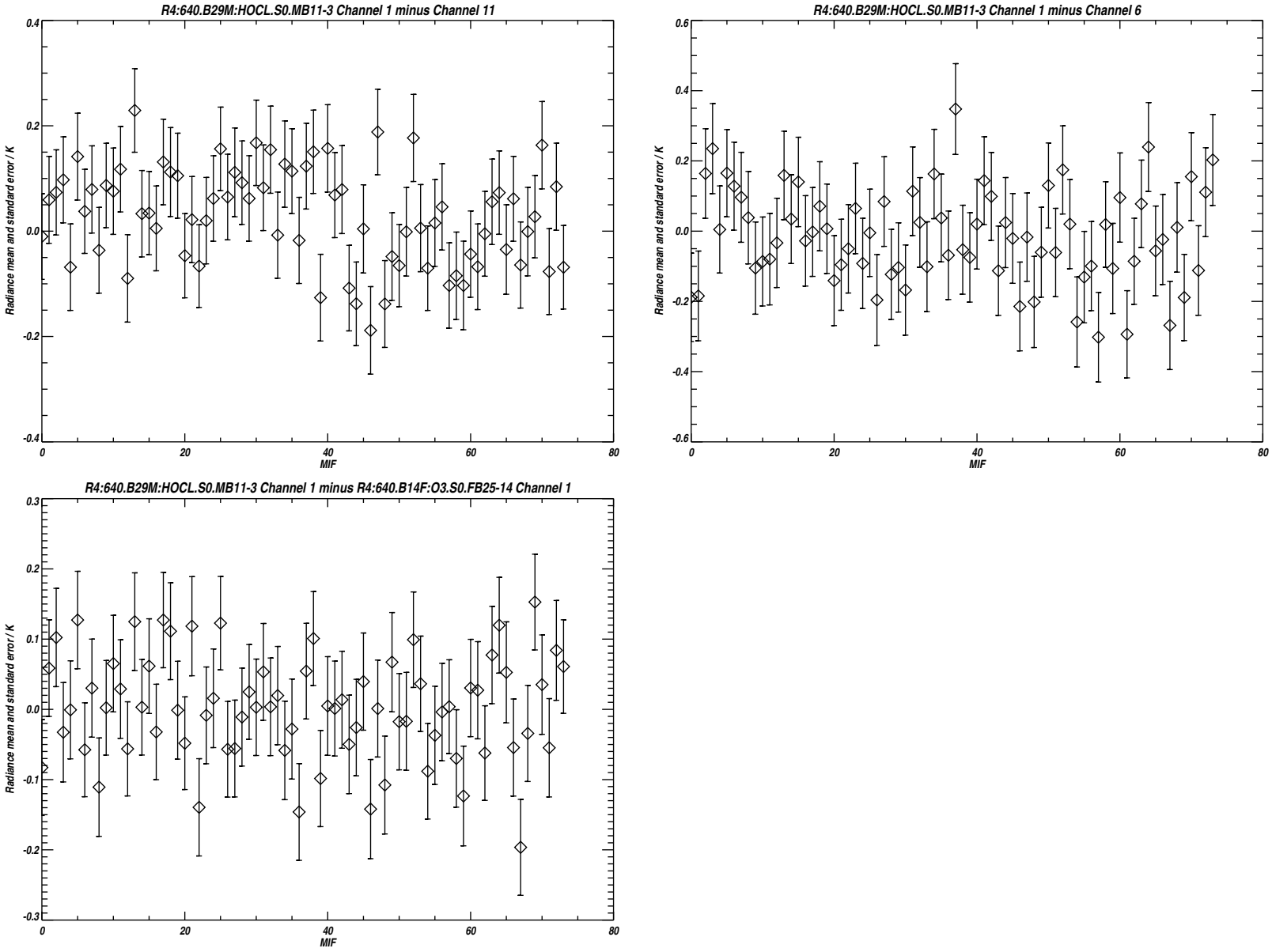

Figure B.72: Radiance differences between the 3 channel pairs plotted in Figure B.71. The vertical bars indicating the *rms* uncertainty due to noise. See text for additional details.

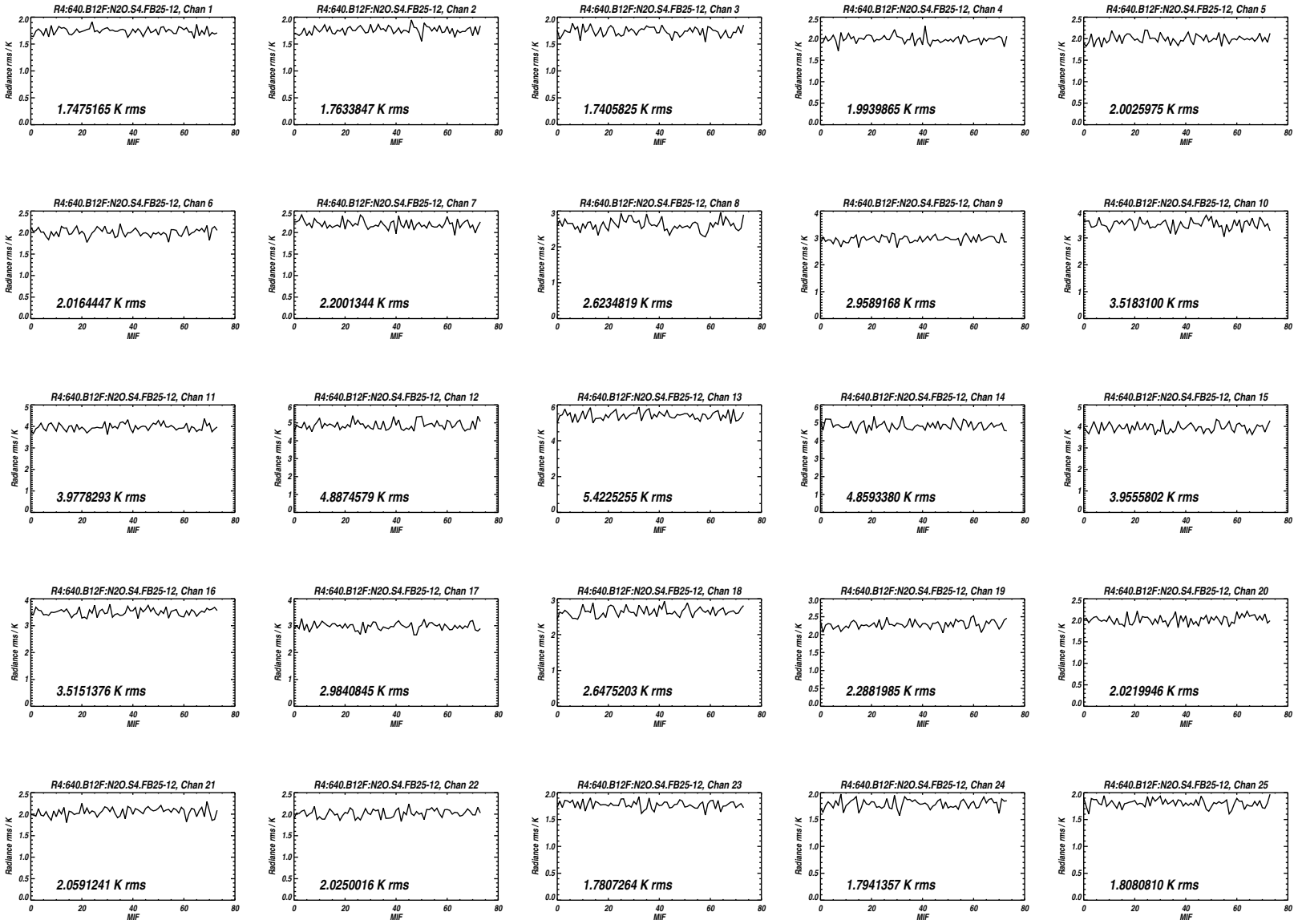

Figure B.73: Measured *rms* noise for all 25 channels of Band 12 for the MIFs treated as Limb views in Level 1 processing.

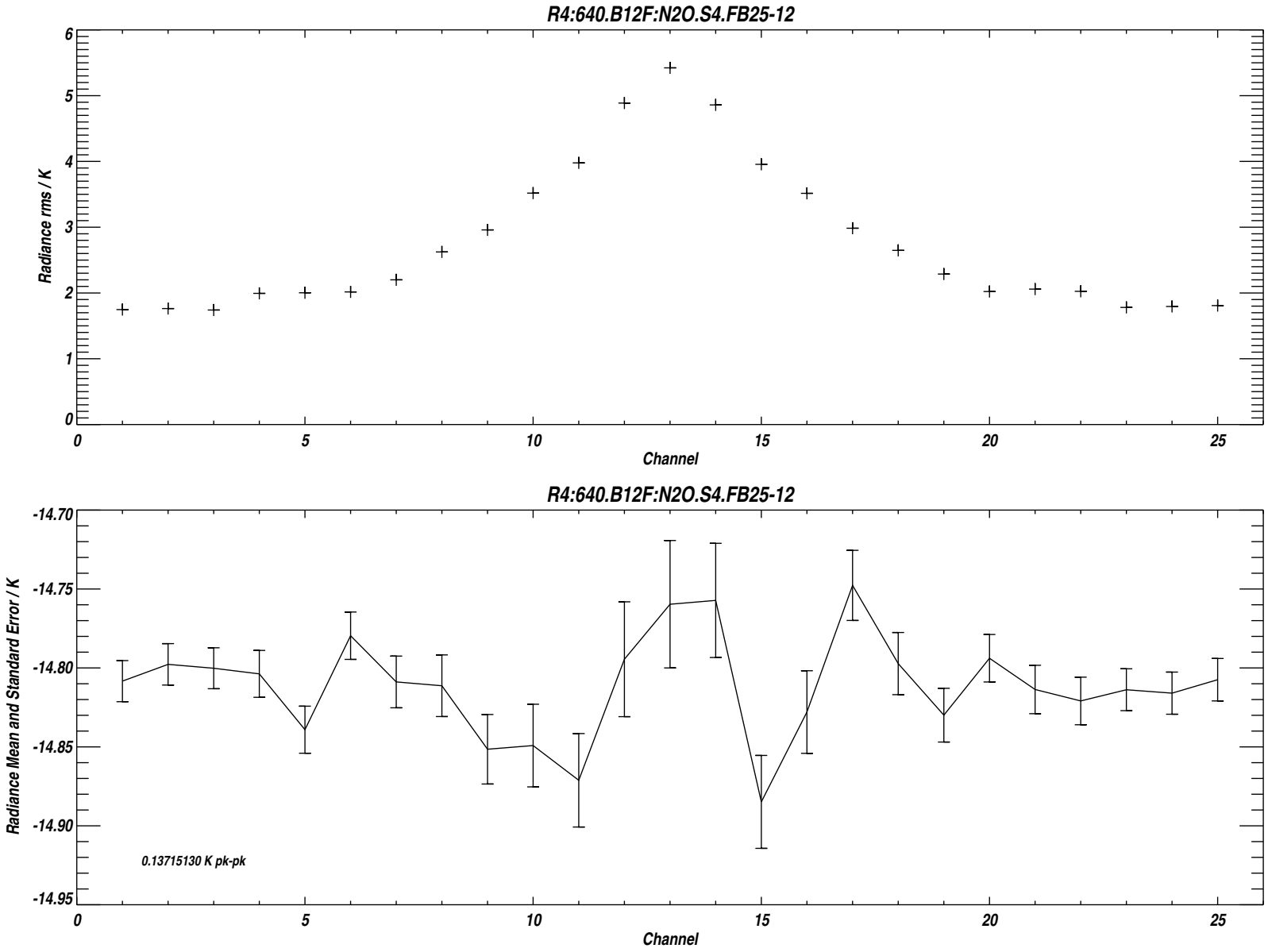

Figure B.74: Measured *rms* noise for each channel of Band 12 (upper panel). The lower panel plots the difference between the mean 'Limb' and reference radiances, the vertical bars indicating the *rms* uncertainty due to noise.

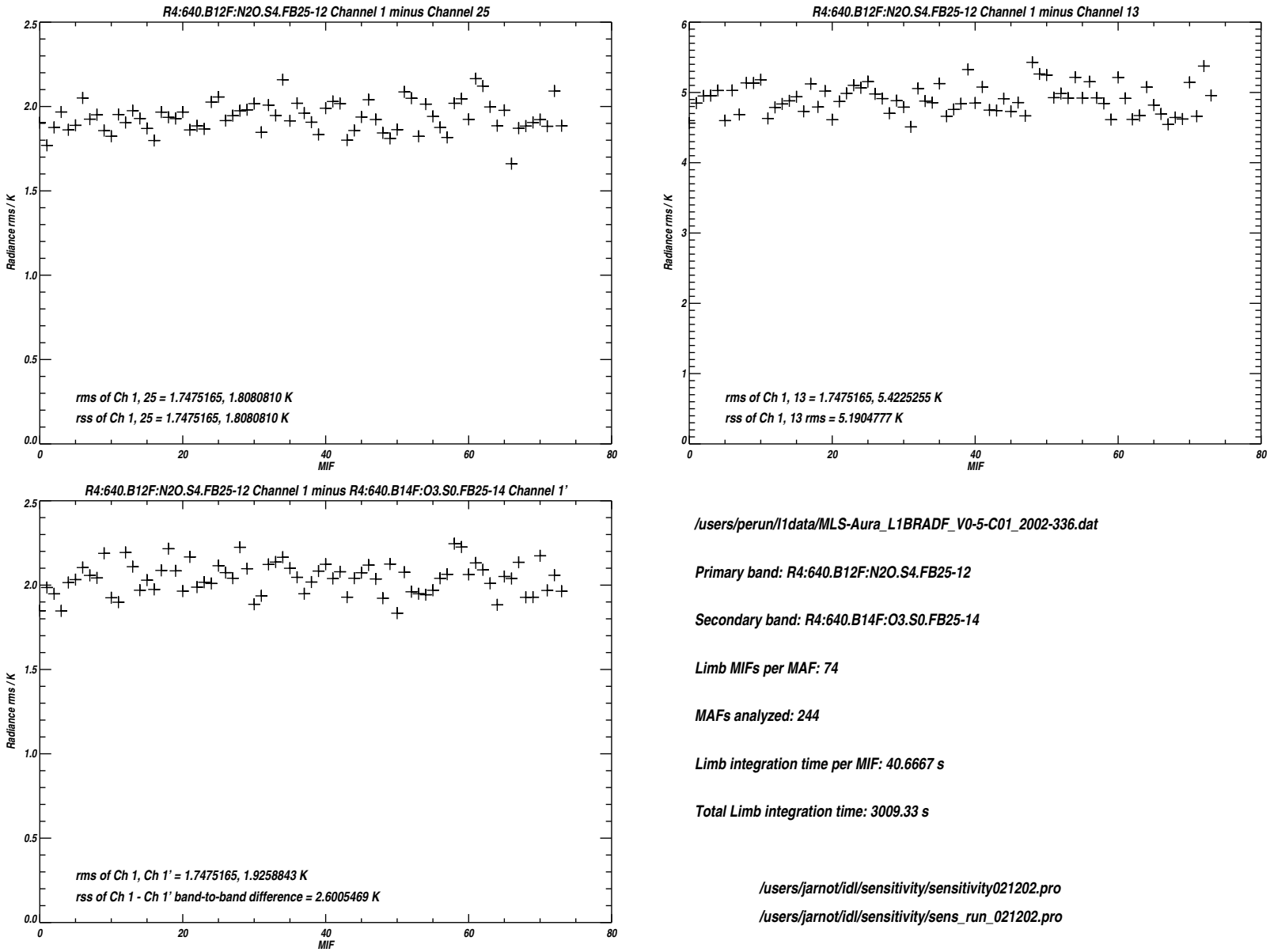

Figure B.75: Measured *rms* noise on the radiance differences between Channels 1 and 25 of Band 12 (upper left panel), Channels 1 and 13 of Band 12 (upper right panel), and between Channel 1 of Band 12 and Channel 1 of Band 14.

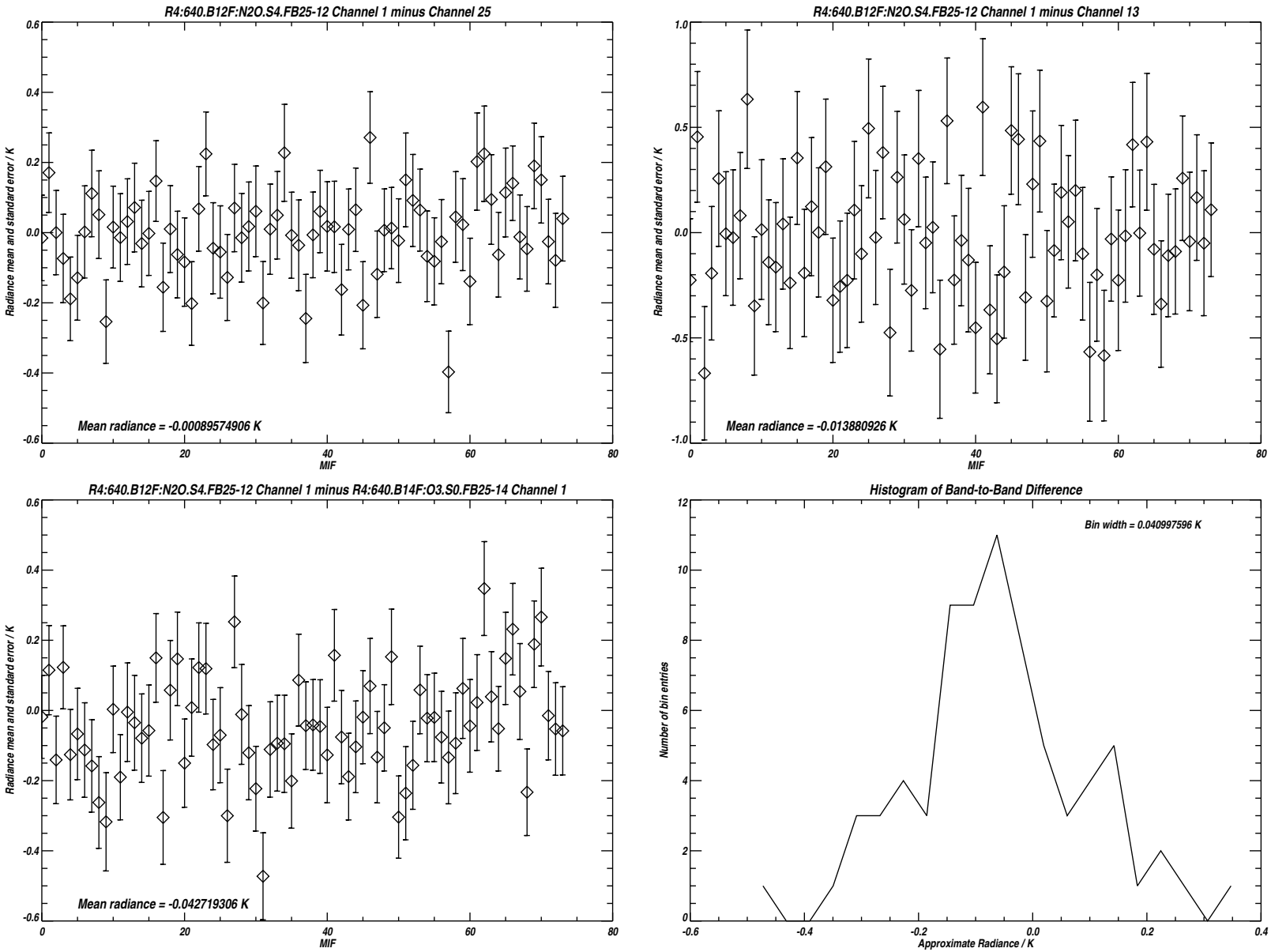

Figure B.76: Radiance differences between the 3 channel pairs plotted in Figure B.75. The vertical bars indicating the *rms* uncertainty due to noise. The lower right hand panel is a histogram of the data in the panel to its left. See text for additional details.

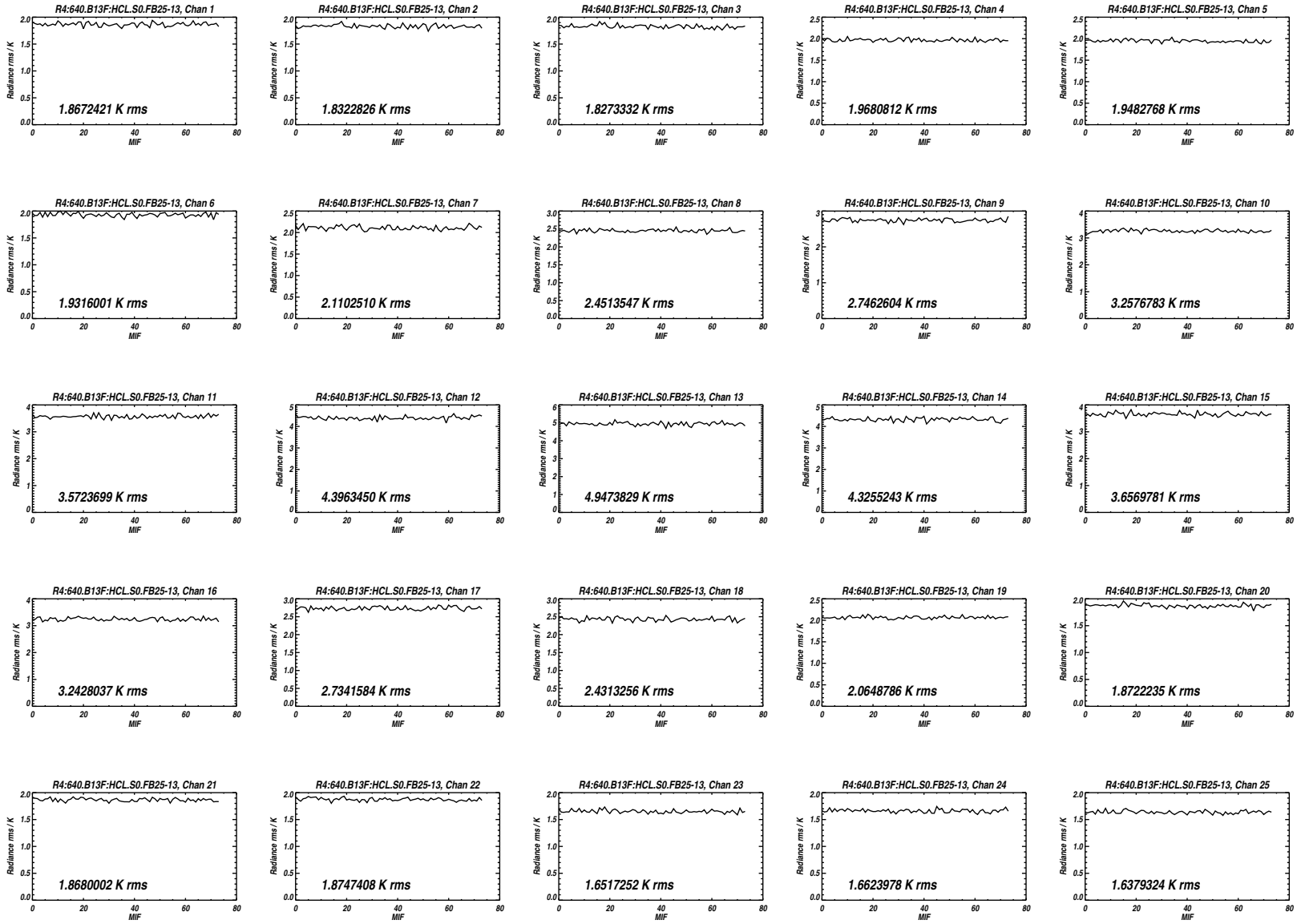

Figure B.77: Measured *rms* noise for all 25 channels of Band 13 for the MIFs treated as Limb views in Level 1 processing.

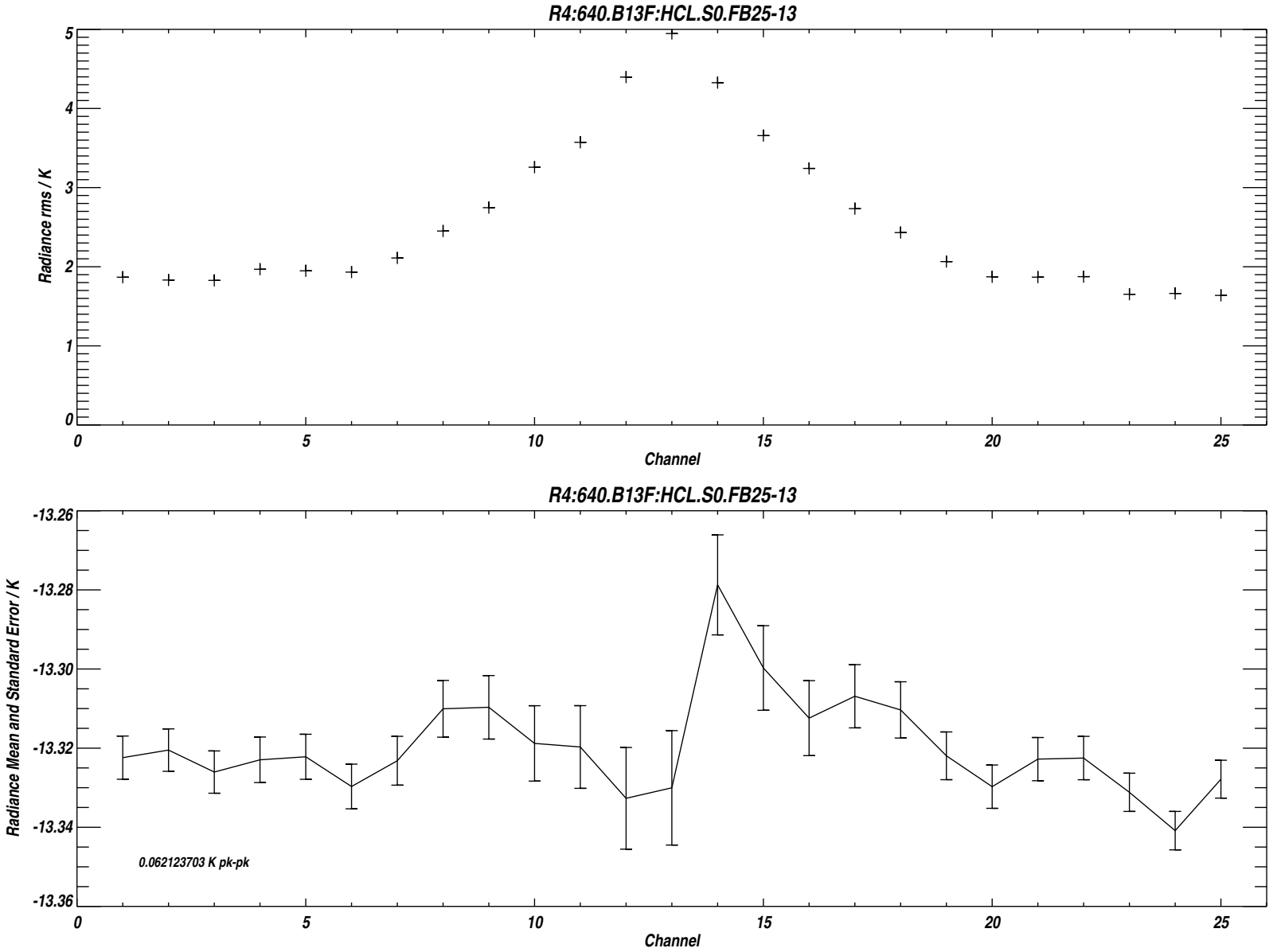

Figure B.78: Measured *rms* noise for each channel of Band 13 (upper panel). The lower panel plots the difference between the mean 'Limb' and reference radiances, the vertical bars indicating the *rms* uncertainty due to noise.

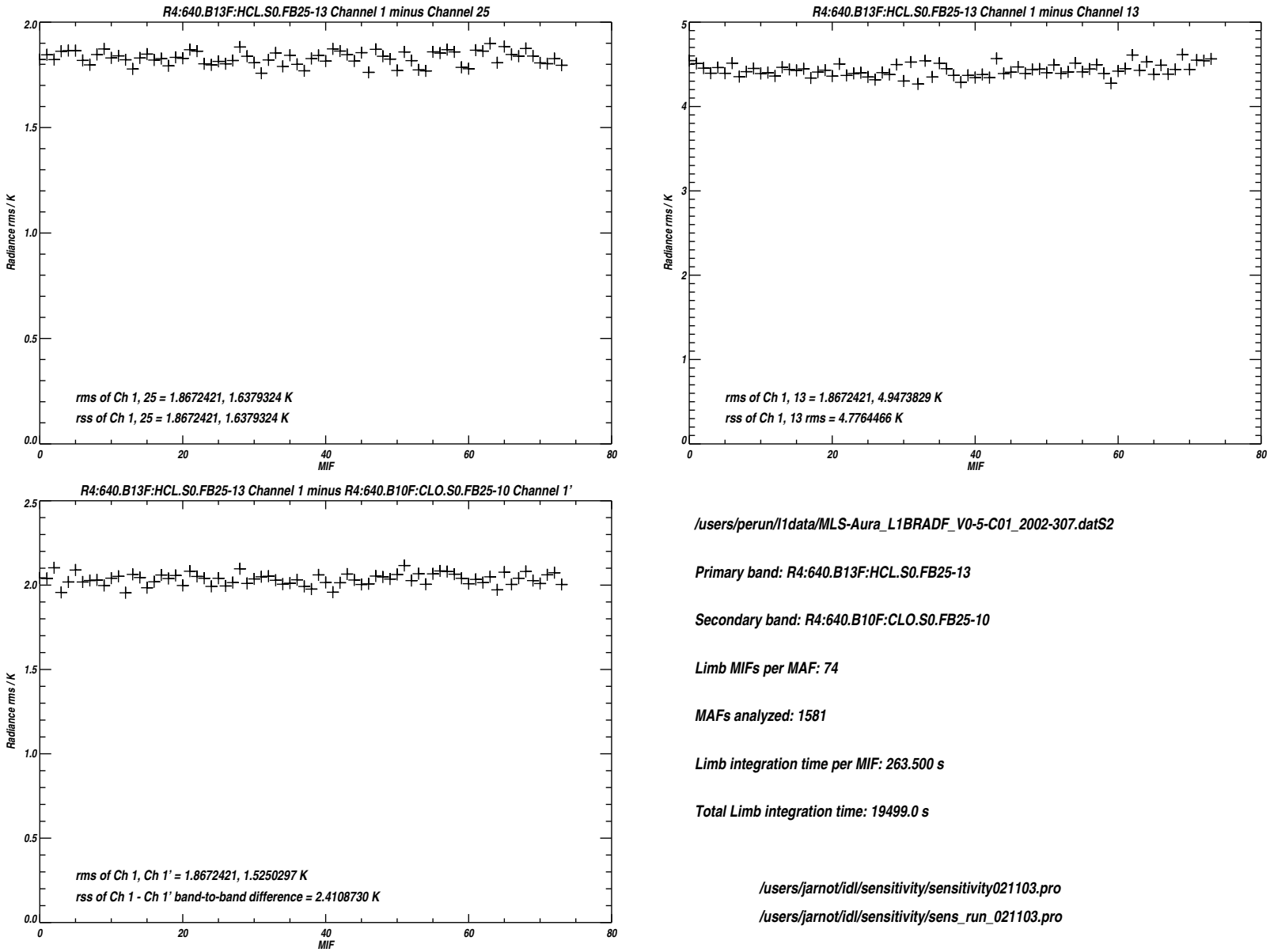

Figure B.79: Measured *rms* noise on the radiance differences between Channels 1 and 25 of Band 13 (upper left panel), Channels 1 and 13 of Band 13 (upper right panel), and between Channel 1 of Band 13 and Channel 1 of Band 10.

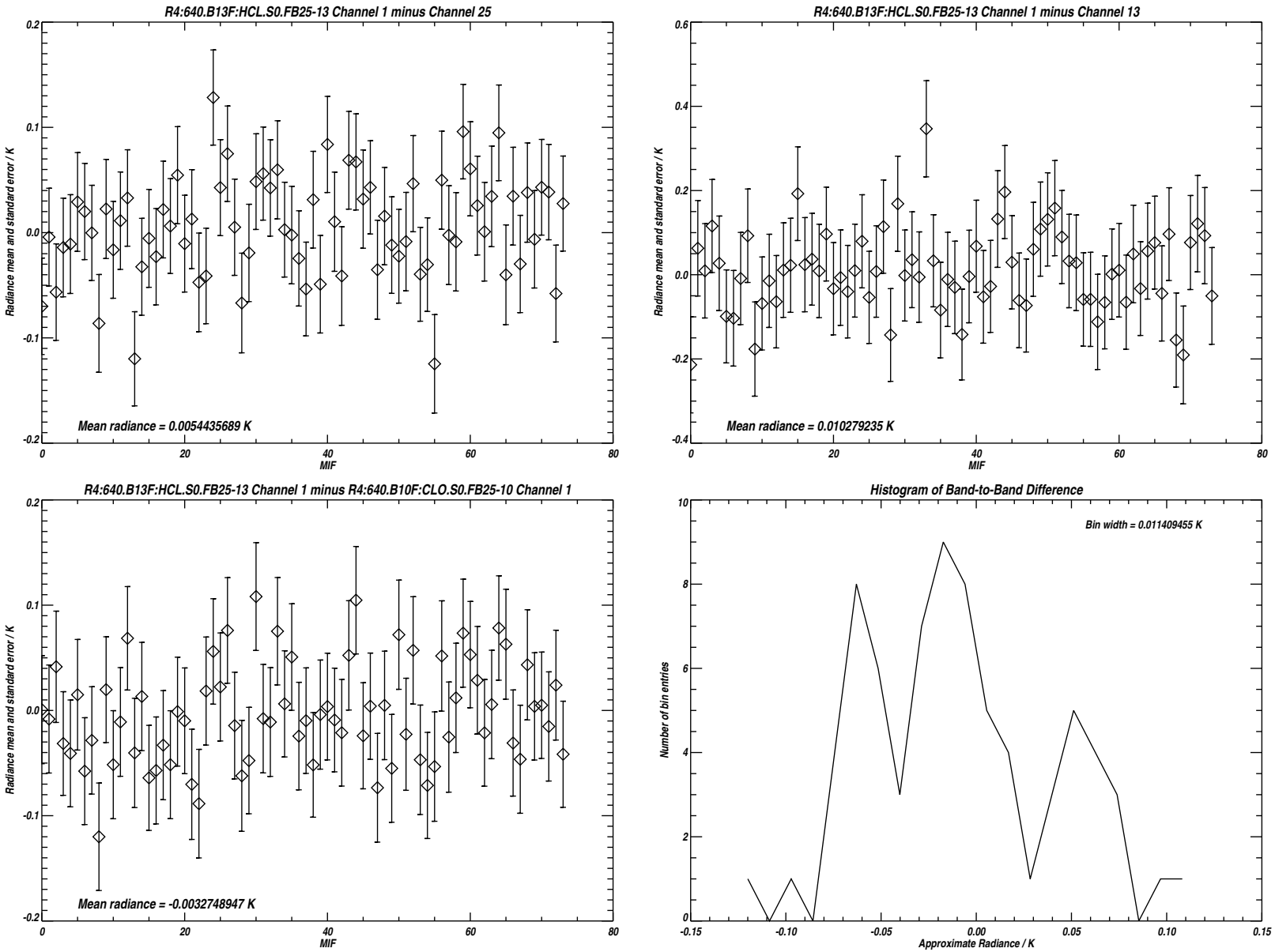

Figure B.80: Radiance differences between the 3 channel pairs plotted in Figure B.79. The vertical bars indicating the *rms* uncertainty due to noise. The lower right hand panel is a histogram of the data in the panel to its left. See text for additional details.

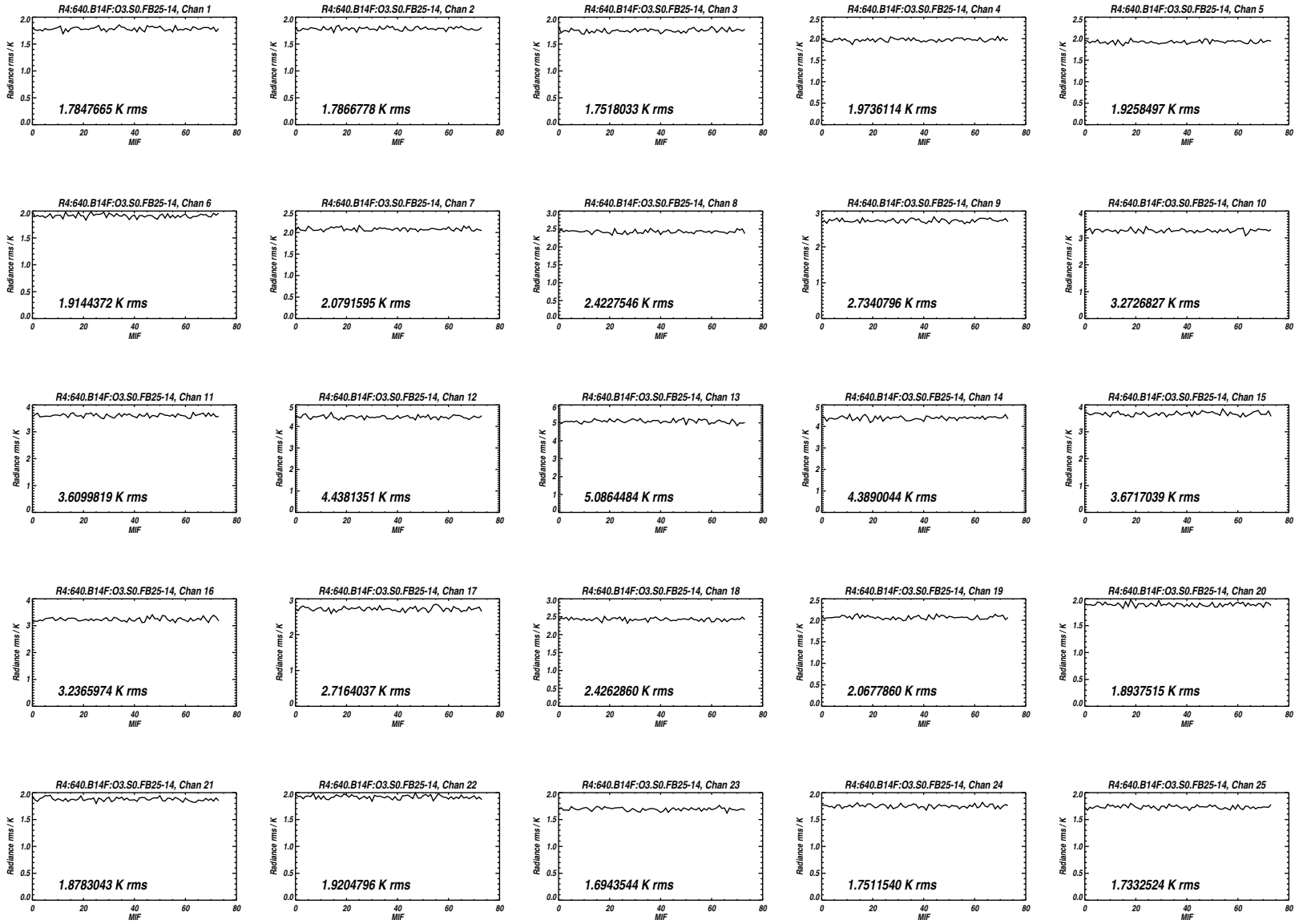

Figure B.81: Measured *rms* noise for all 25 channels of Band 14 for the MIFs treated as Limb views in Level 1 processing.

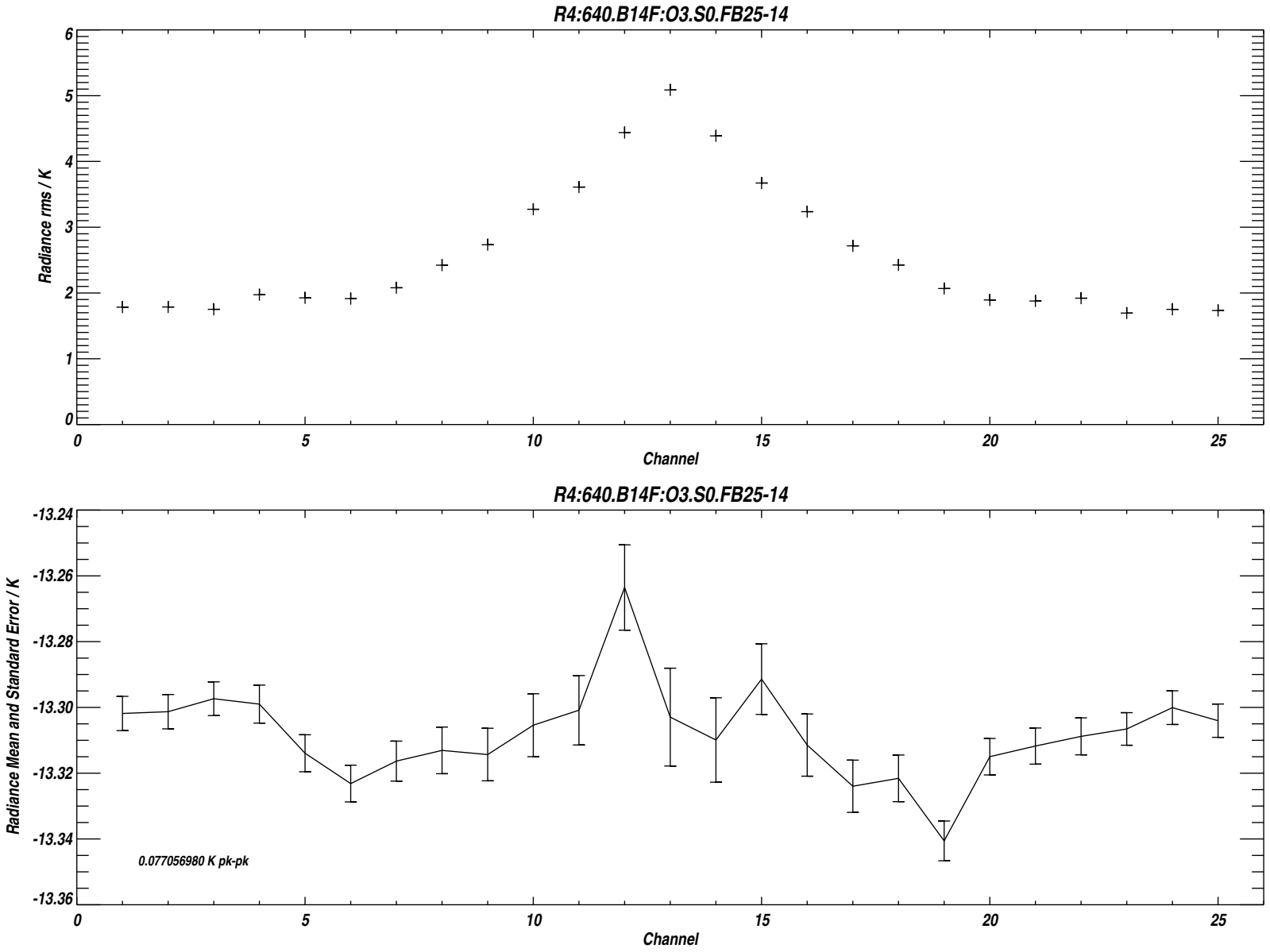

Figure B.82: Measured *rms* noise for each channel of Band 14 (upper panel). The lower panel plots the difference between the mean 'Limb' and reference radiances, the vertical bars indicating the *rms* uncertainty due to noise.

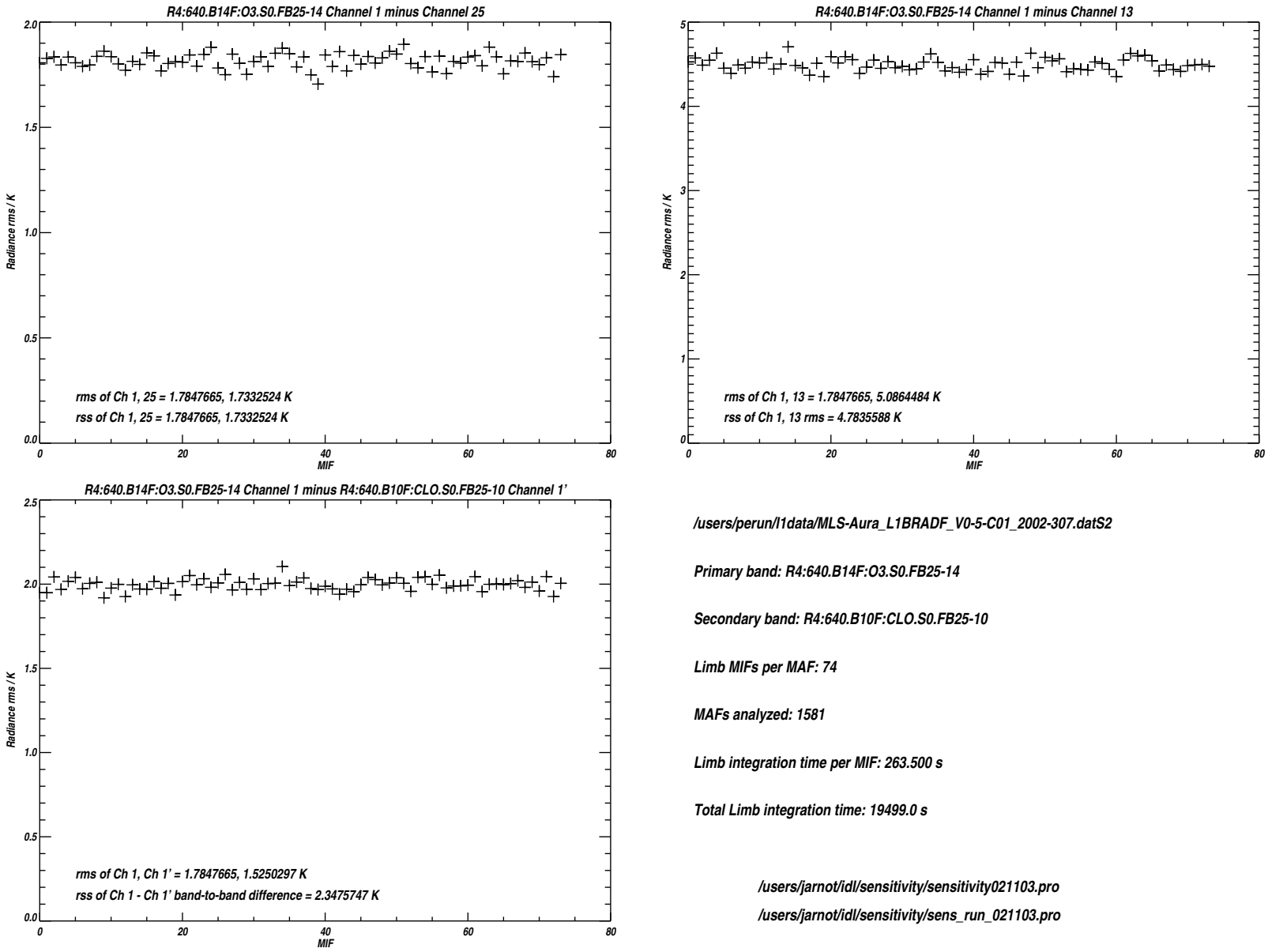

Figure B.83: Measured *rms* noise on the radiance differences between Channels 1 and 25 of Band 14 (upper left panel), Channels 1 and 13 of Band 14 (upper right panel), and between Channel 1 of Band 14 and Channel 1 of Band 10.

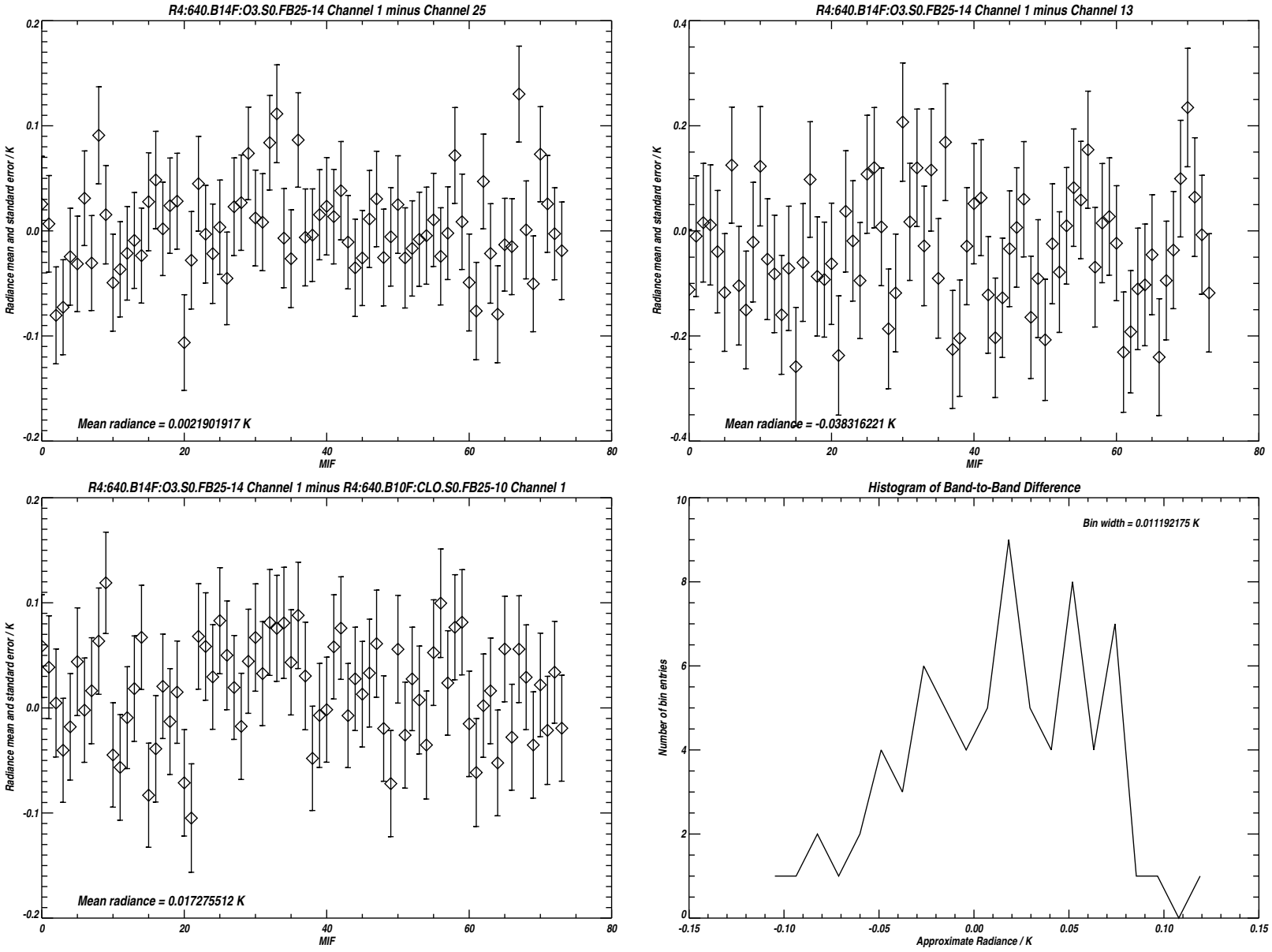

Figure B.84: Radiance differences between the 3 channel pairs plotted in Figure B.83. The vertical bars indicating the *rms* uncertainty due to noise. The lower right hand panel is a histogram of the data in the panel to its left. See text for additional details.

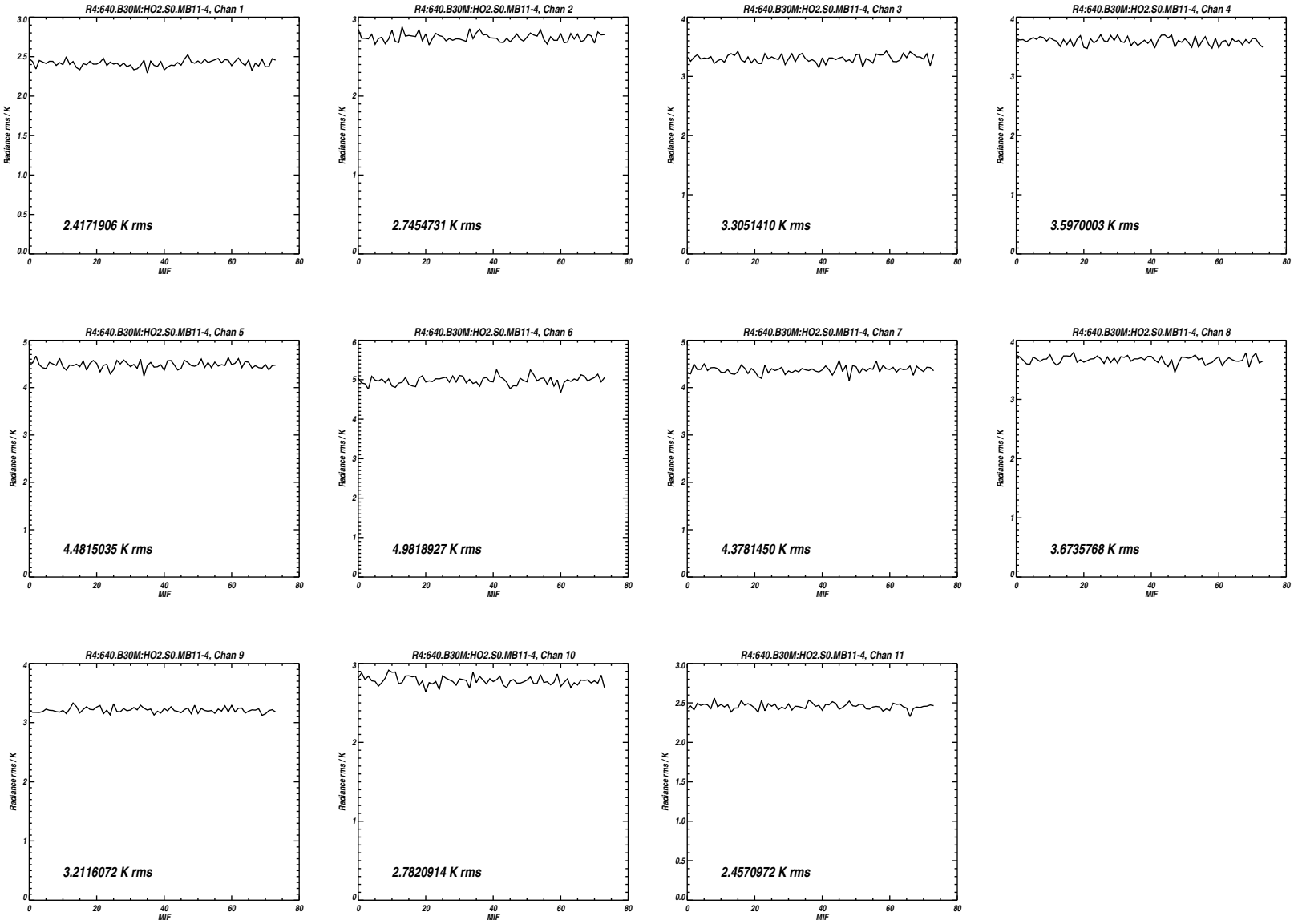

Figure B.85: Measured *rms* noise for all 11 channels of Mid-band 30 for the MIFs treated as Limb views in Level 1 processing.

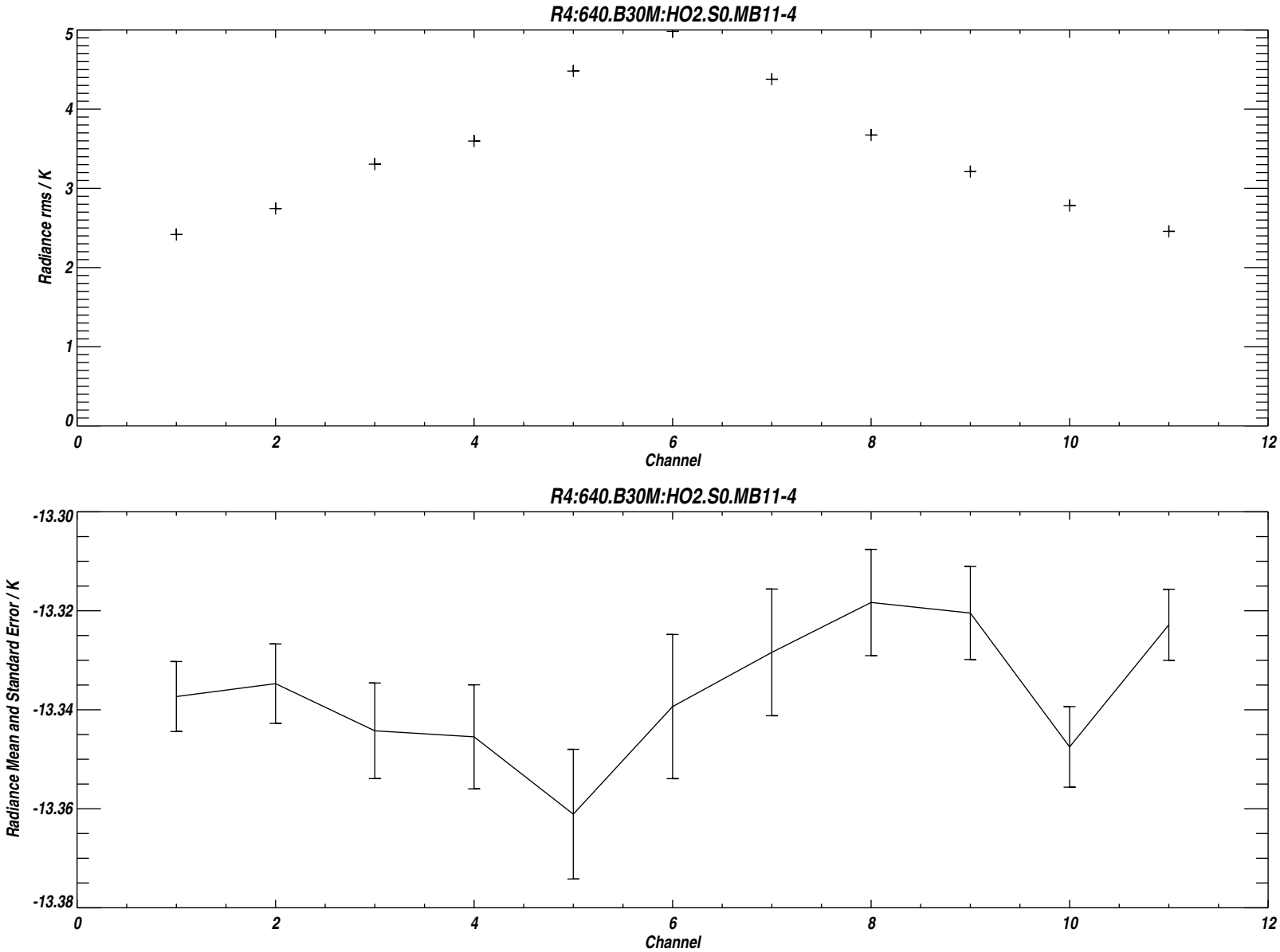

Figure B.86: Measured *rms* noise for each channel of Mid-band 30 (upper panel). The lower panel plots the difference between the mean 'Limb' and reference radiances, the vertical bars indicating the *rms* uncertainty due to noise.

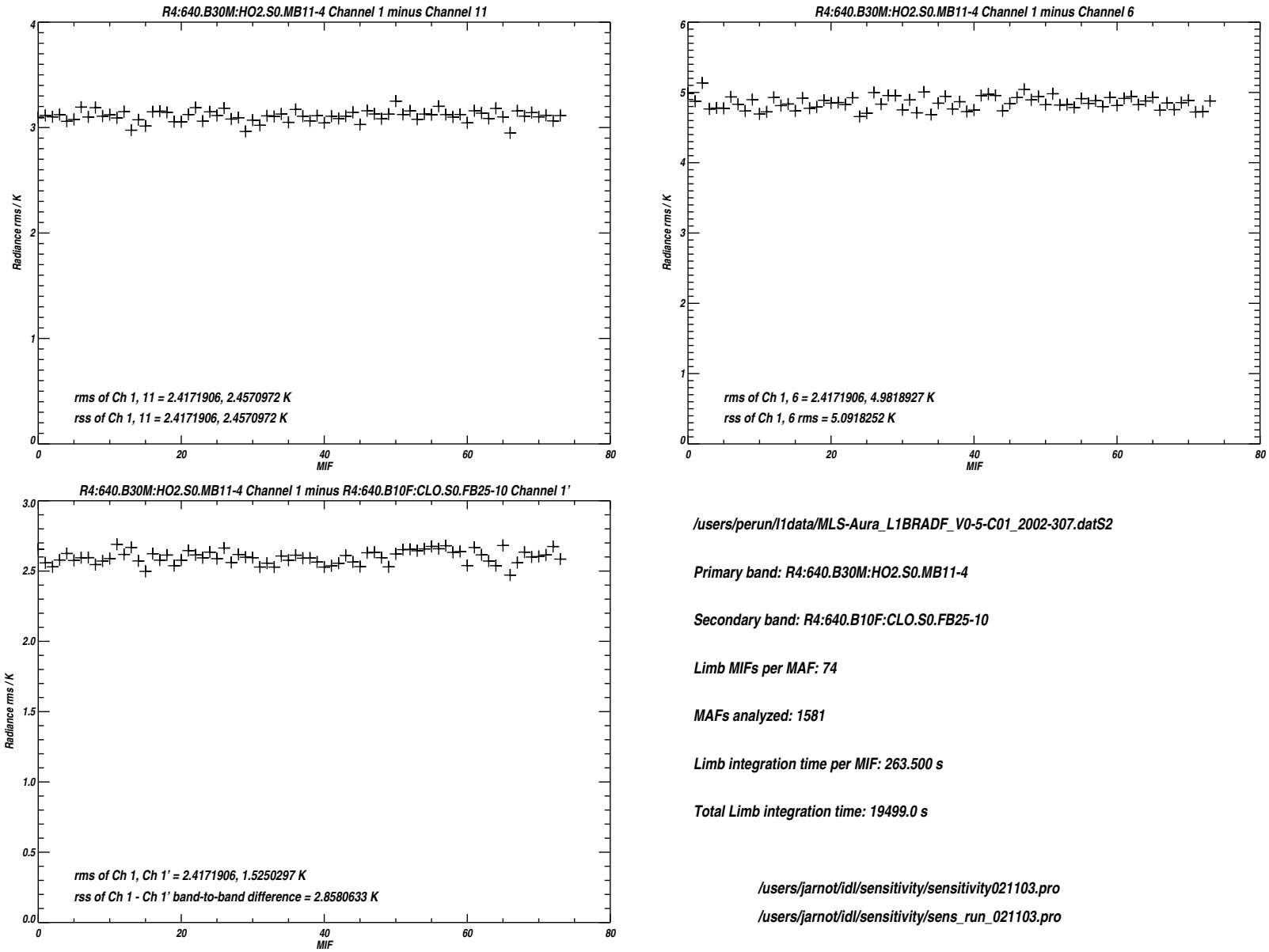

Figure B.87: Measured *rms* noise on the radiance differences between Channels 1 and 11 of Mid-band 30 (upper left panel), Channels 1 and 6 of Mid-band 30 (upper right panel), and between Channel 1 of Mid-band 30 and Channel 1 of Band 10.

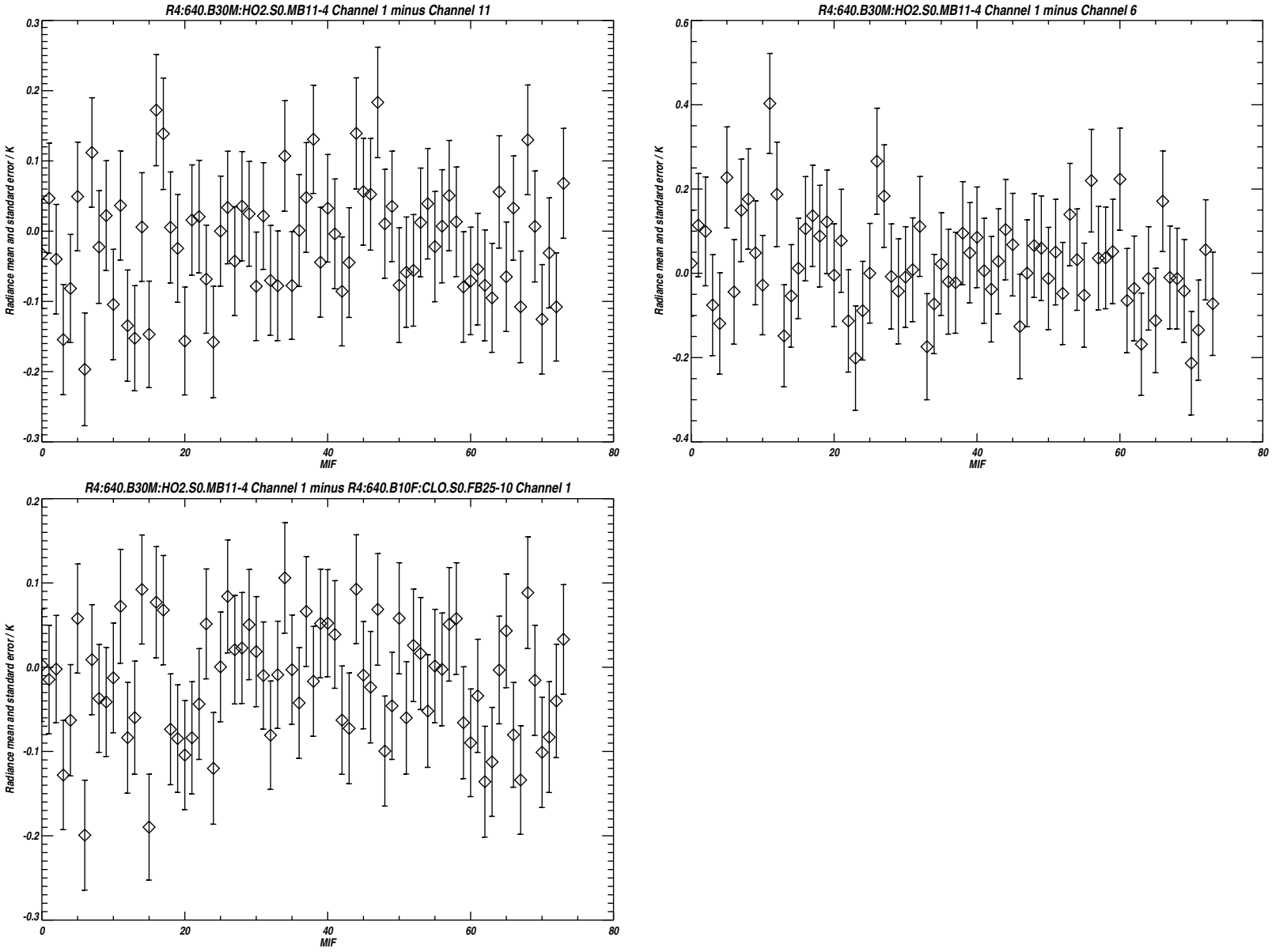

Figure B.88: Radiance differences between the 3 channel pairs plotted in Figure B.87. The vertical bars indicating the *rms* uncertainty due to noise. See text for additional details.

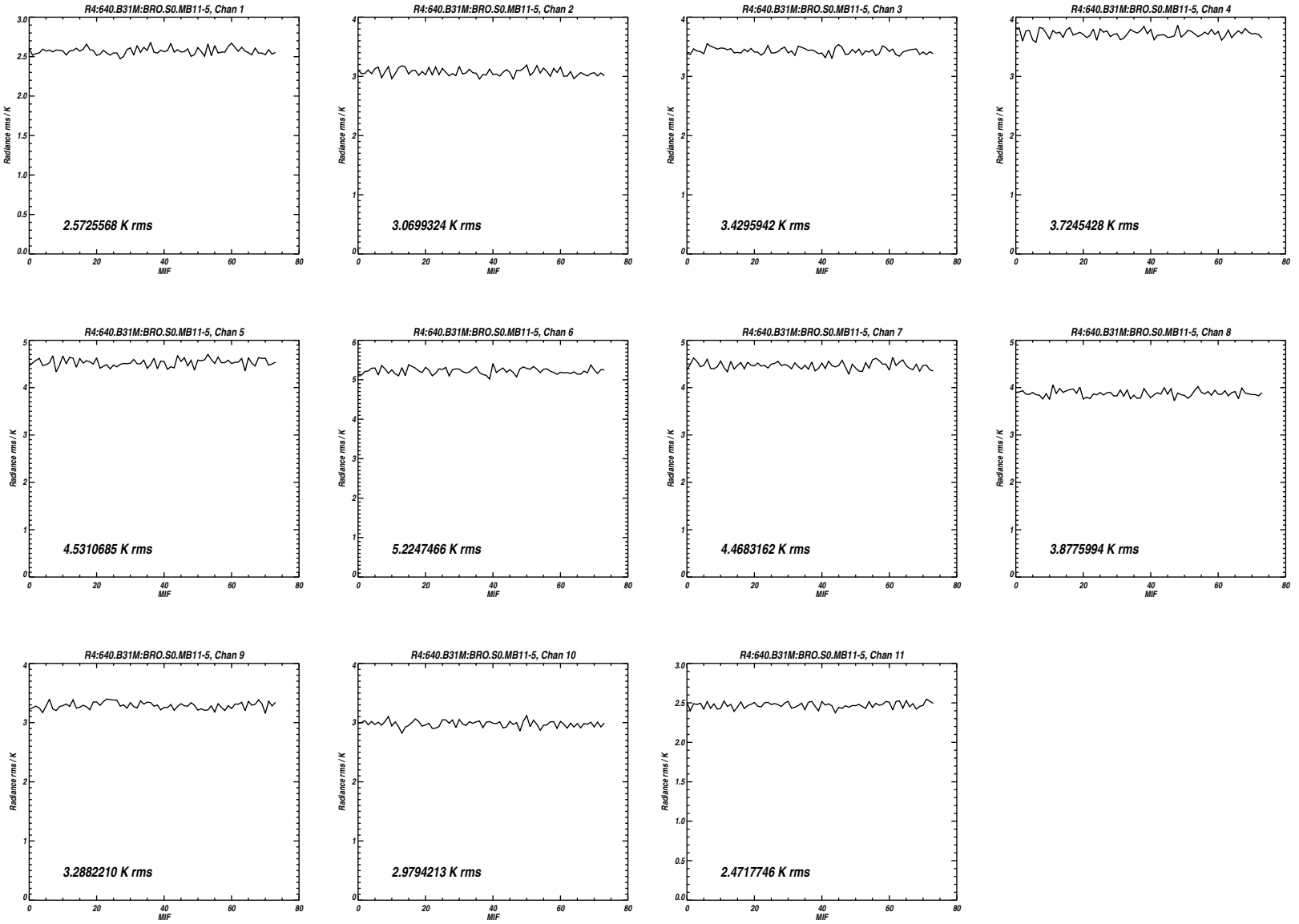

Figure B.89: Measured *rms* noise for all 11 channels of Mid-band 31 for the MIFs treated as Limb views in Level 1 processing.

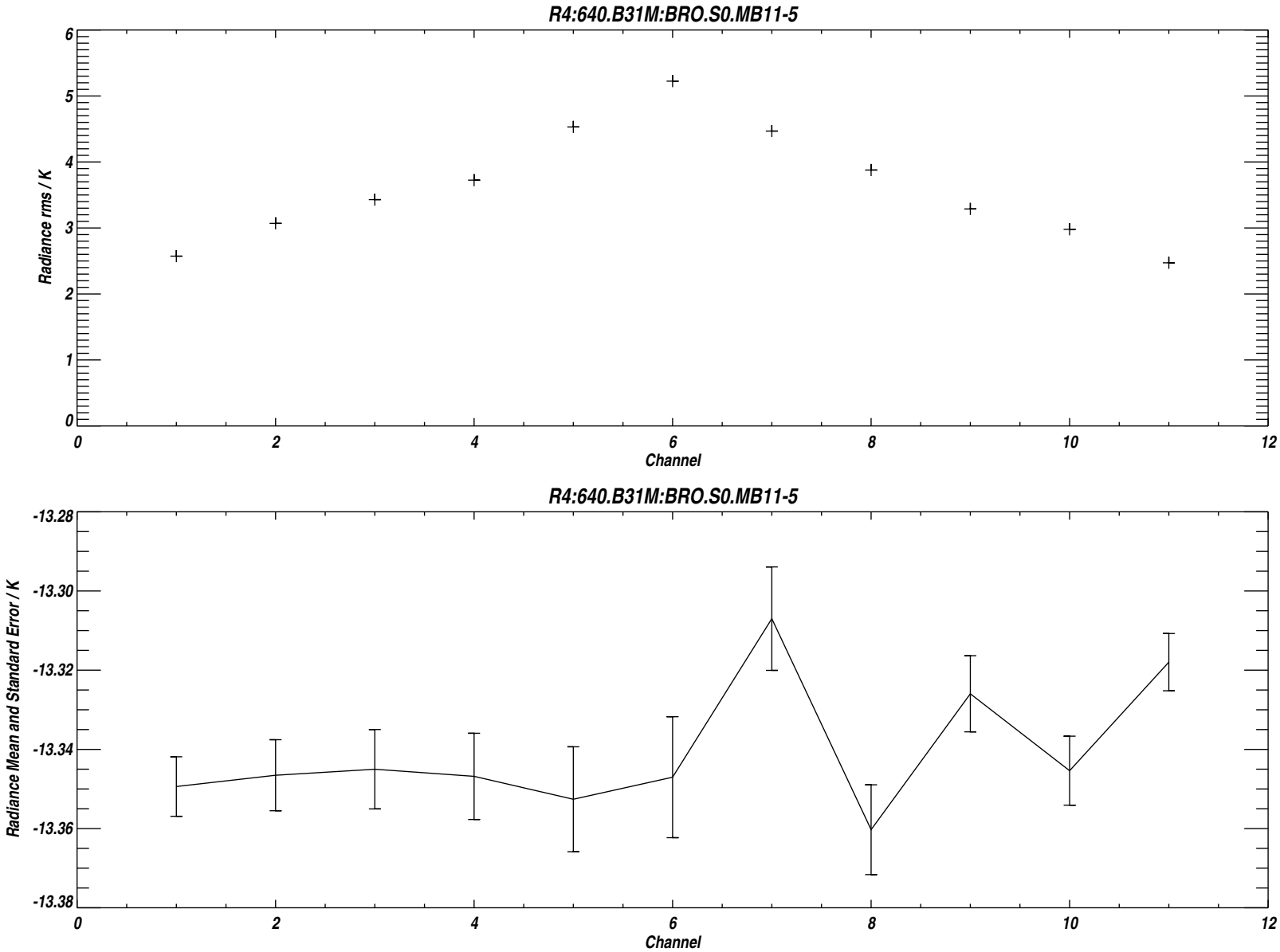

Figure B.90: Measured *rms* noise for each channel of Mid-band 31 (upper panel). The lower panel plots the difference between the mean 'Limb' and reference radiances, the vertical bars indicating the *rms* uncertainty due to noise.

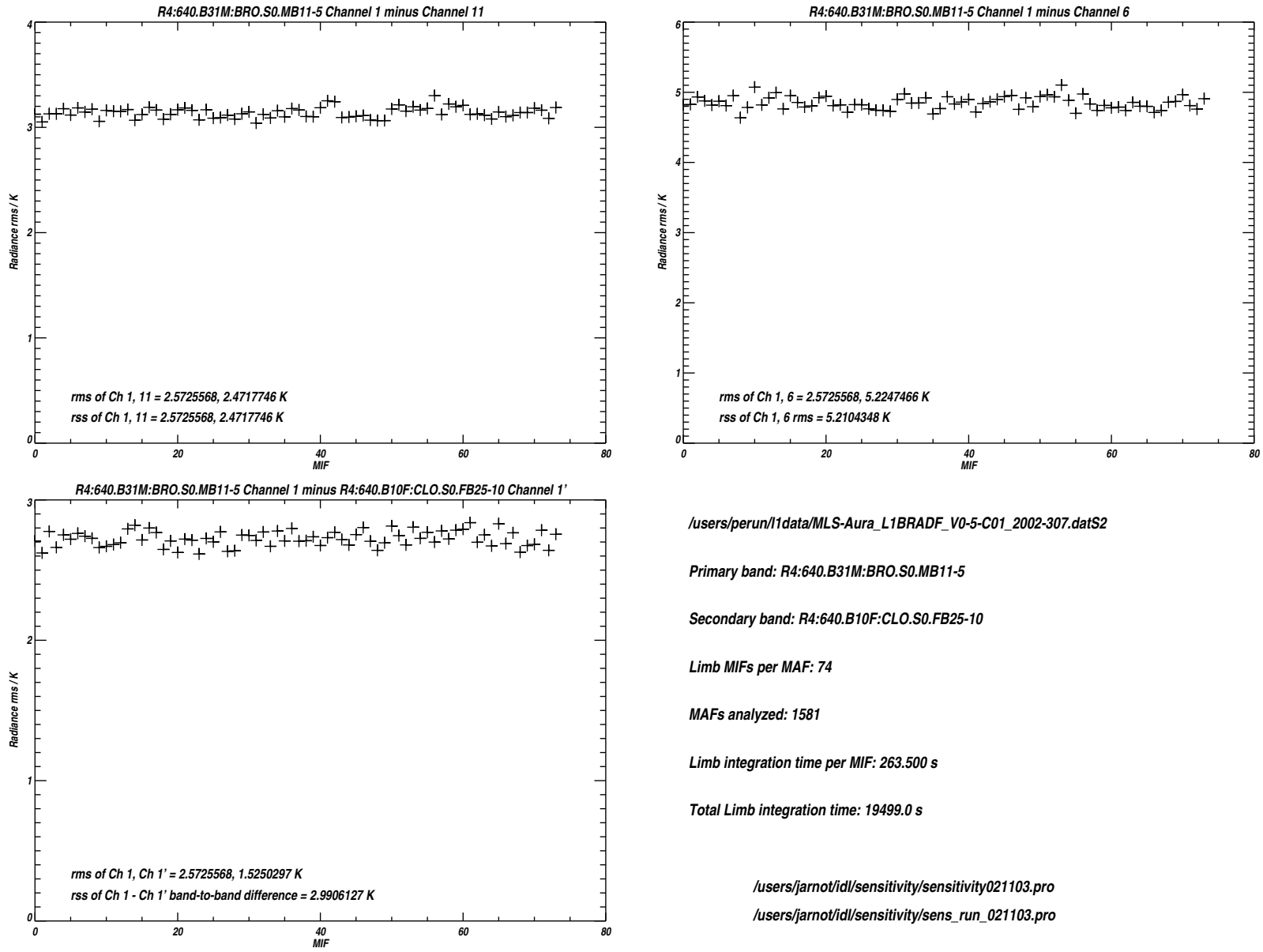

Figure B.91: Measured *rms* noise on the radiance differences between Channels 1 and 11 of Mid-band 31 (upper left panel), Channels 1 and 6 of Mid-band 31 (upper right panel), and between Channel 1 of Mid-band 31 and Channel 1 of Band 10.

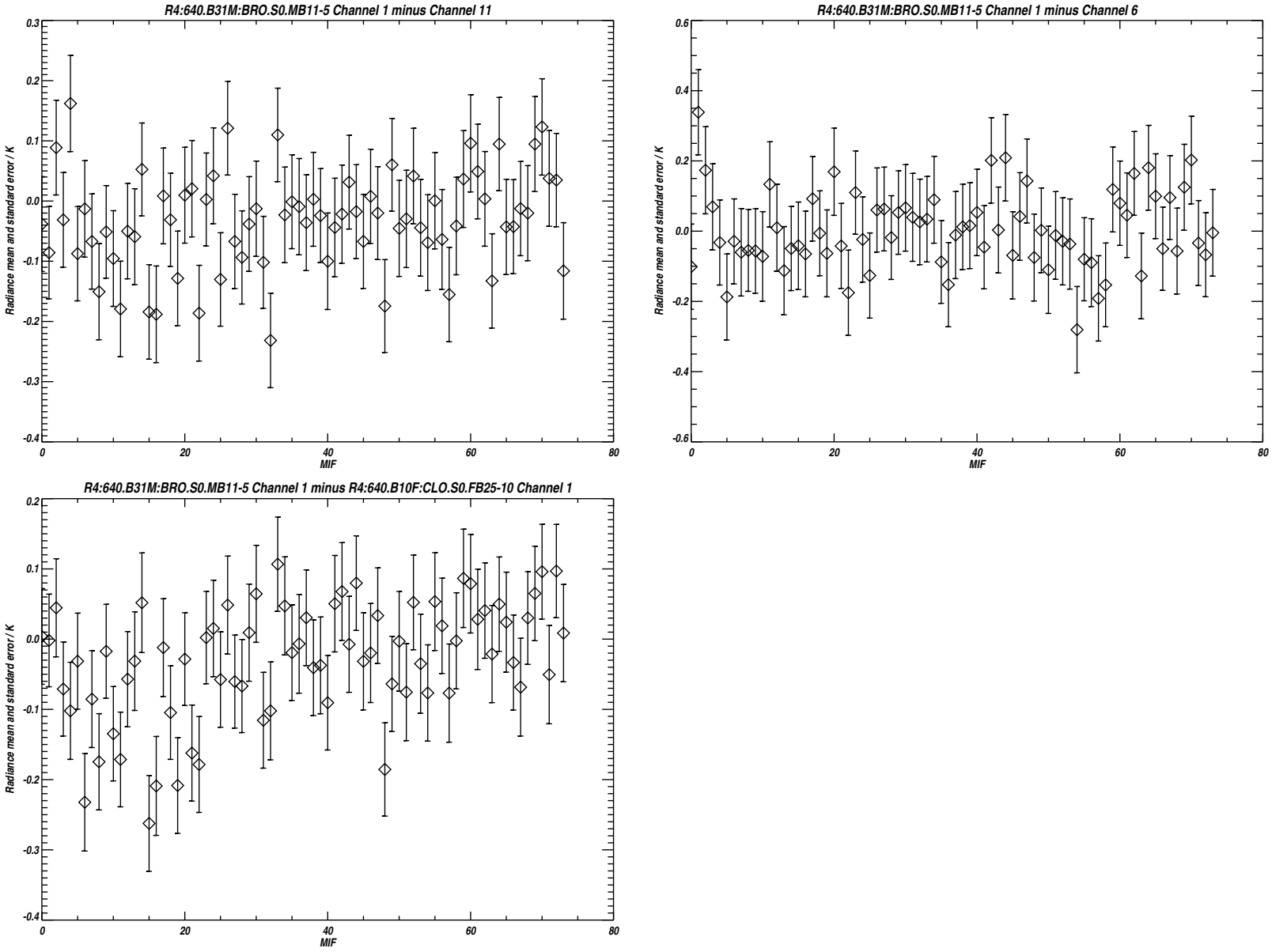

Figure B.92: Radiance differences between the 3 channel pairs plotted in Figure B.91. The vertical bars indicating the *rms* uncertainty due to noise. See text for additional details.

B.2 Linearity Data

The data below were taken on 021103, except for Band 12 (B12) data which were recorded on 021203 (FB12 was recording linearity data from R1B during acquisition of the first data set). The format of these plots is as discussed in Section 2.3 of Volume 1. For the B12 data there are 5 hot target temperature plateaus (one less than for the other bands). The measurement with the external target at ambient temperature was not made (due to a procedural error), but since this measurement provides essentially no linearity data, its absence is not of importance.

The data presented below are discussed in further detail in Chapter 2 of Volume 1. Several linearity data sets similar were taken during the course of instrument integration, test and calibration, all with results very similar to those presented below.

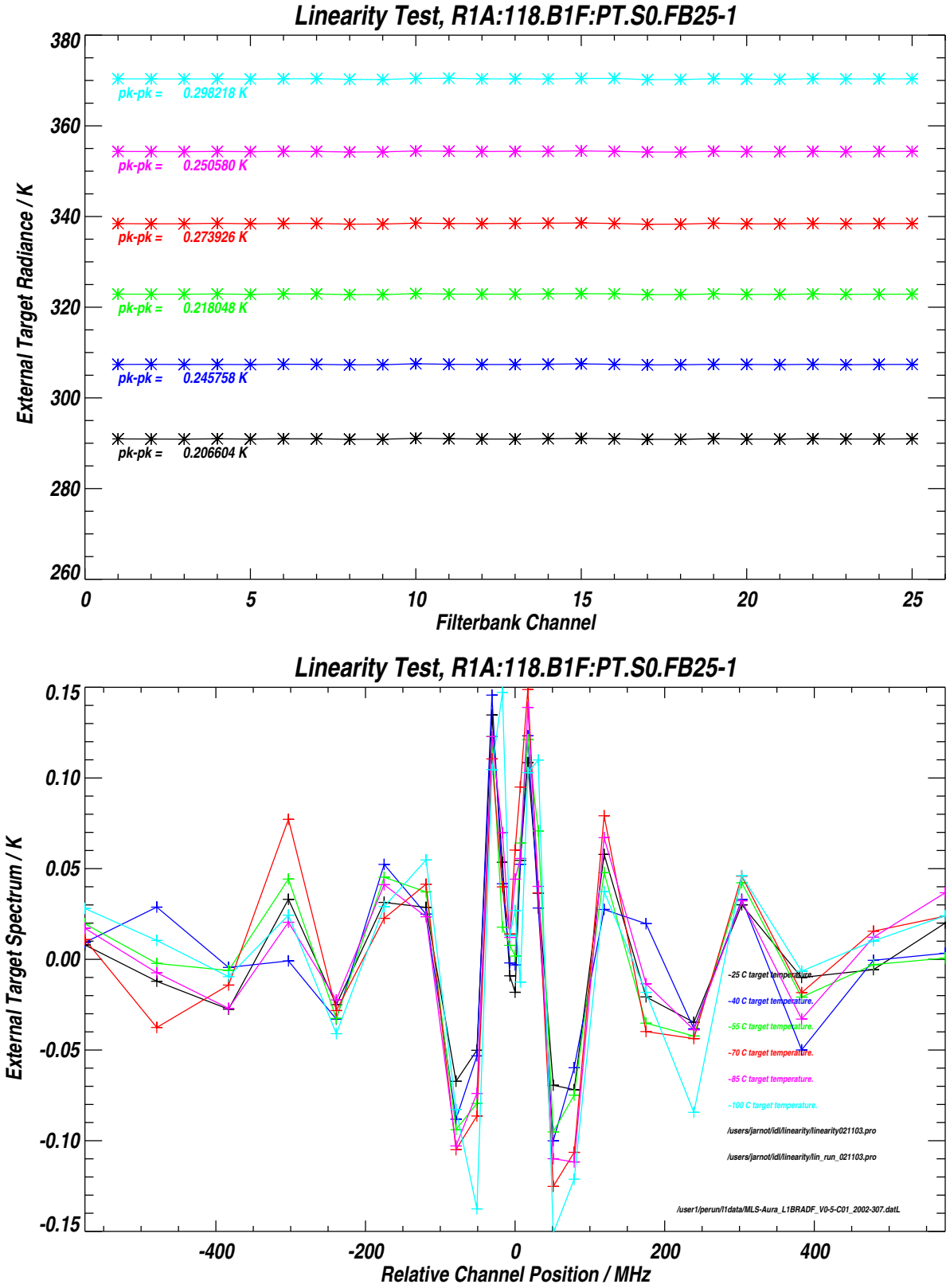

Figure B.93: Hot Target Radiances for the 25 channels of Band 1 for 6 different target temperatures. The lower panel shows the data from the upper panel with the weighted mean radiance subtracted from each measurement group. See text for additional details.

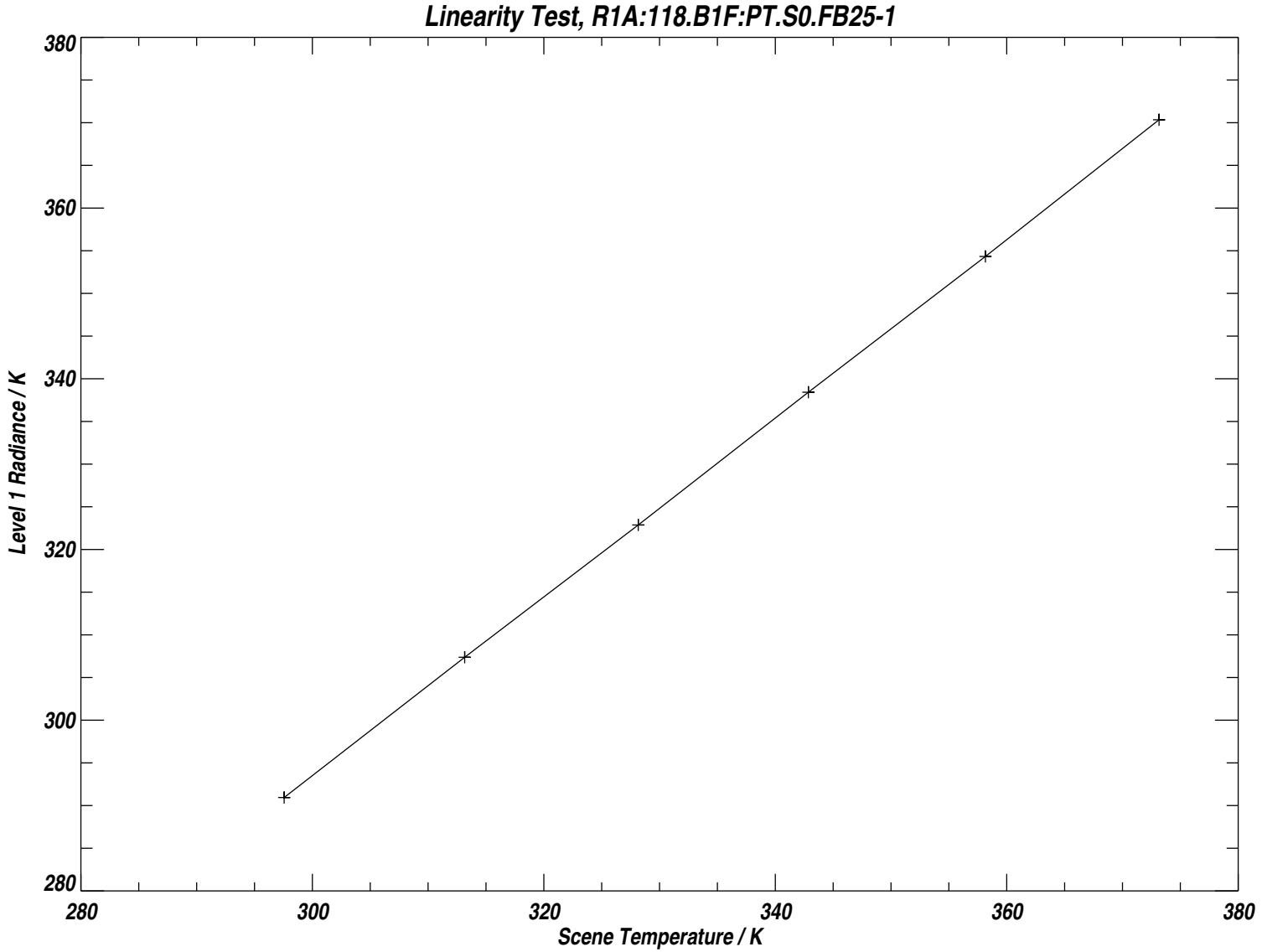

Figure B.94: Data from Figure B.93 with the weighted mean radiance for each measurement group plotted against target temperature. See text for additional details.

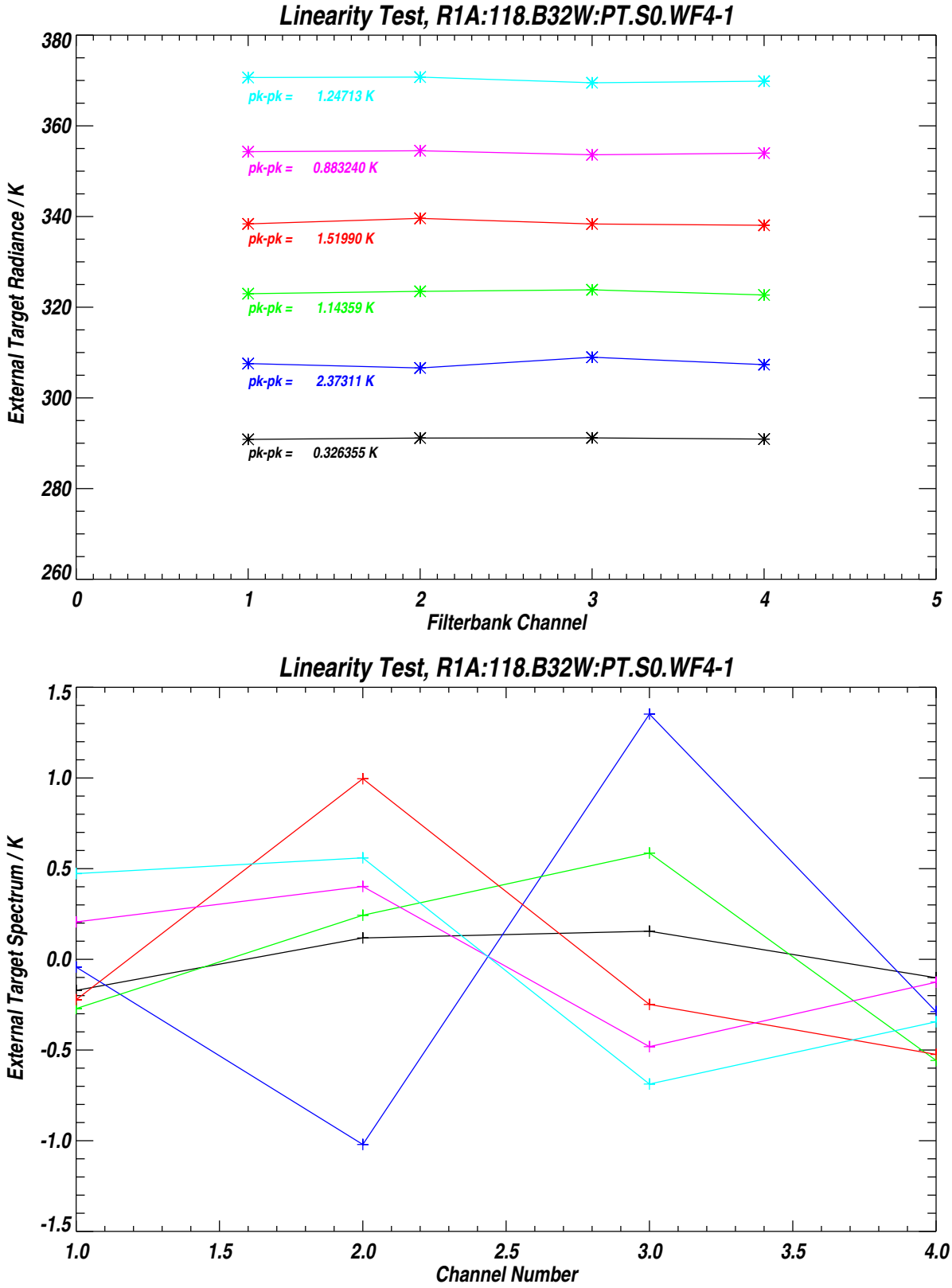

Figure B.95: Hot Target Radiances for the 4 channels of Band 32 (R1A Wide Filters) for 6 different target temperatures. The lower panel shows the data from the upper panel with the weighted mean radiance subtracted from each measurement group. See text for additional details.

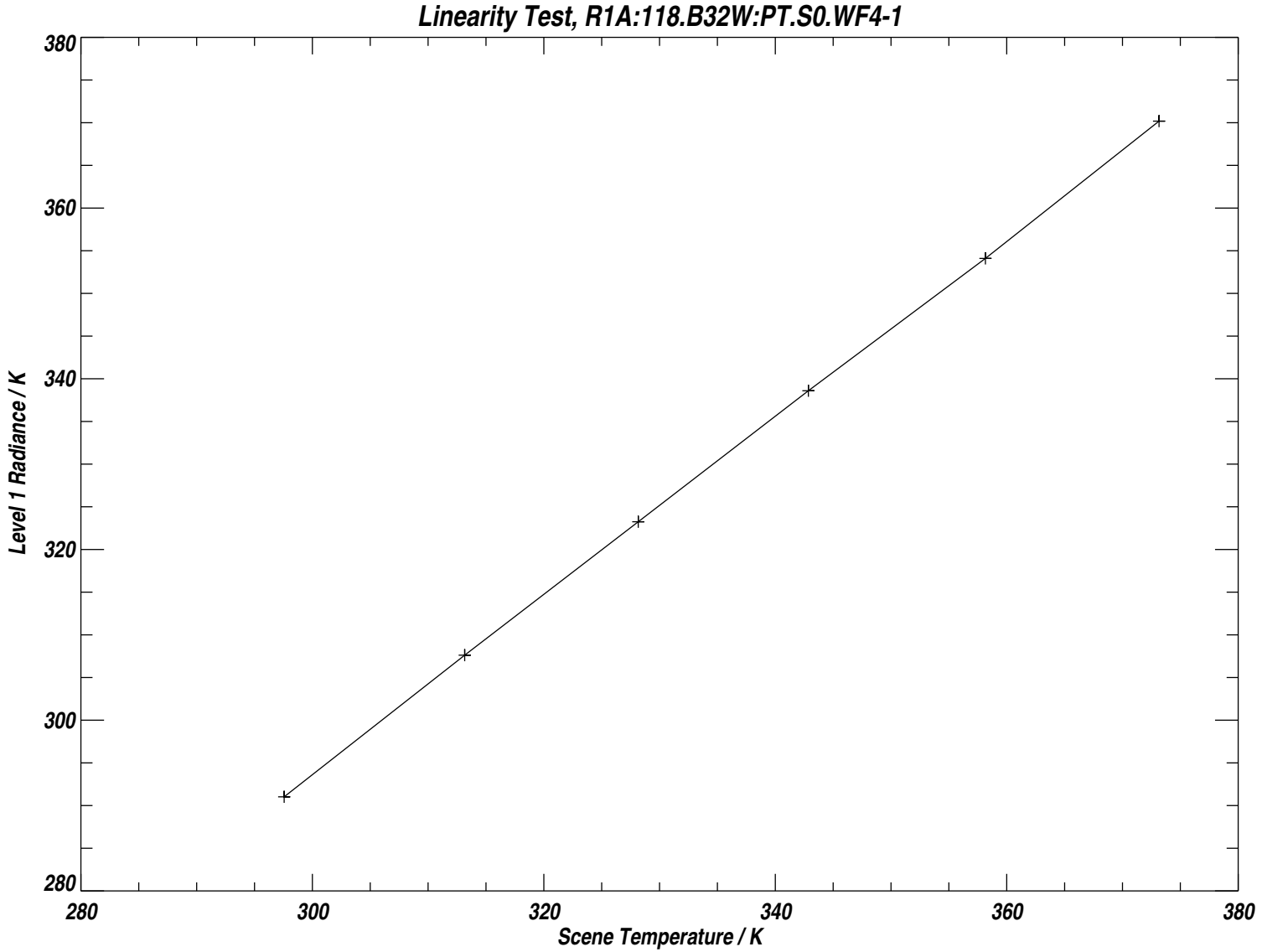

Figure B.96: Data from Figure B.95 with the weighted mean radiance for each measurement group plotted against target temperature. See text for additional details.

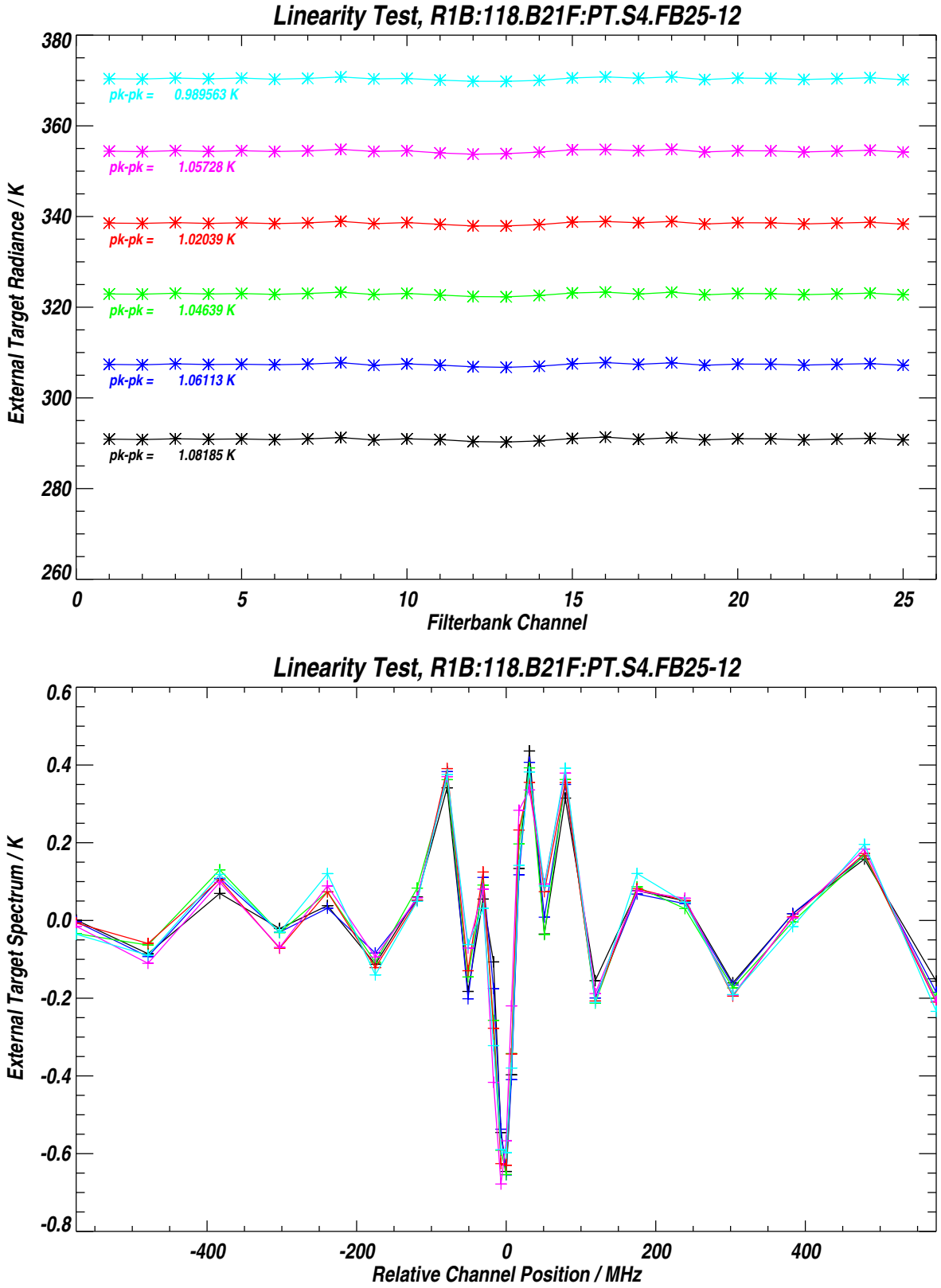

Figure B.97: Hot Target Radiances for the 25 channels of Band 21 (Radiometer R1B) for 6 different target temperatures. The lower panel shows the data from the upper panel with the weighted mean radiance subtracted from each measurement group. See text for additional details.

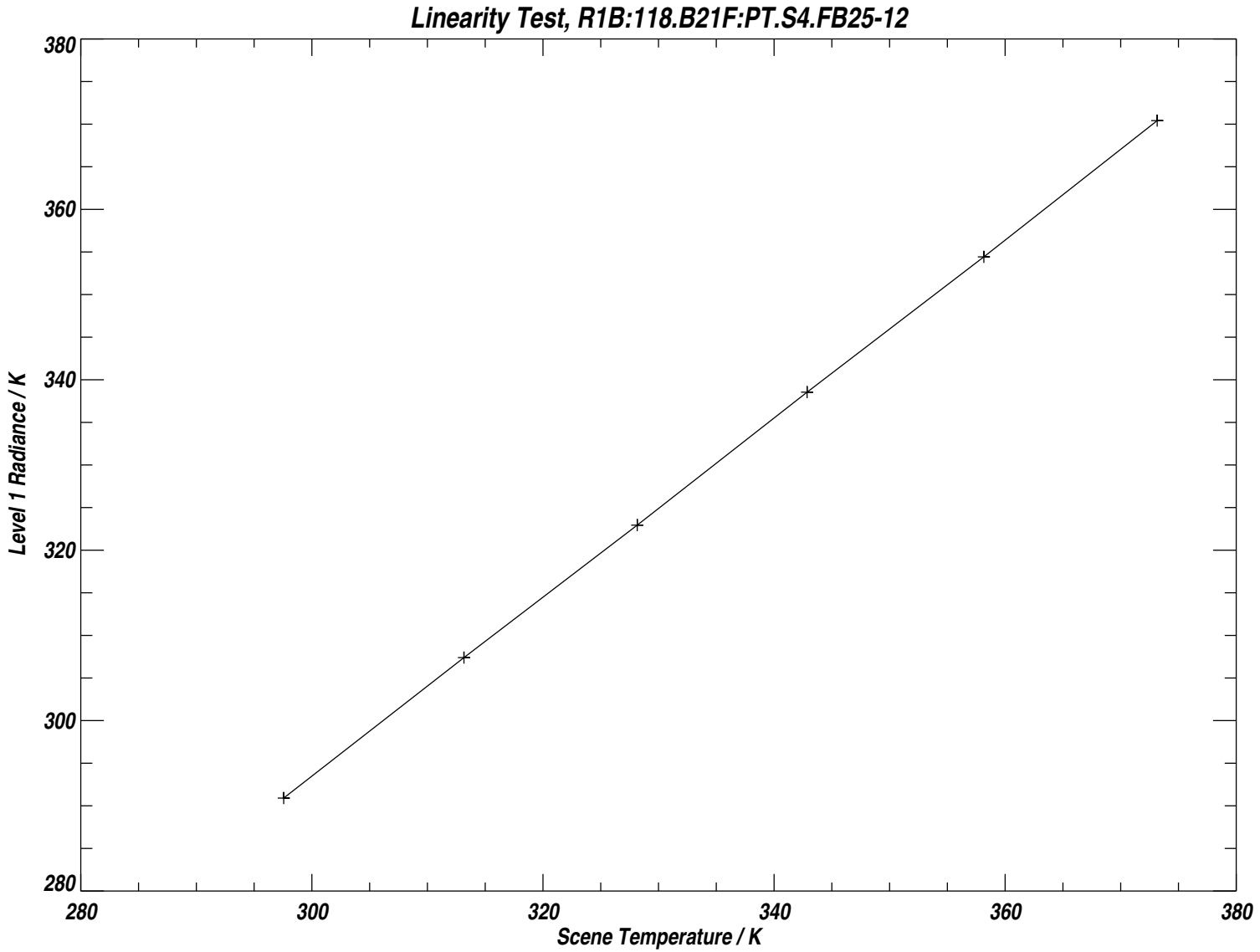

Figure B.98: Data from Figure B.97 with the weighted mean radiance for each measurement group plotted against target temperature. See text for additional details.

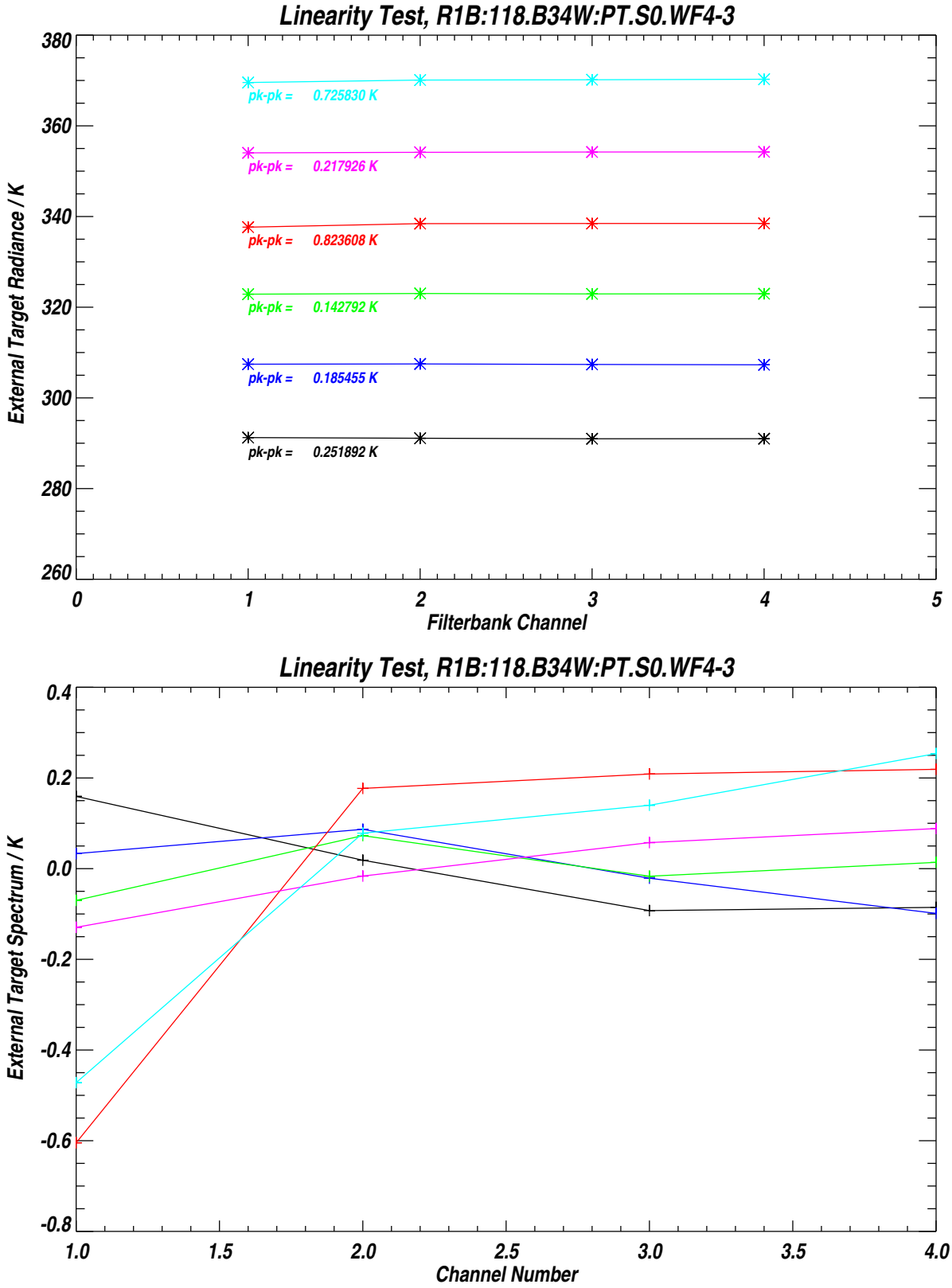

Figure B.99: Hot Target Radiances for the 4 channels of Band 34 (R1B Wide Filters) for 6 different target temperatures. The lower panel shows the data from the upper panel with the weighted mean radiance subtracted from each measurement group. See text for additional details.

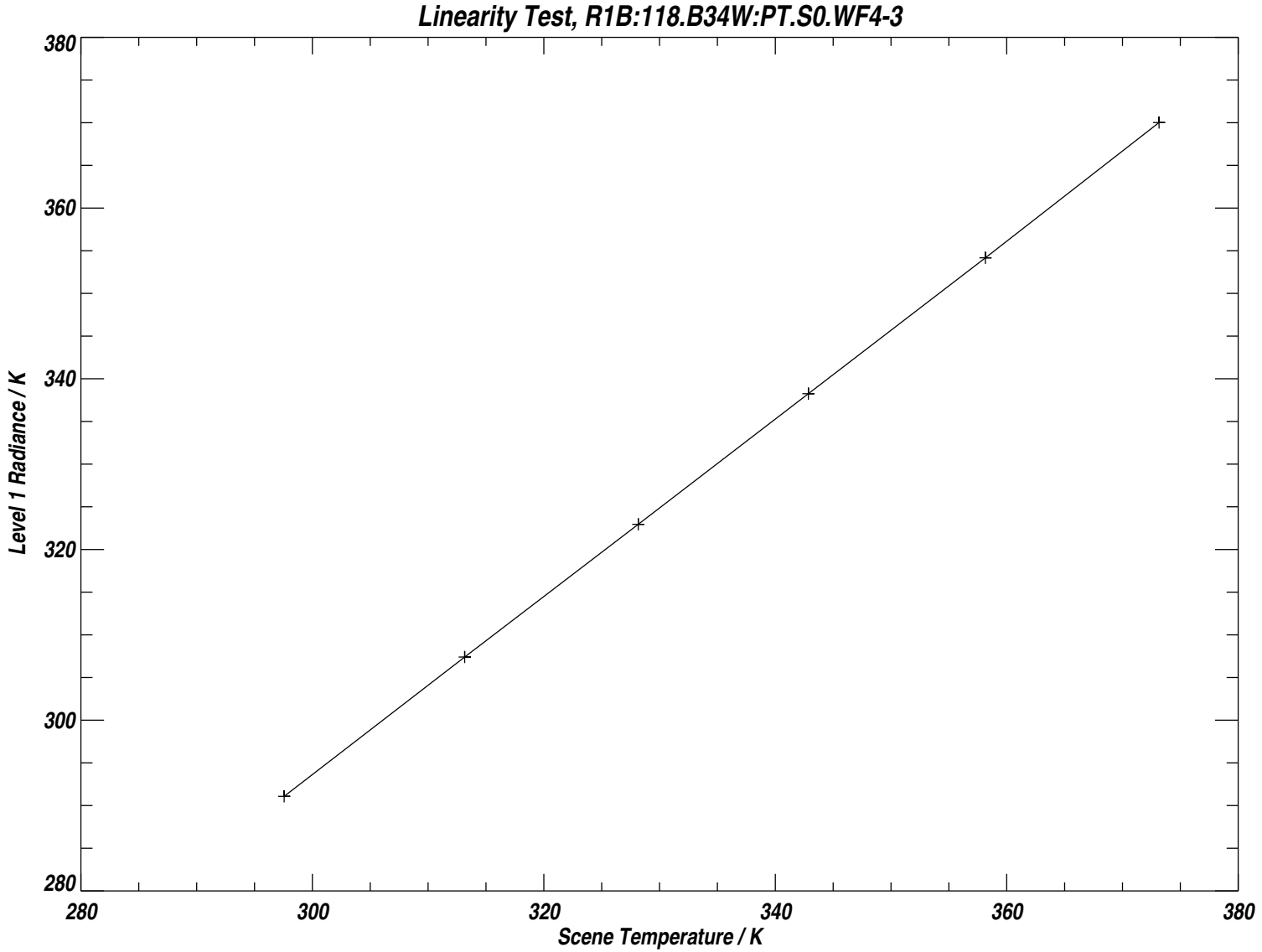

Figure B.100: Data from Figure B.99 with the weighted mean radiance for each measurement group plotted against target temperature. See text for additional details.

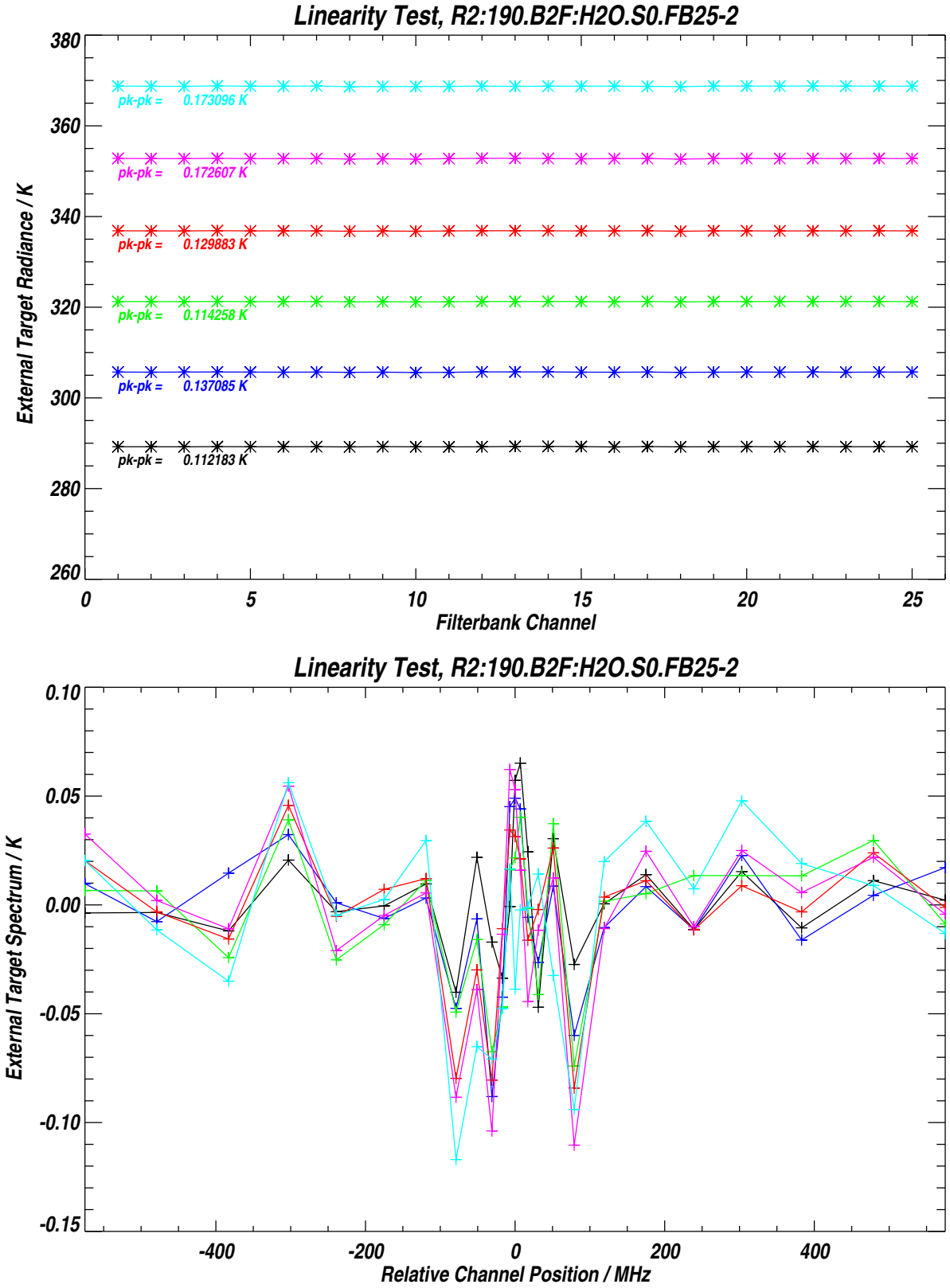

Figure B.101: Hot Target Radiances for the 25 channels of Band 2 for 6 different target temperatures. The lower panel shows the data from the upper panel with the weighted mean radiance subtracted from each measurement group. See text for additional details.

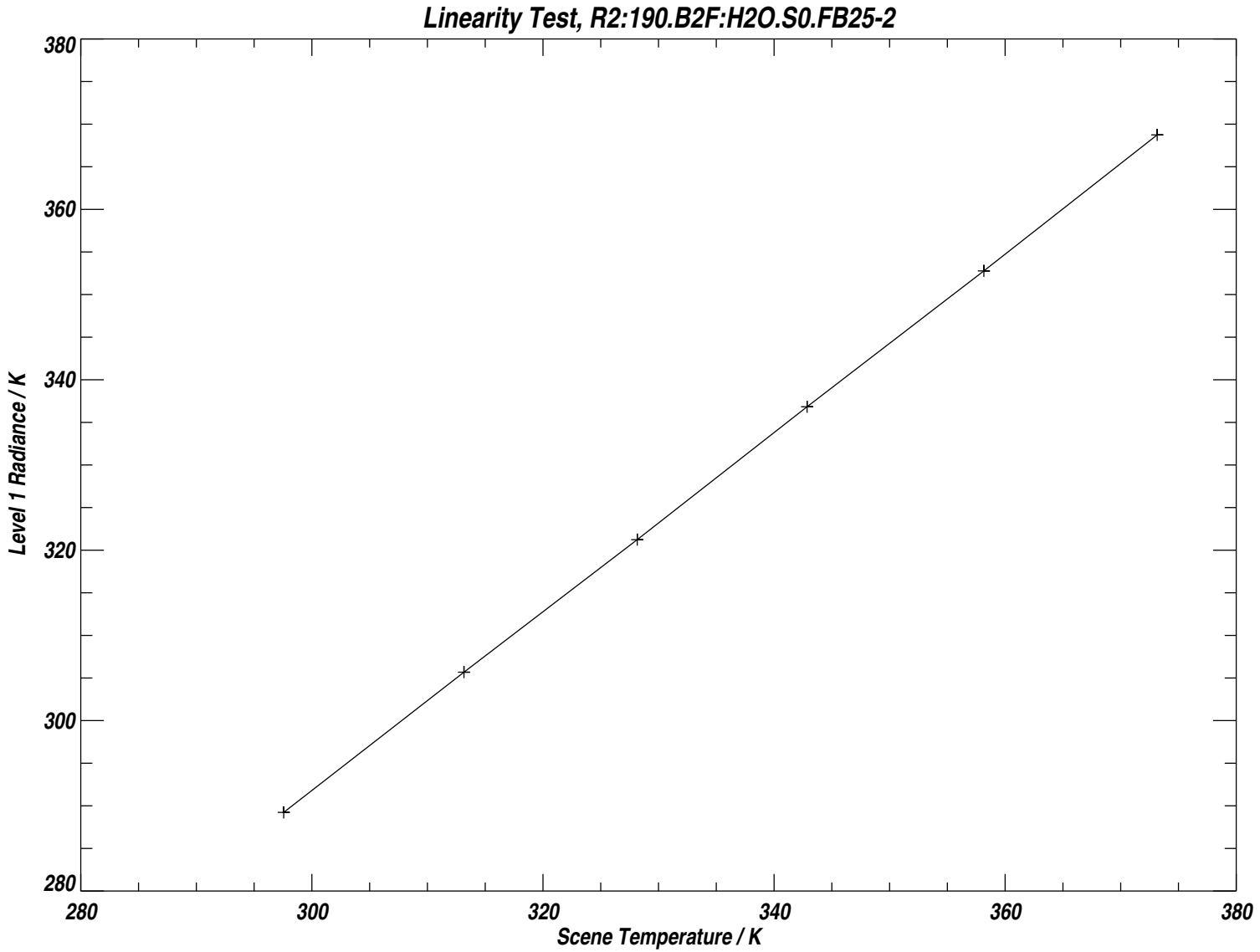

Figure B.102: Data from Figure B.101 with the weighted mean radiance for each measurement group plotted against target temperature. See text for additional details.

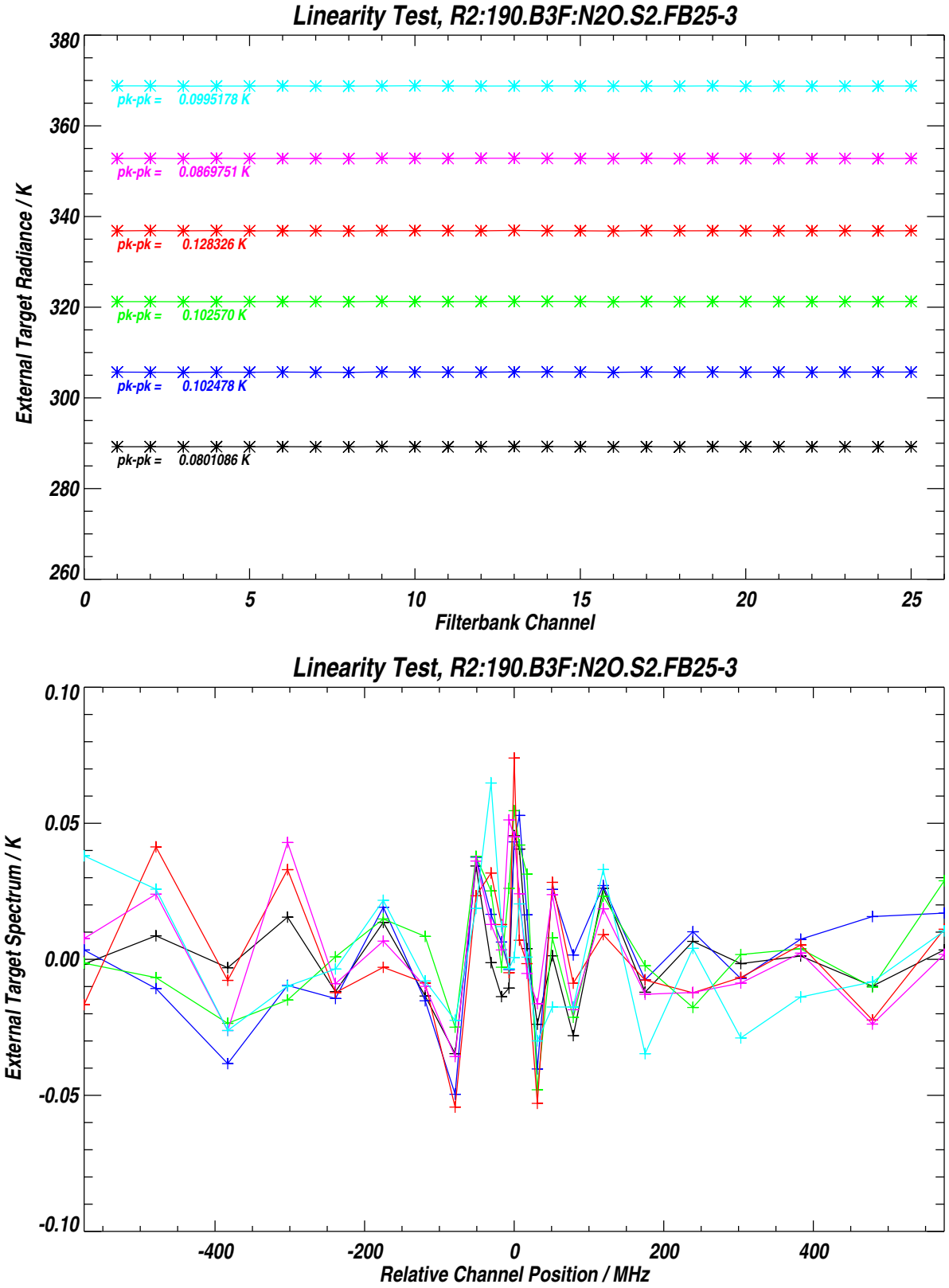

Figure B.103: Hot Target Radiances for the 25 channels of Band 3 for 6 different target temperatures. The lower panel shows the data from the upper panel with the weighted mean radiance subtracted from each measurement group. See text for additional details.

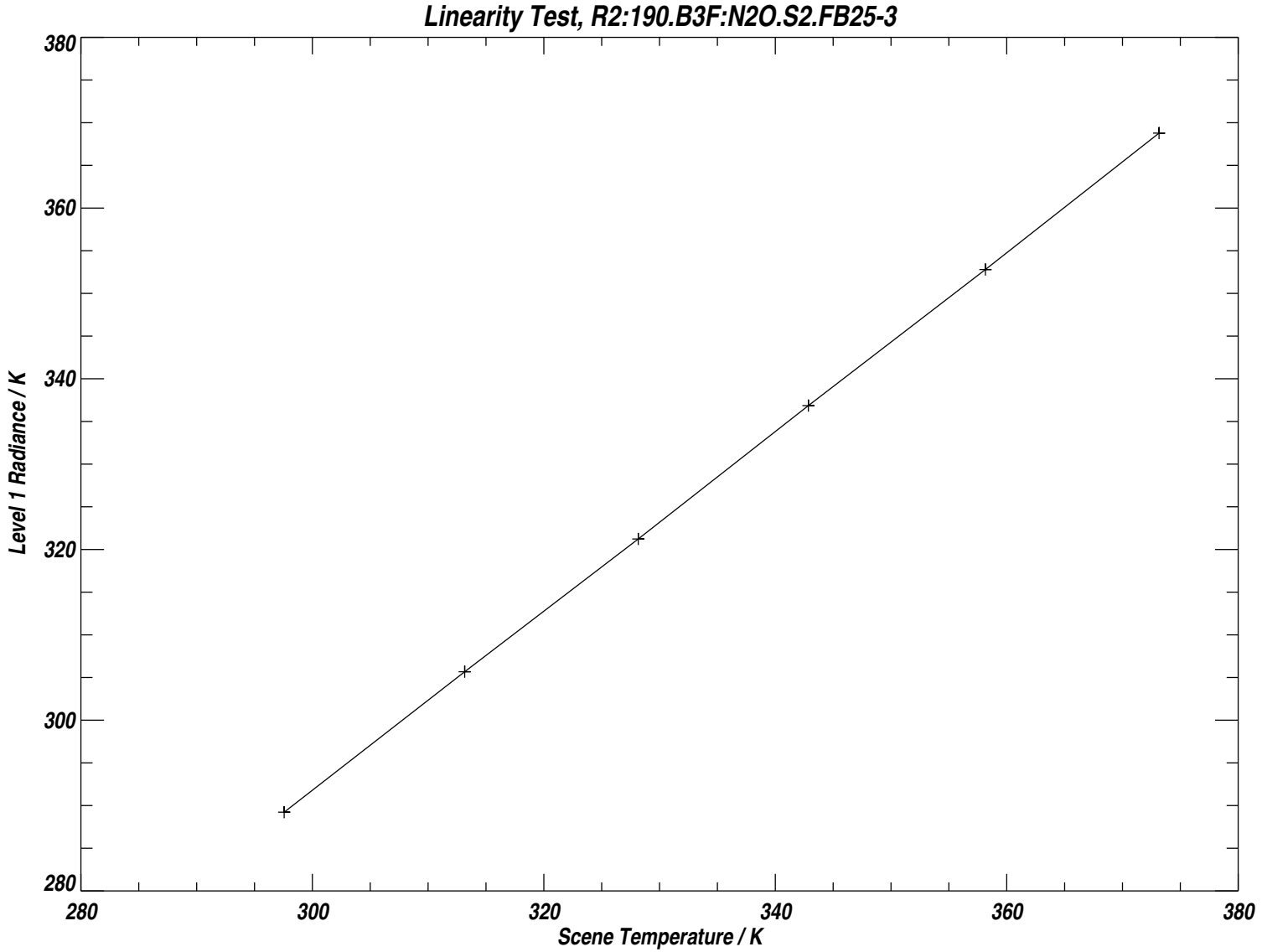

Figure B.104: Data from Figure B.103 with the weighted mean radiance for each measurement group plotted against target temperature. See text for additional details.

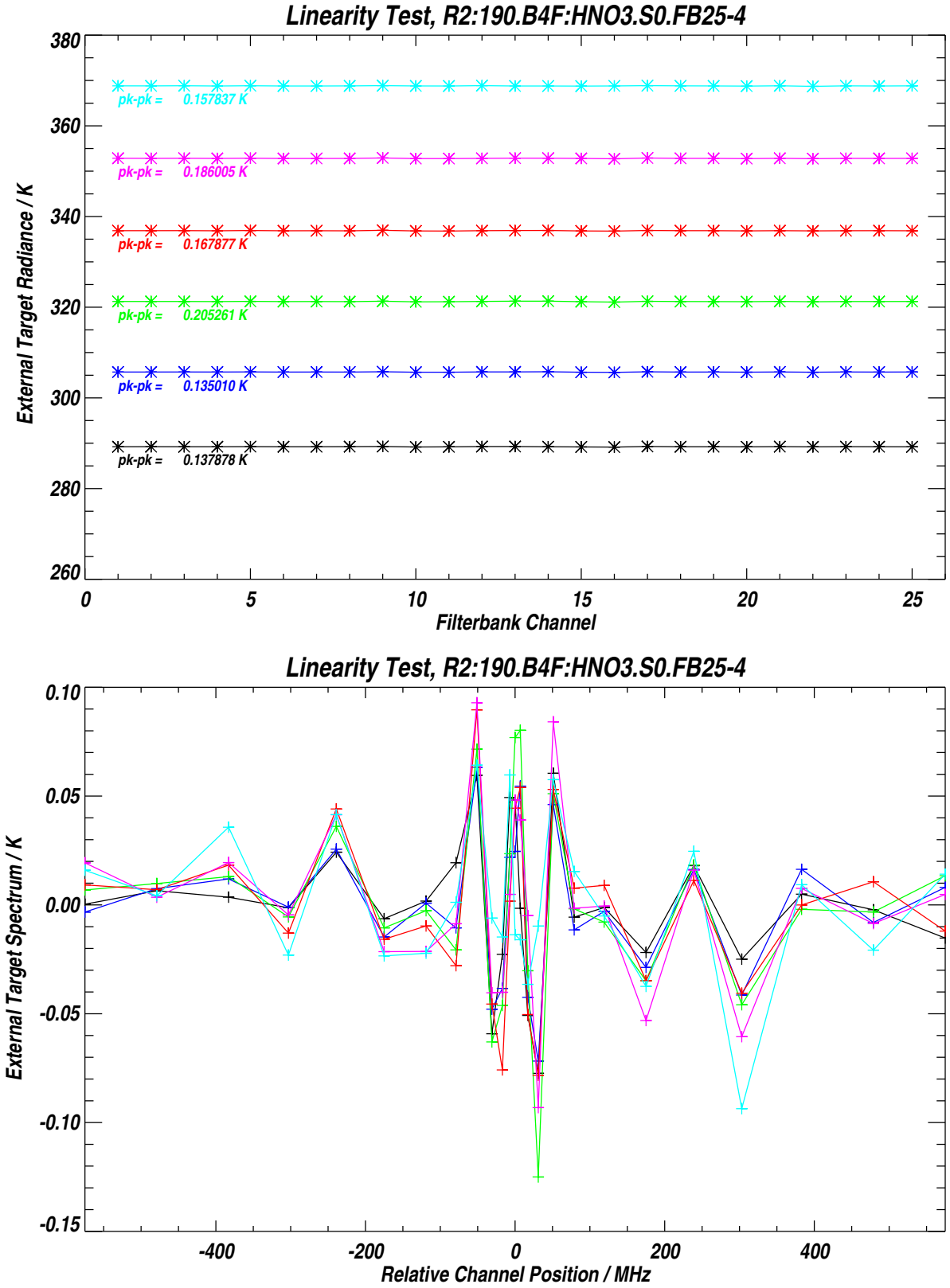

Figure B.105: Hot Target Radiances for the 25 channels of Band 4 for 6 different target temperatures. The lower panel shows the data from the upper panel with the weighted mean radiance subtracted from each measurement group. See text for additional details.

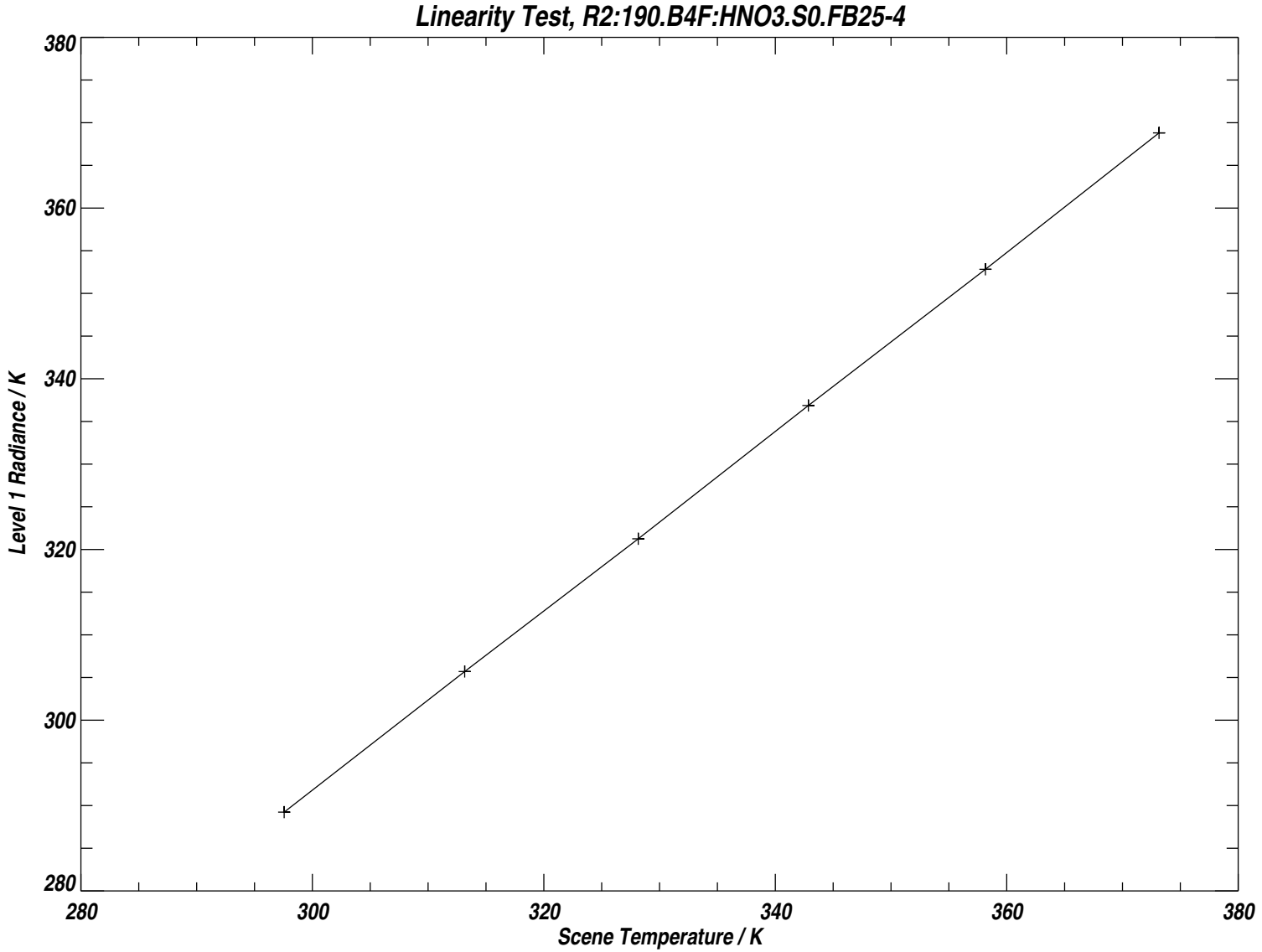

Figure B.106: Data from Figure B.105 with the weighted mean radiance for each measurement group plotted against target temperature. See text for additional details.

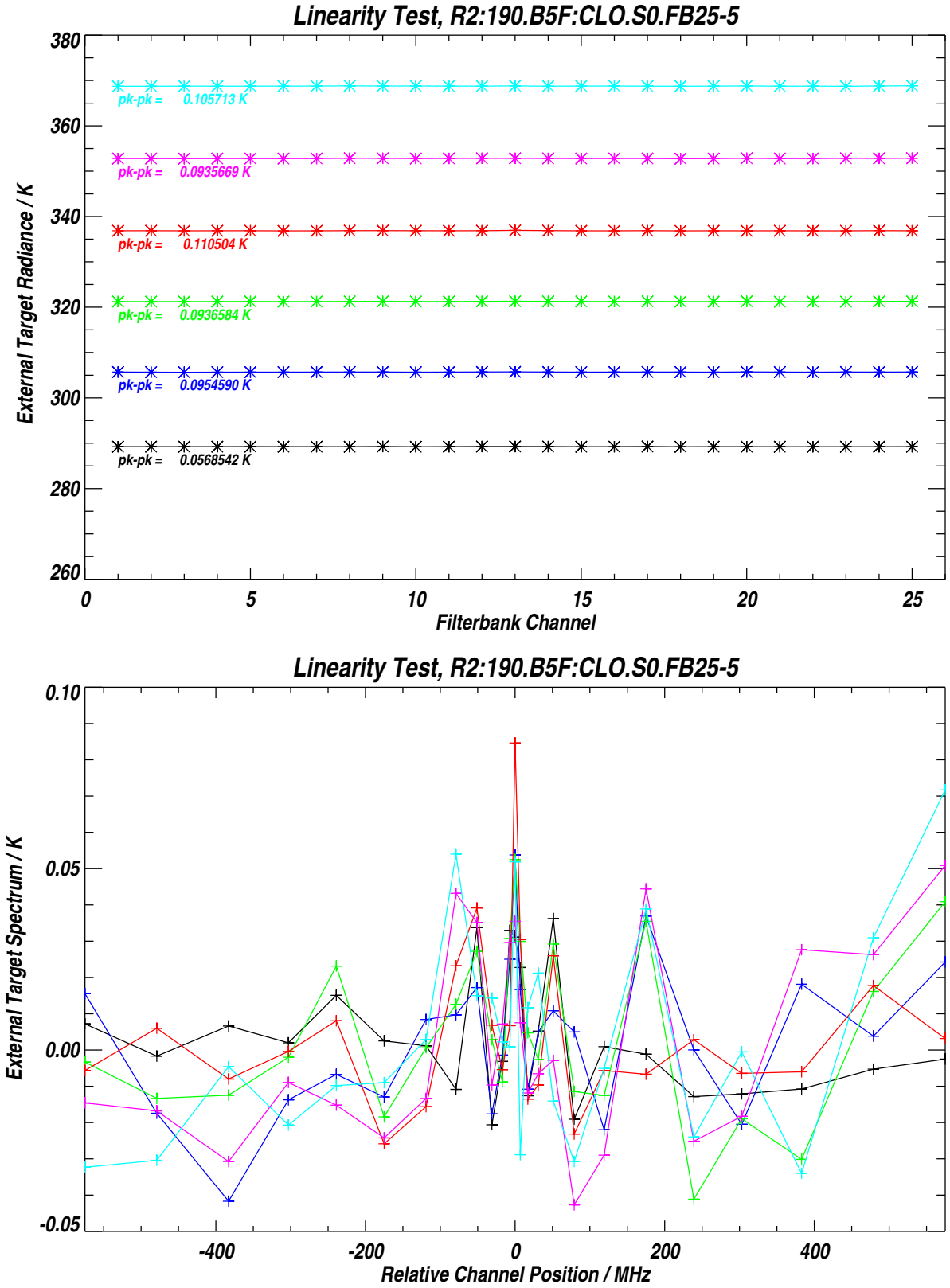

Figure B.107: Hot Target Radiances for the 25 channels of Band 5 for 6 different target temperatures. The lower panel shows the data from the upper panel with the weighted mean radiance subtracted from each measurement group. See text for additional details.

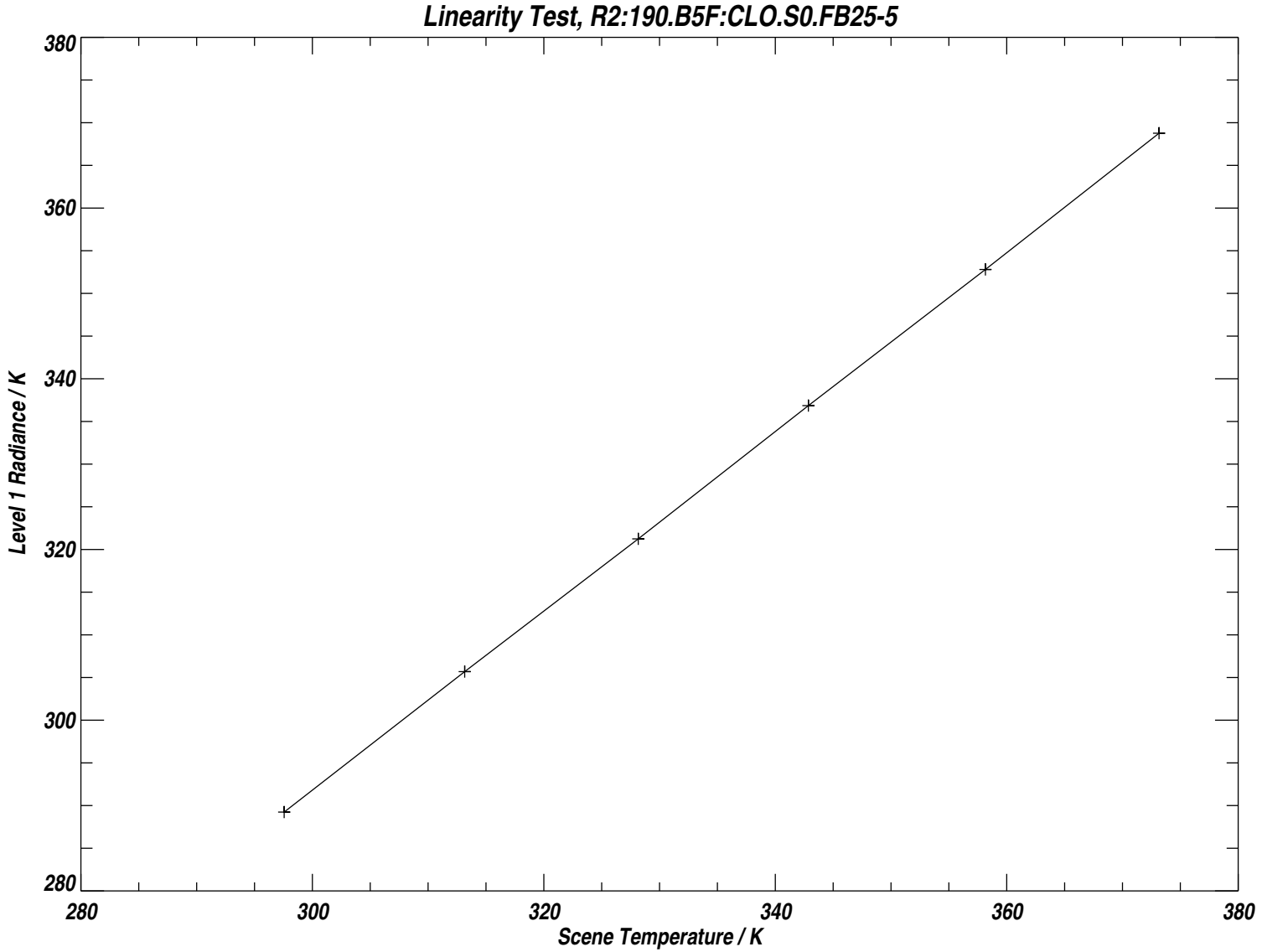

Figure B.108: Data from Figure B.107 with the weighted mean radiance for each measurement group plotted against target temperature. See text for additional details.

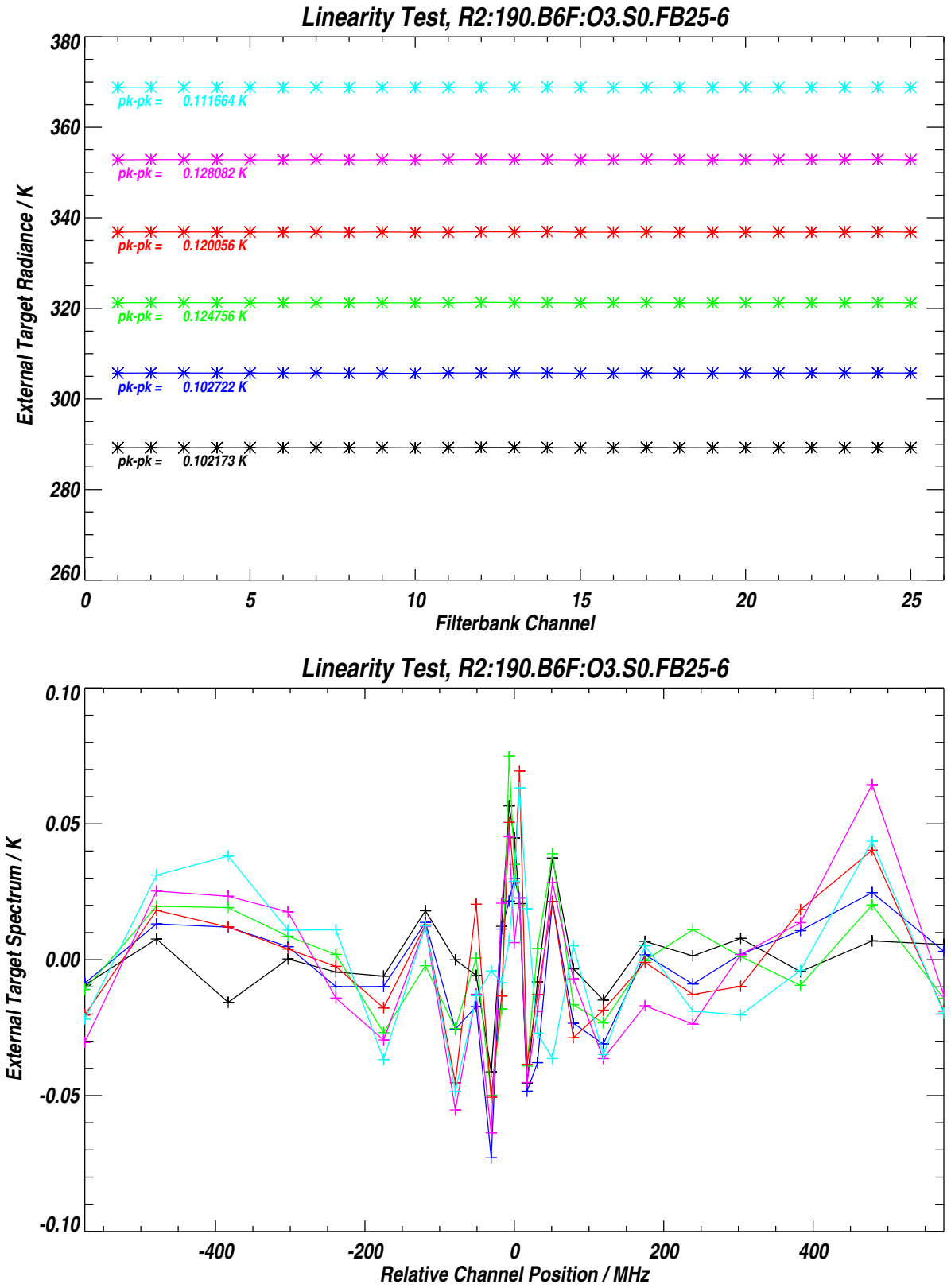

Figure B.109: Hot Target Radiances for the 25 channels of Band 6 for 6 different target temperatures. The lower panel shows the data from the upper panel with the weighted mean radiance subtracted from each measurement group. See text for additional details.

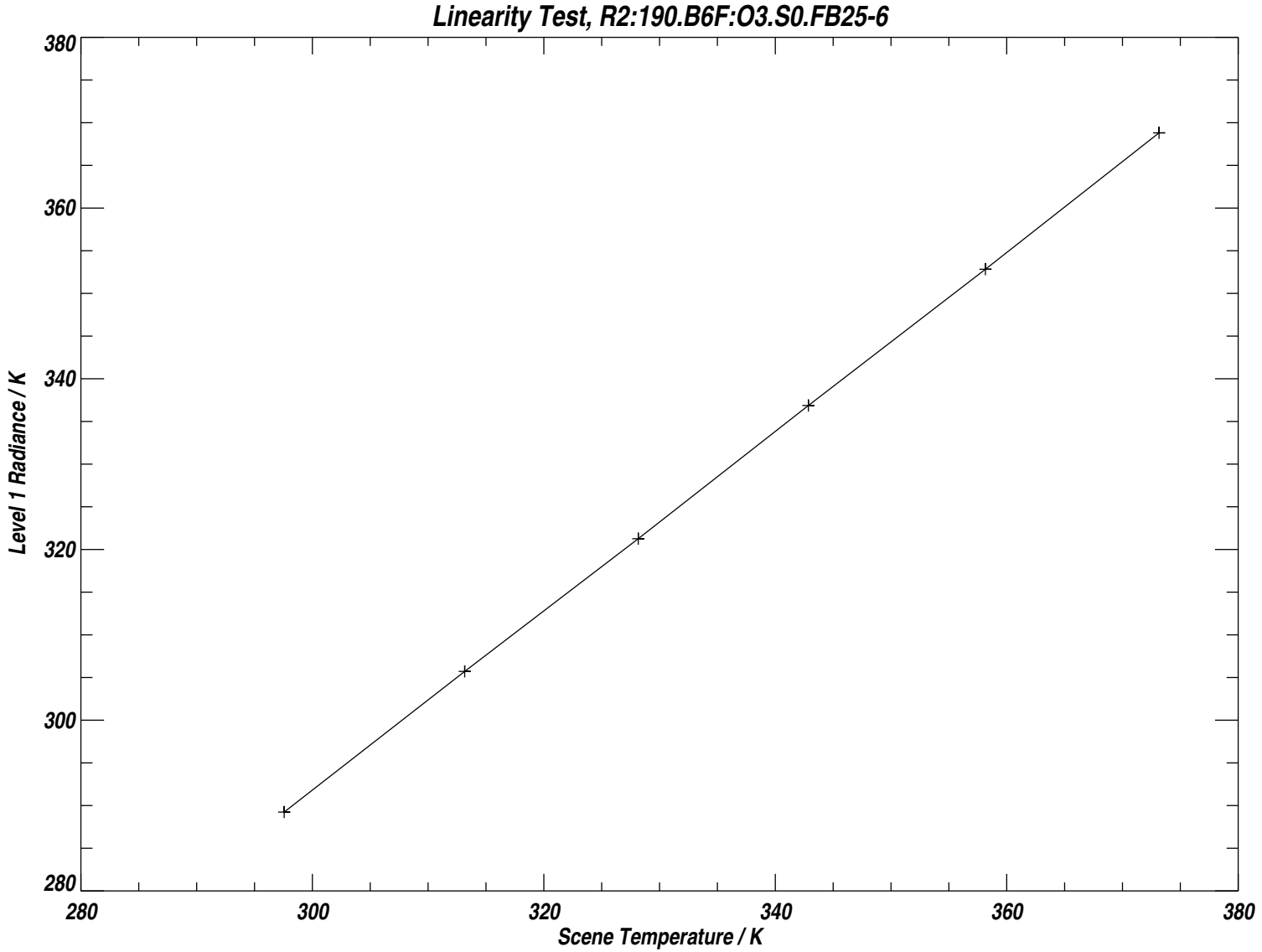

Figure B.110: Data from Figure B.109 with the weighted mean radiance for each measurement group plotted against target temperature. See text for additional details.

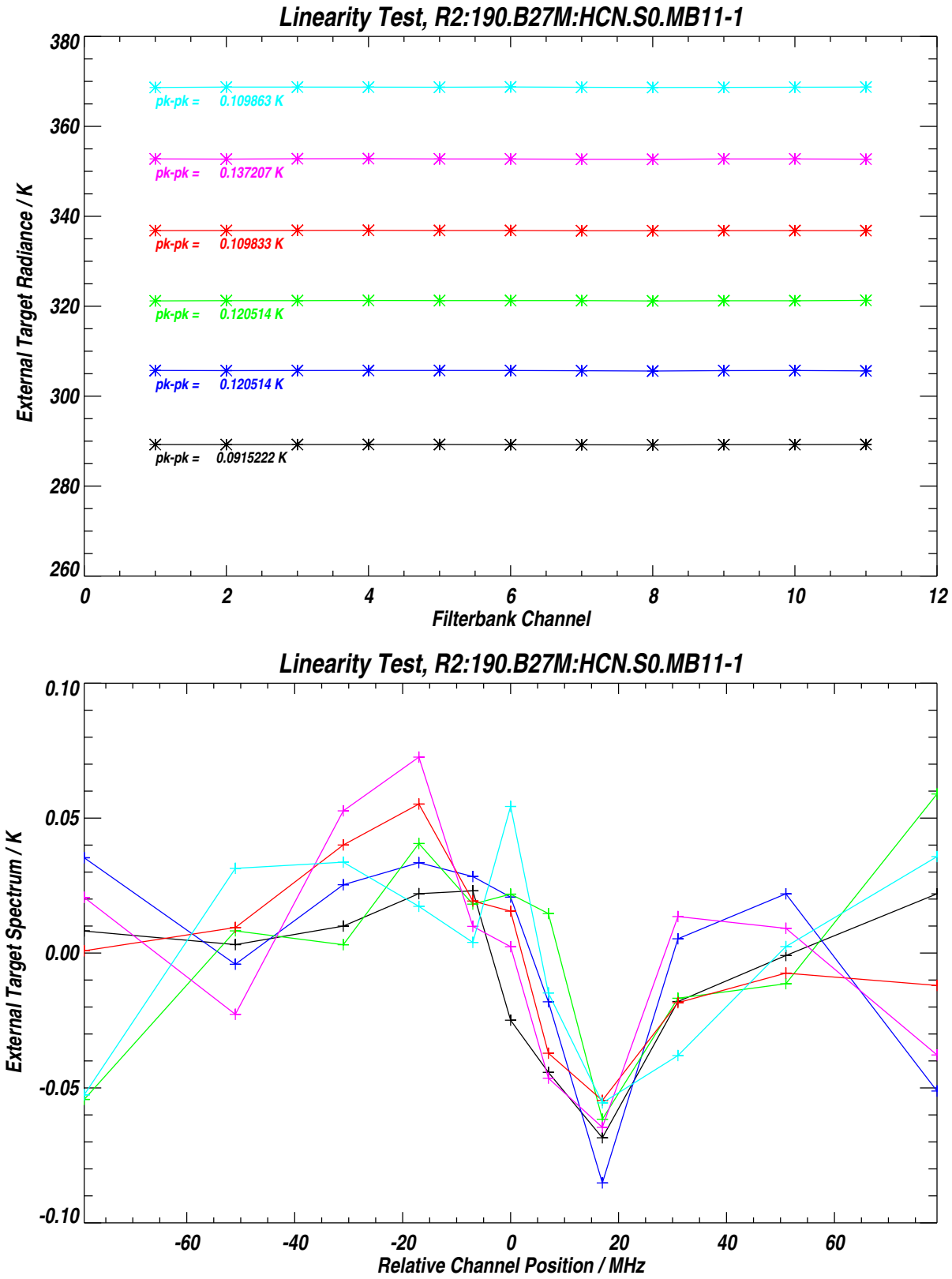

Figure B.111: Hot Target Radiances for the 11 channels of Band 27 for 6 different target temperatures. The lower panel shows the data from the upper panel with the weighted mean radiance subtracted from each measurement group. See text for additional details.

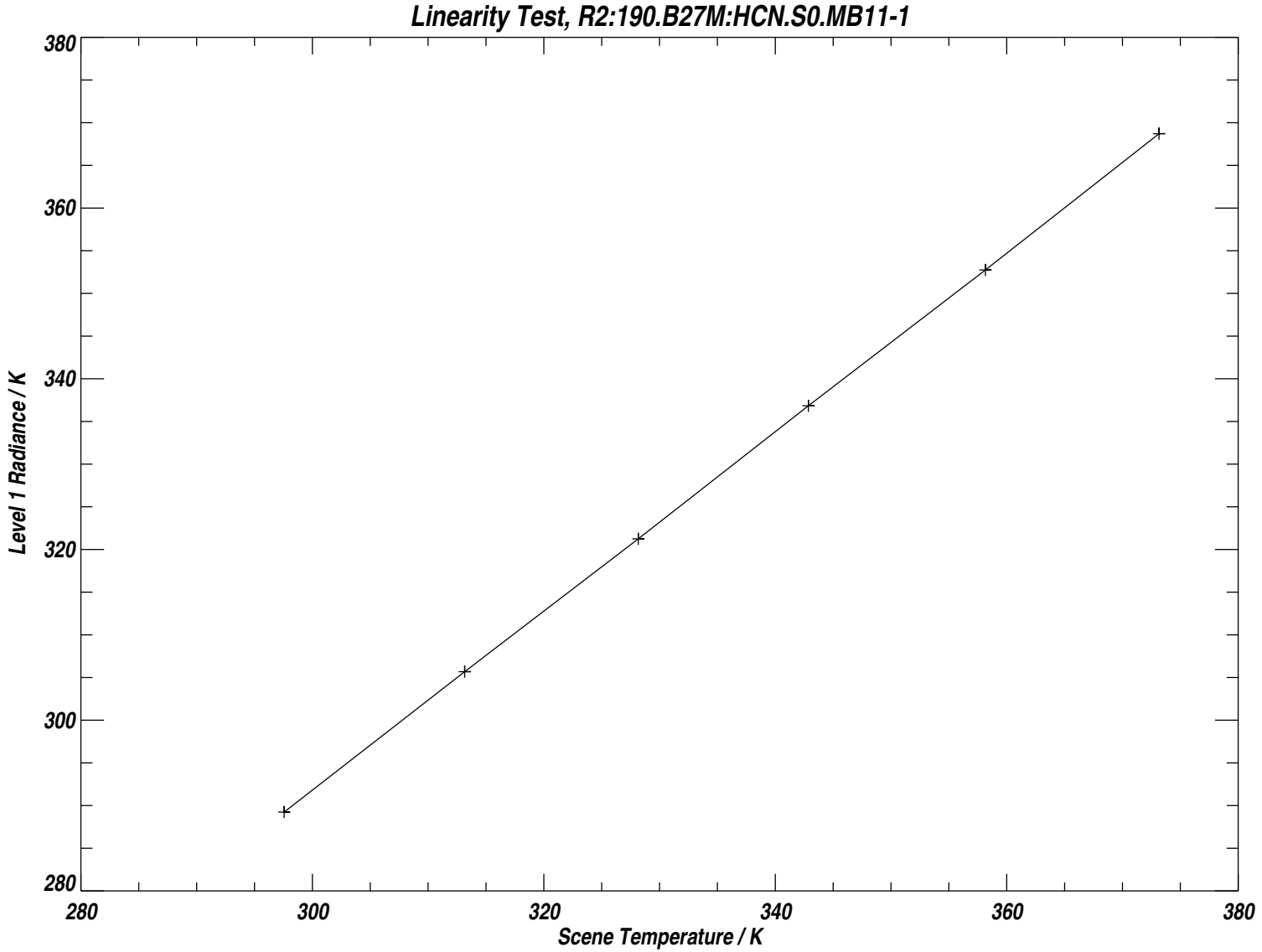

Figure B.112: Data from Figure B.111 with the weighted mean radiance for each measurement group plotted against target temperature. See text for additional details.

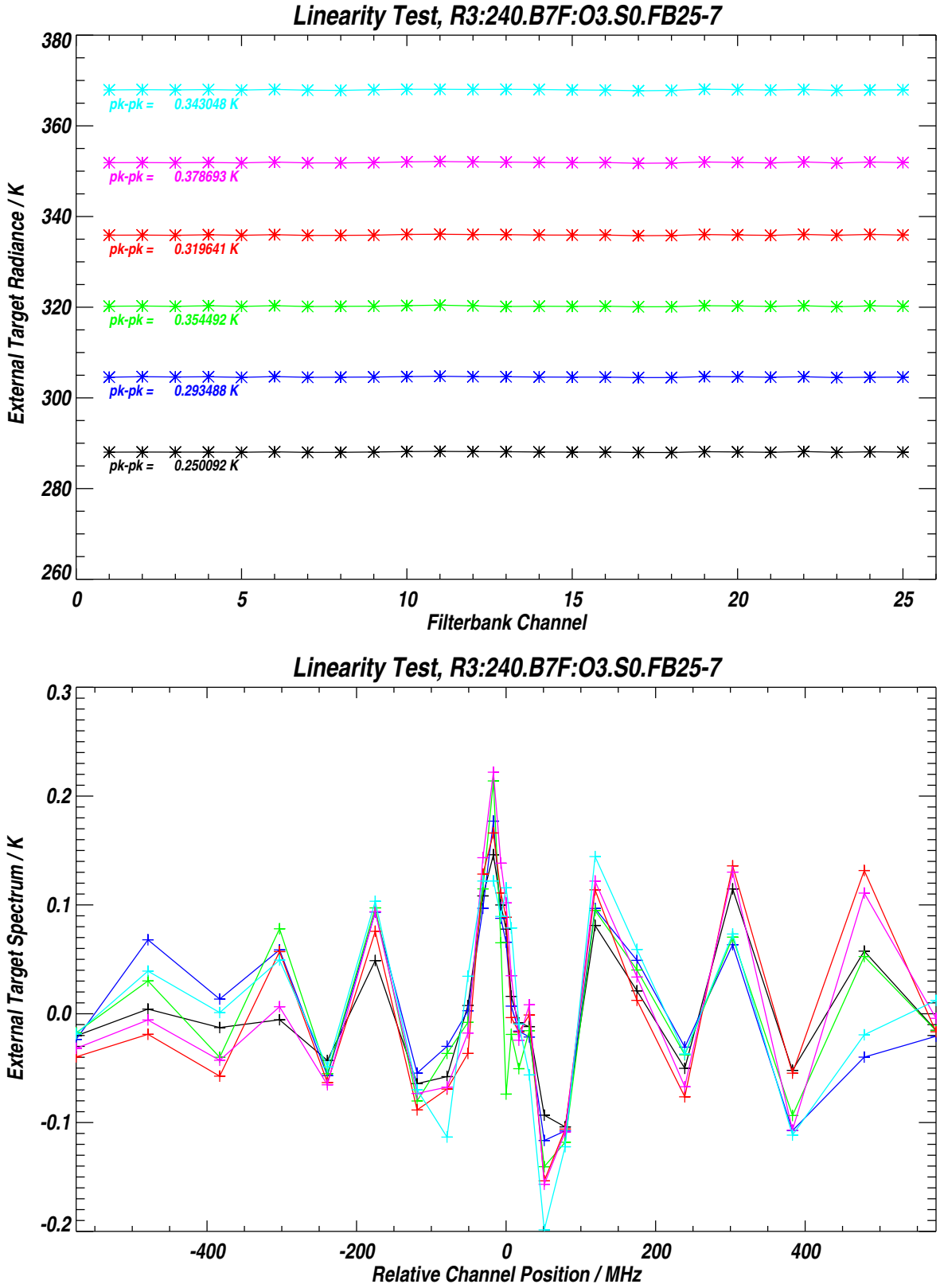

Figure B.113: Hot Target Radiances for the 25 channels of Band 7 for 6 different target temperatures. The lower panel shows the data from the upper panel with the weighted mean radiance subtracted from each measurement group. See text for additional details.

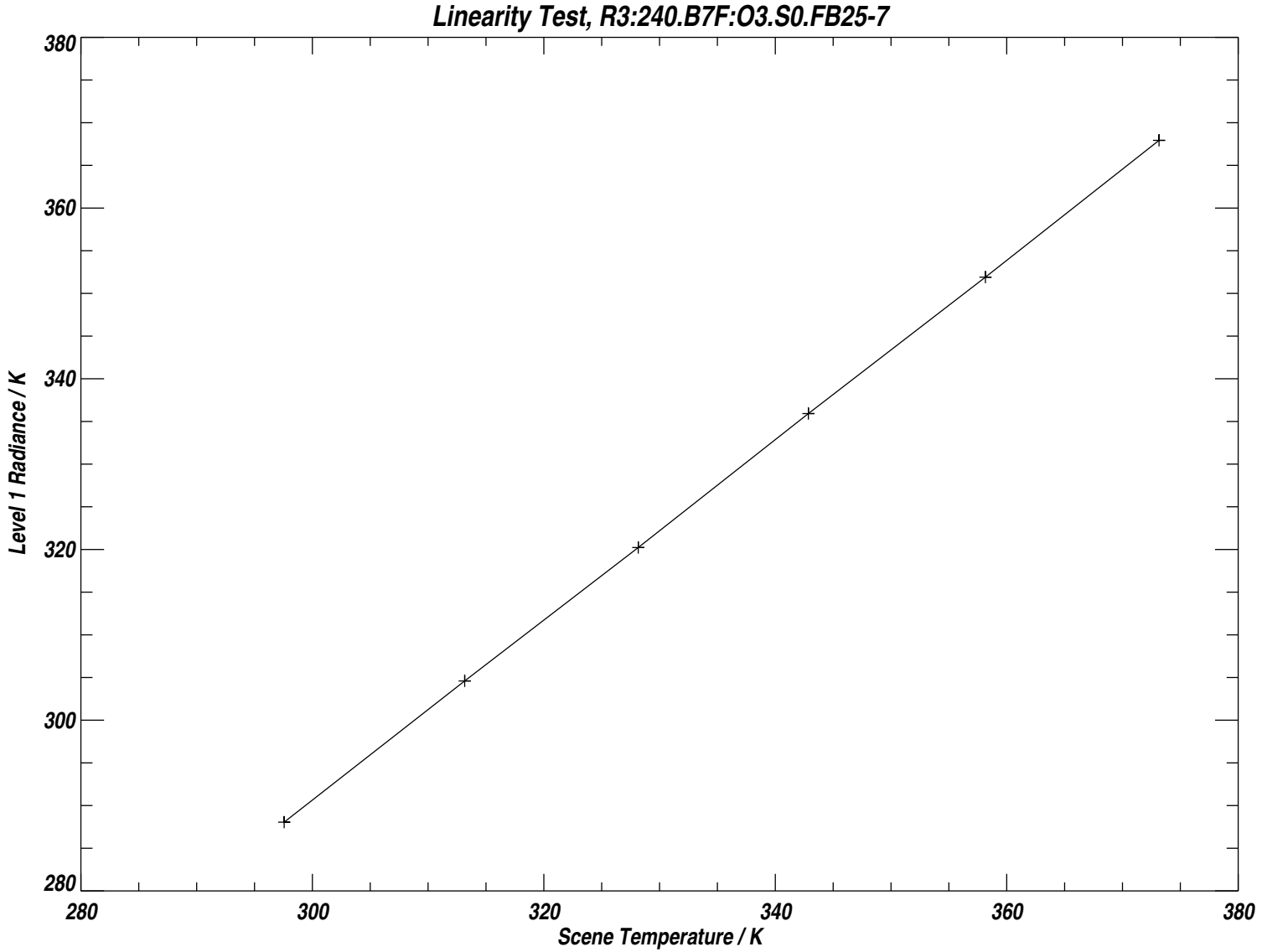

Figure B.114: Data from Figure B.113 with the weighted mean radiance for each measurement group plotted against target temperature. See text for additional details.

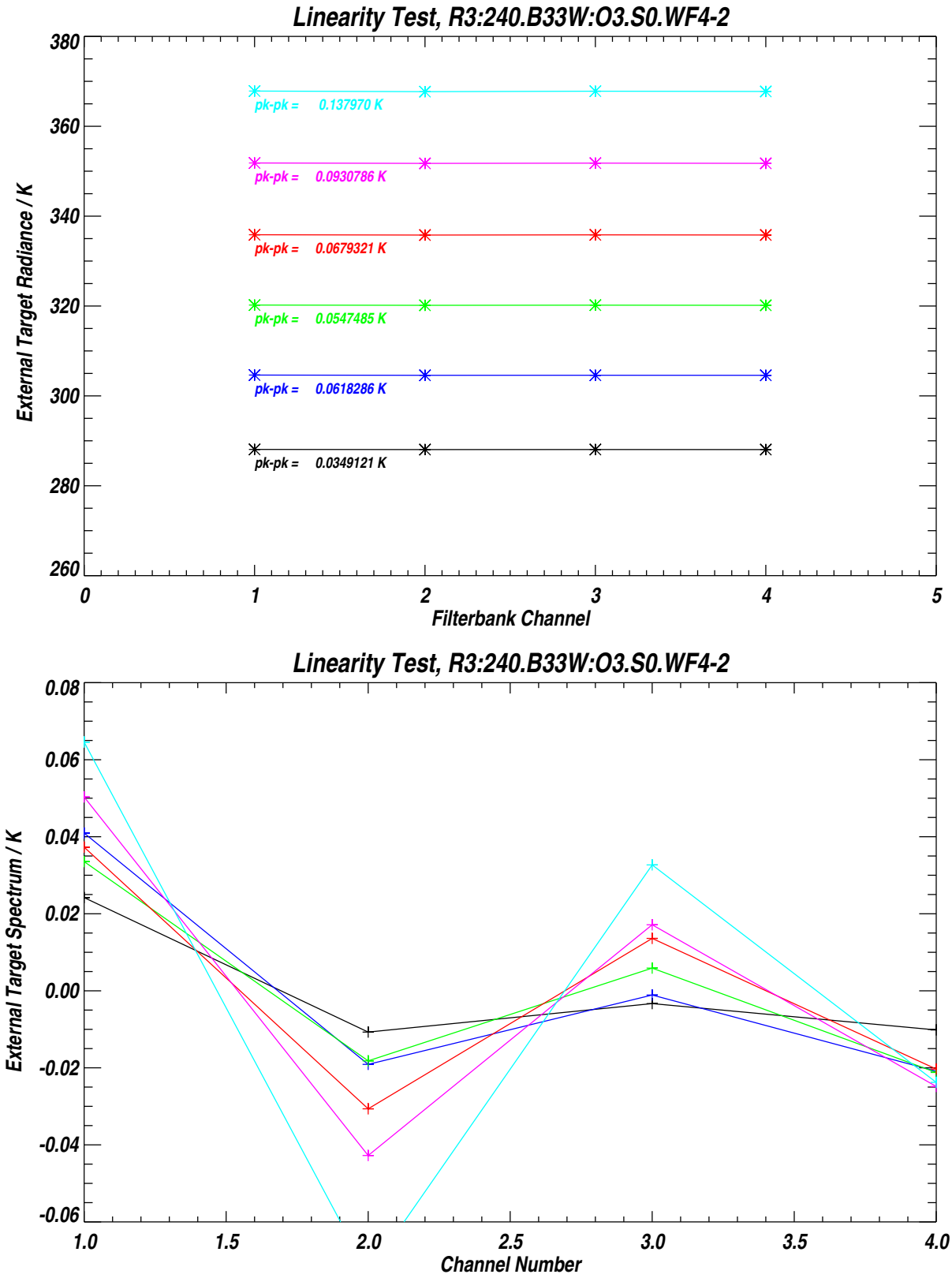

Figure B.115: Hot Target Radiances for the 4 channels of Band 33 (R3 Wide Filters) for 6 different target temperatures. The lower panel shows the data from the upper panel with the weighted mean radiance subtracted from each measurement group. See text for additional details.

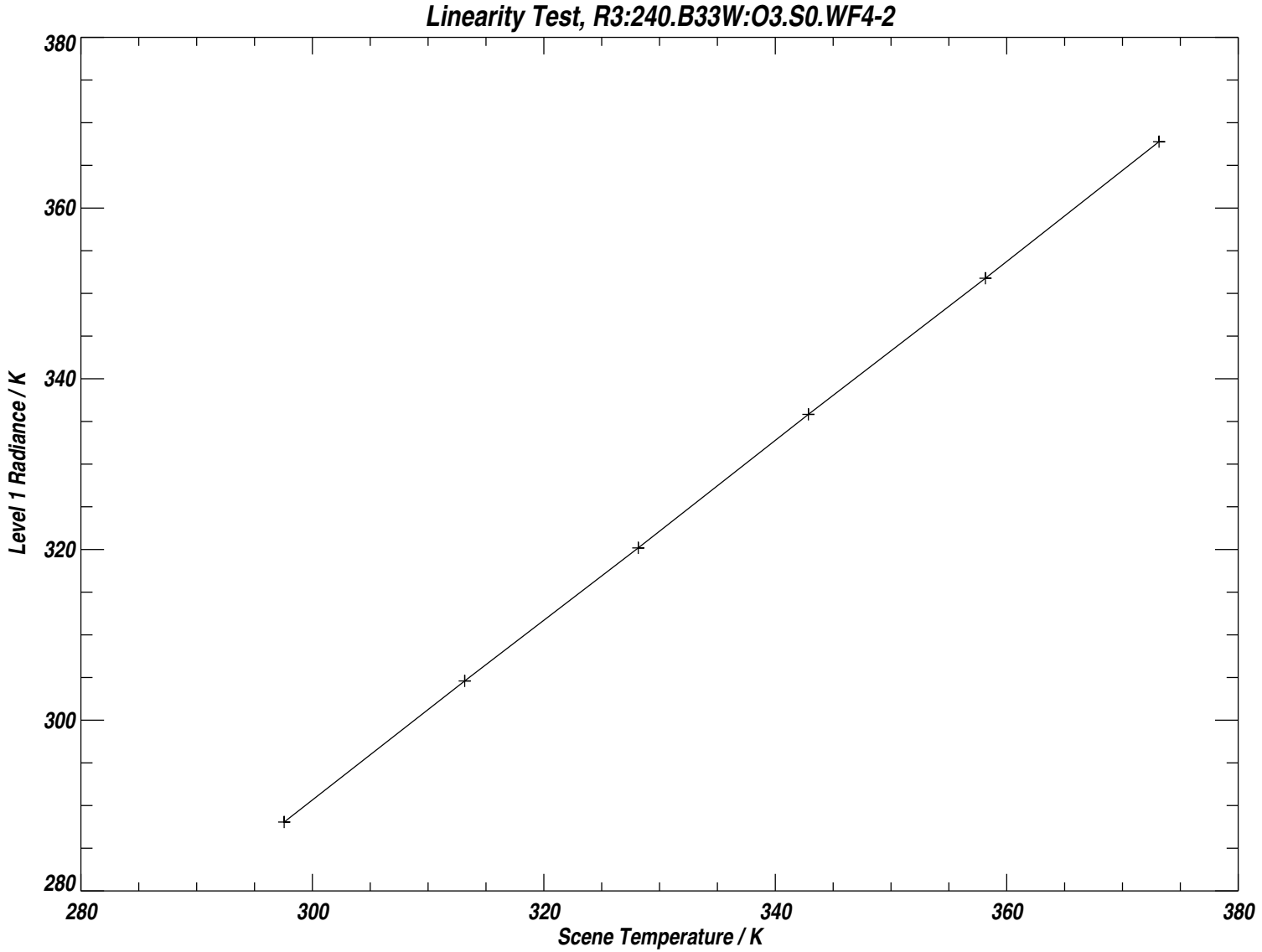

Figure B.116: Data from Figure B.115 with the weighted mean radiance for each measurement group plotted against target temperature. See text for additional details.

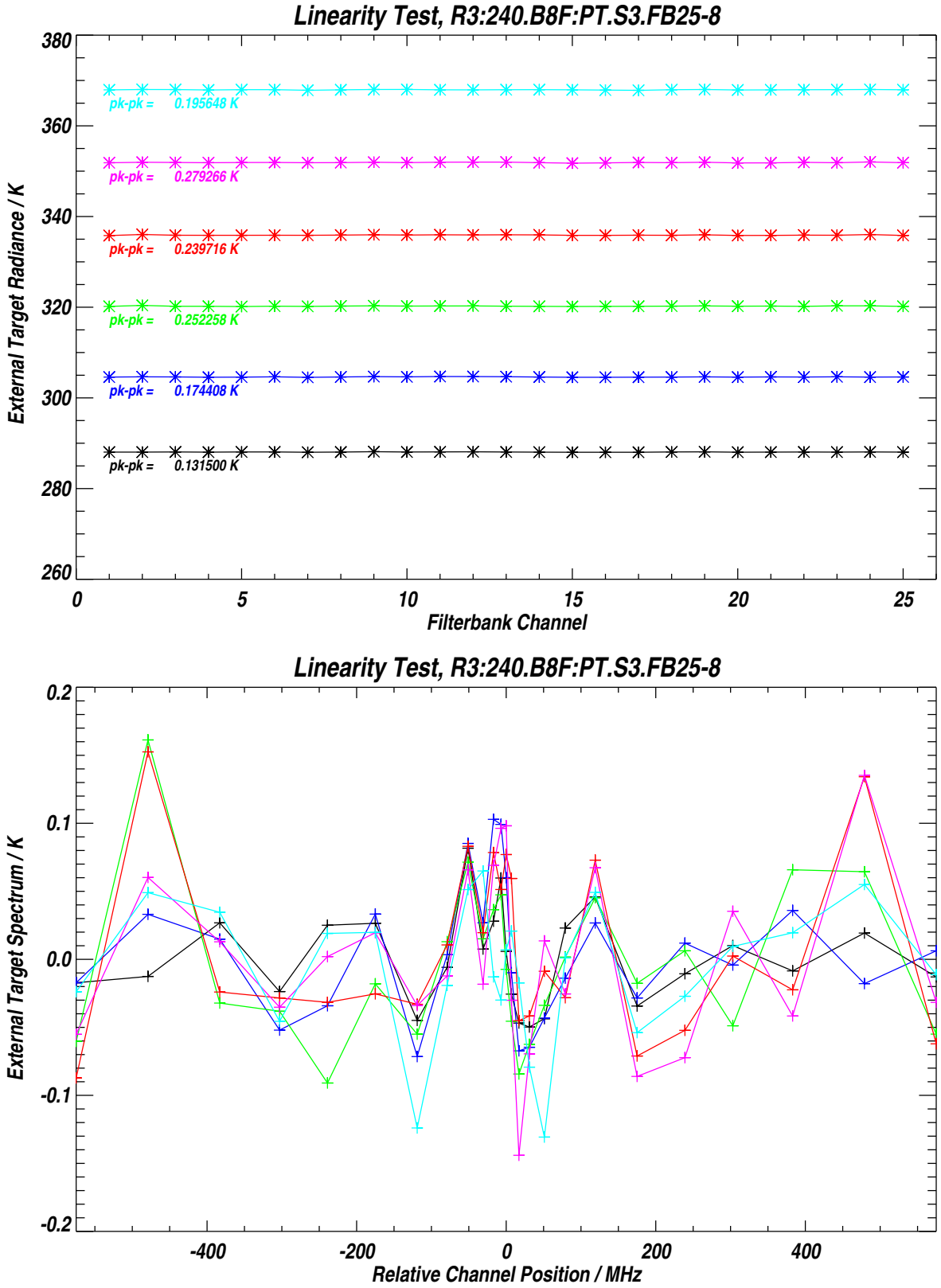

Figure B.117: Hot Target Radiances for the 25 channels of Band 8 for 6 different target temperatures. The lower panel shows the data from the upper panel with the weighted mean radiance subtracted from each measurement group. See text for additional details.

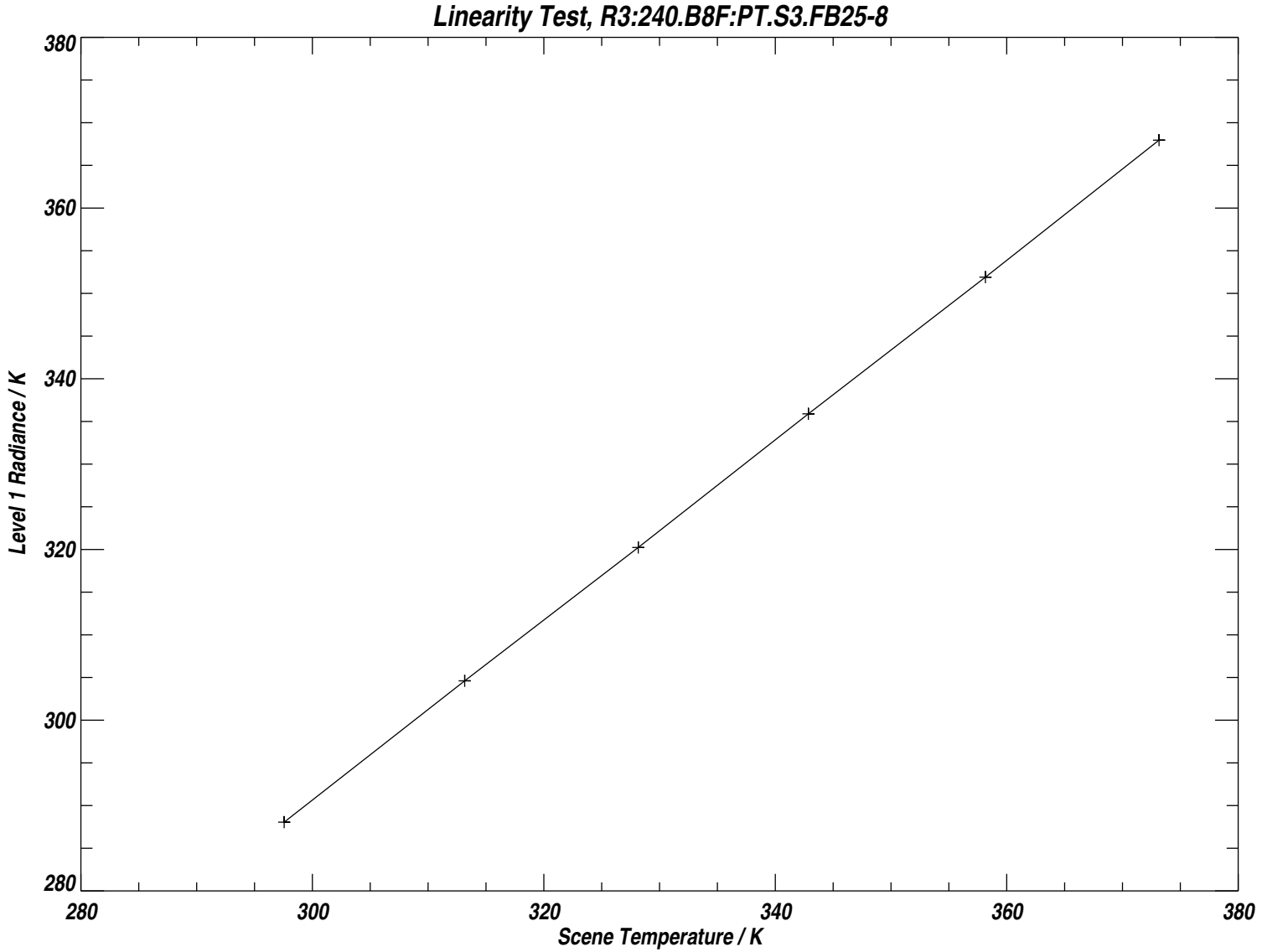

Figure B.118: Data from Figure B.117 with the weighted mean radiance for each measurement group plotted against target temperature. See text for additional details.

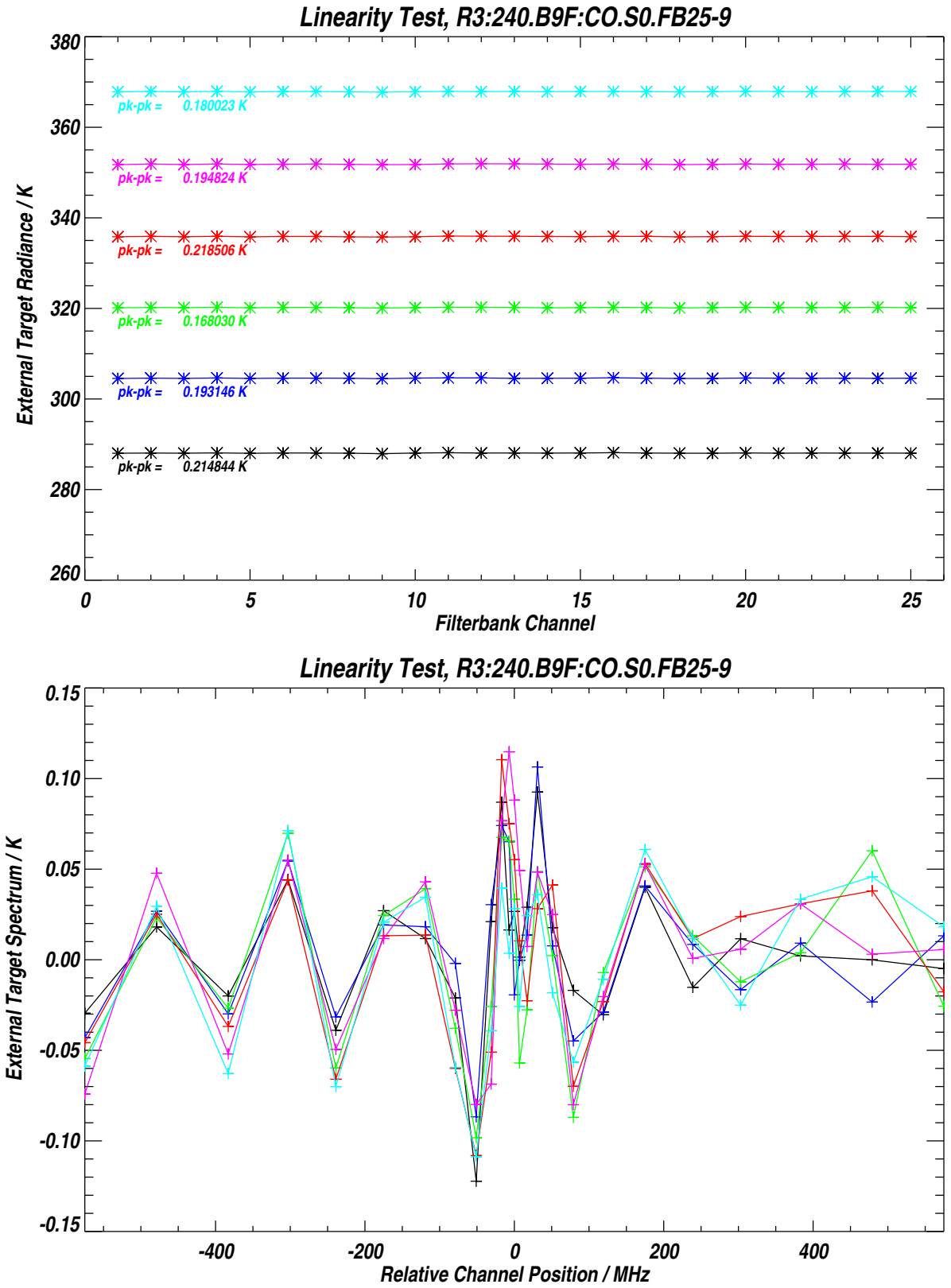

Figure B.119: Hot Target Radiances for the 25 channels of Band 9 for 6 different target temperatures. The lower panel shows the data from the upper panel with the weighted mean radiance subtracted from each measurement group. See text for additional details.

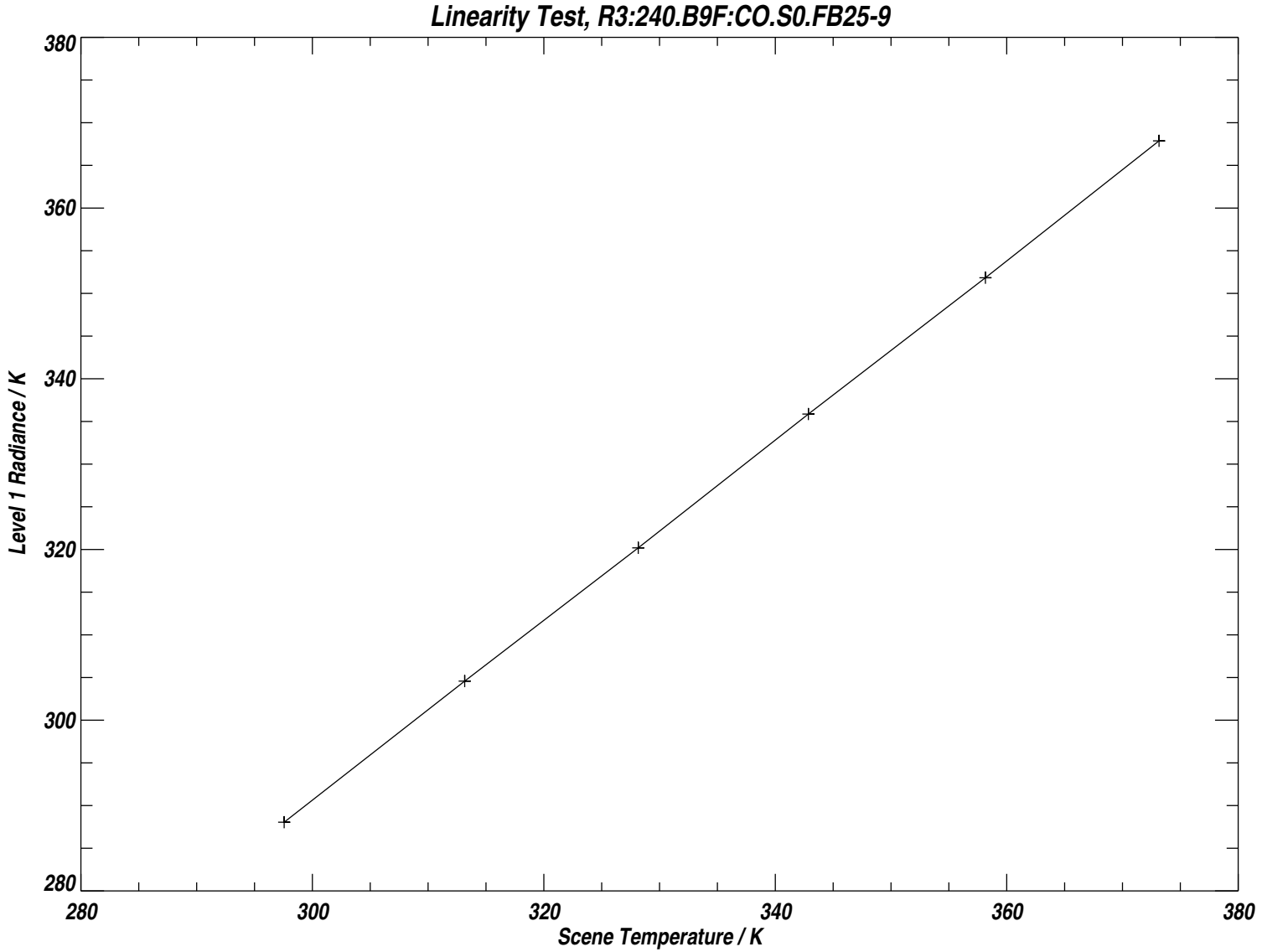

Figure B.120: Data from Figure B.119 with the weighted mean radiance for each measurement group plotted against target temperature. See text for additional details.

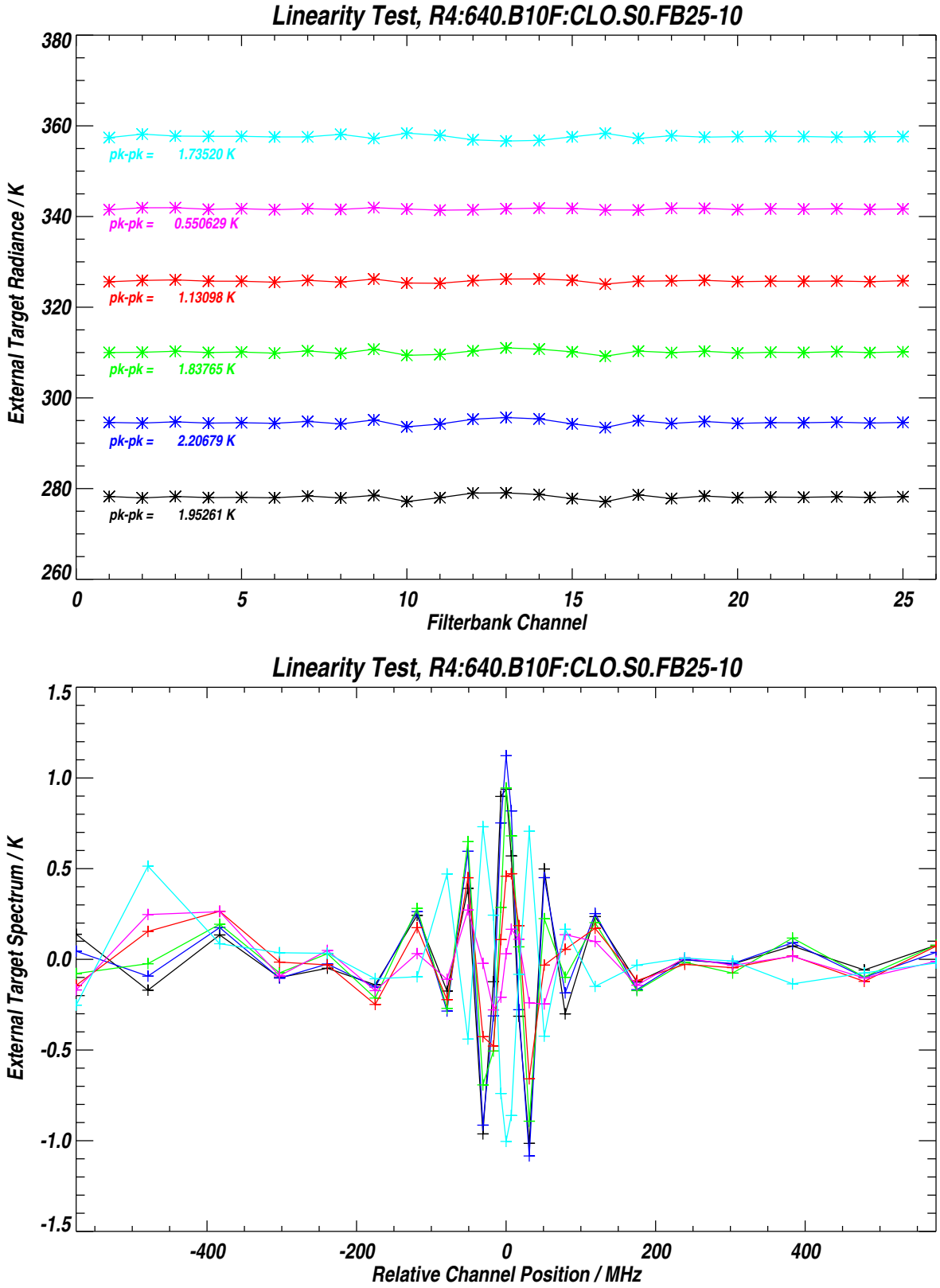

Figure B.121: Hot Target Radiances for the 25 channels of Band 10 for 6 different target temperatures. The lower panel shows the data from the upper panel with the weighted mean radiance subtracted from each measurement group. See text for additional details.

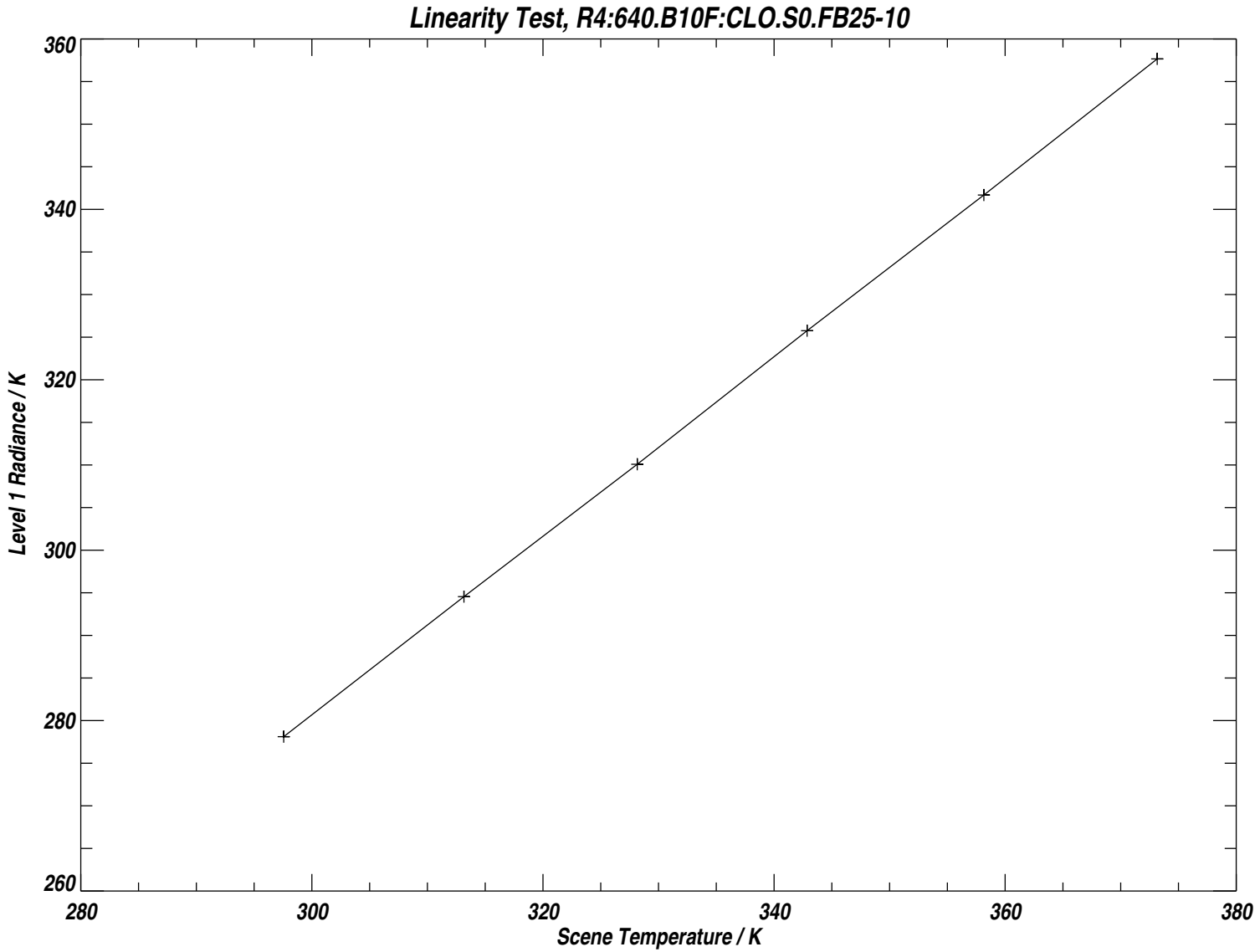

Figure B.122: Data from Figure B.121 with the weighted mean radiance for each measurement group plotted against target temperature. See text for additional details.

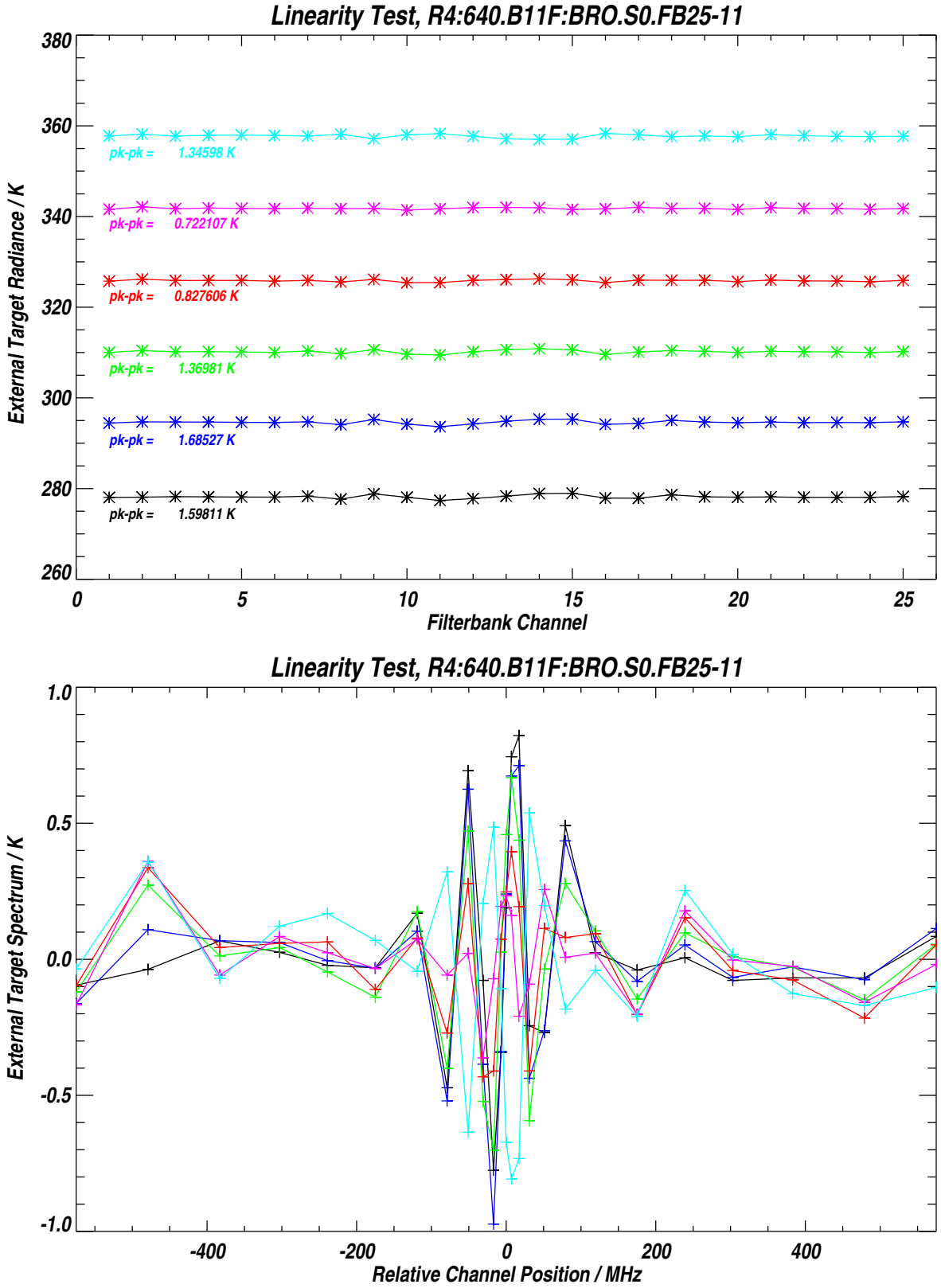

Figure B.123: Hot Target Radiances for the 25 channels of Band 11 for 6 different target temperatures. The lower panel shows the data from the upper panel with the weighted mean radiance subtracted from each measurement group. See text for additional details.

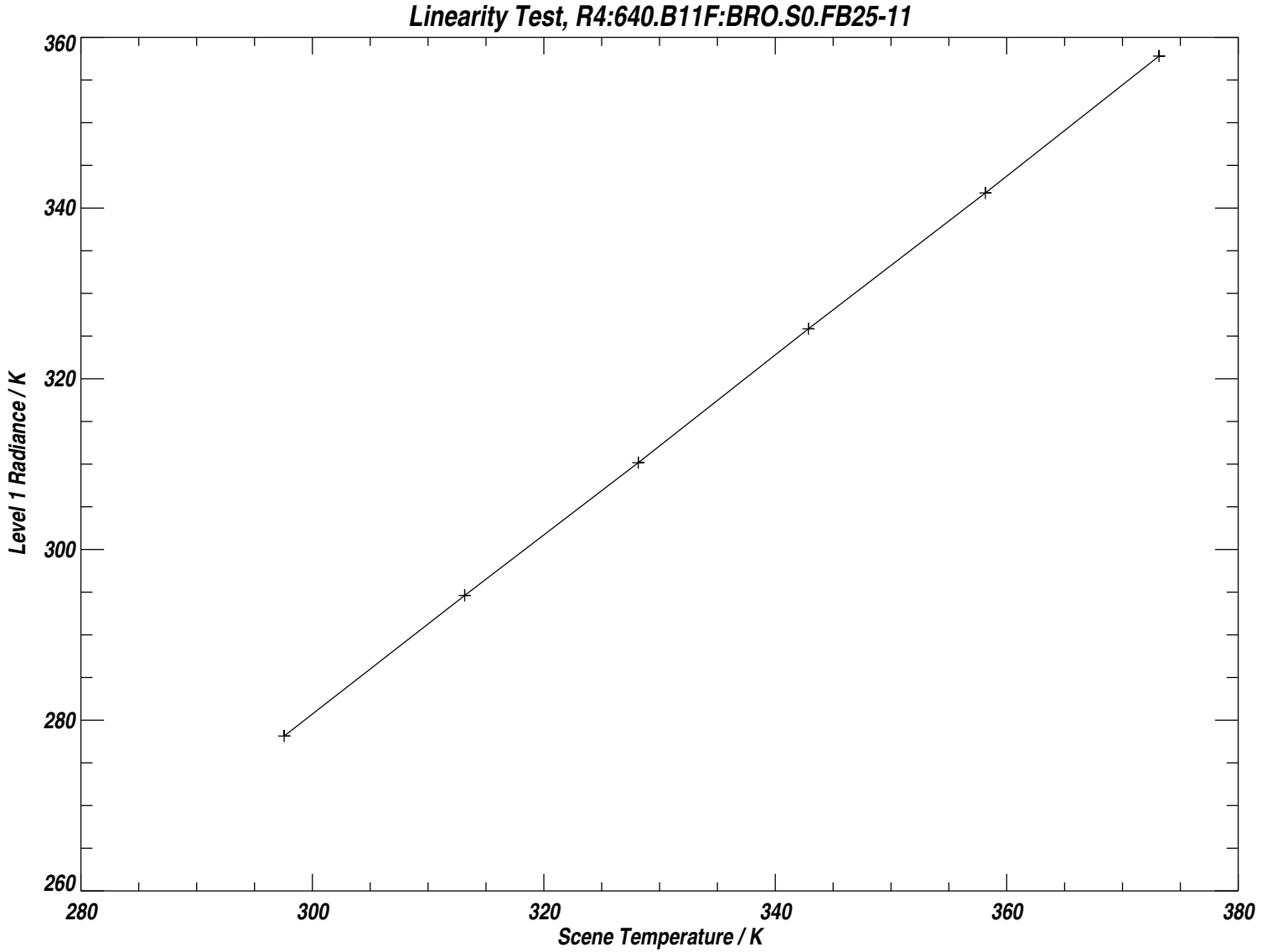

Figure B.124: Data from Figure B.123 with the weighted mean radiance for each measurement group plotted against target temperature. See text for additional details.

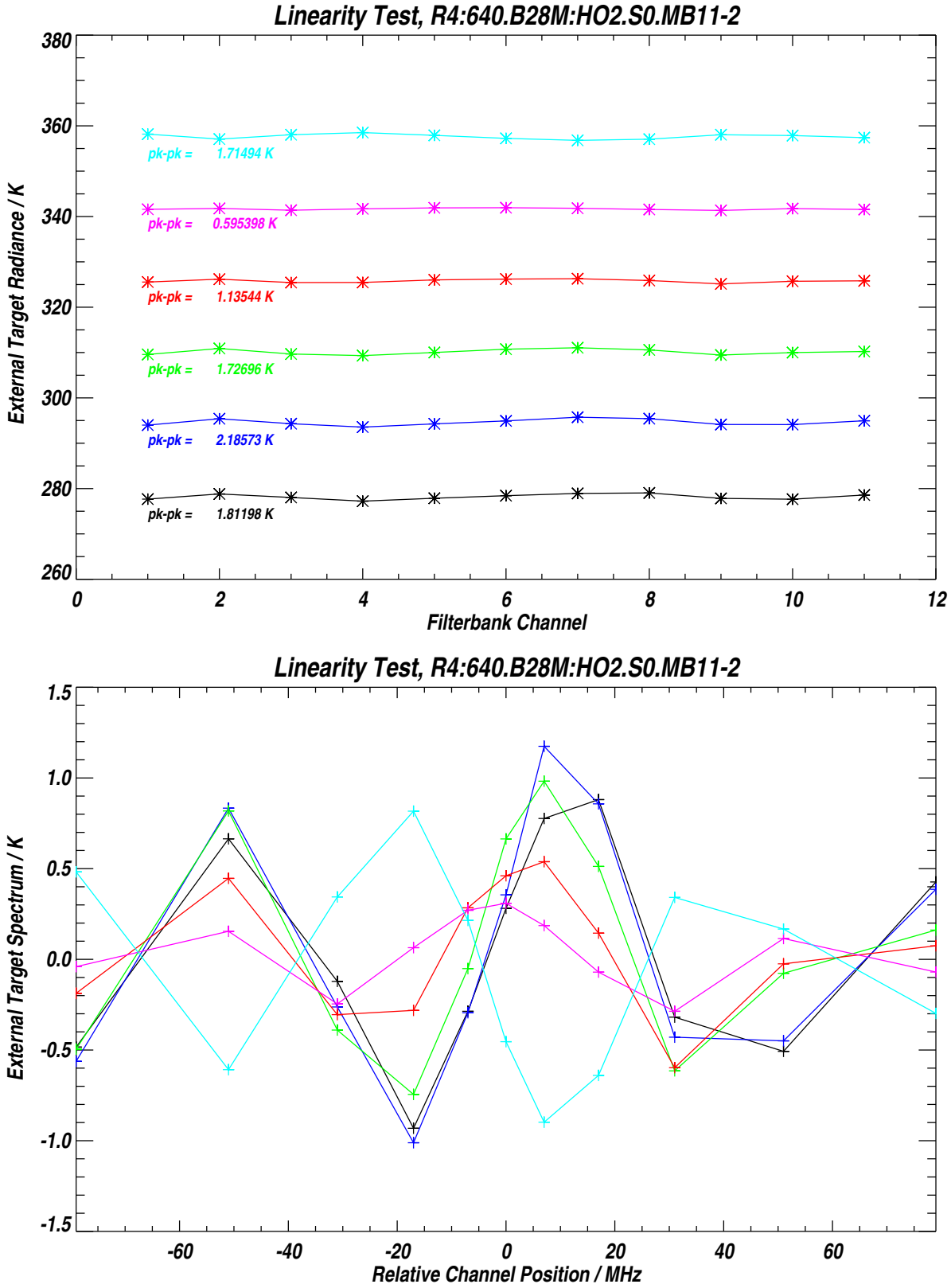

Figure B.125: Hot Target Radiances for the 11 channels of Band 28 for 6 different target temperatures. The lower panel shows the data from the upper panel with the weighted mean radiance subtracted from each measurement group. See text for additional details.

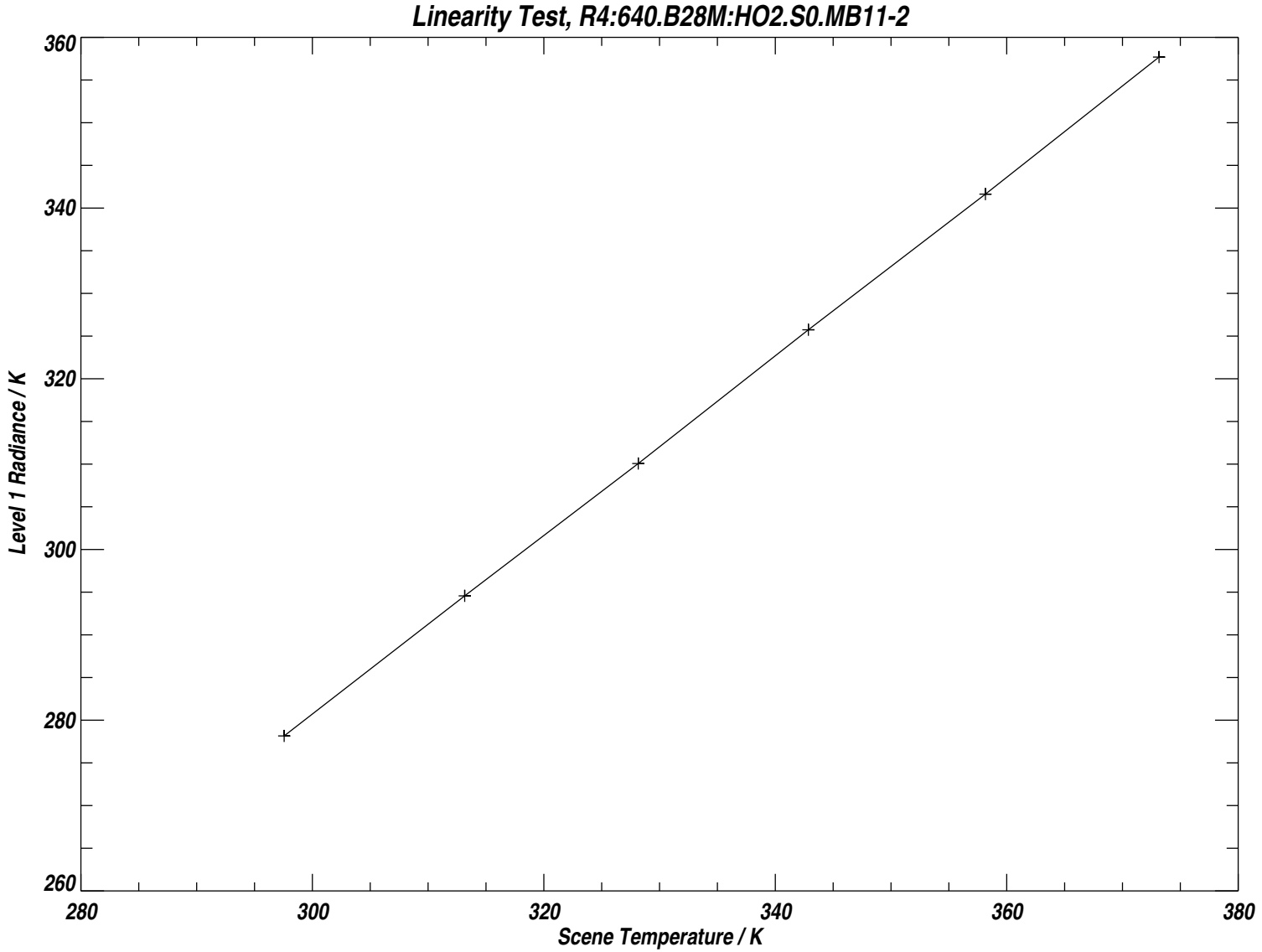

Figure B.126: Data from Figure B.125 with the weighted mean radiance for each measurement group plotted against target temperature. See text for additional details.

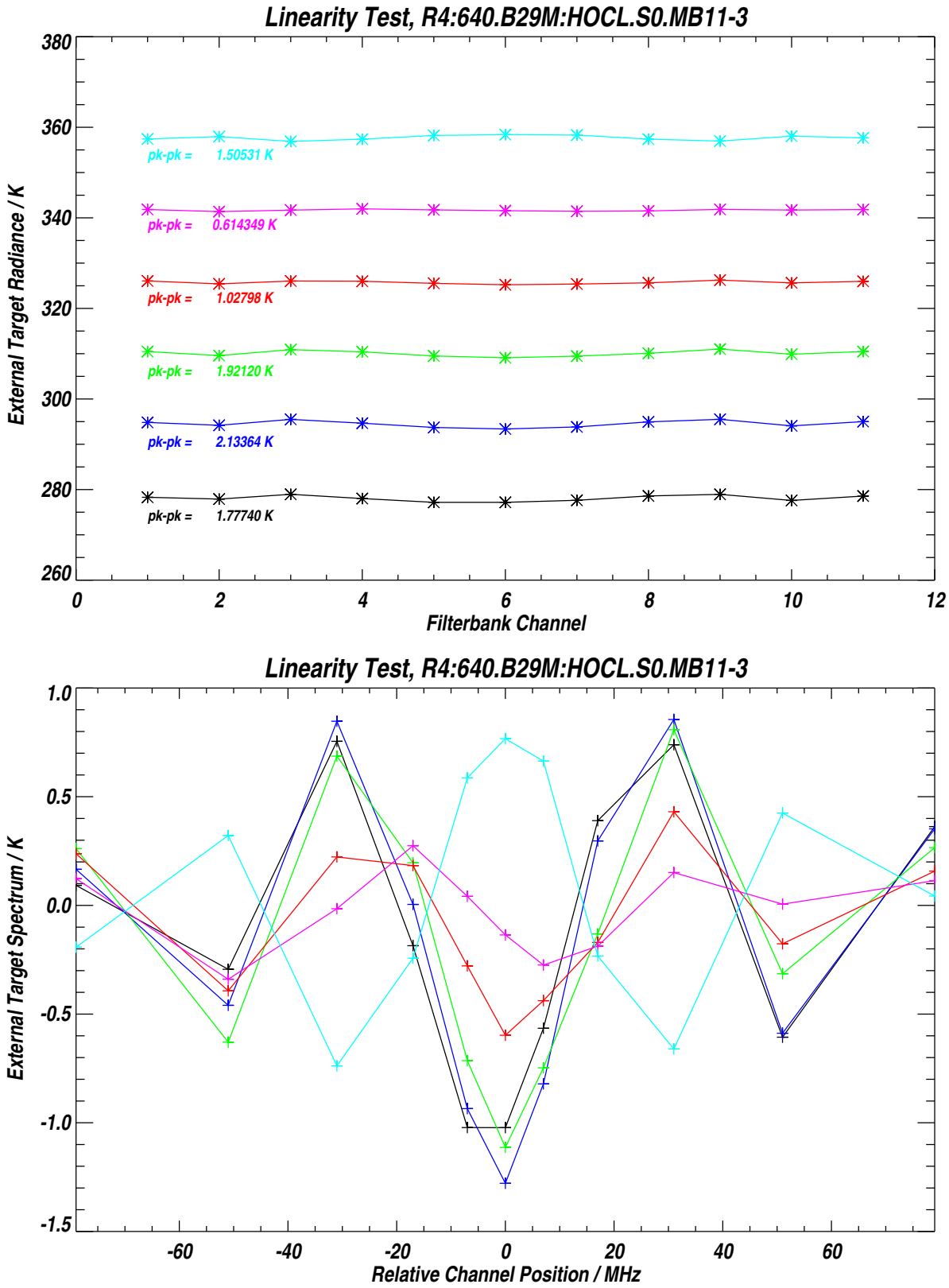

Figure B.127: Hot Target Radiances for the 11 channels of Band 29 for 6 different target temperatures. The lower panel shows the data from the upper panel with the weighted mean radiance subtracted from each measurement group. See text for additional details.

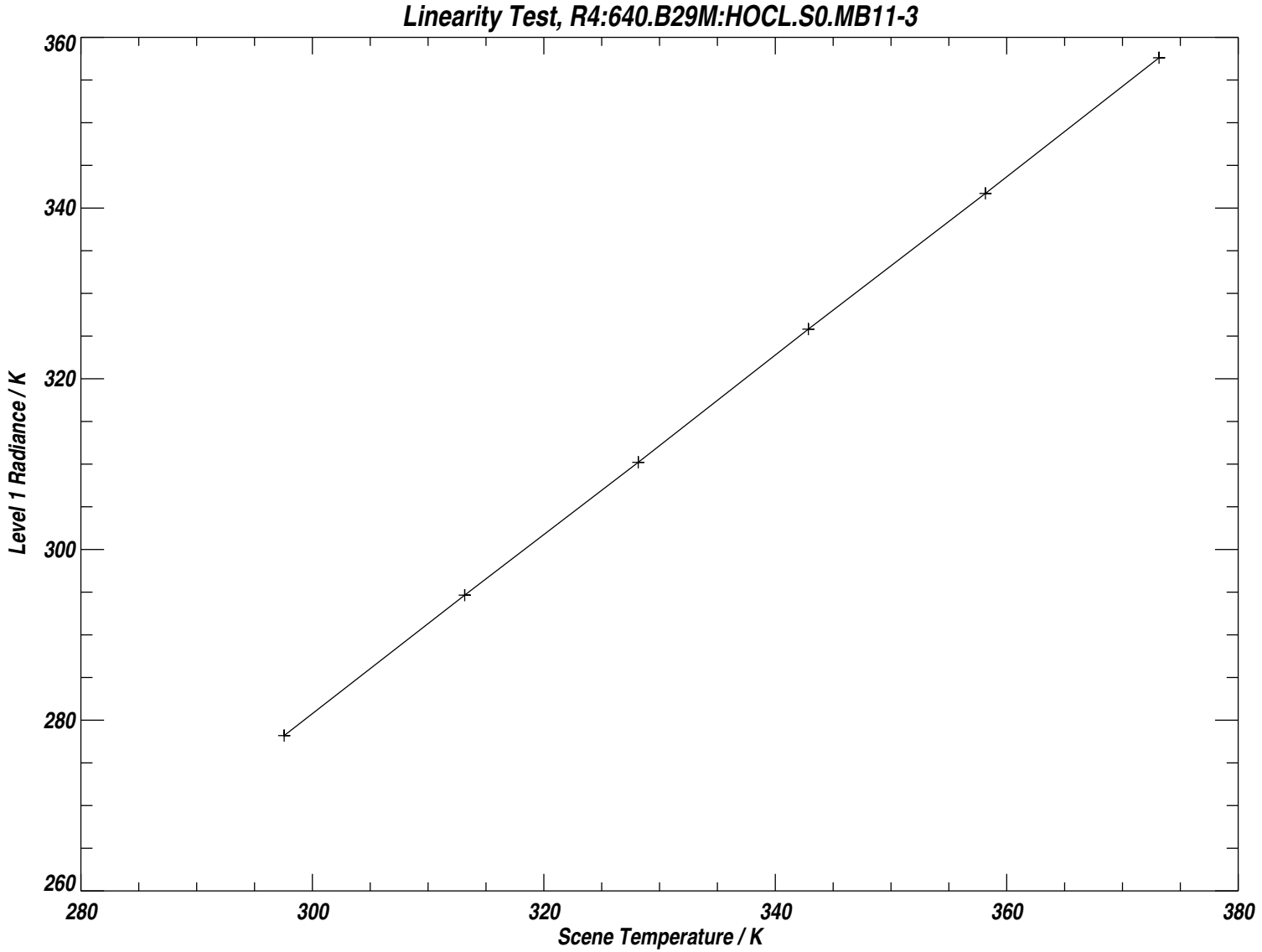

Figure B.128: Data from Figure B.127 with the weighted mean radiance for each measurement group plotted against target temperature. See text for additional details.

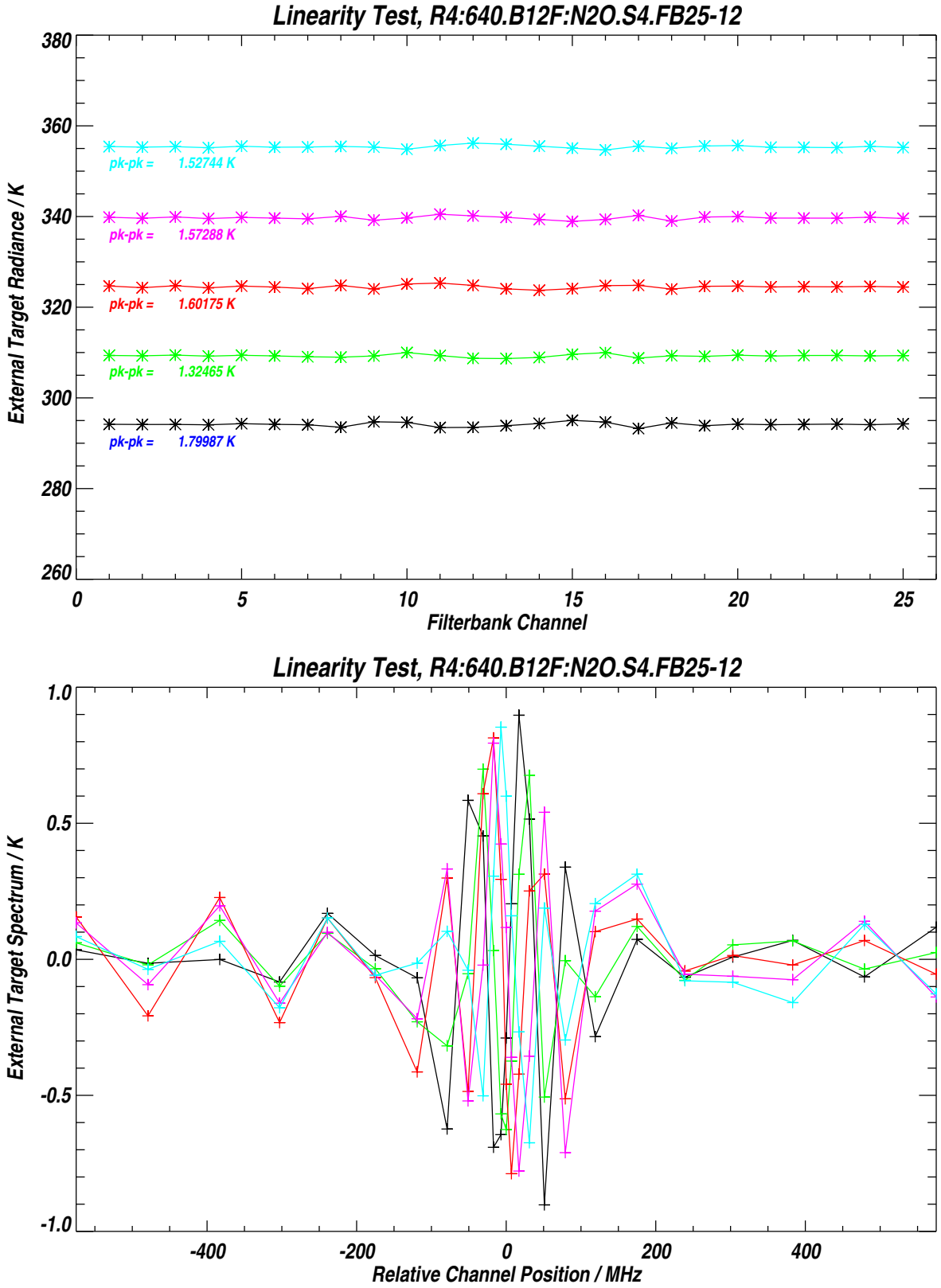

Figure B.129: Hot Target Radiances for the 25 channels of Band 12 for 5 different target temperatures. The lower panel shows the data from the upper panel with the weighted mean radiance subtracted from each measurement group. See text for additional details.

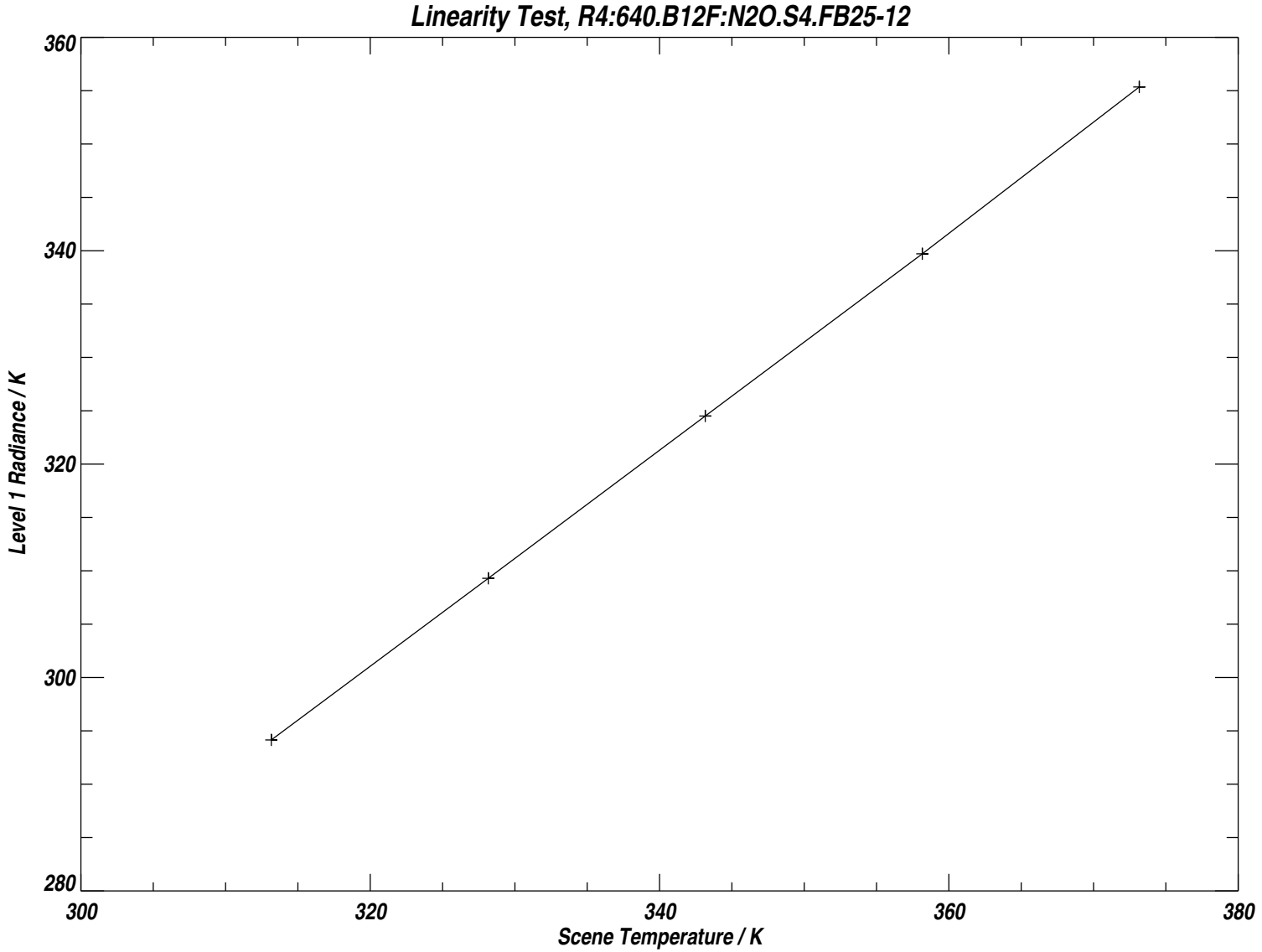

Figure B.130: Data from Figure B.129 with the weighted mean radiance for each measurement group plotted against target temperature. See text for additional details.

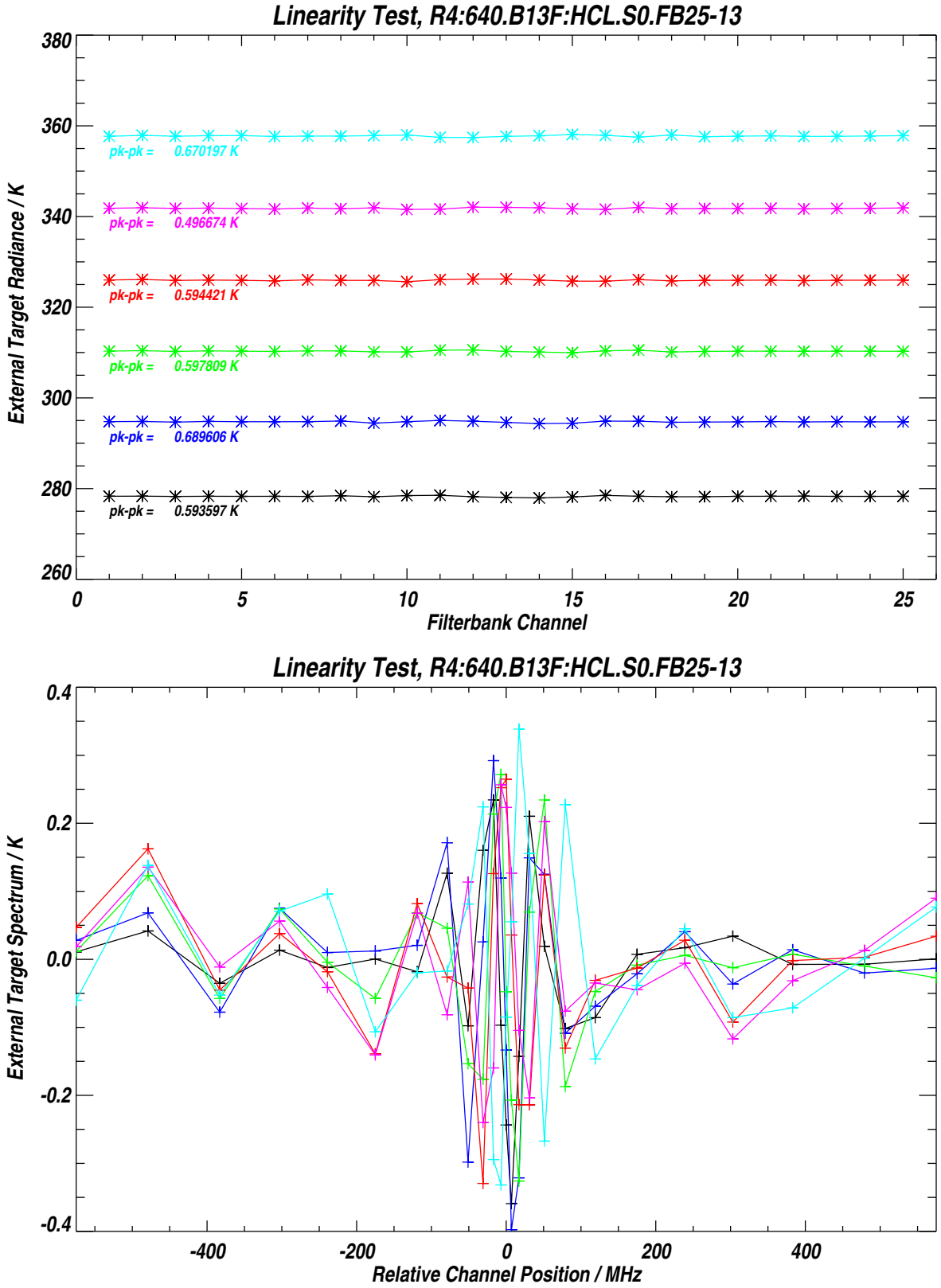

Figure B.131: Hot Target Radiances for the 25 channels of Band 13 for 6 different target temperatures. The lower panel shows the data from the upper panel with the weighted mean radiance subtracted from each measurement group. See text for additional details.

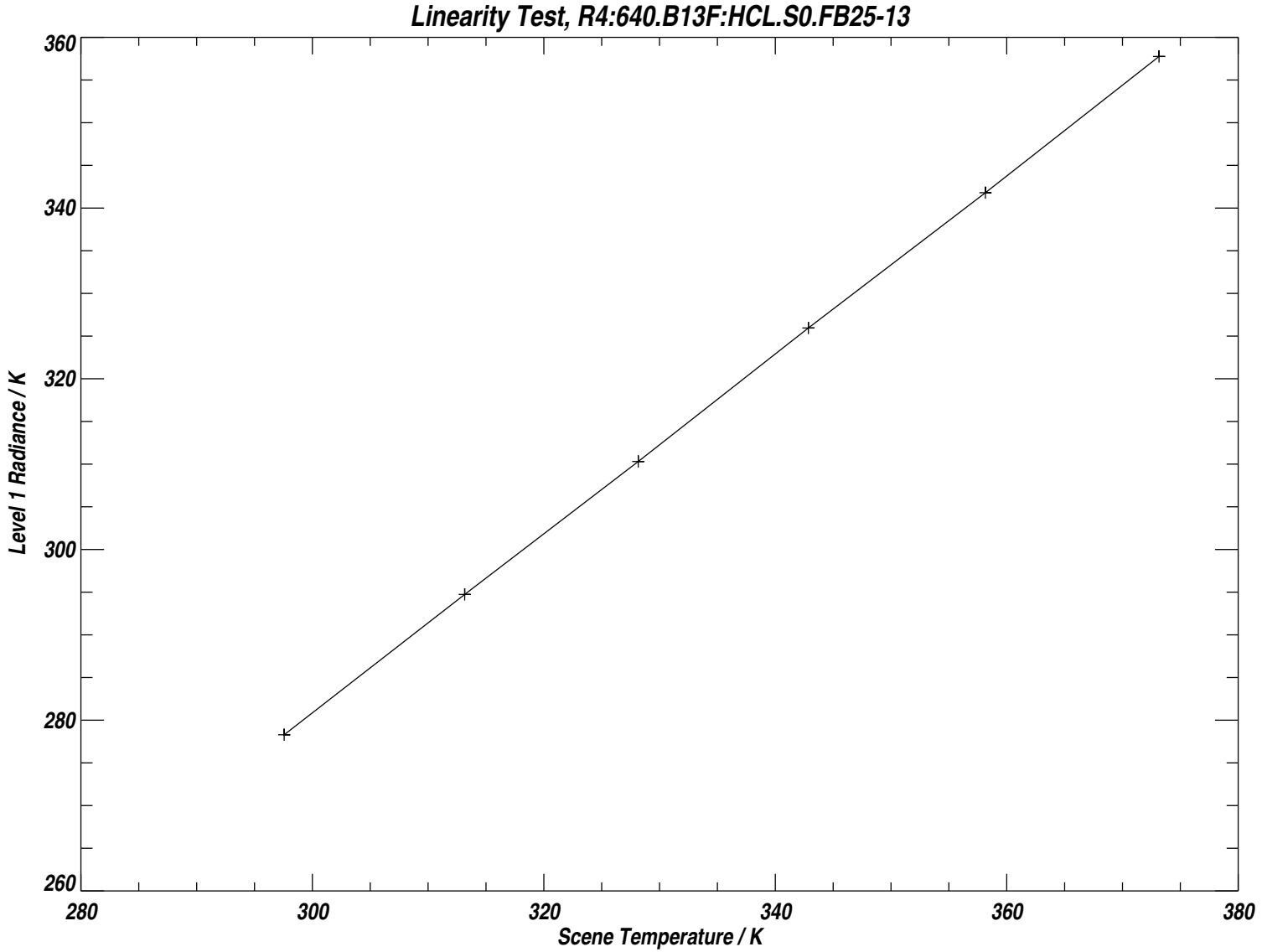

Figure B.132: Data from Figure B.131 with the weighted mean radiance for each measurement group plotted against target temperature. See text for additional details.

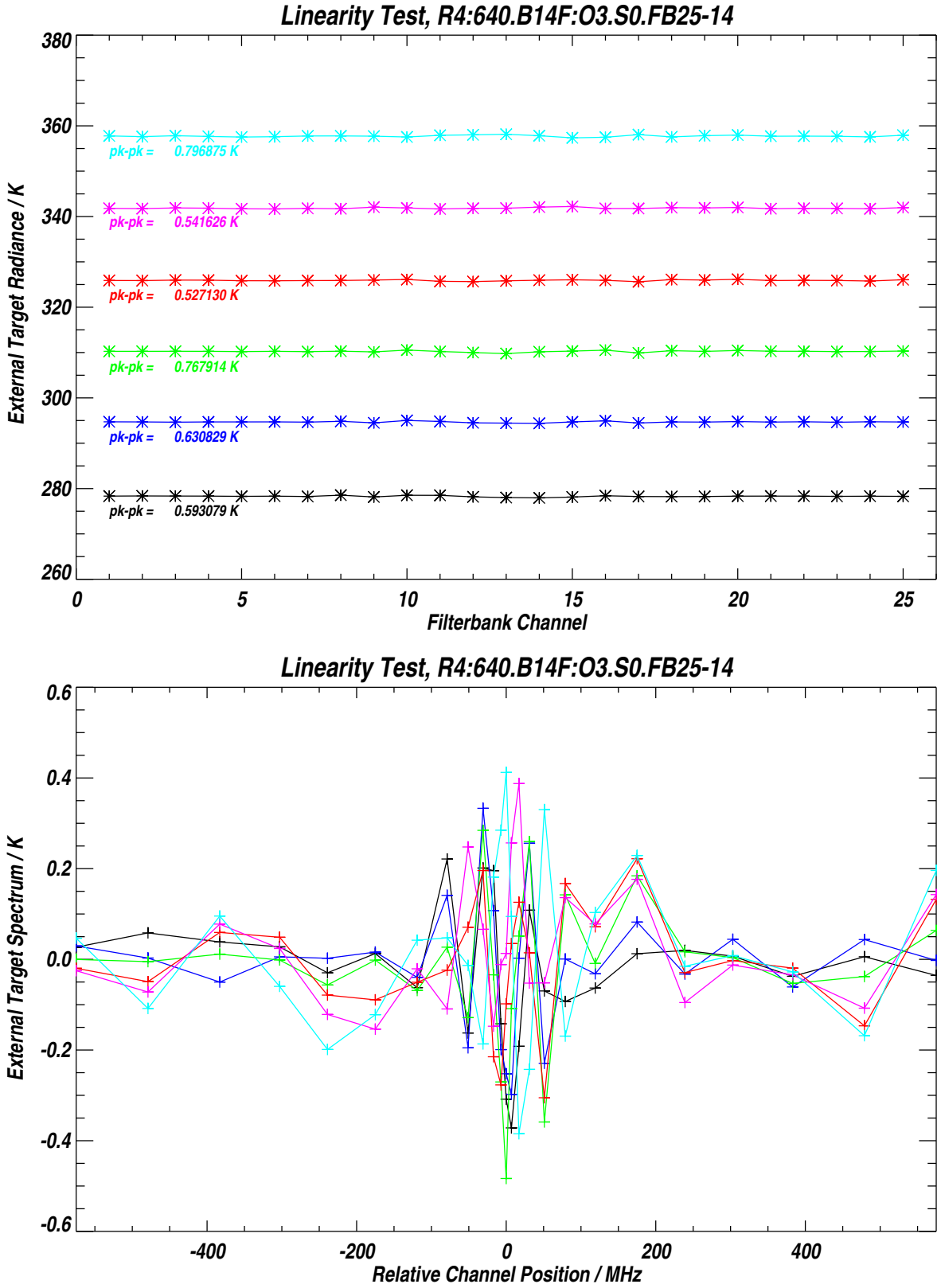

Figure B.133: Hot Target Radiances for the 25 channels of Band 14 for 6 different target temperatures. The lower panel shows the data from the upper panel with the weighted mean radiance subtracted from each measurement group. See text for additional details.

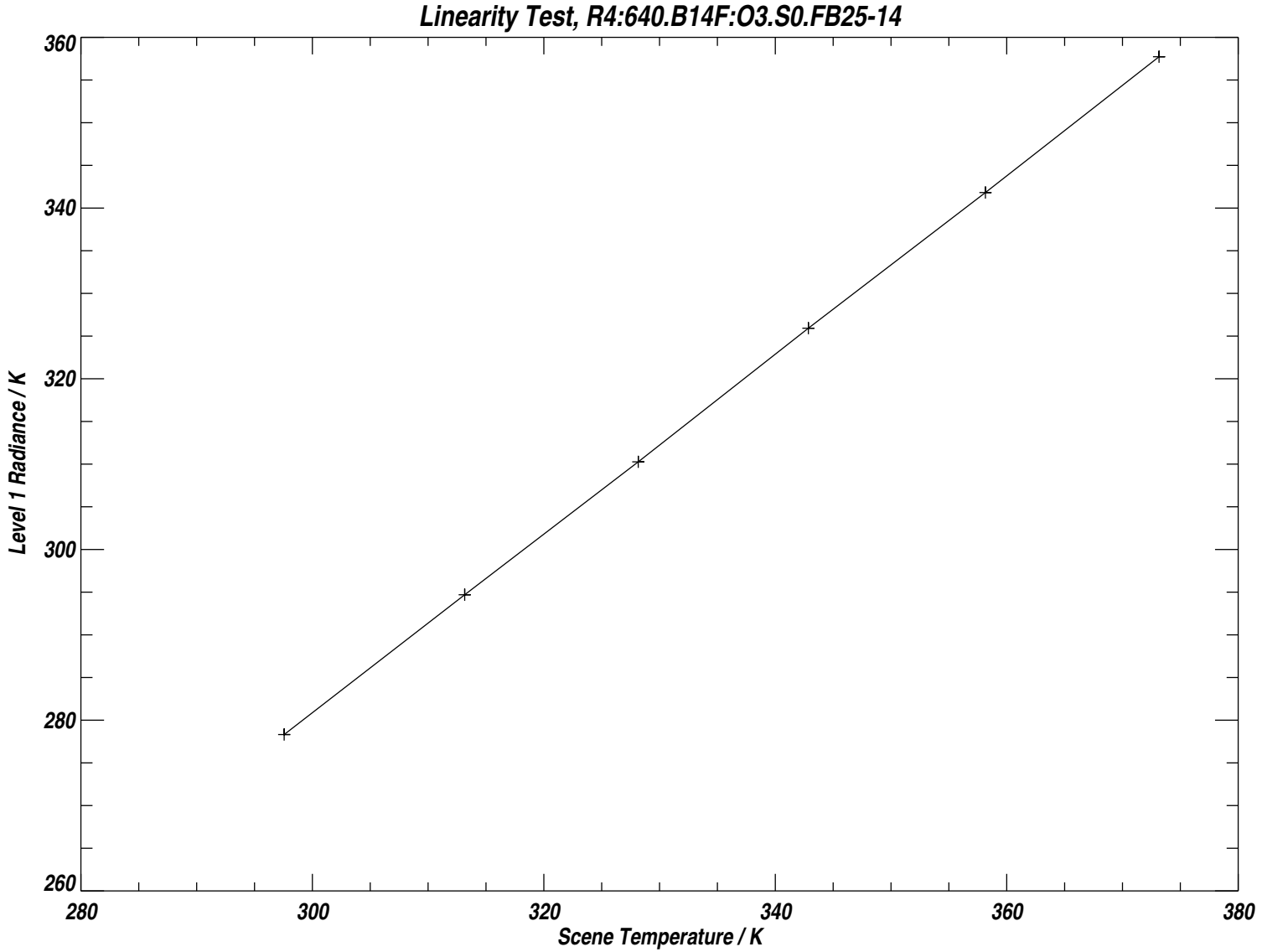

Figure B.134: Data from Figure B.133 with the weighted mean radiance for each measurement group plotted against target temperature. See text for additional details.

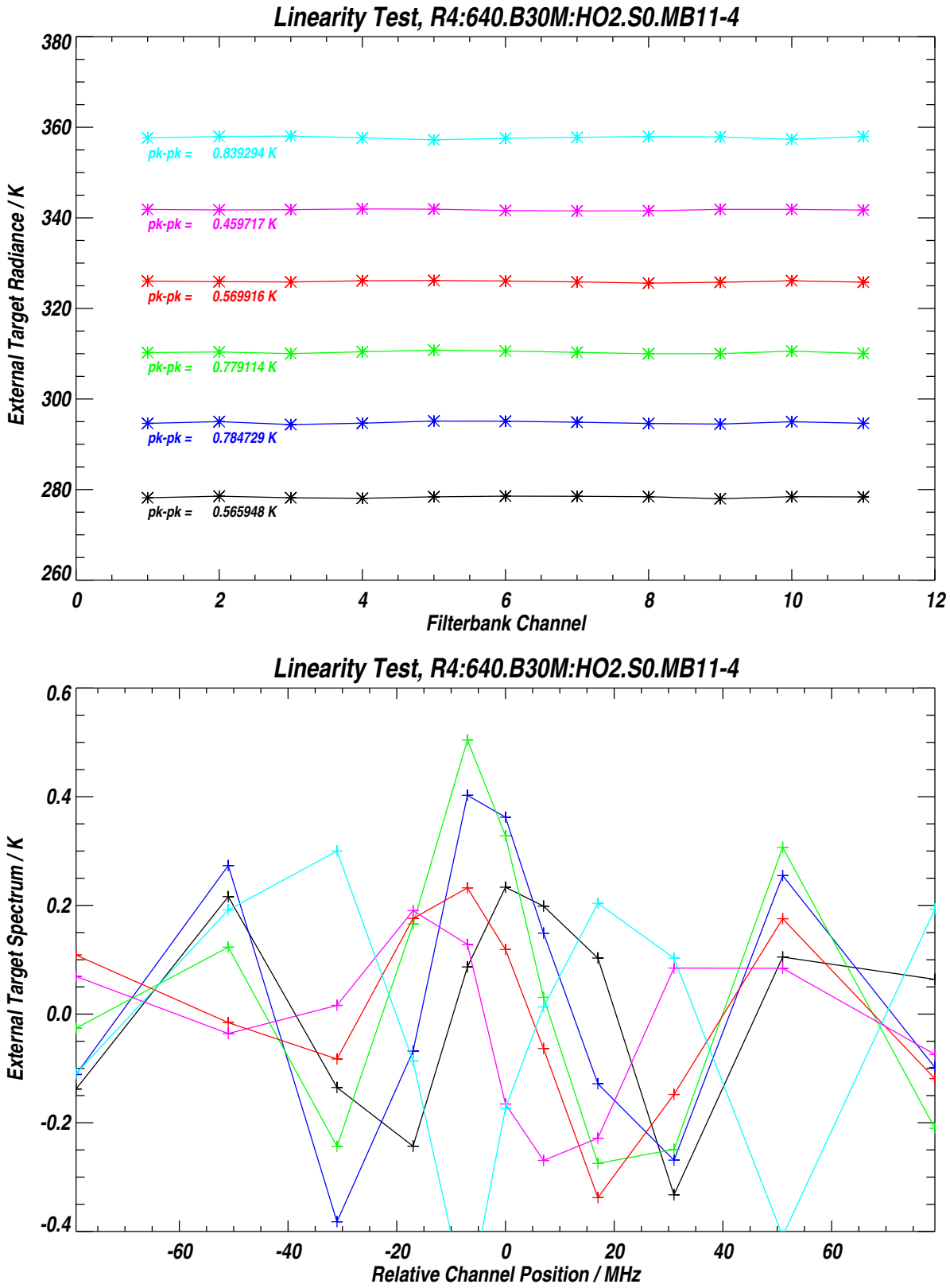

Figure B.135: Hot Target Radiances for the 11 channels of Band 30 for 6 different target temperatures. The lower panel shows the data from the upper panel with the weighted mean radiance subtracted from each measurement group. See text for additional details.

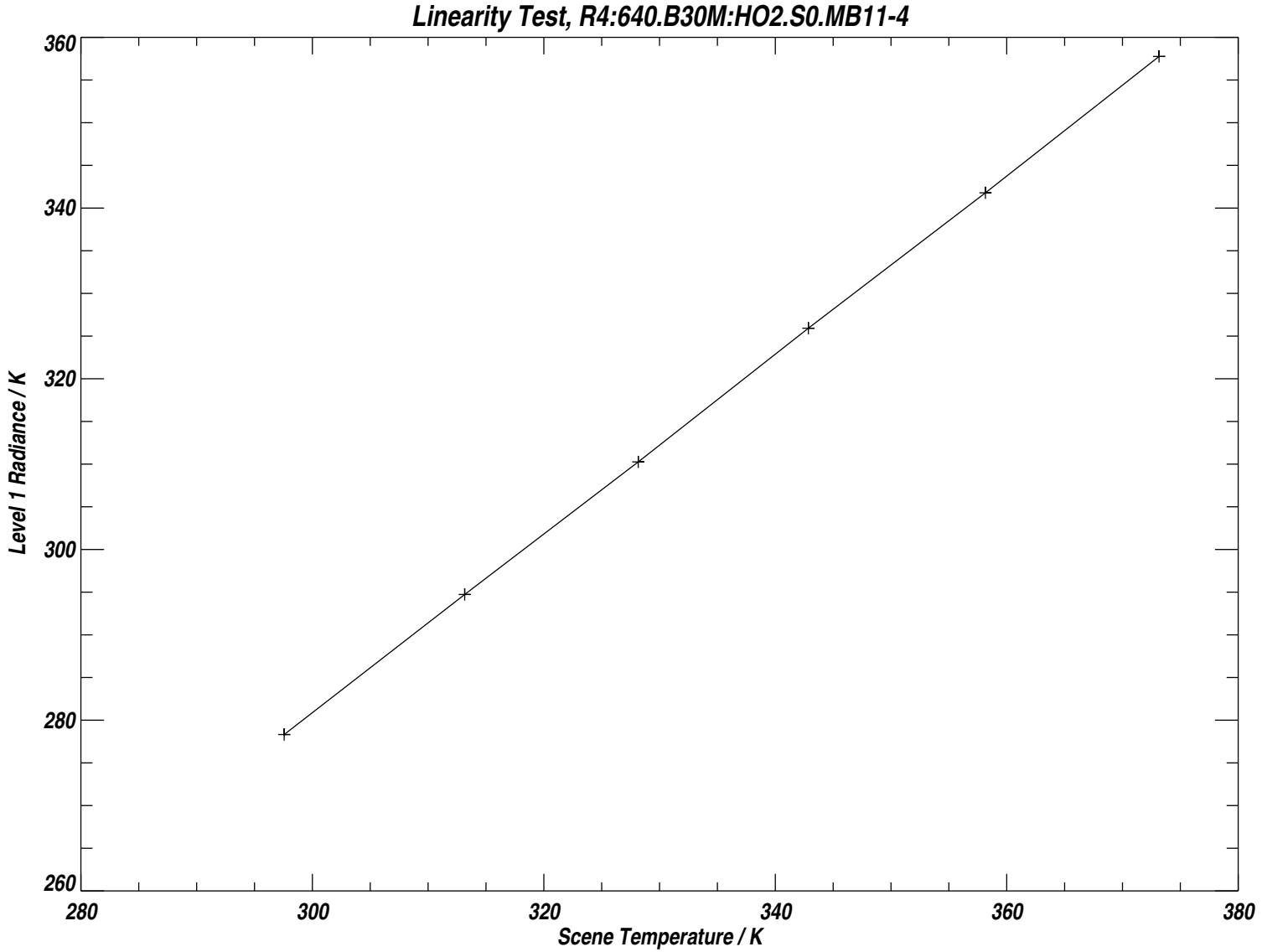

Figure B.136: Data from Figure B.135 with the weighted mean radiance for each measurement group plotted against target temperature. See text for additional details.

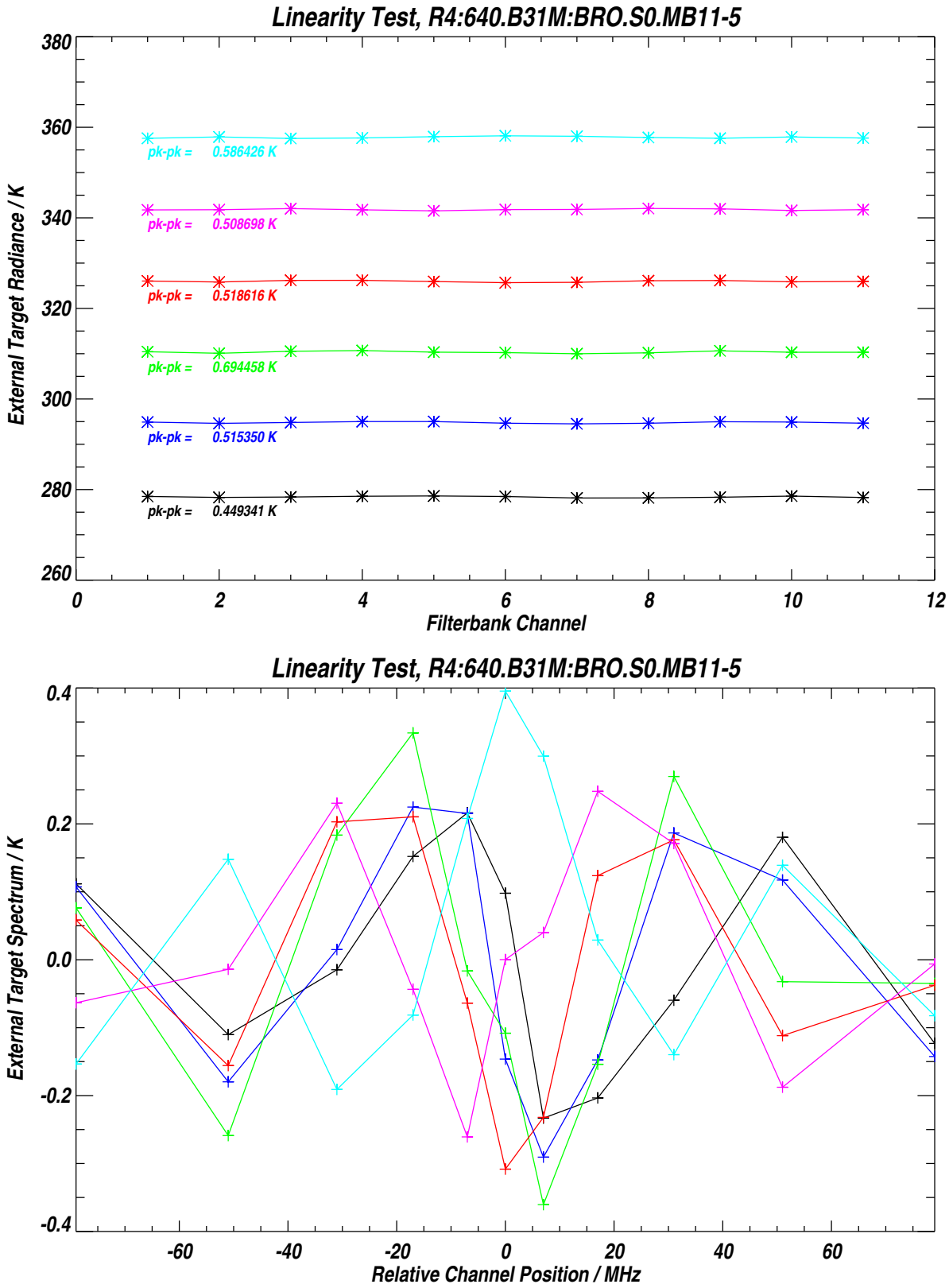

Figure B.137: Hot Target Radiances for the 11 channels of Band 31 for 6 different target temperatures. The lower panel shows the data from the upper panel with the weighted mean radiance subtracted from each measurement group. See text for additional details.

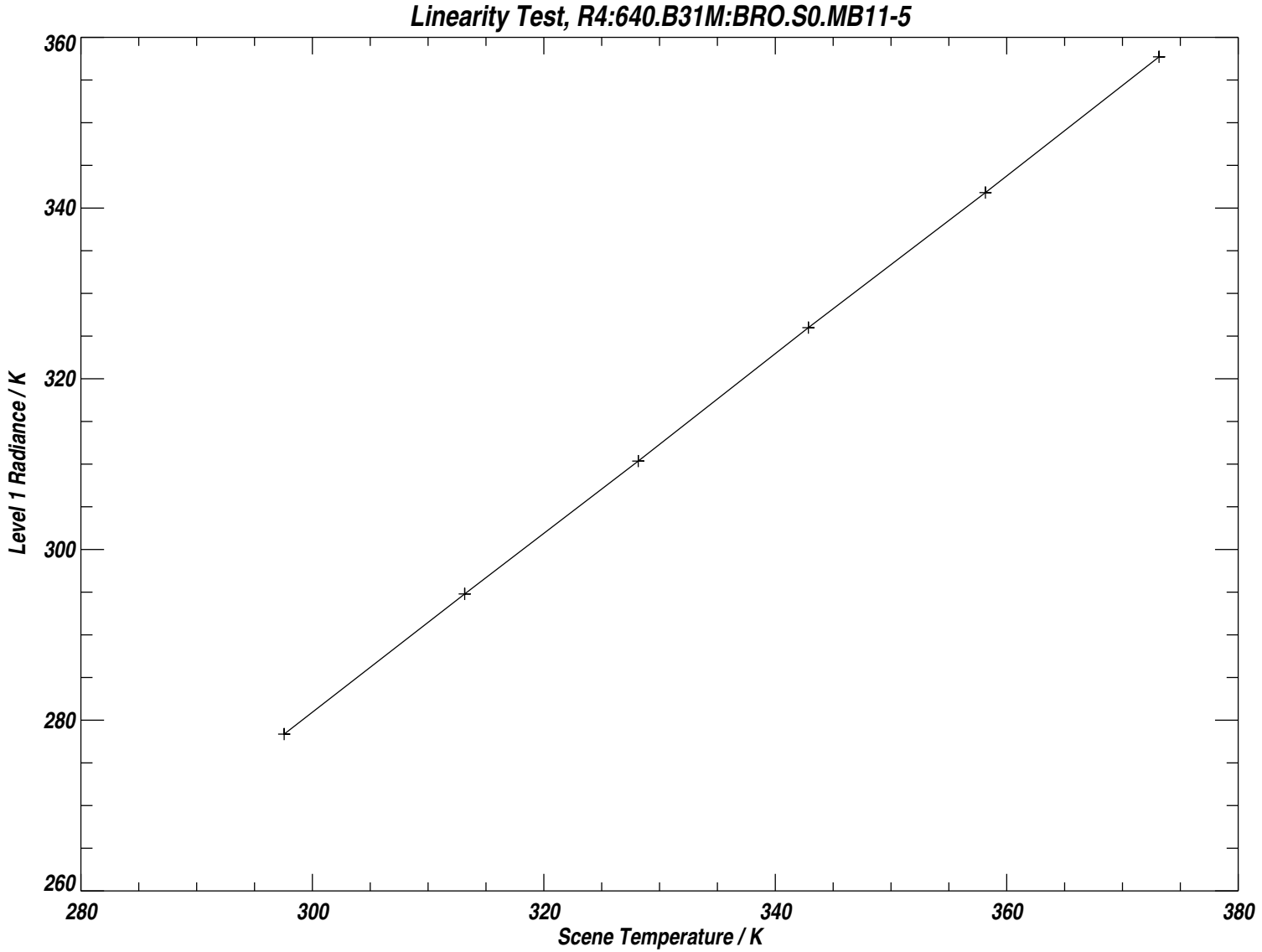

Figure B.138: Data from Figure B.137 with the weighted mean radiance for each measurement group plotted against target temperature. See text for additional details.

B.3 Blue Sky Measurement Data

The complete Blue Sky data (Limb port minus Space port radiances) for three antenna positions: short, nominal and long strut, are presented below. For this test the GHz Antenna Scan Actuator (ASE) was replaced by a manually operated turnbuckle, referred to here as the strut. The short strut position corresponds to the antenna scan angle with the scan mechanism compressed to its shortest extent (equivalent to viewing $\sim 6^\circ$ above the Earth's Limb in orbit. The long strut position corresponds to the antenna scan angle with the scan mechanism extended to its maximum length (equivalent to viewing $\sim 6^\circ$ below the Earth's Limb surface. The nominal strut position corresponds to antenna viewing the Earth's nominal tangent point in orbit, ignoring the Earth's oblateness. Data from each strut position are plotted twice. For the short strut orientation the entire data set is presented in the first pair of plots, followed by a subset with measurement duration similar to the subsequent plots with different strut positions. The nominal and long strut data follow, with two different, non-overlapping time intervals analysed for each pair of plots. This ensemble of data provides a sufficient number of independent measurements to provide confidence that no measurement artifacts exist that represent performance issues with the instrument.

These six sets of plots are to be compared for systematic differences. No obvious differences are observable in these data, leading us to believe that on-orbit data from the GHz radiometers of MLS will not exhibit any serious antenna scan-dependencies. In Chapter 2 the first nominal strut data set is also presented as observed Limb and Space port radiances to show that sufficient thermal constrast was present between the internal calibration targets and external scene views for this to be a useful and valuable test. The 640 GHz radiometer bands did not have sufficient thermal contrast to provide the same information regarding scan dependent artifacts, but since these higher frequency measurements illuminate a substantially smaller area of the antenna optical surfaces than the lower frequency ones, we feel that this set of measurements is sufficient to provide high confidence in the quality of the data from the highest frequency ones.

When the strut length was altered to reflect the three antenna orientations chosen for this test, the upper reflector shown in Figure 2.15 was moved so that the antenna beam continued to strike it centrally. In addition, minor changes to the angle of this reflector were made to maintain close balance between Limb port and Space port signals, necessitated by changes in atmospheric conditions during the course of these measurements (a Santa Ana condition prevailed during the course of these tests, fortuitously providing a very 'dry' atmosphere, ideal for these measurements).

B.3.1 A comment on data quality

For these measurements, the spectrometer power supply modification needed to remove the artifacts present in the mid-band section of the 25-channels filterbanks (and the 11-channel filterbanks), and to correct the odd/even MIF difference problem, had not been made. It was this set of measurements that were instrumental in identifying this problem, and there was not sufficient time to repeat this somewhat lengthy test after these instrument modifications had been made. Sufficient evidence that the modifications had fully corrected these performance problems was provided by data from subsequent sensitivity characterizations and relative sideband response calibrations.

For these Blue Sky test data channel 22 of Band 5 exhibited slightly larger noise levels

than expected from the performance of neighboring channels, an effect caused by a low level interference from an internal oscillator. This excess noise remains in the delivered instrument, but is at a sufficiently low level that performance objectives are met. Due to the lengthy data sets averaged in the Blue Sky data presented below, the excess noise in this channel is not readily apparent.

An additional 'feature' of these data is that the least significant byte of the 16-bit data word for channel 13 of Band 9 was forced to zero by the spacecraft interface simulator (part of the IGSE). Once again, this appears to have had no deleterious effect on the final data set, and this debug-related feature of the IGSE has since been corrected.

Finally, it should be noted that the *differences* between the Limb port minus Space port radiances spectra for all of the data sets presented below are very small and consistent, indicating the lack of any obvious GHz antenna scan angle dependencies. The small magnitude of the observed differences is all the more remarkable given the substantial variations in atmospheric opacity brought about by the varying Santa Ana wind conditions during the course of the measurements, and gives us high confidence in the performance of the MLS GHz optical system.

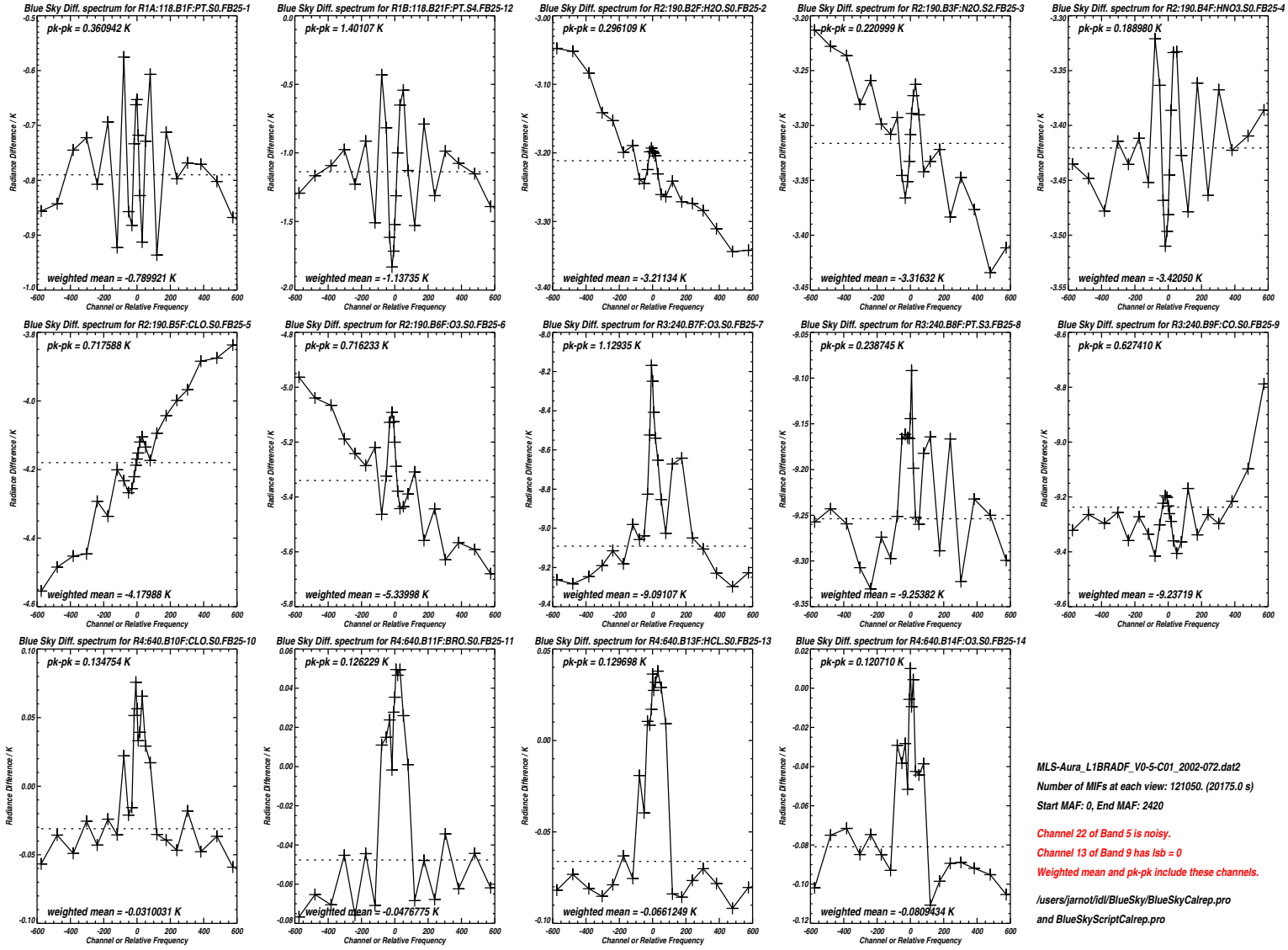

Figure B.139: Plots of Blue Sky test Limb port minus Space port radiance differences for the GHz filter spectrometer bands. These data were taken observing the sky near zenith for both port views, and with the antenna in its 'short strut' position. These data encompass the entire data set for this measurement configuration. See text for further details.

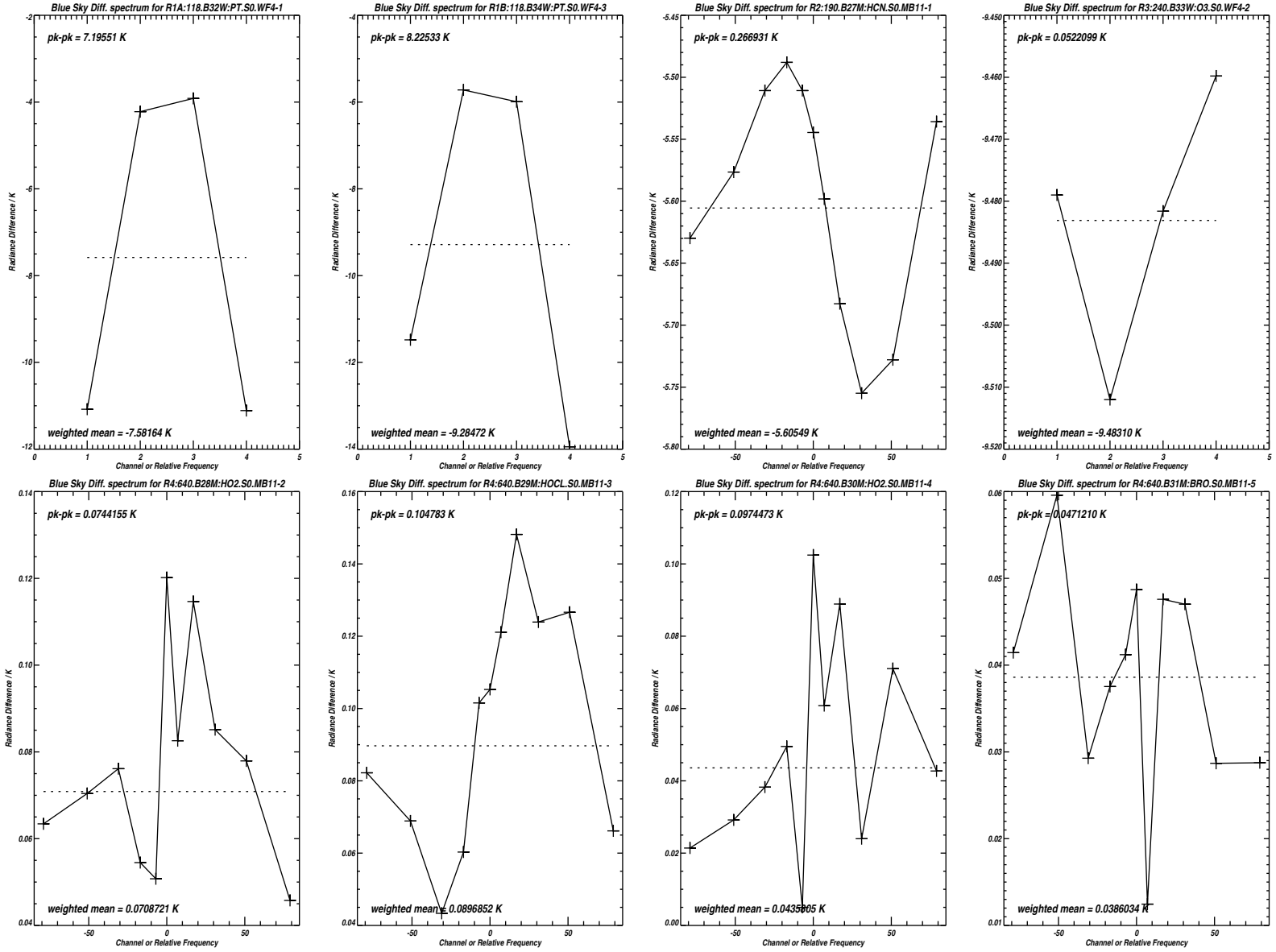

Figure B.140: Plots of Blue Sky test Limb port minus Space port radiance differences for the GHz filter spectrometer bands not included in Figure B.139.

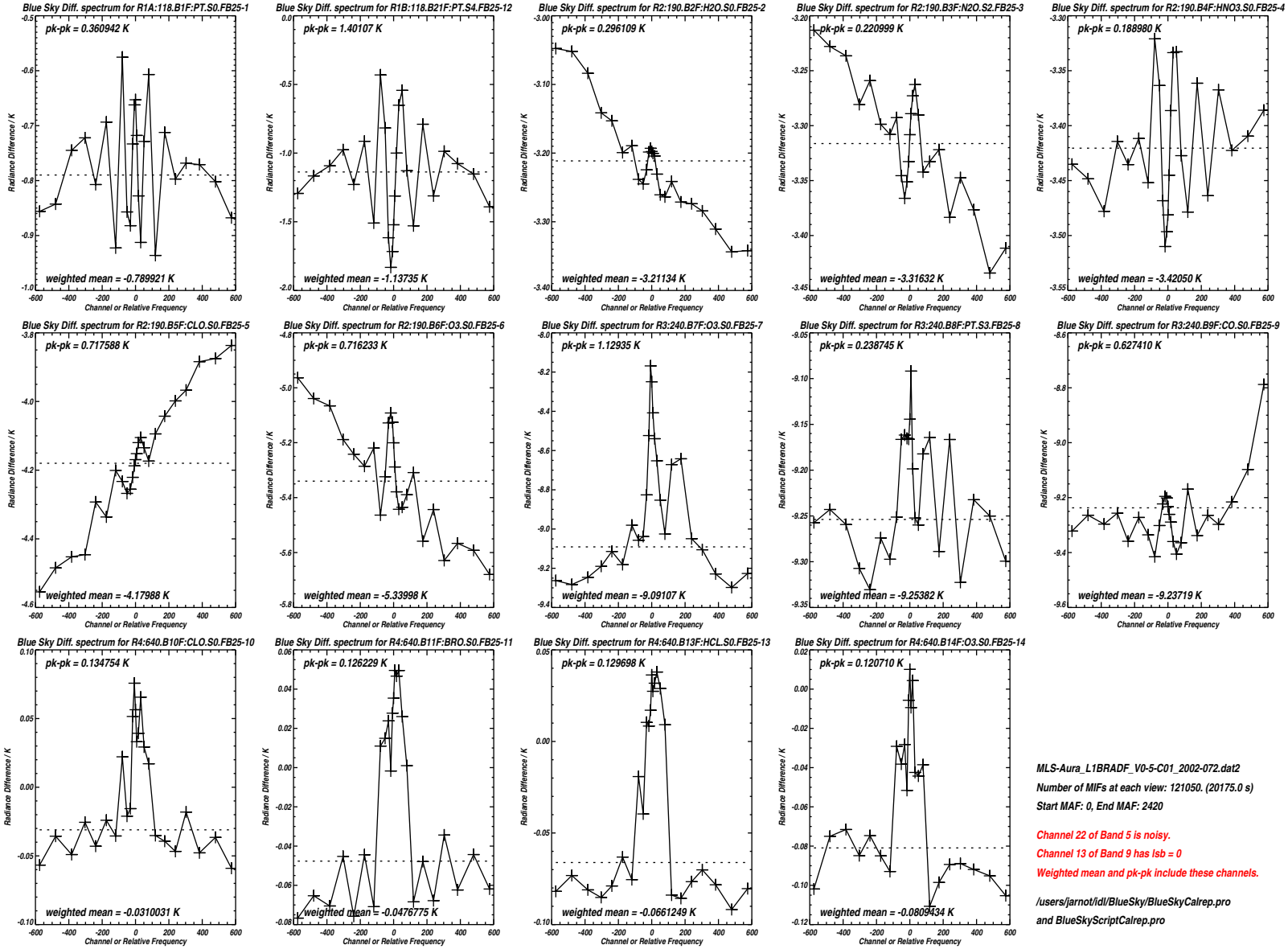

Figure B.141: Plots of Blue Sky test Limb port minus Space port radiance differences for the GHz filter spectrometer bands. These data were taken observing the sky near zenith for both port views, and with the antenna in its 'short strut' position. These data encompass a subset of the data included in the previous two figures. See text for further details.

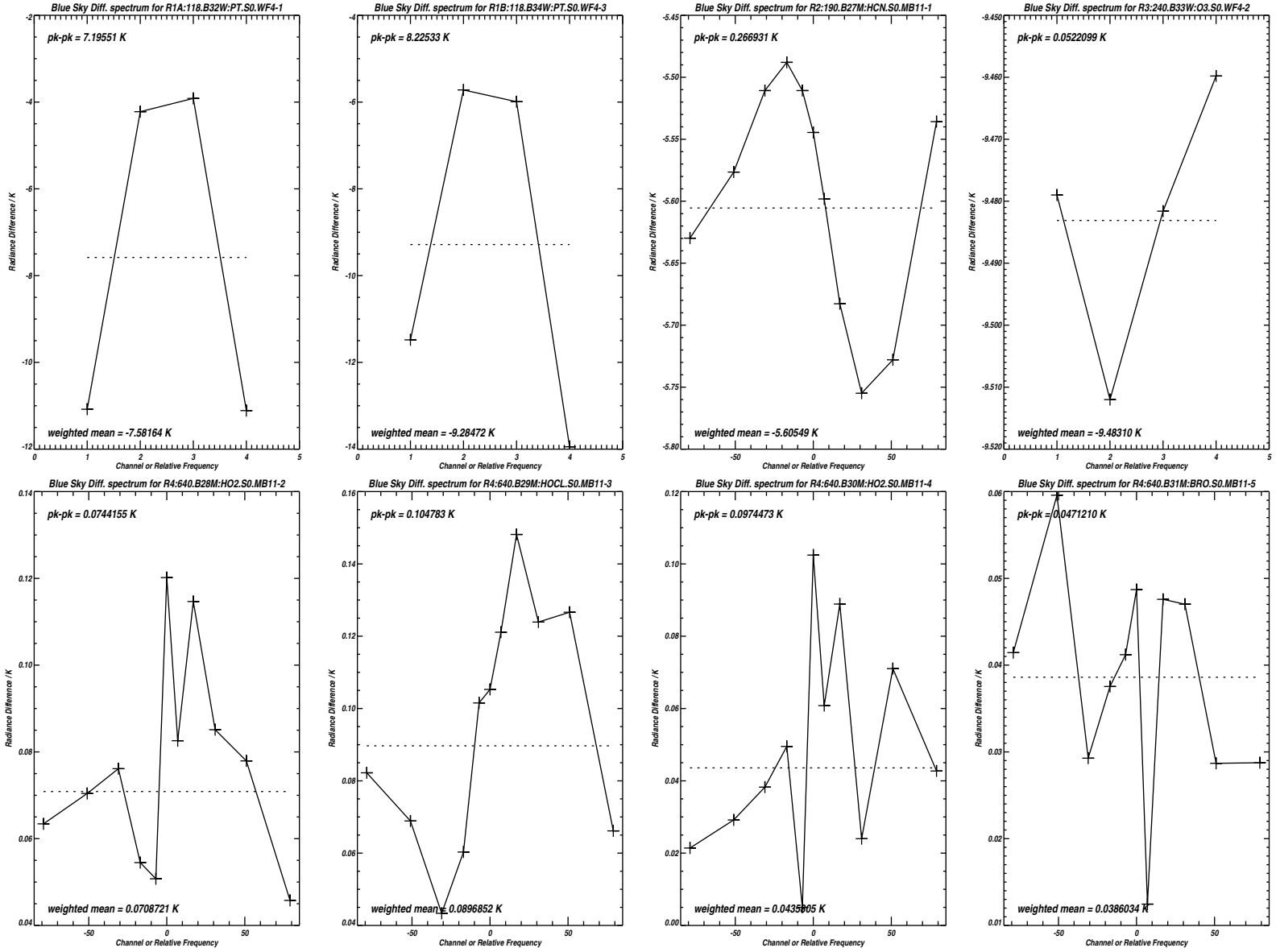

Figure B.142: Plots of Blue Sky test Limb port minus Space port radiance differences for the GHz filter spectrometer bands not included in Figure B.141.

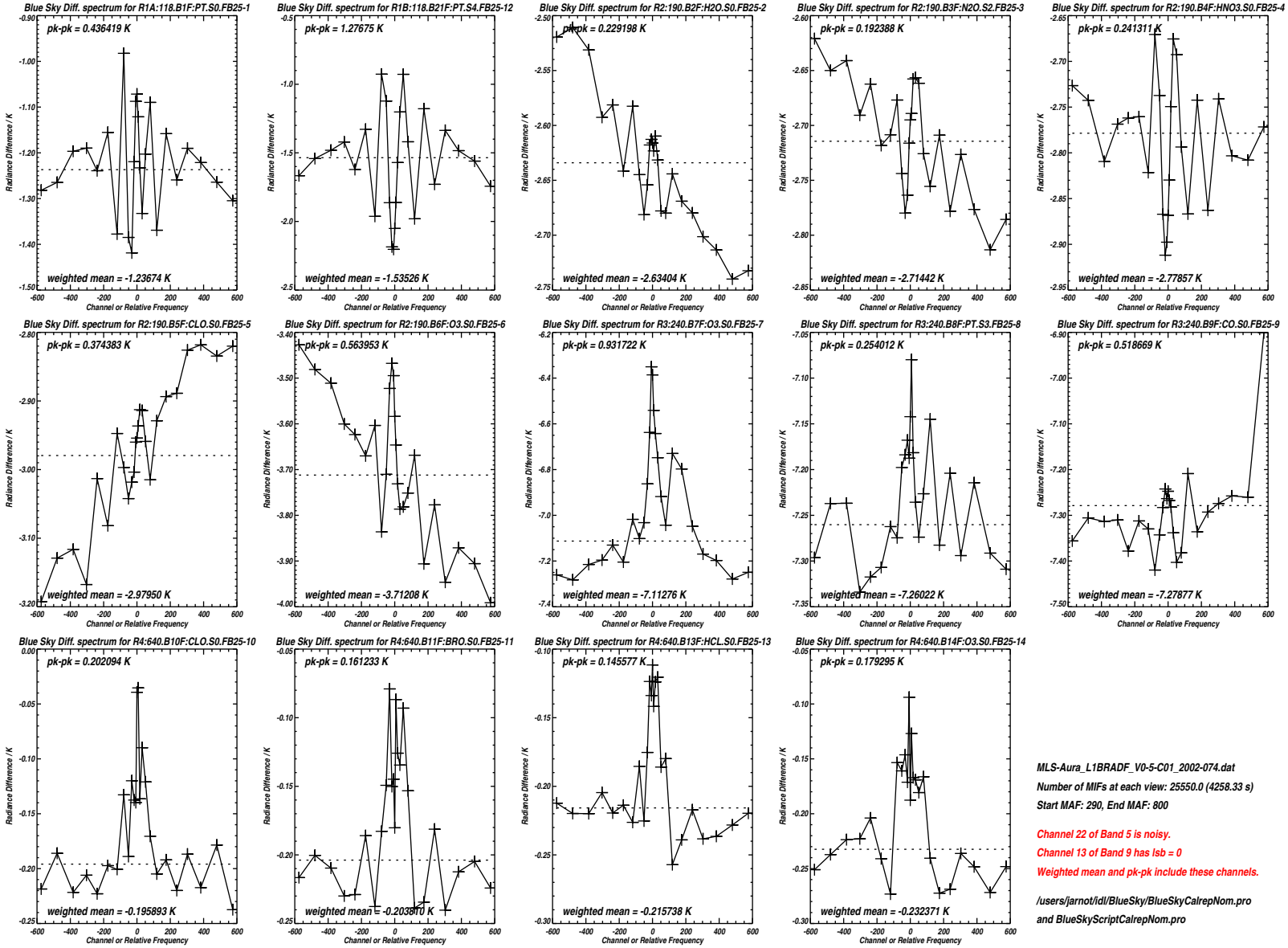

Figure B.143: Plots of Blue Sky test Limb port minus Space port radiance differences for the GHz filter spectrometer bands. These data were taken observing the sky near zenith for both port views, and with the antenna in its 'nominal' position. See text for further details.

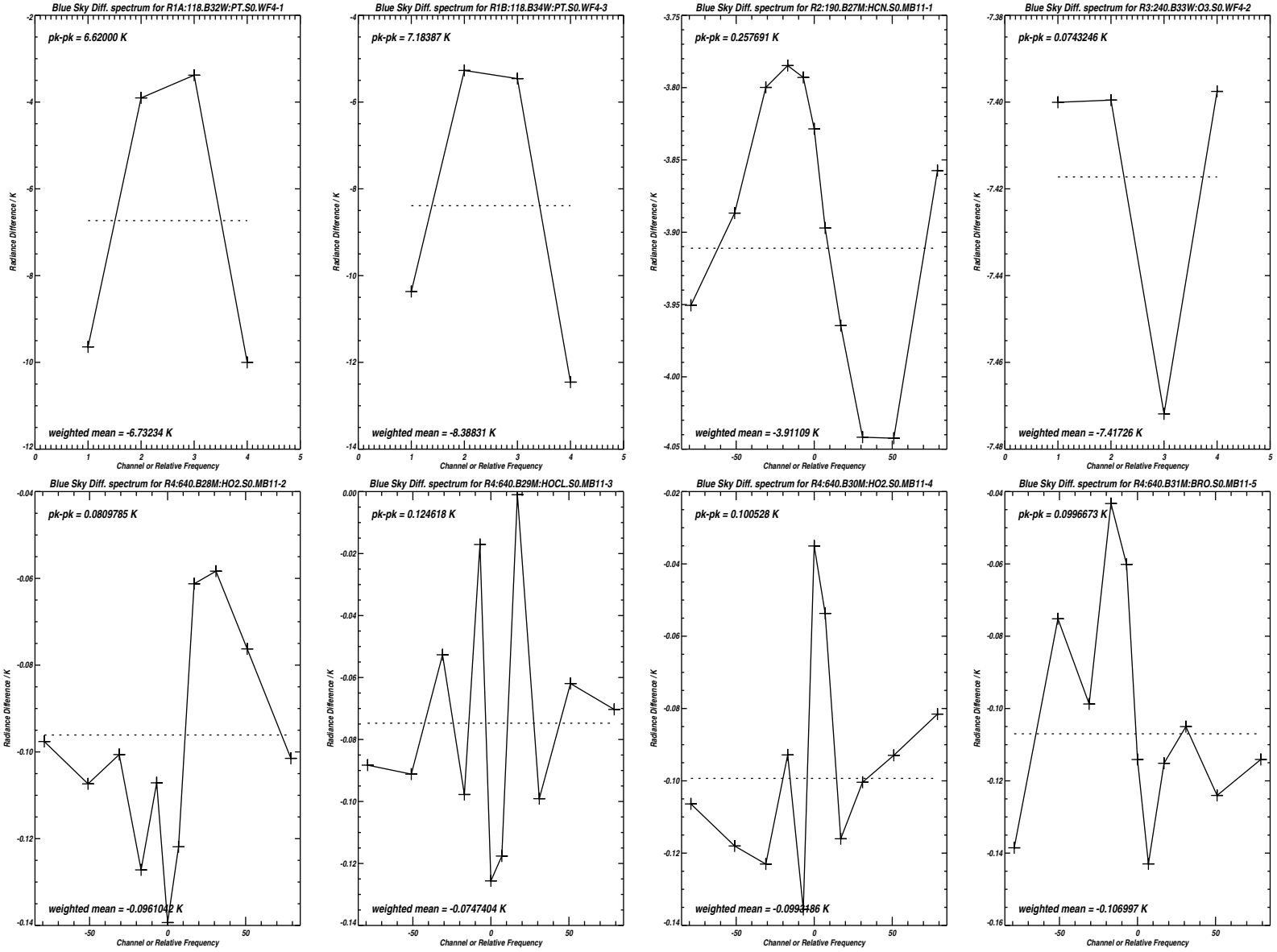

Figure B.144: Plots of Blue Sky test Limb port minus Space port radiance differences for the GHz filter spectrometer bands not included in Figure B.143.

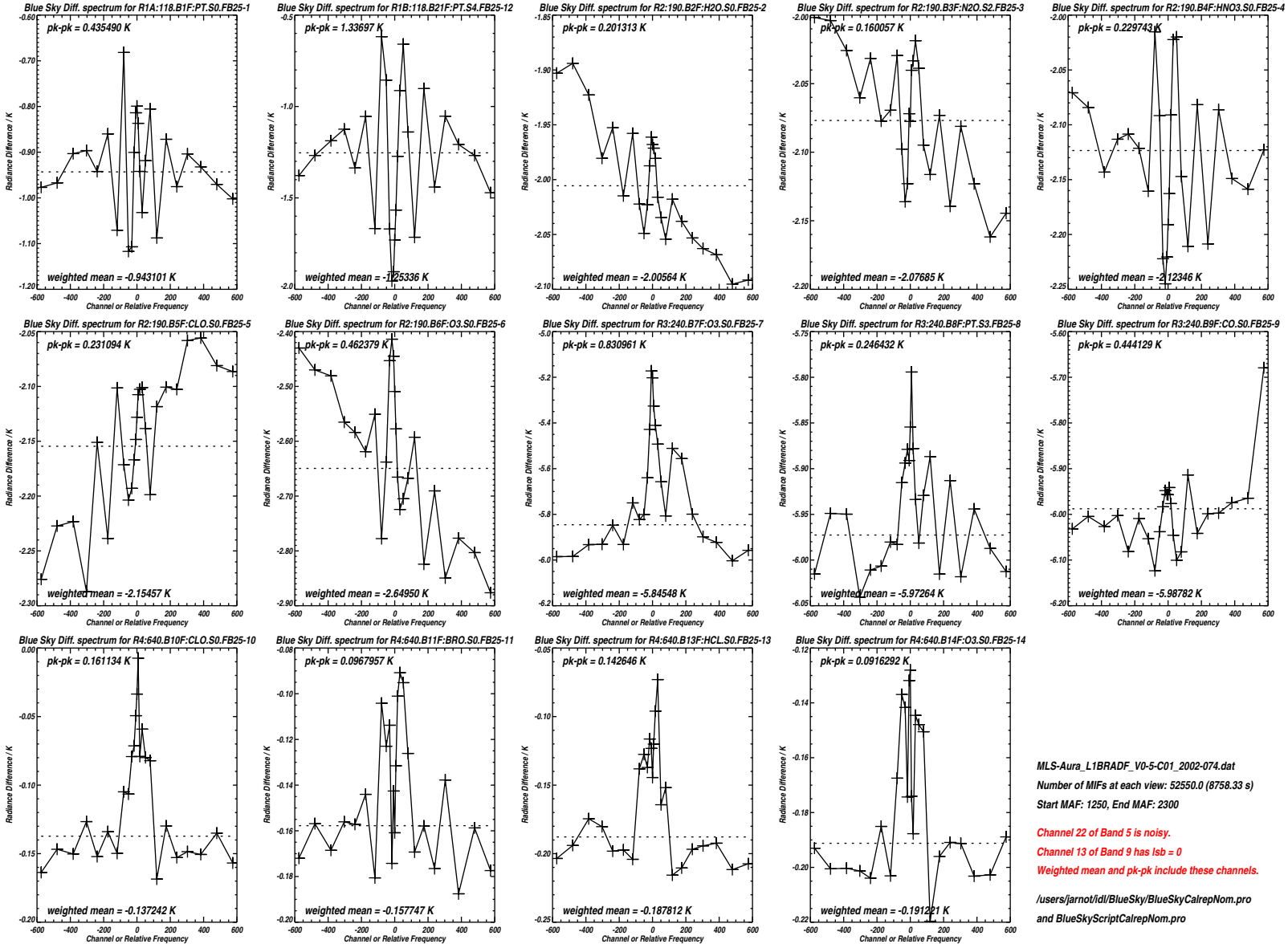

Figure B.145: Plots of Blue Sky test Limb port minus Space port radiance differences for the GHz filter spectrometer bands for a different time period than in the previous two plots. See text for further details.

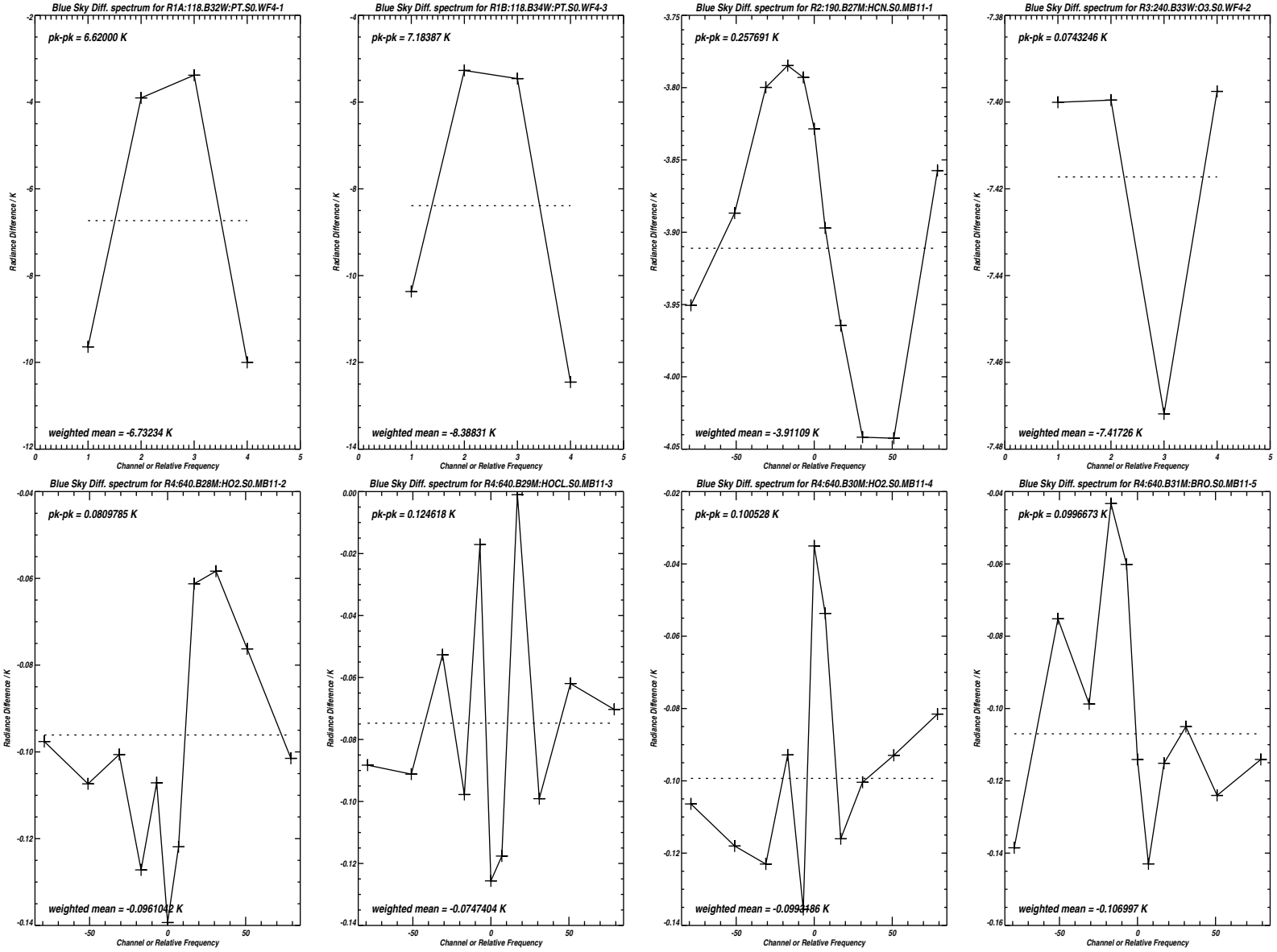

Figure B.146: Plots of Blue Sky test Limb port minus Space port radiance differences for the GHz filter spectrometer bands not included in Figure B.145.

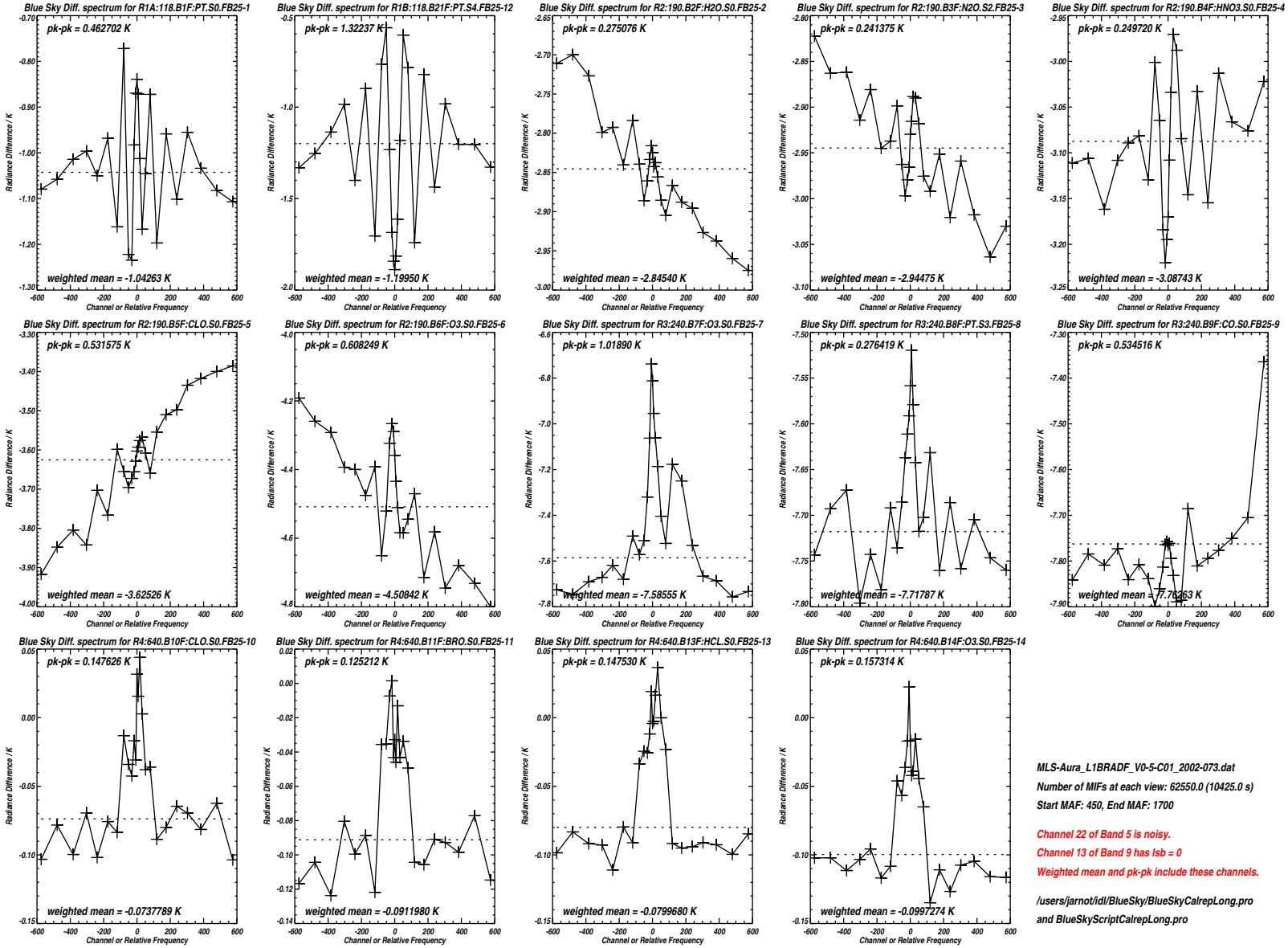

Figure B.147: Plots of Blue Sky test Limb port minus Space port radiance differences for the GHz filter spectrometer bands. These data were taken observing the sky near zenith for both port views, and with the antenna in its 'long strut' position. See text for further details.

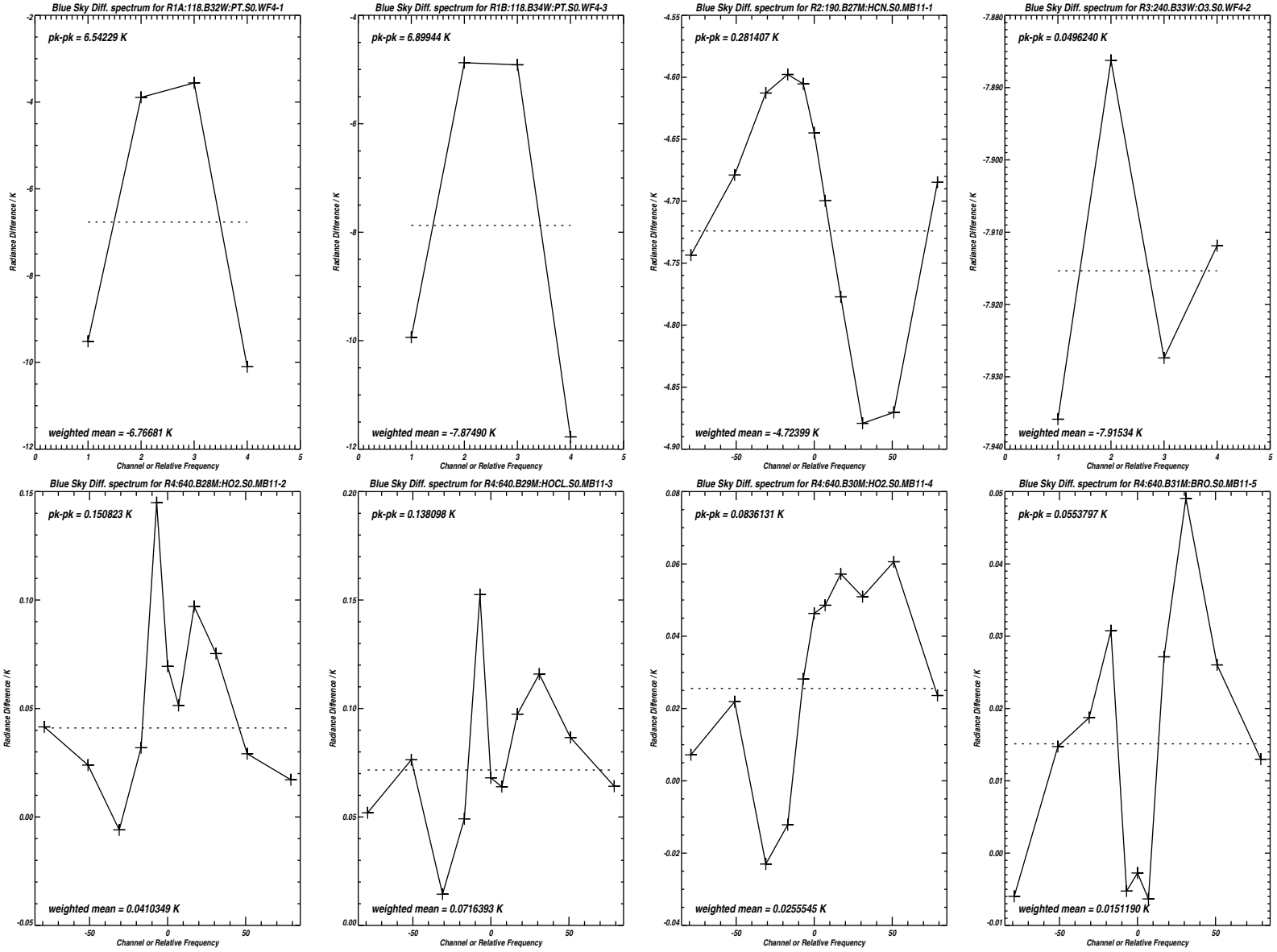

Figure B.148: Plots of Blue Sky test Limb port minus Space port radiance differences for the GHz filter spectrometer bands not included in Figure B.147.

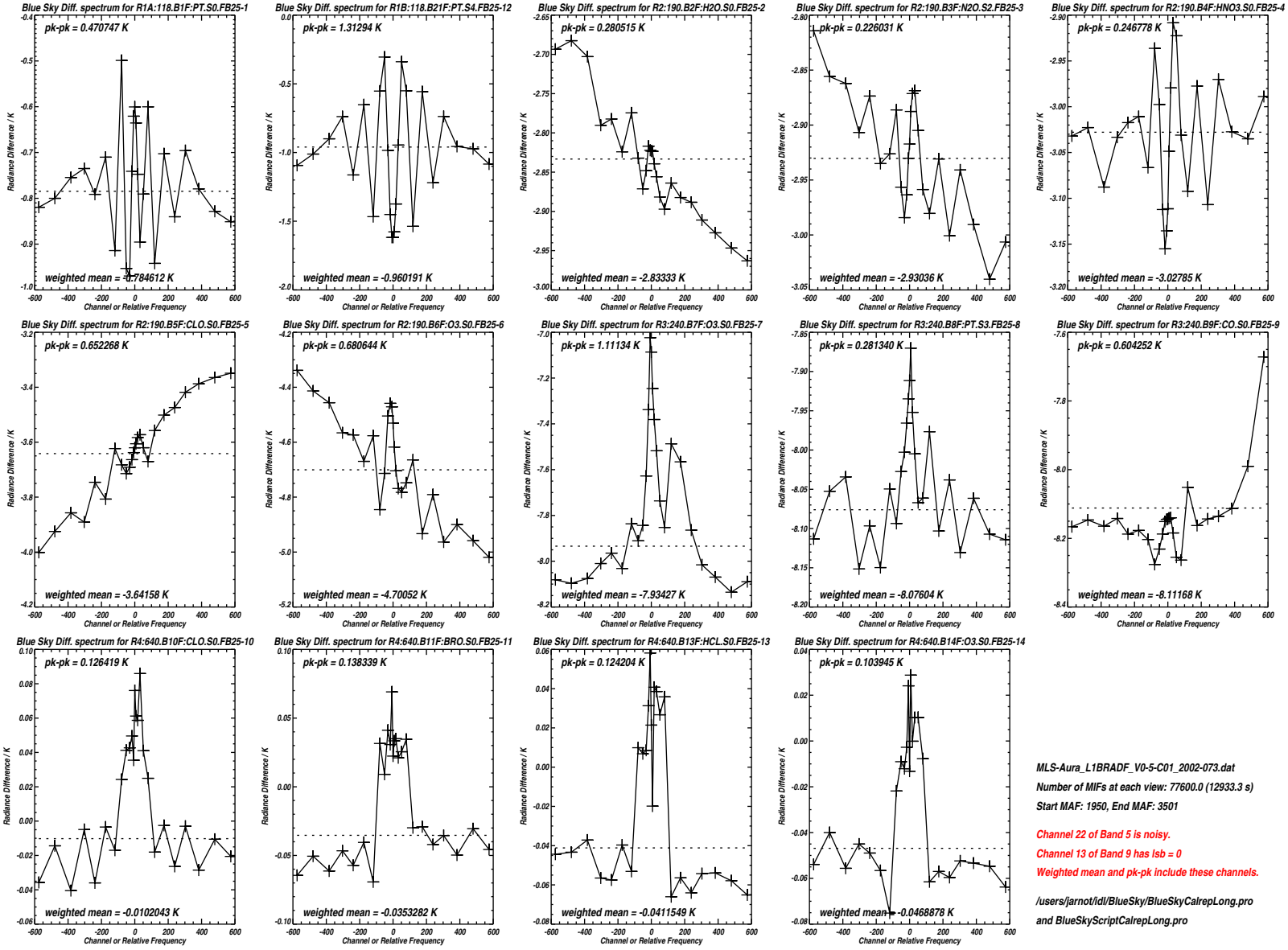

Figure B.149: Plots of Blue Sky test Limb port minus Space port radiance differences for the GHz filter spectrometer bands for a different time period than in the previous two plots. See text for further details.

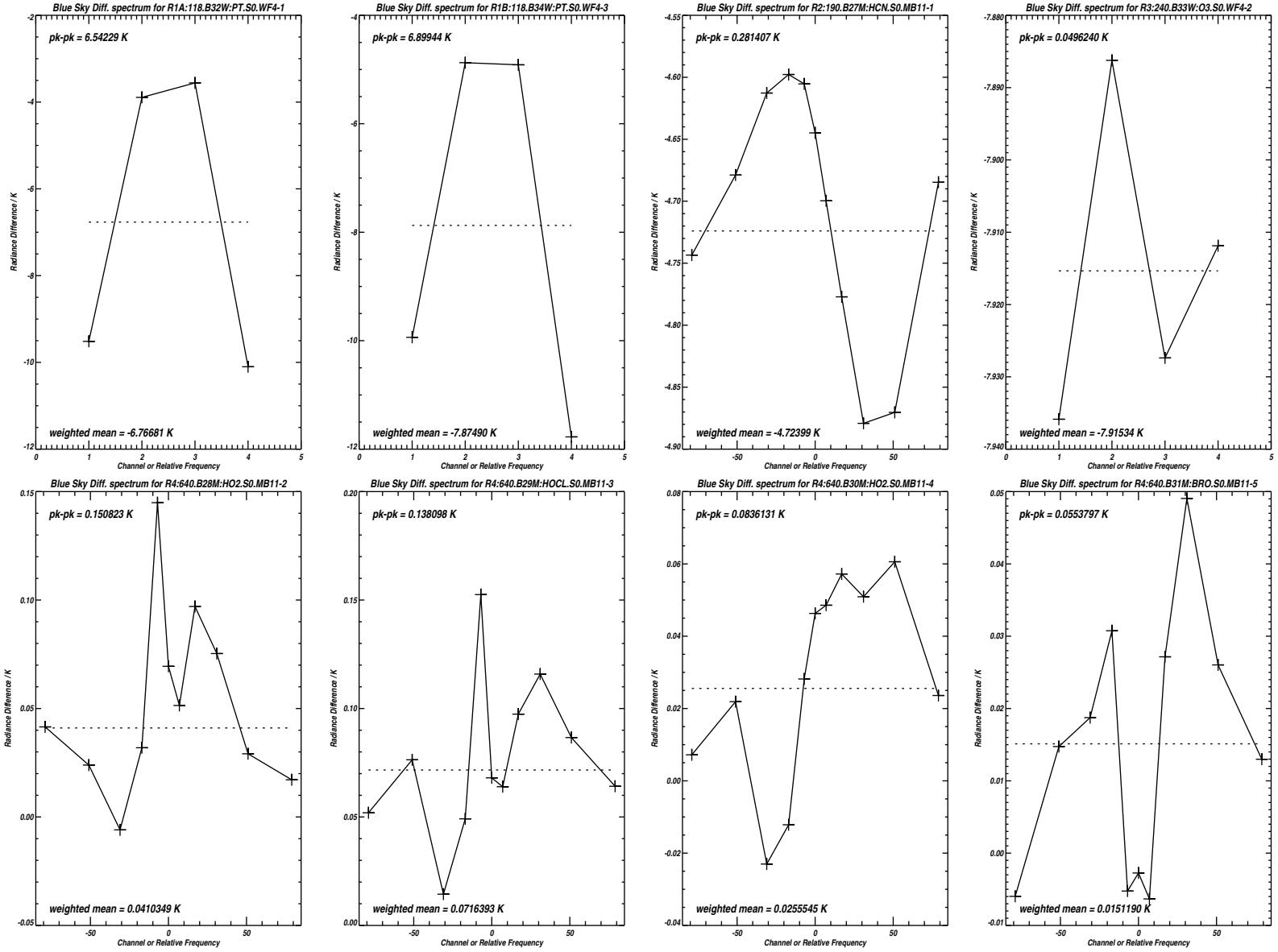

Figure B.150: Plots of Blue Sky test Limb port minus Space port radiance differences for the GHz filter spectrometer bands not included in Figure B.149.

Appendix C

Relative Sideband Calibration

Details of the measurement technique, and overall results, are presented in Chapter 3 of Volume 1. Below we present details of the data sets for each GHz band. A detailed description of the data analyses is provided in Volume 1. Refer to Volume 4 of this report for details of the changes to relative sideband response brought about by the R4 tripler changeout that took place after these calibrations were performed.

C.1 GHz Relative Sideband Data and Analysis Results

The relative sideband sweeps of the GHz bands encompassed several orders of the Fabry-Pérot for all bands. Analyses were performed on different individual orders in each band, as well as multiple orders, with nominally identical results. We thus chose to select single, well differentiated orders for definitive sideband analyses, and these data are presented in the following pages. The data for Bands 2 through 9 (and Band 33) were taken during the same measurement run, and another run (with finer grids) provided the data for Bands 10 through 14. These results are discussed further in Chapter 3 of Volume 1.

The data for all GHz bands are presented in a common format below, with two plots on facing pages (Figures C.1 to C.27). The first plot shows the data (black crosses) and fit from the retrieval model (green line) for each channel in the band. The differences between measurement and fit (magnified by a factor of 10) are indicated by the blue crosses. The horizontal green dashed line indicates the radiance level below which measurements are excluded from the retrieval, and the horizontal red dashed line is at 0 K as a visual aid to observing systematic offsets in the radiance residuals.

Band 33 (R3 Wide Filter) data are shown in Figure C.27 without the accompanying sideband fraction plot. The retrieved relative sideband response of each Wide Filter channel is printed in the panel for that channel.

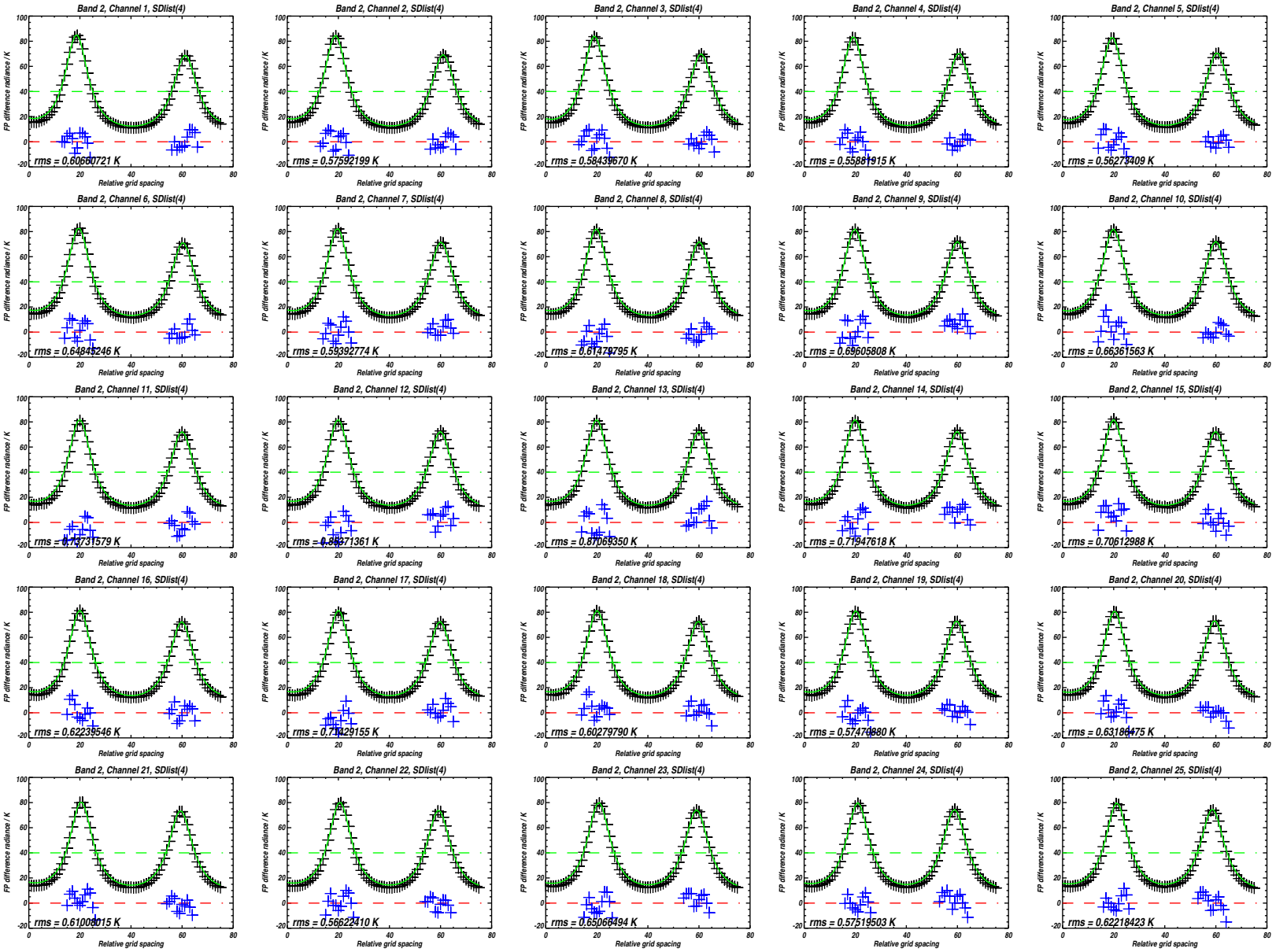

Figure C.1: Fabry-Pérot data for Band 2 (black crosses) and theoretical prediction (green line) for the grids spacings chosen for the fit. The blue crosses are the residual to the fit (difference between measurements and model) multiplied by a factor of 10.

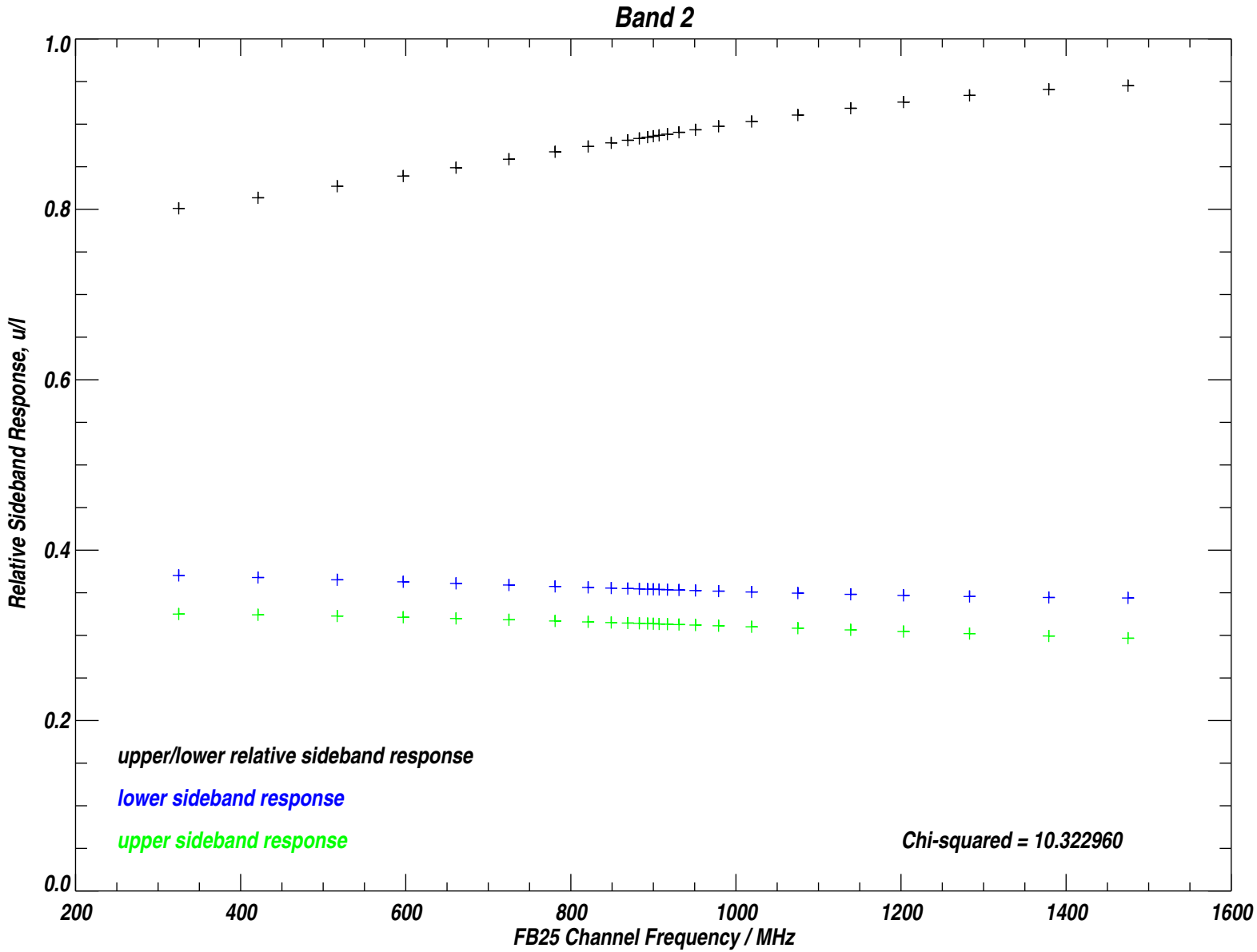

Figure C.2: Results of the fit to the data shown in the facing page. The lower and upper relative sideband responses are shown as sideband fractions (blue and green crosses), and the ratio of the response in each sideband is indicated by the black crosses (upper/lower sideband response). See text for further details.

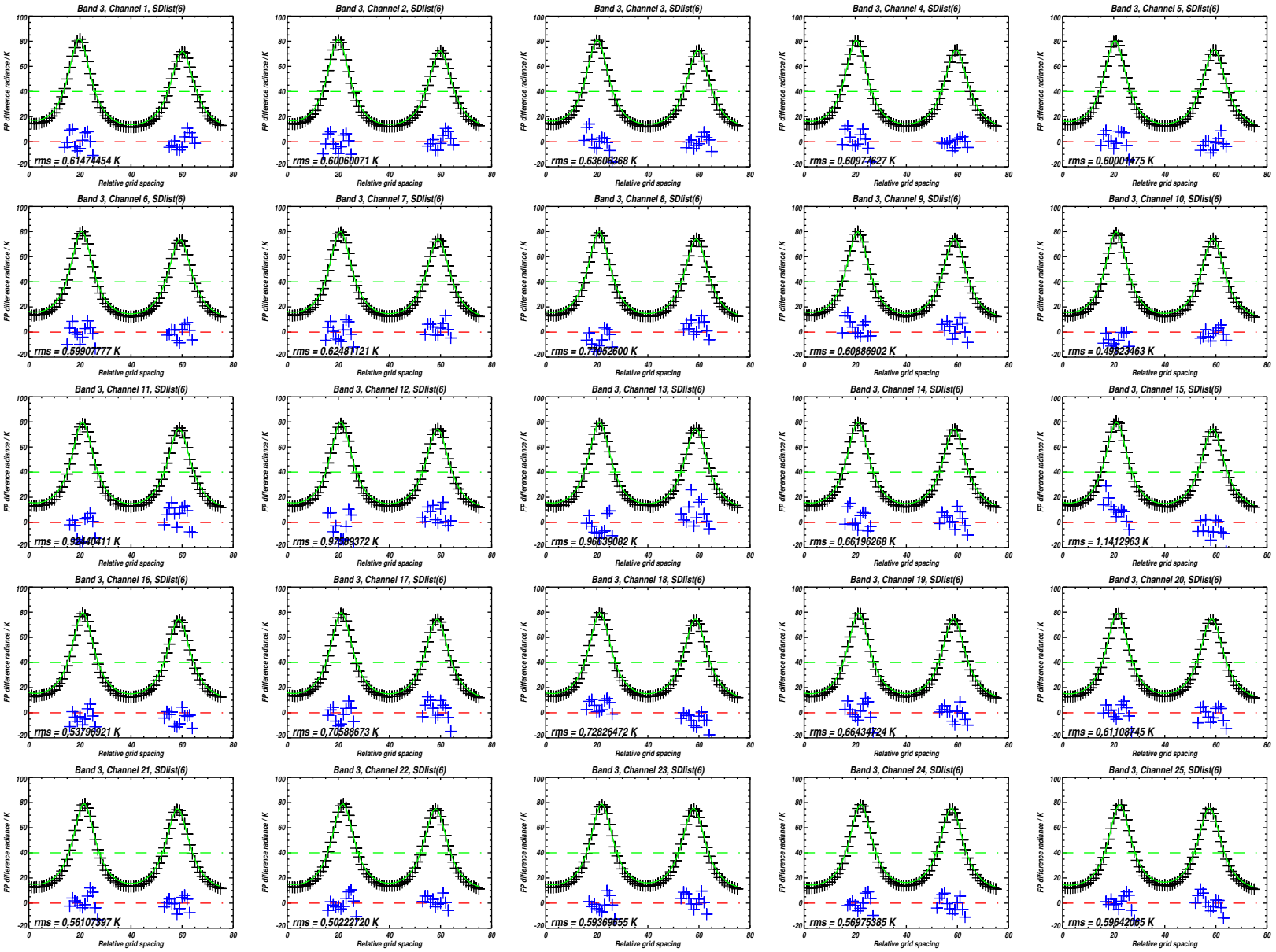

Figure C.3: Fabry-Pérot data for Band 3 (black crosses) and theoretical prediction (green line) for the grids spacings chosen for the fit. The blue crosses are the residual to the fit (difference between measurements and model) multiplied by a factor of 10.

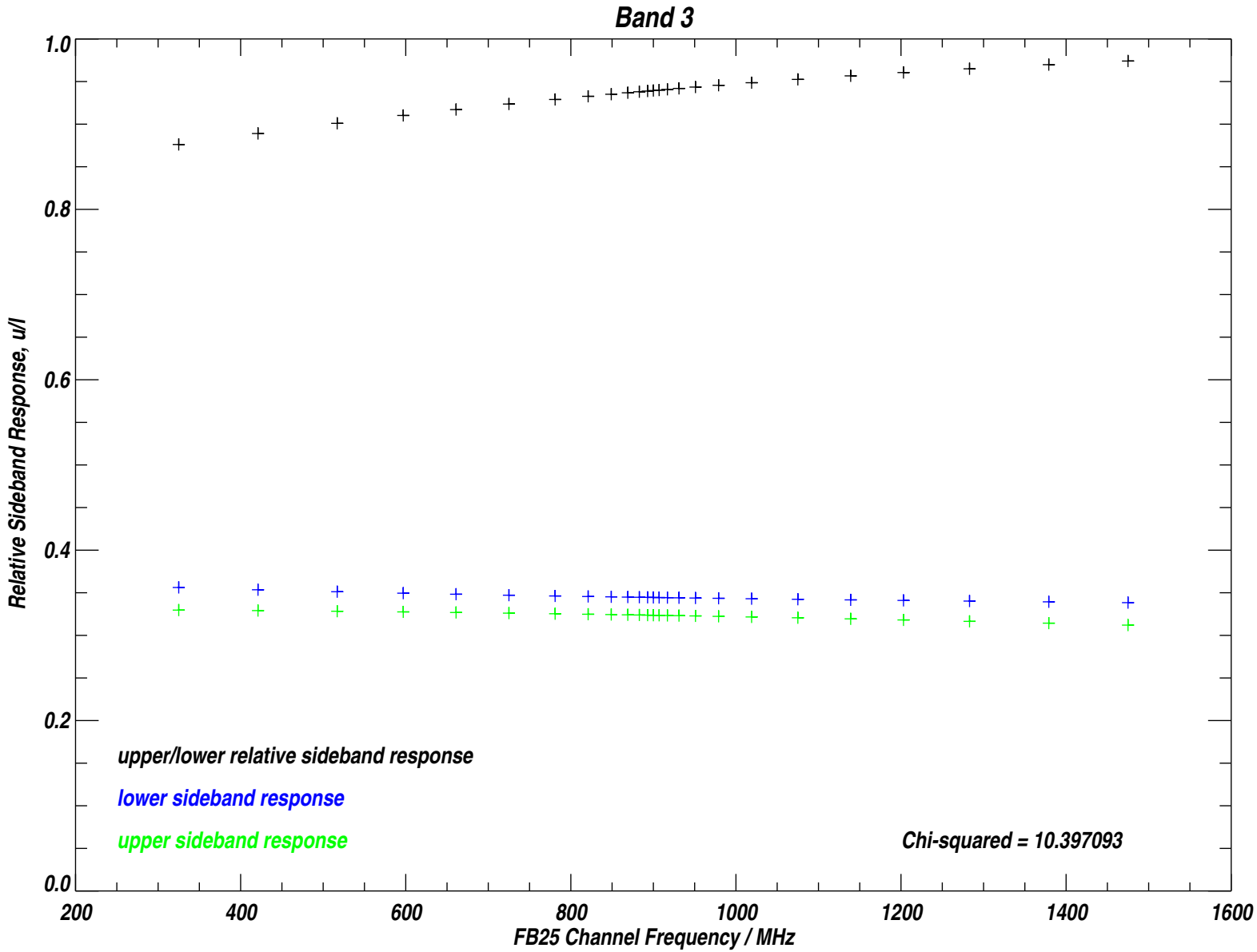

Figure C.4: Results of the fit to the data shown in the facing page. The lower and upper relative sideband responses are shown as sideband fractions (blue and green crosses), and the ratio of the response in each sideband is indicated by the black crosses (upper/lower sideband response). See text for further details.

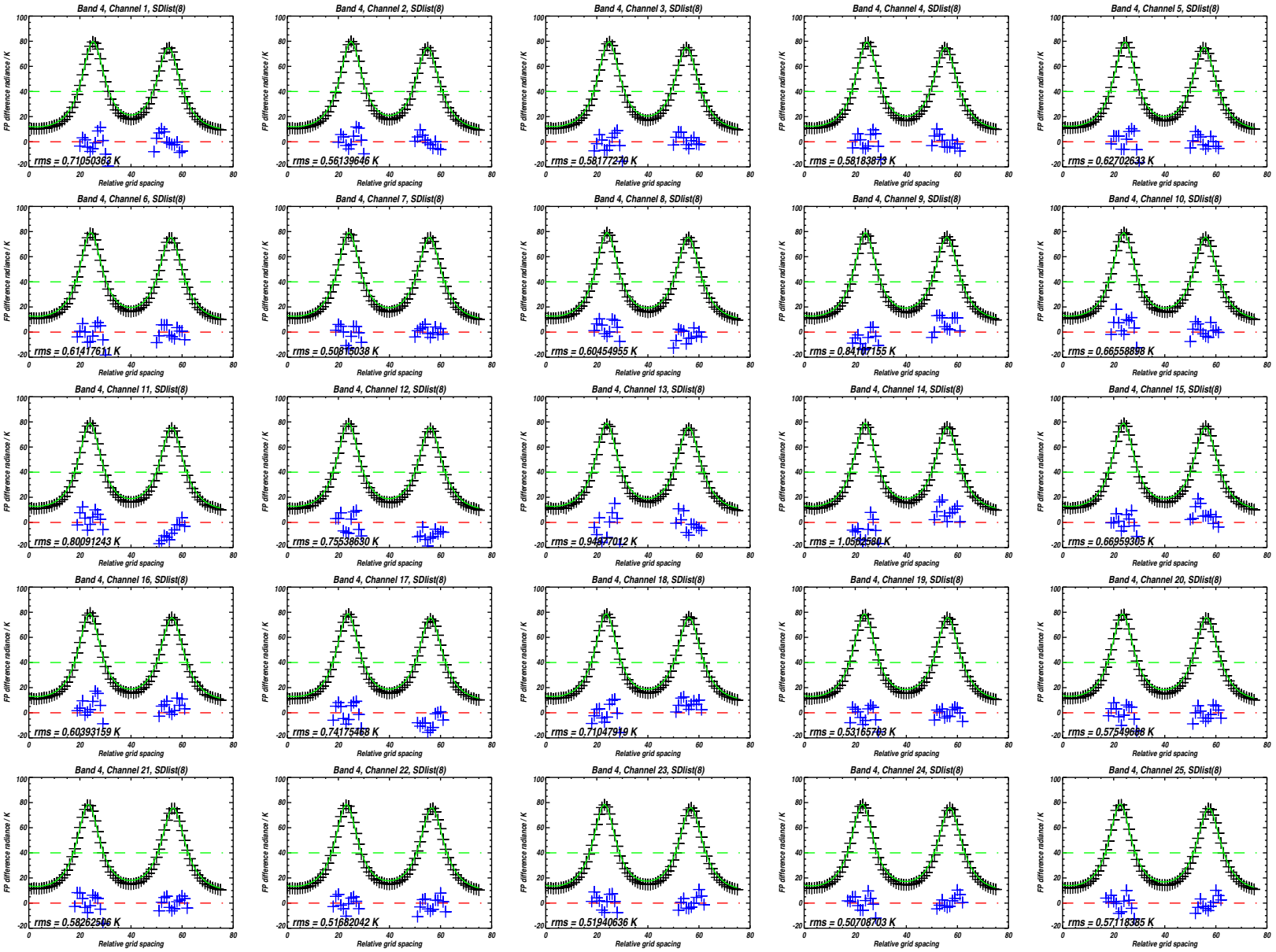

Figure C.5: Fabry-Pérot data for Band 4 (black crosses) and theoretical prediction (green line) for the grids spacings chosen for the fit. The blue crosses are the residual to the fit (difference between measurements and model) multiplied by a factor of 10.

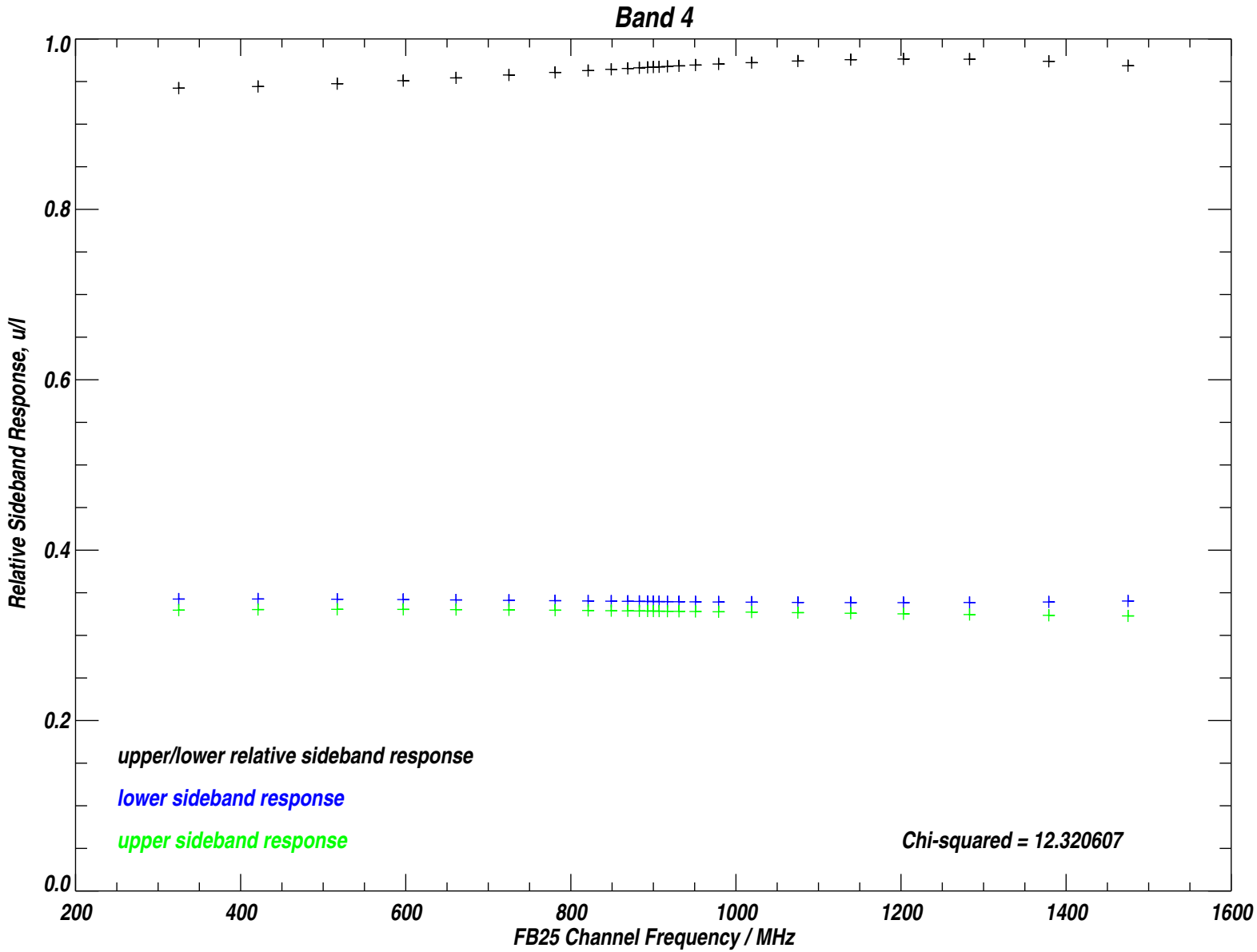

Figure C.6: Results of the fit to the data shown in the facing page. The lower and upper relative sideband responses are shown as sideband fractions (blue and green crosses), and the ratio of the response in each sideband is indicated by the black crosses (upper/lower sideband response). See text for further details.

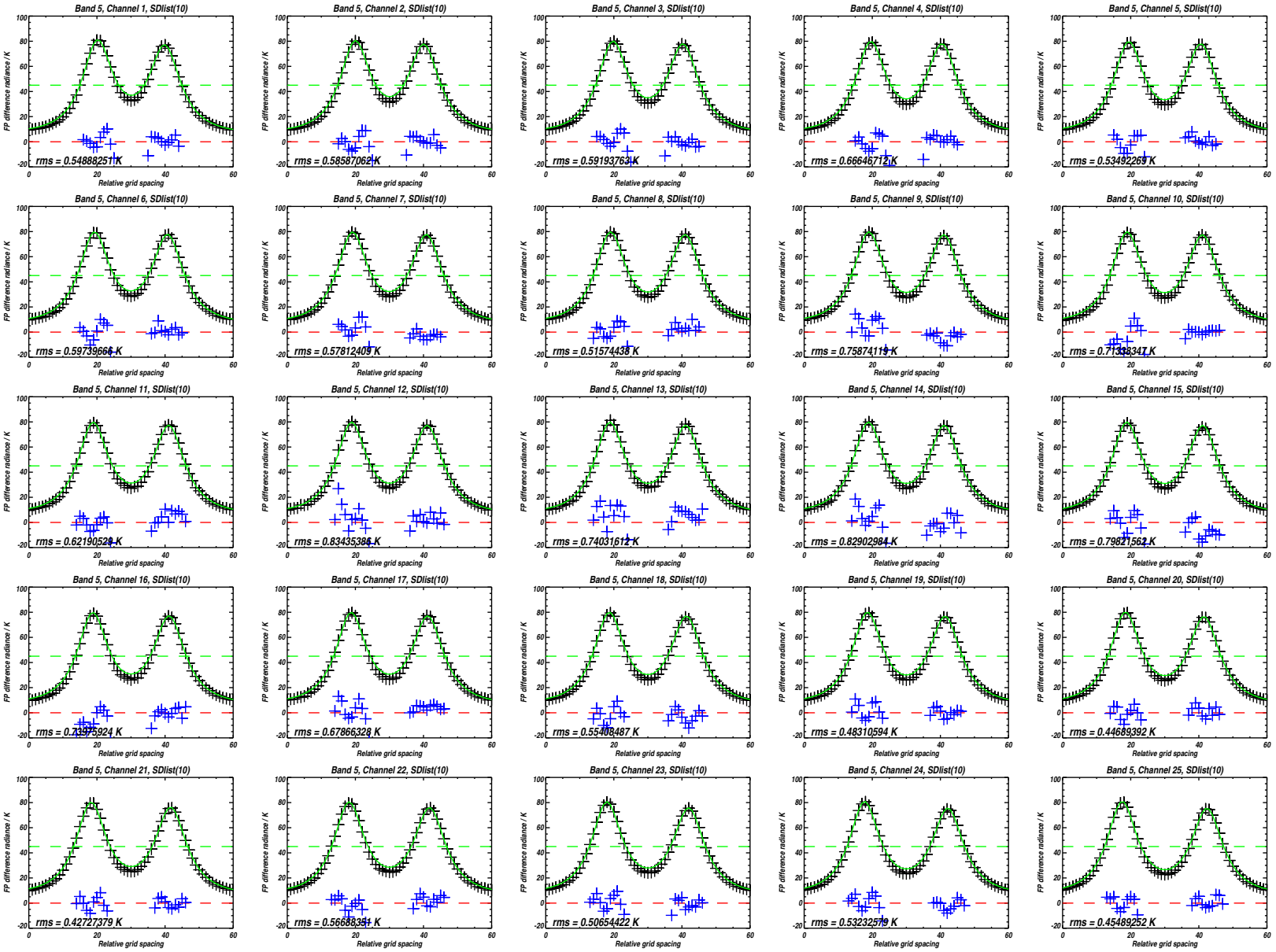

Figure C.7: Fabry-Pérot data for Band 5 (black crosses) and theoretical prediction (green line) for the grids spacings chosen for the fit. The blue crosses are the residual to the fit (difference between measurements and model) multiplied by a factor of 10.

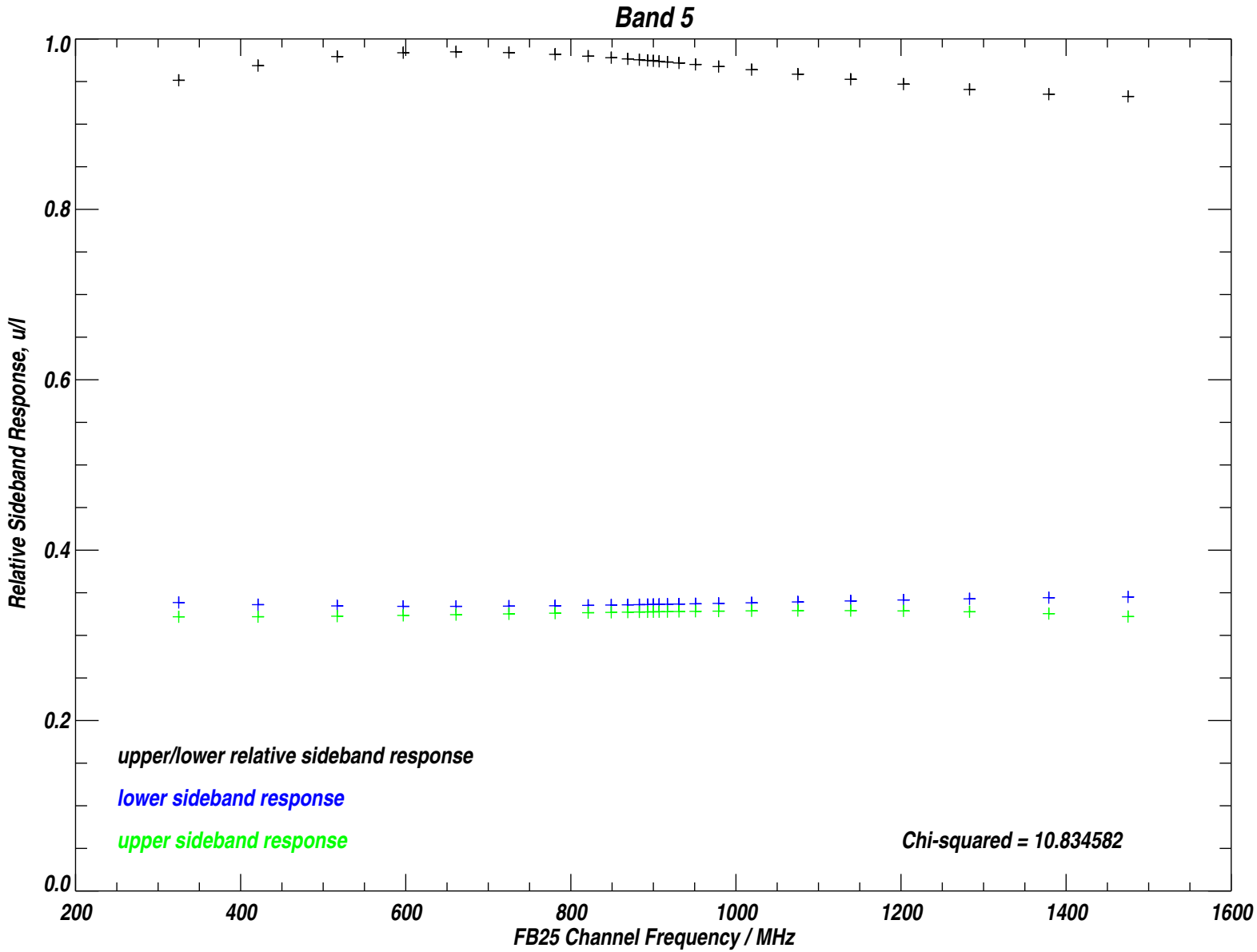

Figure C.8: Results of the fit to the data shown in the facing page. The lower and upper relative sideband responses are shown as sideband fractions (blue and green crosses), and the ratio of the response in each sideband is indicated by the black crosses (upper/lower sideband response). See text for further details.

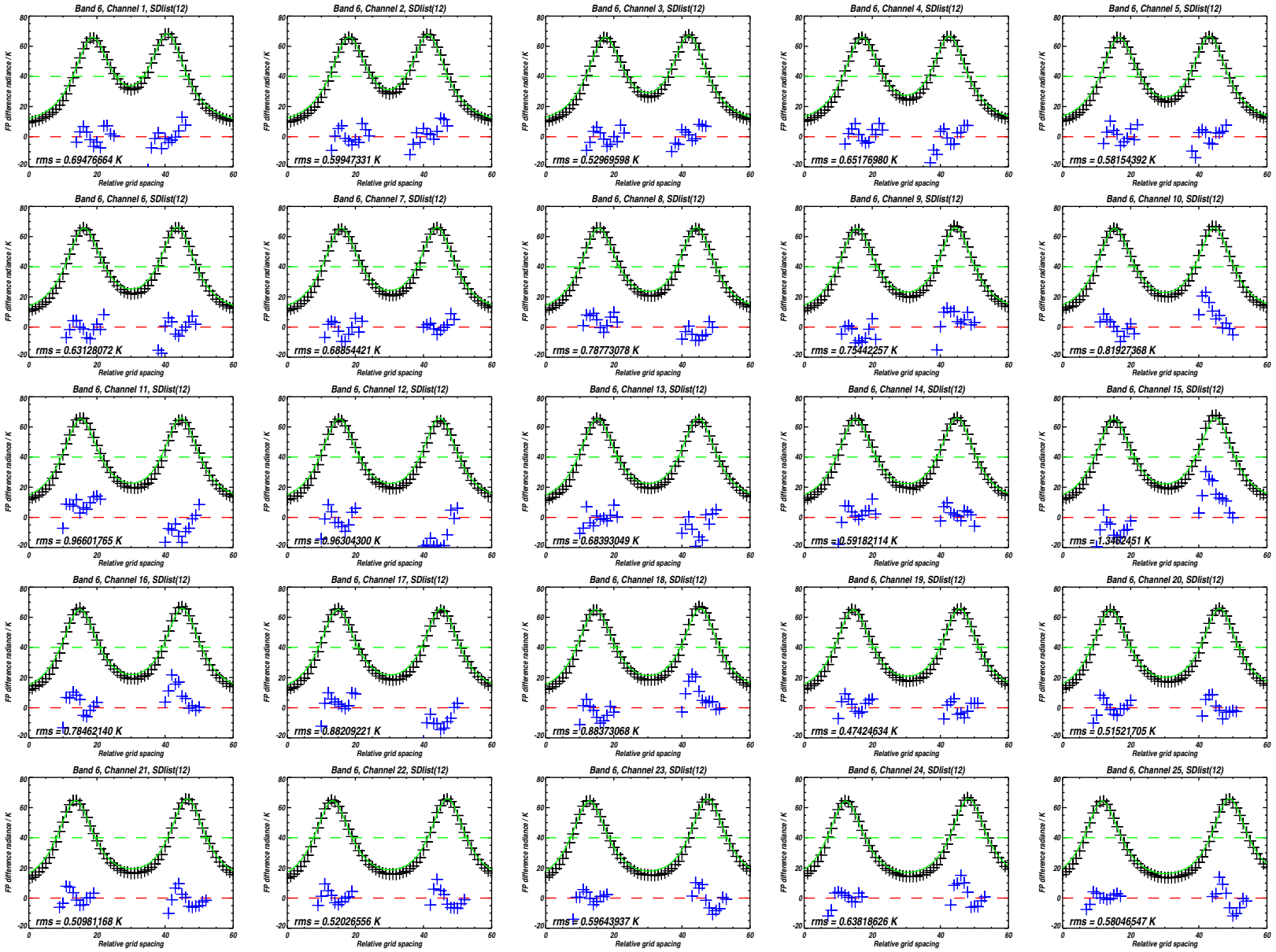

Figure C.9: Fabry-Pérot data for Band 6 (black crosses) and theoretical prediction (green line) for the grids spacings chosen for the fit. The blue crosses are the residual to the fit (difference between measurements and model) multiplied by a factor of 10.

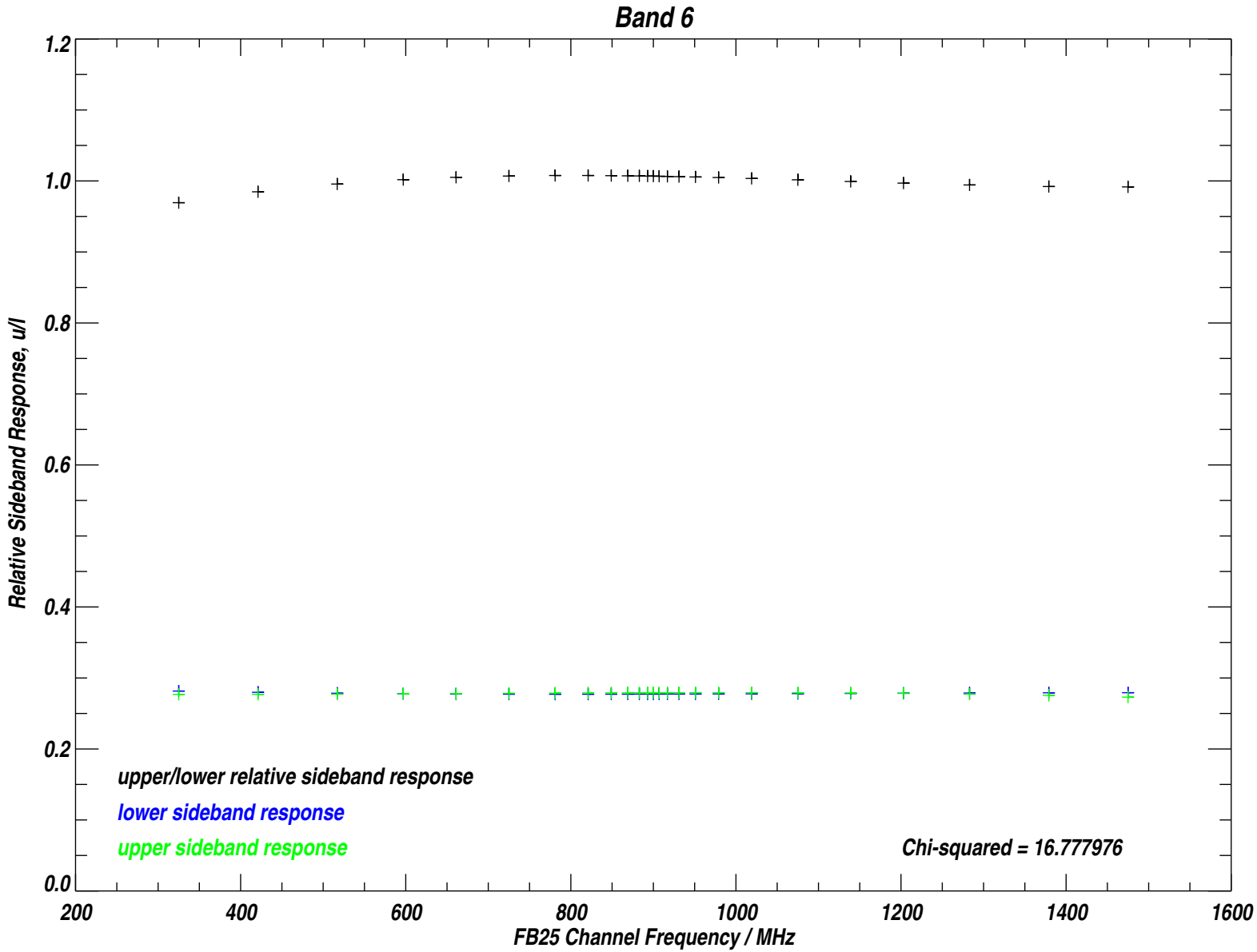

Figure C.10: Results of the fit to the data shown in the facing page. The lower and upper relative sideband responses are shown as sideband fractions (blue and green crosses), and the ratio of the response in each sideband is indicated by the black crosses (upper/lower sideband response). See text for further details.

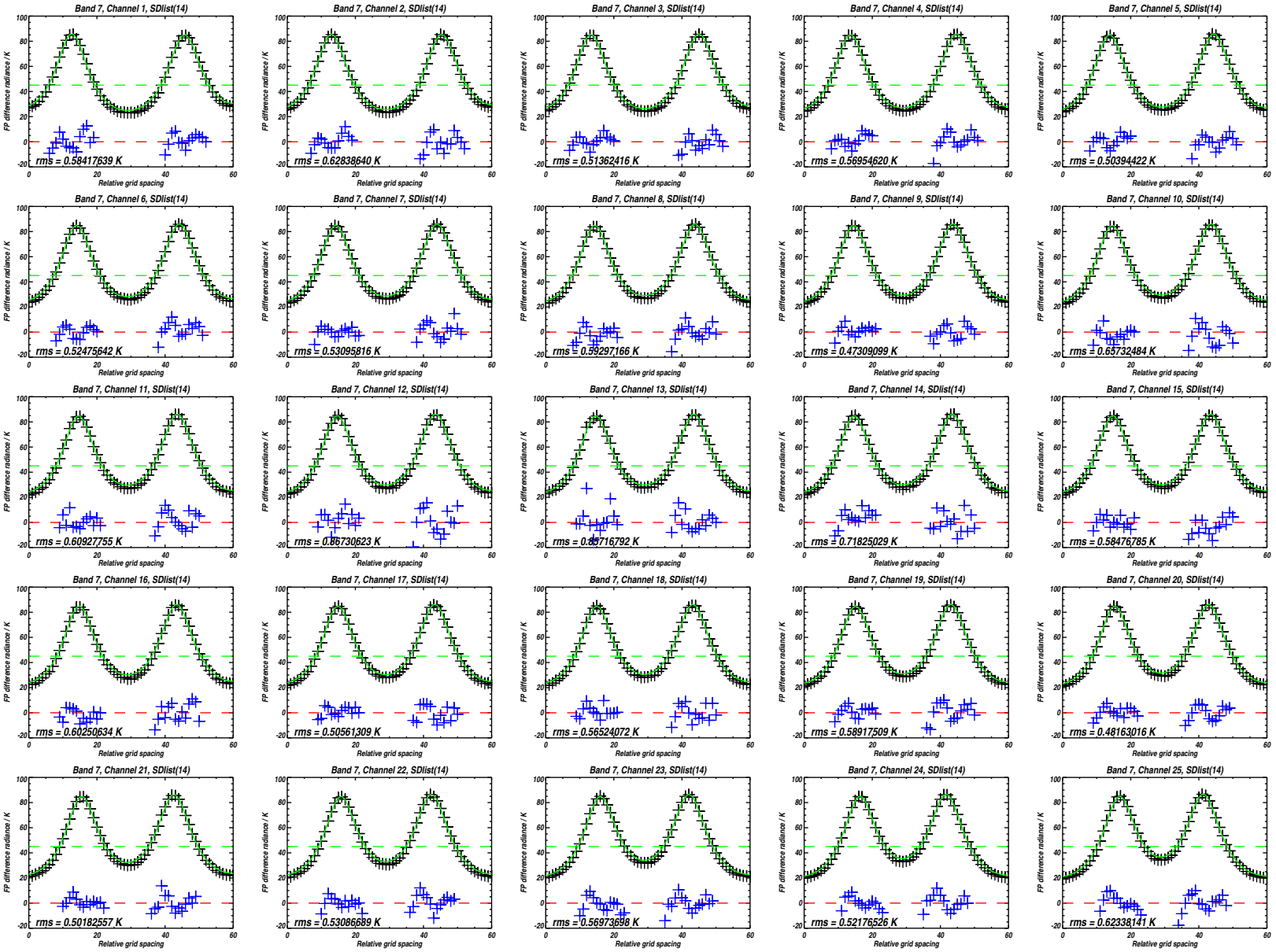

Figure C.11: Fabry-Pérot data for Band 7 (black crosses) and theoretical prediction (green line) for the grids spacings chosen for the fit. The blue crosses are the residual to the fit (difference between measurements and model) multiplied by a factor of 10.

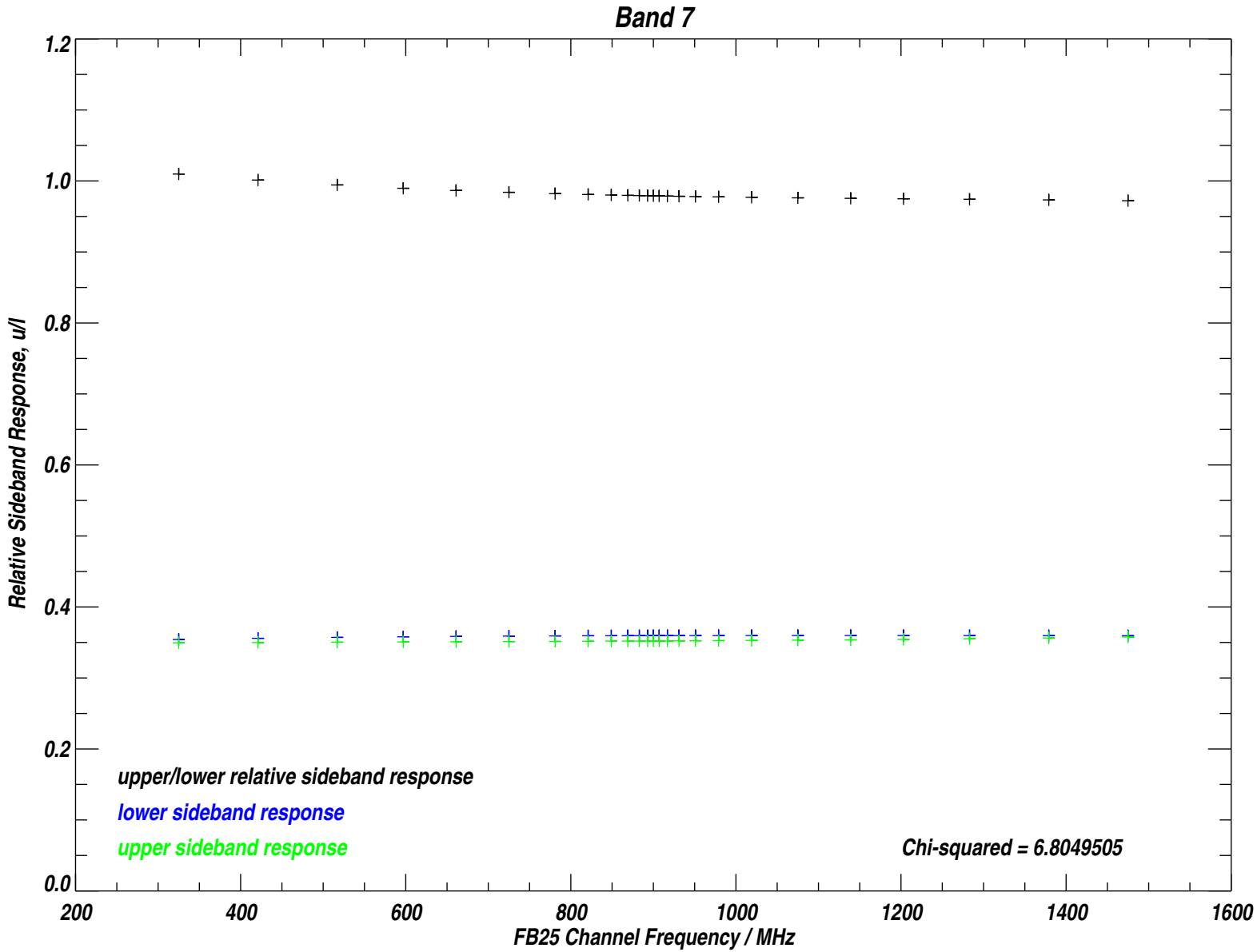

Figure C.12: Results of the fit to the data shown in the facing page. The lower and upper relative sideband responses are shown as sideband fractions (blue and green crosses), and the ratio of the response in each sideband is indicated by the black crosses (upper/lower sideband response). See text for further details.

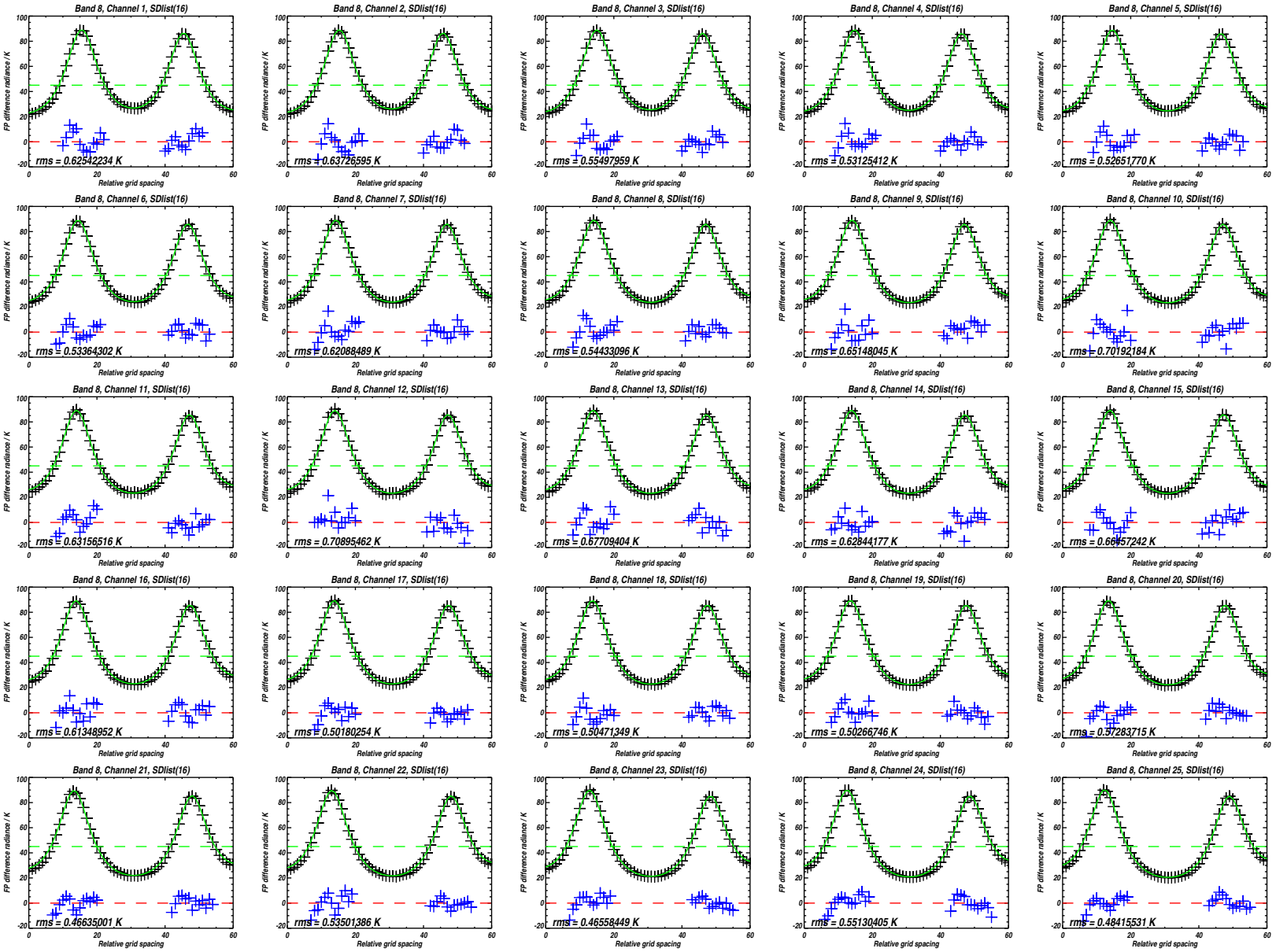

Figure C.13: Fabry-Pérot data for Band 8 (black crosses) and theoretical prediction (green line) for the grids spacings chosen for the fit. The blue crosses are the residual to the fit (difference between measurements and model) multiplied by a factor of 10.

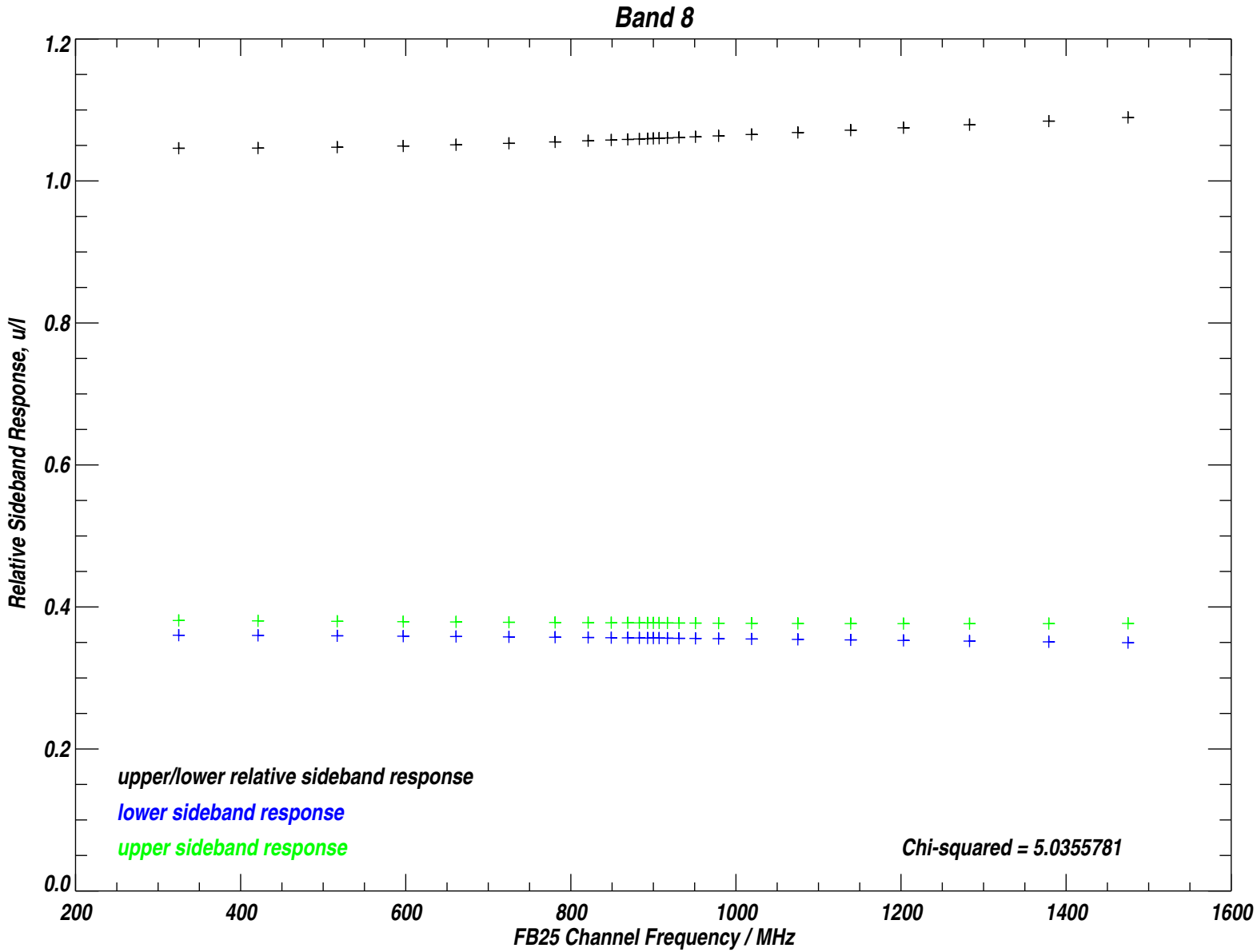

Figure C.14: Results of the fit to the data shown in the facing page. The lower and upper relative sideband responses are shown as sideband fractions (blue and green crosses), and the ratio of the response in each sideband is indicated by the black crosses (upper/lower sideband response). See text for further details.

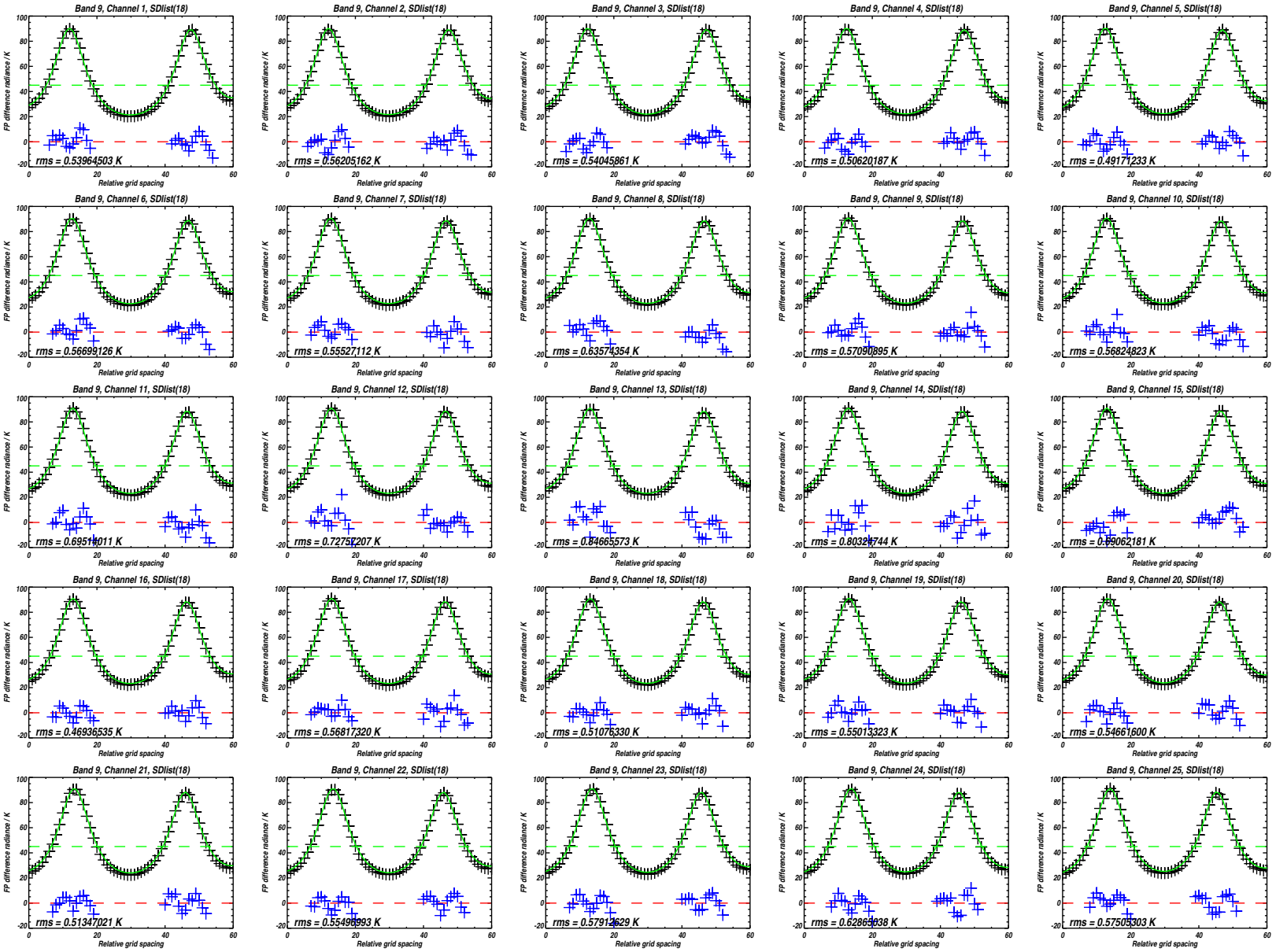

Figure C.15: Fabry-Pérot data for Band 9 (black crosses) and theoretical prediction (green line) for the grids spacings chosen for the fit. The blue crosses are the residual to the fit (difference between measurements and model) multiplied by a factor of 10.

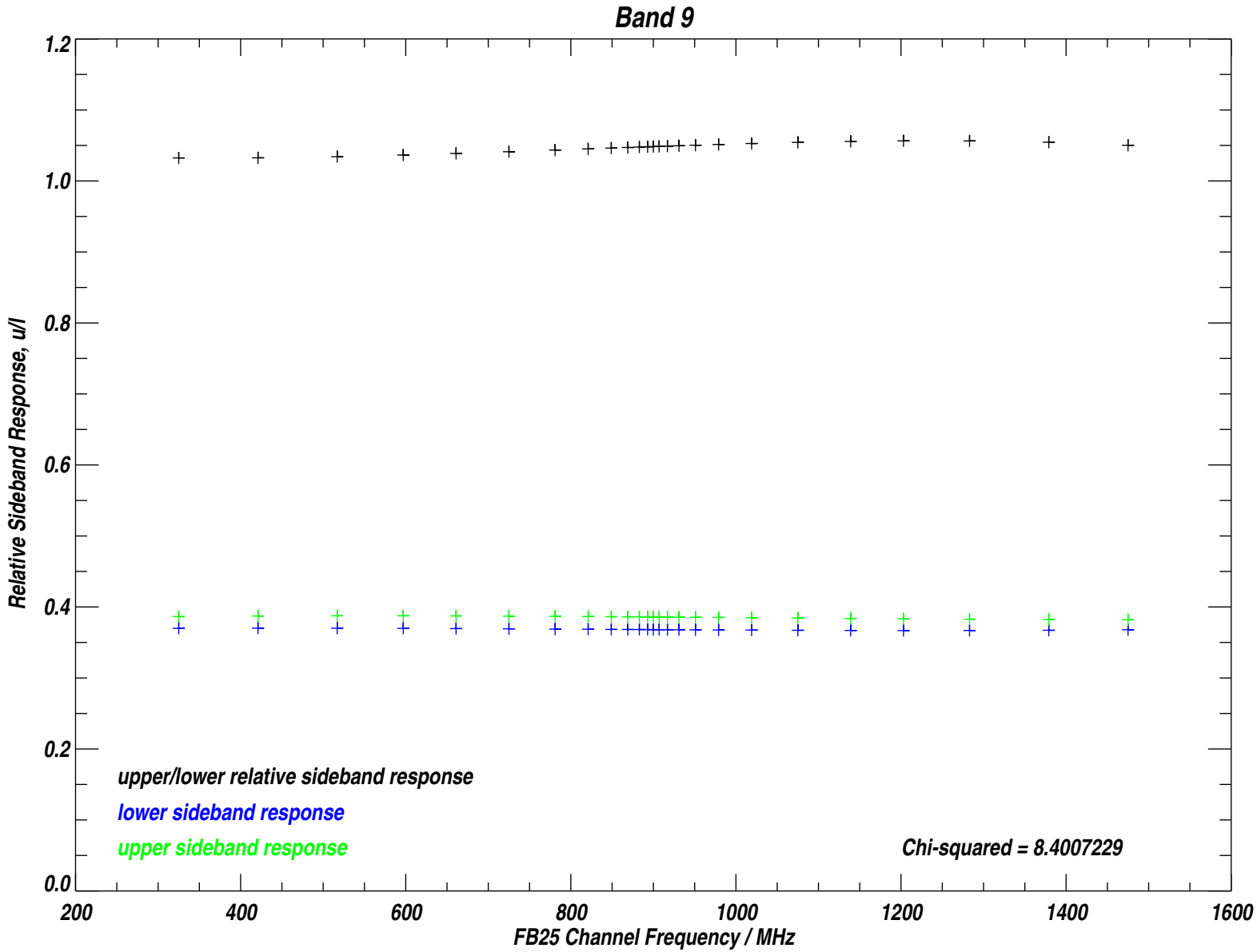

Figure C.16: Results of the fit to the data shown in the facing page. The lower and upper relative sideband responses are shown as sideband fractions (blue and green crosses), and the ratio of the response in each sideband is indicated by the black crosses (upper/lower sideband response). See text for further details.

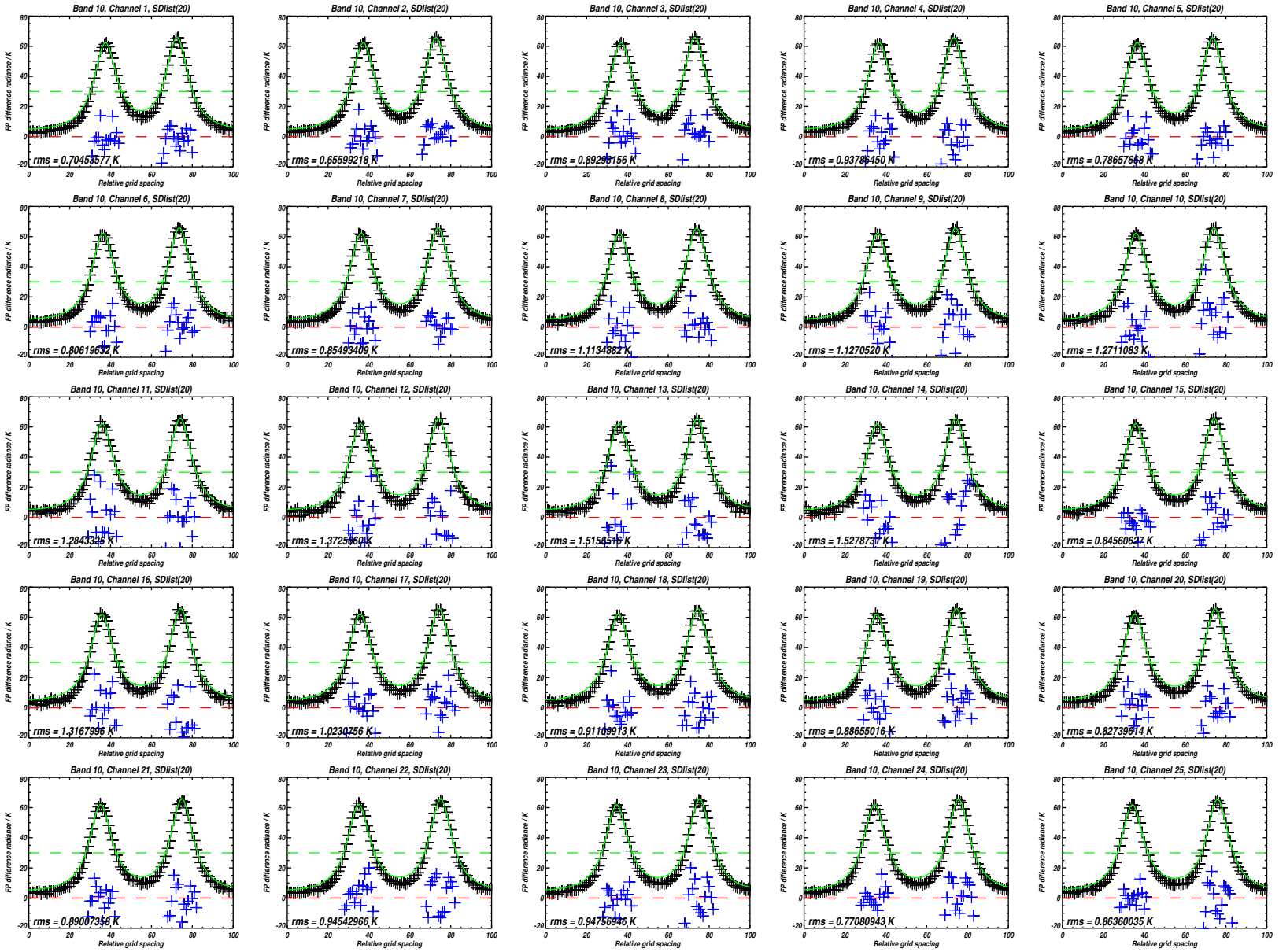

Figure C.17: Fabry-Pérot data for Band 10 (black crosses) and theoretical prediction (green line) for the grids spacings chosen for the fit. The blue crosses are the residual to the fit (difference between measurements and model) multiplied by a factor of 10.

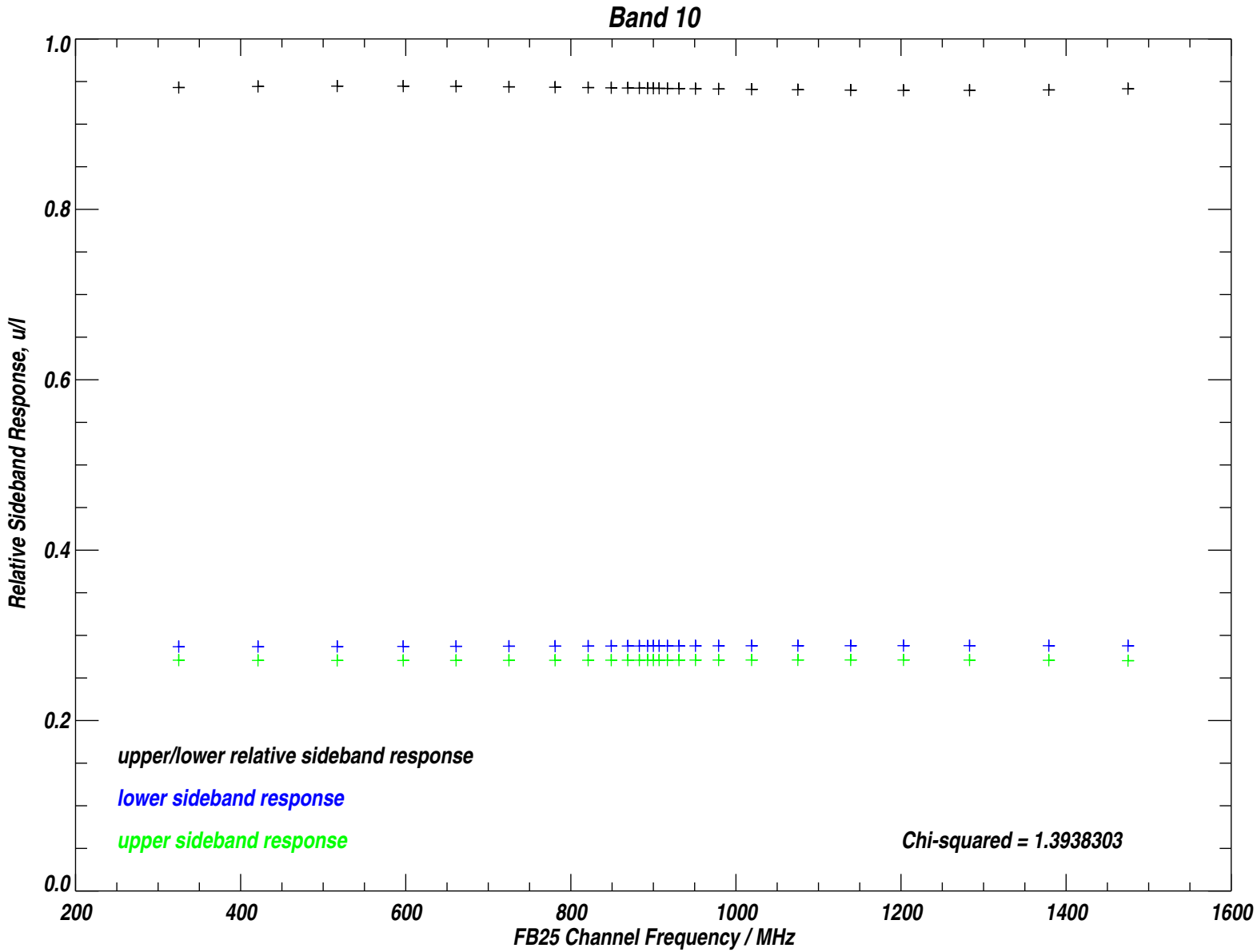

Figure C.18: Results of the fit to the data shown in the facing page. The lower and upper relative sideband responses are shown as sideband fractions (blue and green crosses), and the ratio of the response in each sideband is indicated by the black crosses (upper/lower sideband response). See text for further details.

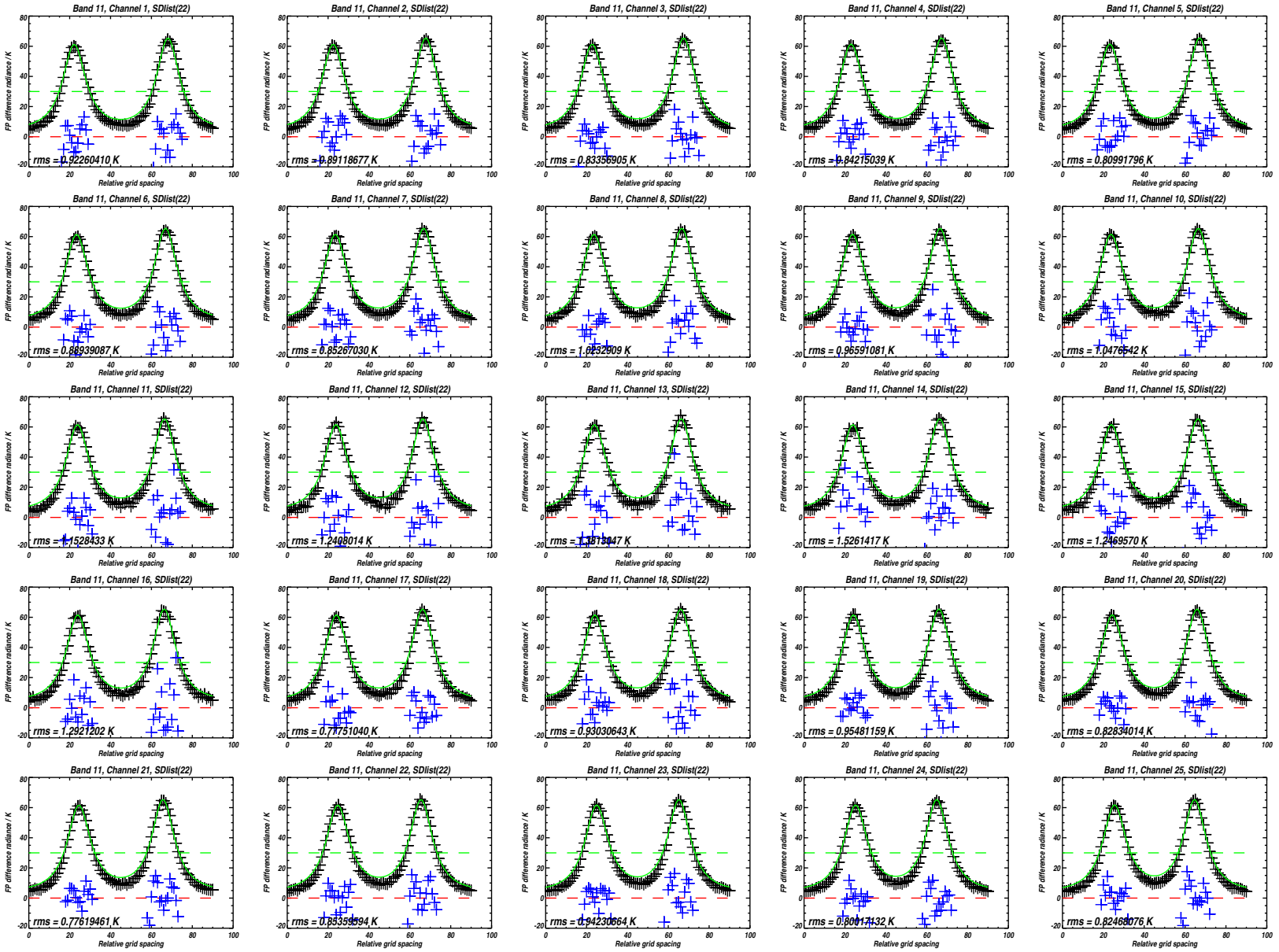

Figure C.19: Fabry-Pérot data for Band 11 (black crosses) and theoretical prediction (green line) for the grids spacings chosen for the fit. The blue crosses are the residual to the fit (difference between measurements and model) multiplied by a factor of 10.

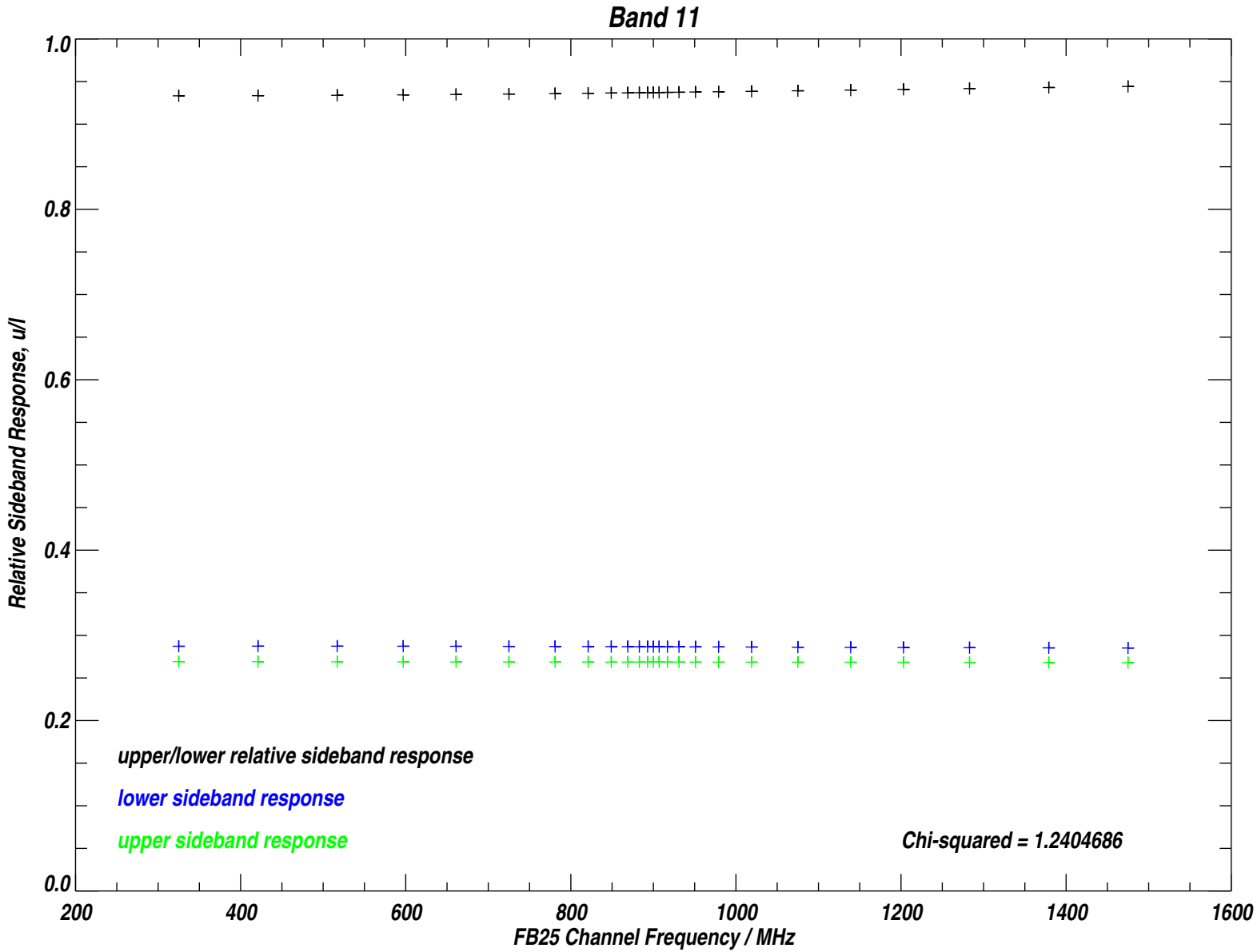

Figure C.20: Results of the fit to the data shown in the facing page. The lower and upper relative sideband responses are shown as sideband fractions (blue and green crosses), and the ratio of the response in each sideband is indicated by the black crosses (upper/lower sideband response). See text for further details.

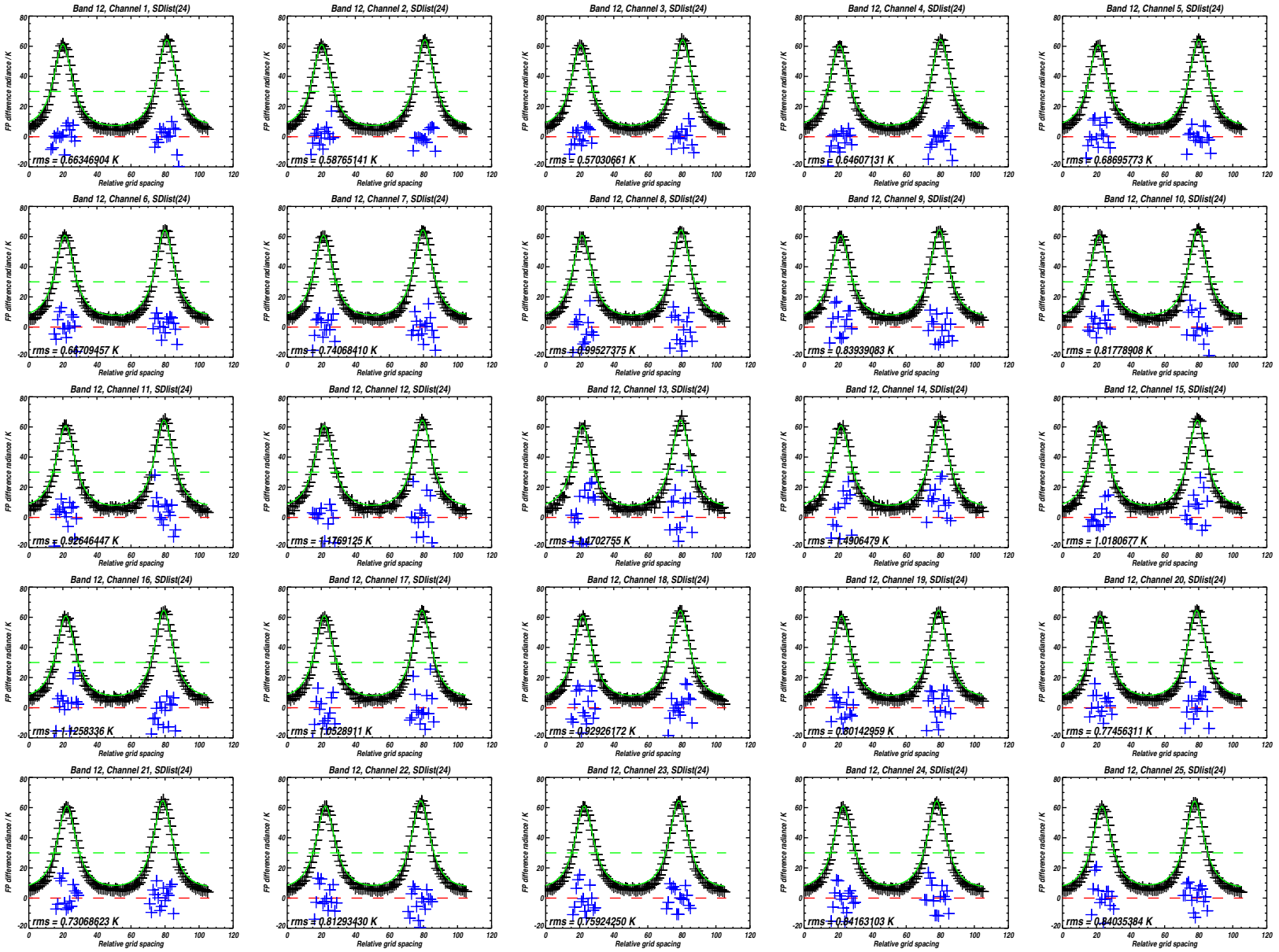

Figure C.21: Fabry-Pérot data for Band 12 (black crosses) and theoretical prediction (green line) for the grids spacings chosen for the fit. The blue crosses are the residual to the fit (difference between measurements and model) multiplied by a factor of 10.

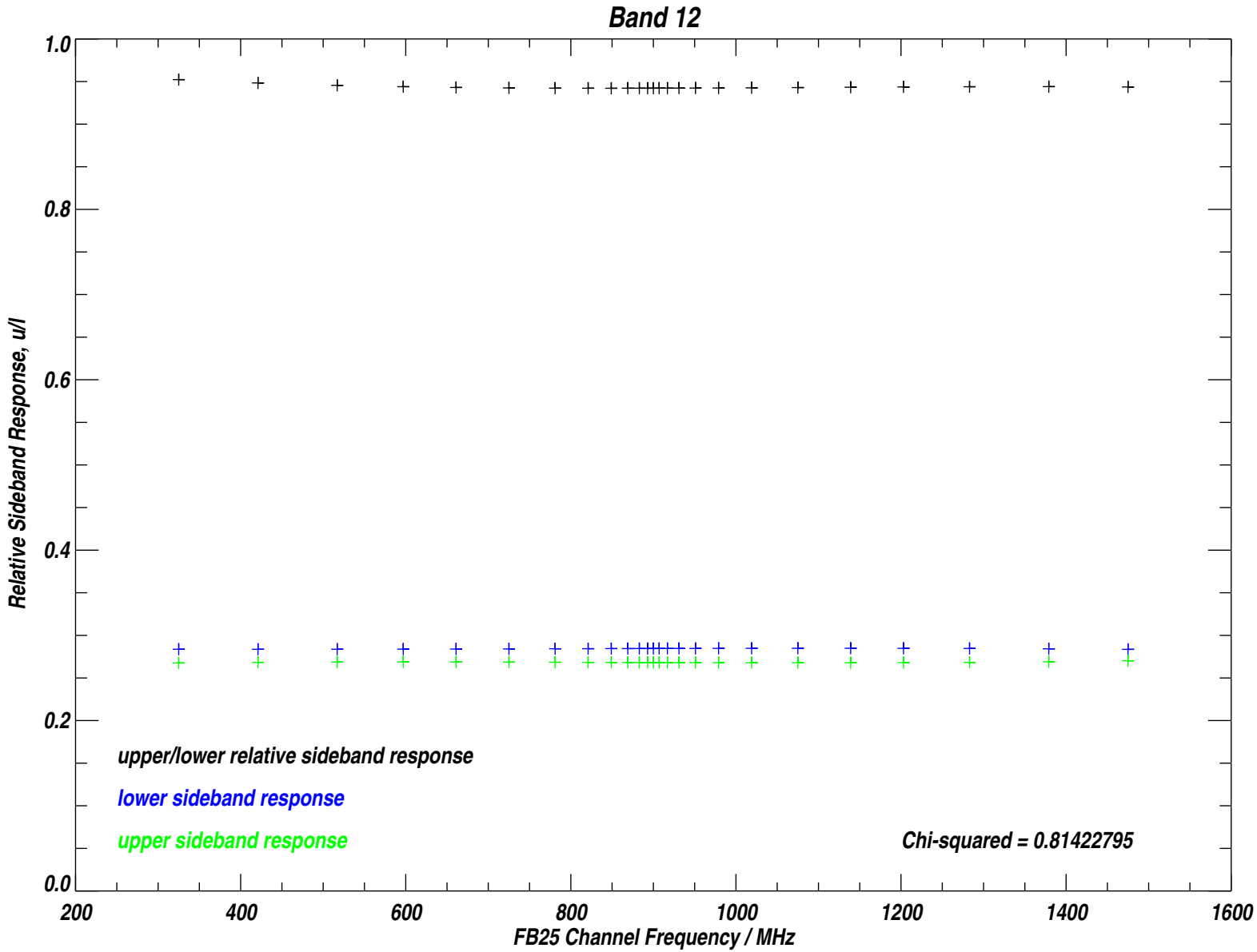

Figure C.22: Results of the fit to the data shown in the facing page. The lower and upper relative sideband responses are shown as sideband fractions (blue and green crosses), and the ratio of the response in each sideband is indicated by the black crosses (upper/lower sideband response). See text for further details.

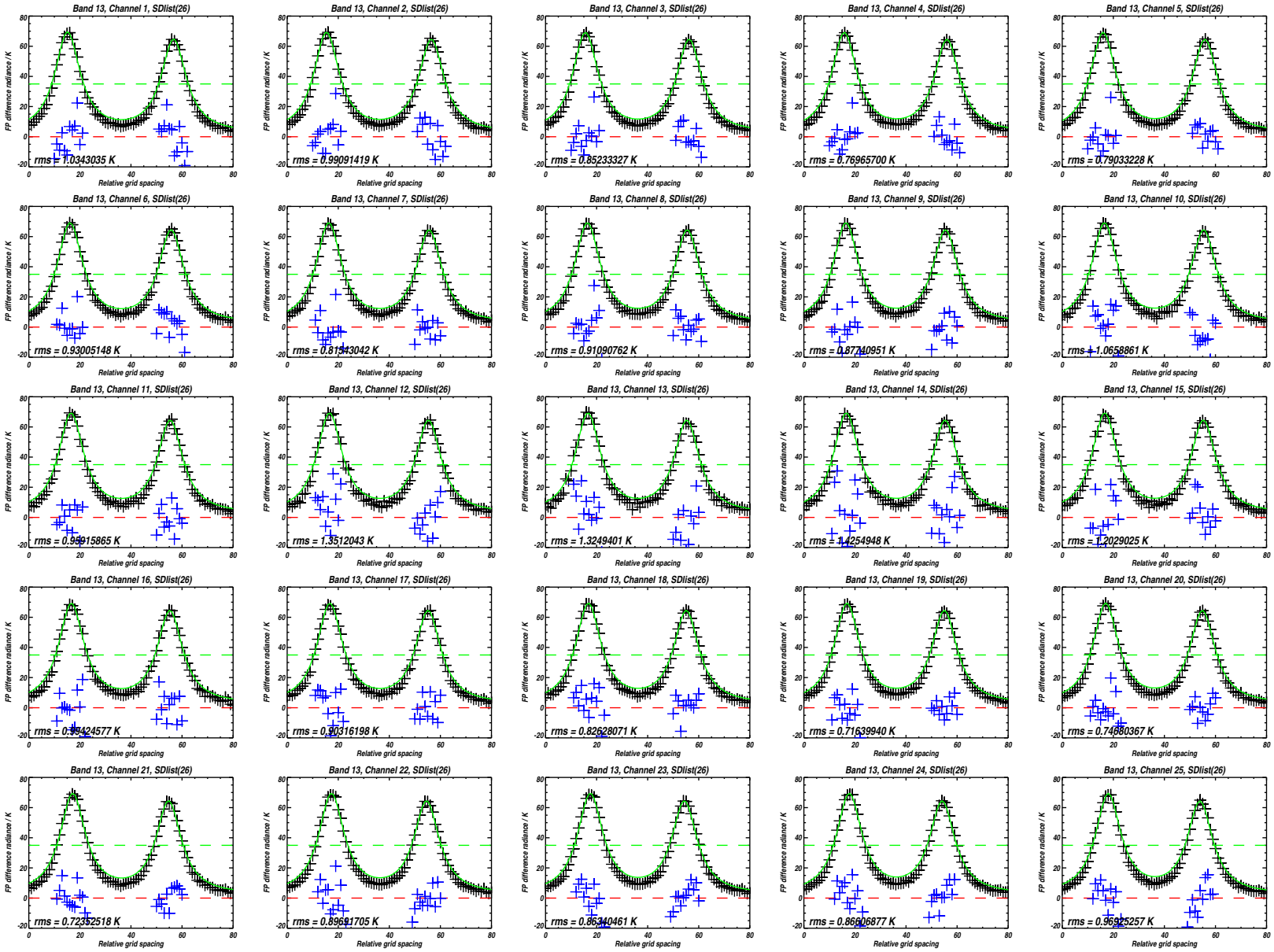

Figure C.23: Fabry-Pérot data for Band 13 (black crosses) and theoretical prediction (green line) for the grids spacings chosen for the fit. The blue crosses are the residual to the fit (difference between measurements and model) multiplied by a factor of 10.

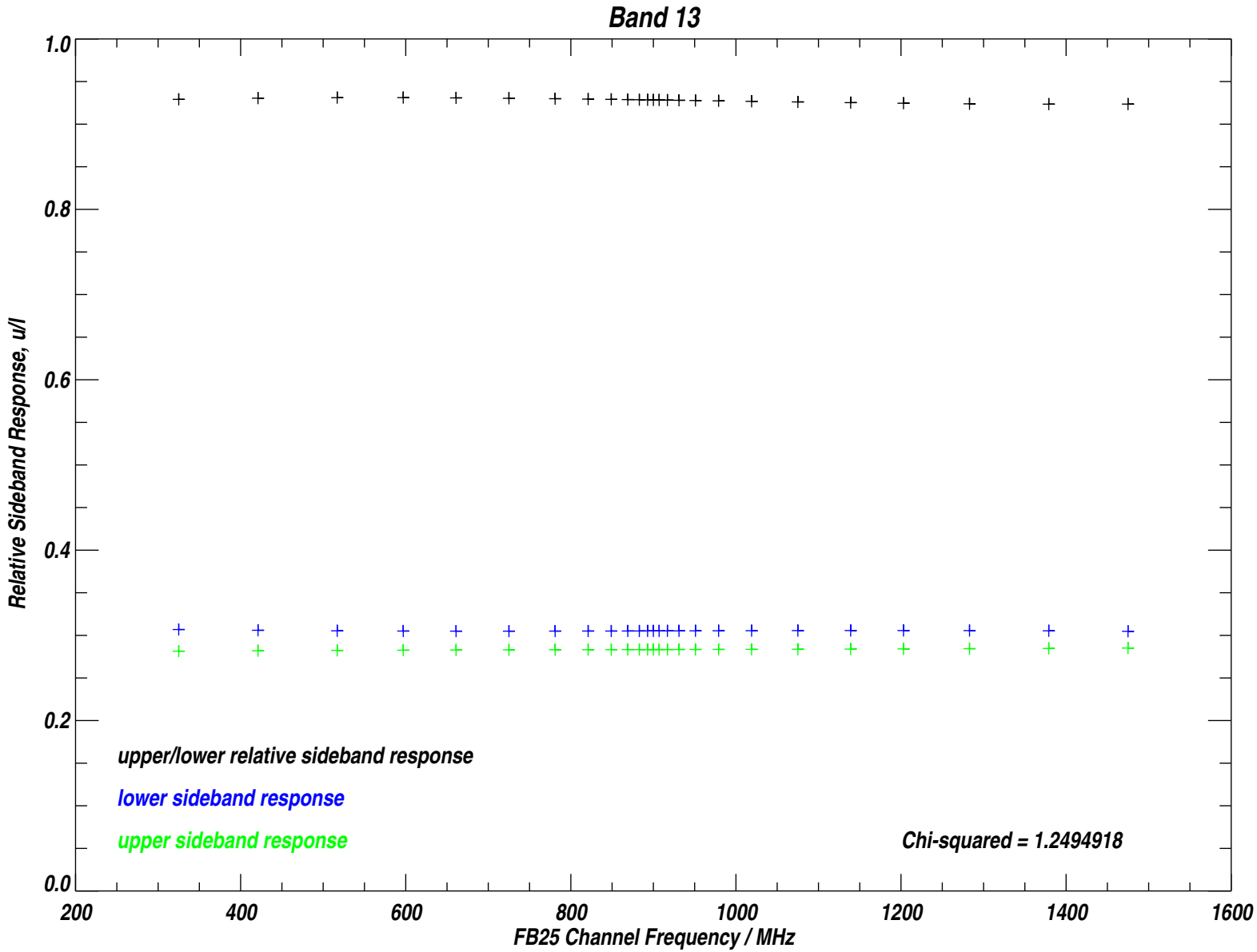

Figure C.24: Results of the fit to the data shown in the facing page. The lower and upper relative sideband responses are shown as sideband fractions (blue and green crosses), and the ratio of the response in each sideband is indicated by the black crosses (upper/lower sideband response). See text for further details.

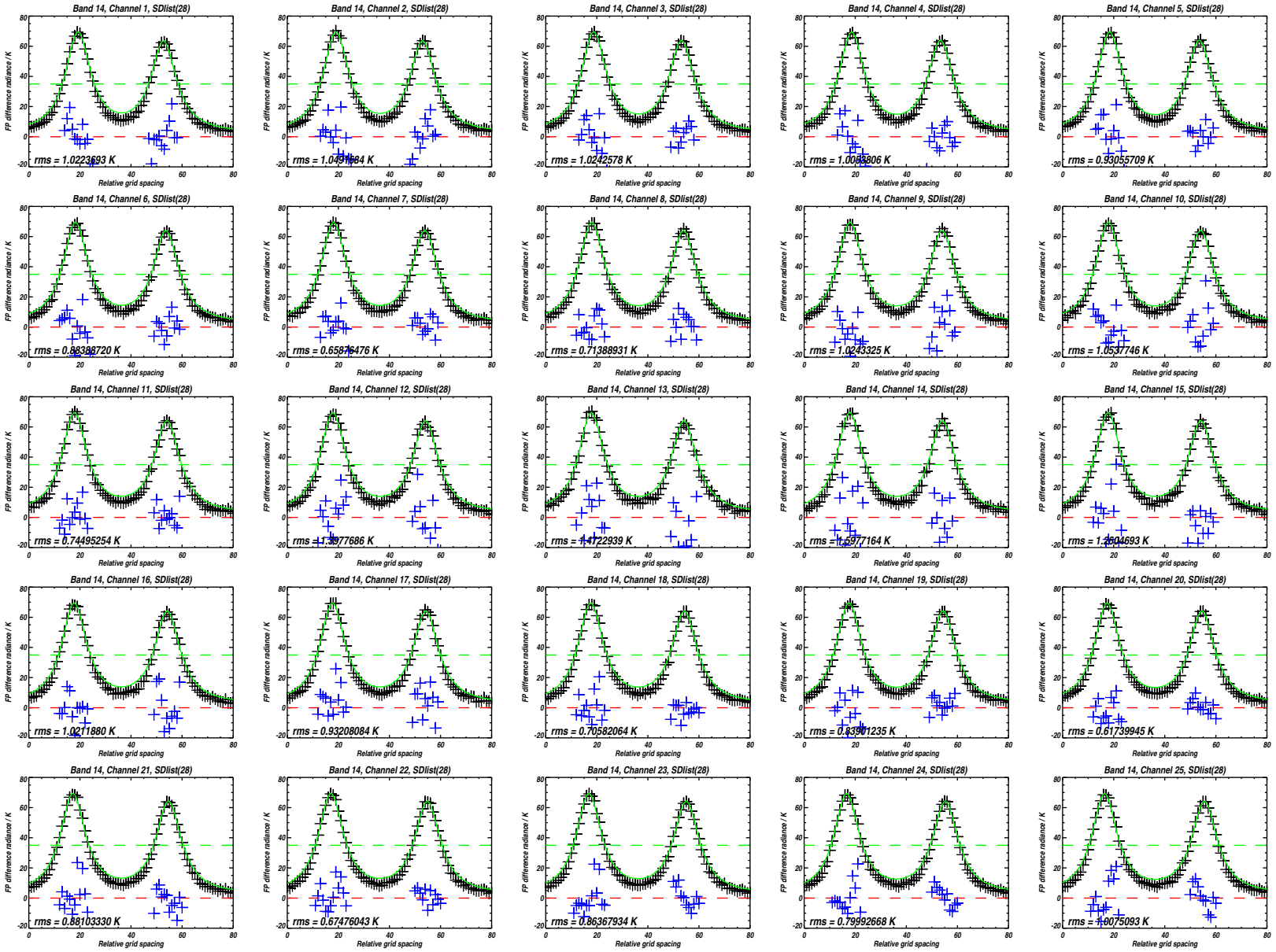

Figure C.25: Fabry-Pérot data for Band 14 (black crosses) and theoretical prediction (green line) for the grids spacings chosen for the fit. The blue crosses are the residual to the fit (difference between measurements and model) multiplied by a factor of 10.

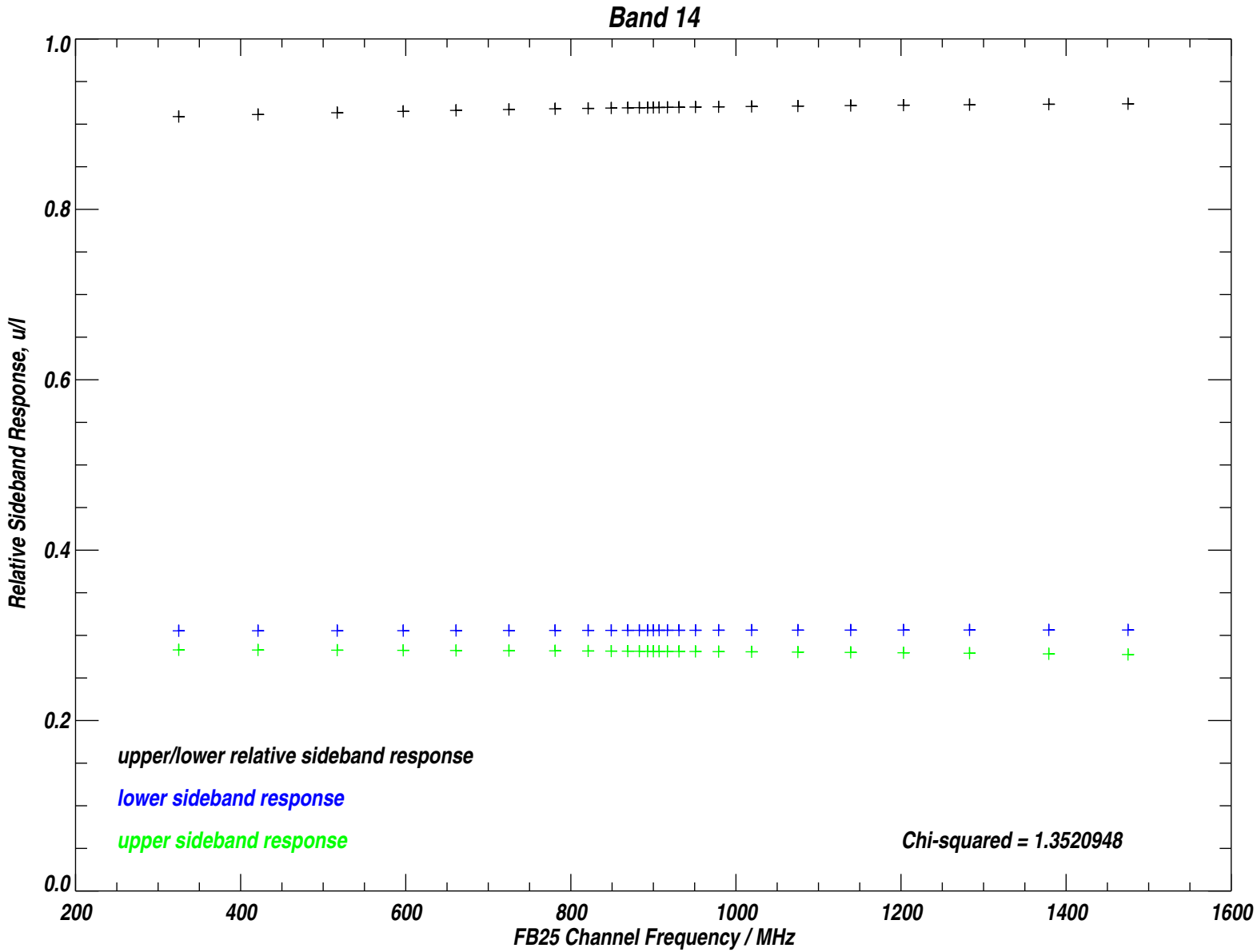

Figure C.26: Results of the fit to the data shown in the facing page. The lower and upper relative sideband responses are shown as sideband fractions (blue and green crosses), and the ratio of the response in each sideband is indicated by the black crosses (upper/lower sideband response). See text for further details.

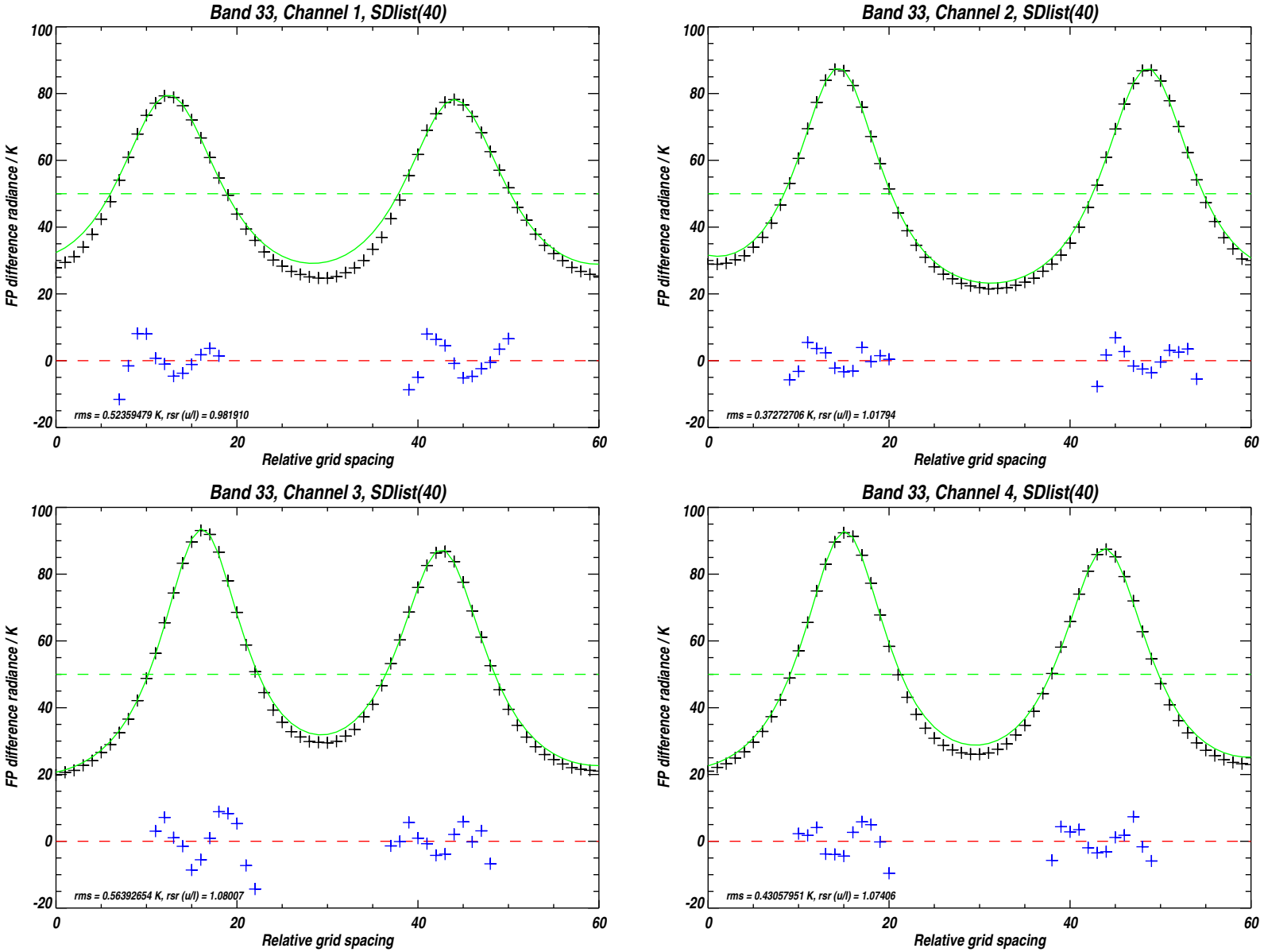

Figure C.27: Fabry-Pérot data for Band 33 (individual Wide Filters in R3). See text for further details.

The second data plot for each band shows the fractional sideband response (sideband fraction) deduced from the retrieval (blue and green crosses), with the relative sideband response (lower/upper) indicated by the black crosses.

An indication of the quality of the fit in the retrieval is given by the value of χ^2 in the bottom right hand corner of each FB25 data plot. This parameter was computed in a simplified manner assuming just radiometer equation noise contributions, fixed room temperature scenes for all Fabry-Pérot view data, and default values for channel noise bandwidths. The default noise bandwidths tend to be slightly smaller than the values derived from the high resolution sweep data, and the combination of these two factors leads to the values of χ^2 in the plots being optimistic by ∼20%. Nontheless, they provide some interesting observations:

- ❑ For the 190 GHz bands (2 through 6), χ^2 ranges from ∼10 to ∼16. Small systematic effects are clearly visible in some channels of these bands.
- ❑ For the 240 GHz bands (7 through 9), χ^2 ranges from ∼5 to ∼8. Systematic effects are far less evident in these data than in the data for bands 2 through 6.
  - ⇨ Since these data were taken at the same time, using the same Fabry-Pérot grids and test setup, we conclude that the bands in R2 are more subject to systematic effects that those in R3. At the present time it is not clear why these small behavioral differences exist the bands of these 2 radiometers.
- ❑ The data for the 640 GHz bands (10 through 14) clearly show the poorer signal-to-noise ratio of these measurements compared to those made at lower frequencies, but the measurement χ^2 are close to unity. The sub-unity χ^2 for Band 12 is merely an indication of the approximations made in the determination of this parameter.
  - ⇨ The close-to-unity χ^2 for all bands in R4 are most likely a result of the low dynamic range of these measurements compared to those in the lower frequency bands.

C.2 THz Sideband Calibration

To be added by Herb.

Point out the the THz relative sideband retrievals use a source significantly narrower than the broadest filterbank channels. The sideband retrieval was performed assuming 'flat' filters in the filterbank, and hence we must assume mirrored filter responses (except for magnitude) in each sideband.

Appendix D

FOV Calibration for the GHz Module

The GHz module for EOS-MLS has receiver bands at 118, 190, 240, and 640 GHz. With a primary antenna measuring 0.8 by 1.6 m, the far field for the highest frequency begins at $R_{FF} = \frac{2L^2}{\lambda} = \frac{2\times1.6^2}{4.7\times10^{-4}} = 1.1 \times 10^4$ m. Atmospheric attenuation and the geography around JPL preclude measuring the field of view from the far field. Both near field and compact range techniques would allow field of view calibrations in a comparatively small space. Near field techniques were used to calibrate both the SWAS and MIRO instruments at 560 GHz [1]. The success of these measurements gave us the confidence to employ a near field range for the MLS instrument FOV calibration. An added advantage of using an NFR is the modest size of the range allows for calibration in the test and assembly area. This saved time in the instrument schedule by eliminating a move to a test range, and allowed for time sharing with other calibration and assembly tasks.

D.1 Near Field Range Concepts

Near Field measurement techniques are described in most texts on antenna design and testing. A good text specifically on the subject is "Near Field Antenna Measurements" [2]. Briefly, the concept is to feed a tone into the antenna of interest and measure the relative phase and amplitude of the emitted radiation on a surface completely enclosing the the antenna. The amplitude in the far field can then be calculated by integrating the contributions from every point. In practical terms, for a high gain antenna with very low edge illumination such as the one used on MLS, virtually all of the radiation passes through a plane immediately in front of the antenna. We can then measure the antenna's beam pattern by scanning a probe in a plane in front of the antenna.

Insert some discussion here. The far field pattern, $F(K_x, K_y)$, can then by calculated by integrating the complex electric field distribution $f(x, y)$, where:

$$F(K_x, K_y) = \int f(x, y) e^{-i(K_x x + K_y y)}\, dx\, dy \tag{D.1}$$

This is exactly a Fourier transform. Discuss aliasing and spacing between points.

Figure D.1: NFR Concept. This will be a nice picture of the concept behind near field range measurements.

D.2 Interferometer Design

We developed interferometers for each of the four frequency bands using the GHz antenna on EOS MLS. In each case the downconverter was the actual flight receiver front-end. Directional couplers (10 dB) were permanently added to the coaxial lines between the receiver front-ends and the second IFs. The coupled signals were directed to a breakout panel between the radiator panels. Test points (described in the sections below) were included in each of the receiver front-ends to obtain the necessary LO frequency and phase information. No critical RF connections on the instrument needed to be broken for FOV calibration[1]. This ensured that the FOV measurements would not compromise the integrity of the instrument environmental qualification, and allowed for time sharing between FOV and radiometric/spectral calibrations.

The frequency and phase information for the source was carried on a 15′ flexible coaxial cable running from a fixed position on the scanner to the moving probe mount. For each receiver band a temperature-controlled test box was built to generate a frequency equal to the difference between the LO and the source. This was then compared to the IF signal from the RFE. The phase and amplitude were measured using an HP 8511 downconverter followed by an HP 8530 microwave receiver.

D.2.1 Radiometers R1A and R1B

Figure D.2 shows a simplified layout of the interferometer for the R1 receivers. The local oscillator for R1A is generated by multiplying the output from a phase-locked 15.85 GHz dielectric resonator oscillator (DRO) by 8. A portion of the DRO output is coupled to a test port. To generate a test signal to transmit to the receiver, the 15.85 GHz signal is downconverted by a frequency f ($0.6 \leq f \leq 1.5$ GHz) generated by synthesizer. This is in turn amplified and fed to a Millitech 8× multiplier mounted on the scanning stage, giving a transmitted frequency $F_{Tr} = F_{LO} - 8f$. The IF signal returned from the receiver front-end at frequency $F_{IF} = 8f$ is then compared to a reference signal generated by multiplying the synthesizer signal by 8 via multipliers in the test box. In this process, spurious signals will be generated at spacing of f that will appear in the signal and reference port. Care was taken to ensure that the microwave receiver did not lock to these spurs[2]. The R1B receiver has the same design as R1A, so the same equipment was used for FOV calibration of both radiometers.

[1]The only disassembly of the flight instrument required for this testing was the removal of: MLI panels covering the test ports; "loop back cables" for some detectors used only for housekeeping; and terminations on several coaxial test ports.

[2]In retrospect, a wiser design would have used a synthesizer to drive the multiplier. Some of the synthesizer output would be coupled to a mixer where it would be mixed with the RFE DRO signal. The mixer IF would then be multiplied by 8 to generate the reference to compare to the IF from the RFE.

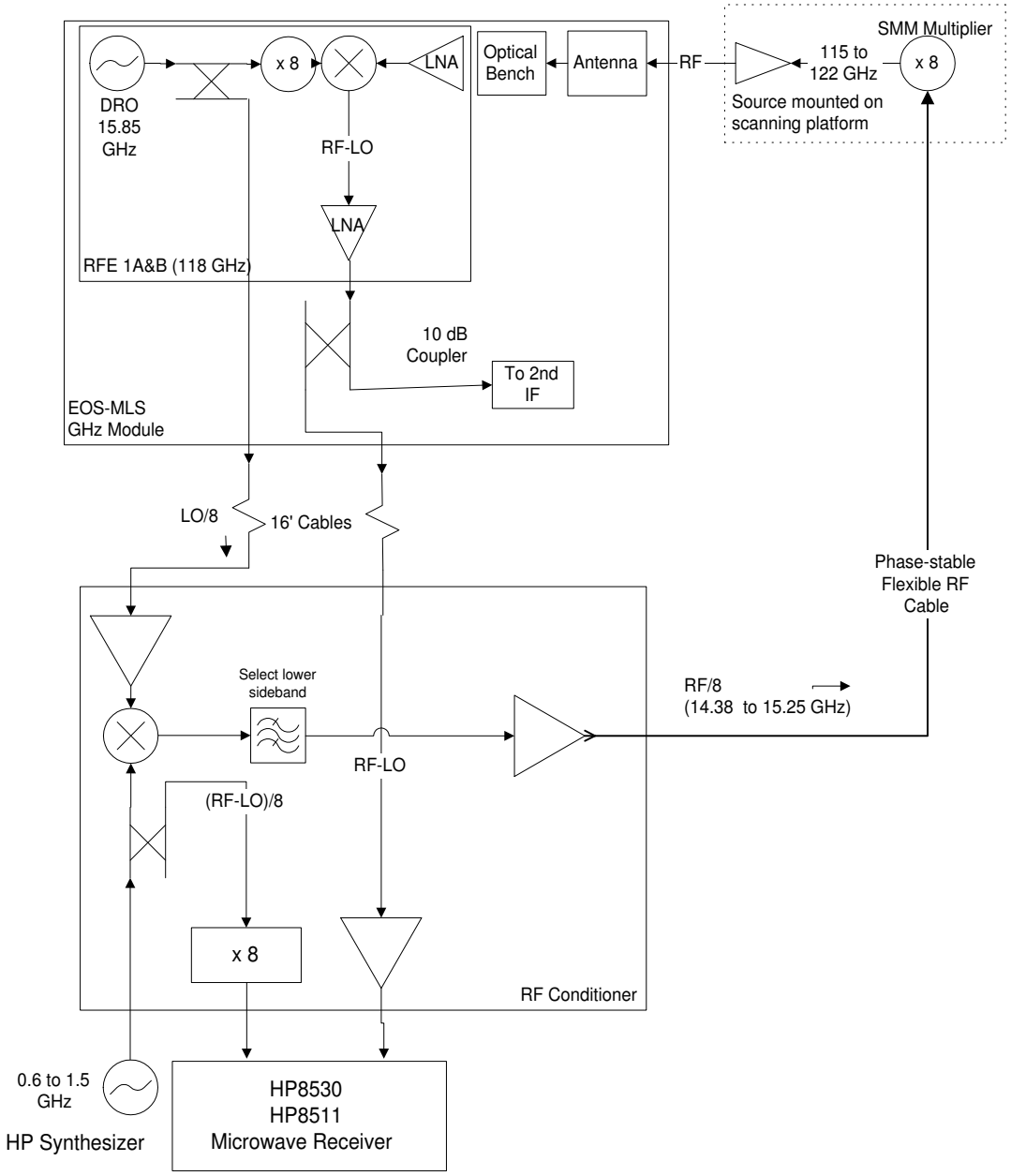

Figure D.2: Electronics for field of view calibration of R1A and R1B. See description in text.

D.2.2 Radiometers R2 and R3

The R2 and R3 receiver front-ends use phase-locked Gunn diode oscillators (GDO) for their LOs. The receiver front-end downconverter mixers are sub-harmonically pumped meaning that the circuitry in the mixer effectively doubles the LO, so in the case of R2 a 95.95 GHz GDO drives a mixer such that $F_{IF} = |191.9 - F_{RF}|$. A portion of the GDO output is coupled to a detector for monitoring the GDO's output power, and to a harmonic mixer that is used to phase-lock the GDO to a DRO. The detector can be used as a harmonic mixer. To accommodate this application during FOV calibration, the coaxial line connecting the RFE

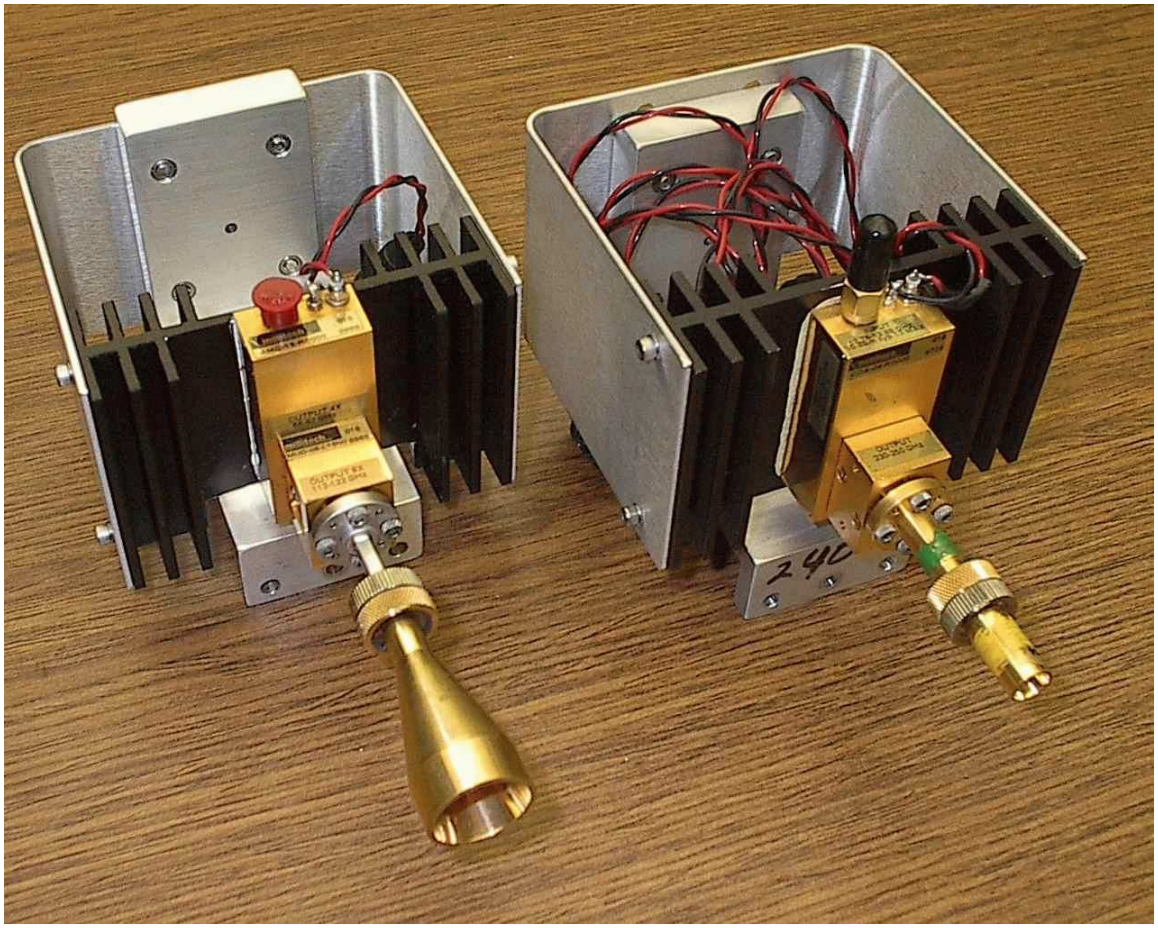

Figure D.3: Multiplied sources for 118 and 240 GHz radiometer calibrations attached to their support brackets.

to the Receiver COntrol unit (RCO) is looped out and back into the same test port panel used for the IF test signals. A short loop of cable is removed during FOV calibration, allowing the detector to be used to sample the GDO signal. Figure D.4 is a sketch of the R2 interferometer. The source is a Millitech 12× multiplier similar to the multipliers shown in Figure D.3. The output from a synthesizer set at a frequency of F_S is fed into a power divider with half of its signal sent to the multiplier on scanner stage where $F_{RF} = 12F_S$ is generated. The IF returned from the R2 RFE has a frequency $F_{IF} = |F_{RF} - 191.9\ \text{GHz}| = |12F_S - 191.9\,\text{GHz}|$ and caries the phase and amplitude information needed for the measurements. The second output from the power divider is used to pump the detector (being used as a harmonic mixer). The returned IF $F_{Hmix} = |6F_S - 95.95\,\text{GHz}| = 0.5\,F_{IF}$ is separated from the pump signal in a diplexer then doubled to generate the reference signal for the microwave receiver.

The R3 interferometer shown in Figure D.5 uses the same design with the substitution of a 18× multiplier and 119.88 GHz GDO.

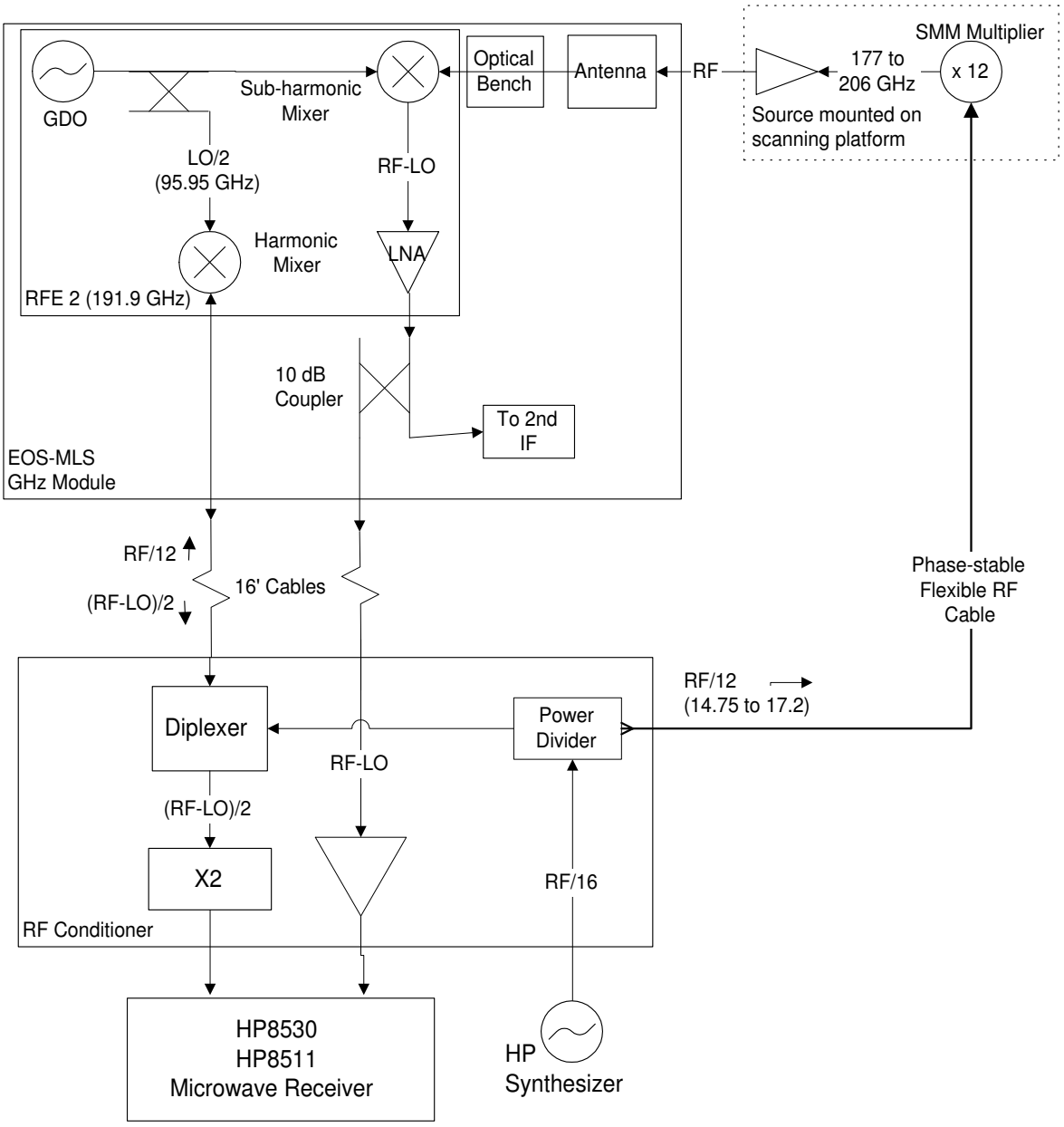

Figure D.4: Simplified design for the interferometer for R2 beam pattern measurements. See text for description of operation

D.2.3 Radiometer R4

The R4 receiver front-end design is very similar to that of R2 and R3 with the exception that the GDO output is multiplied by 3 before being fed into the sub-harmonic mixer LO port. The additional challenge of this interferometer was the multiplied GDO source[3] shown

[3]A better choice for the source would probably have been a 16 GHz synthesizer followed by a doubler, then a 20× multiplier available from Virginia Diodes. We were unaware of the availability of this multiplier at the time we were designing this system and the multiplied GDO source was available from earlier efforts to develop a fundamentally pumped 640 GHz RFE for MLS.

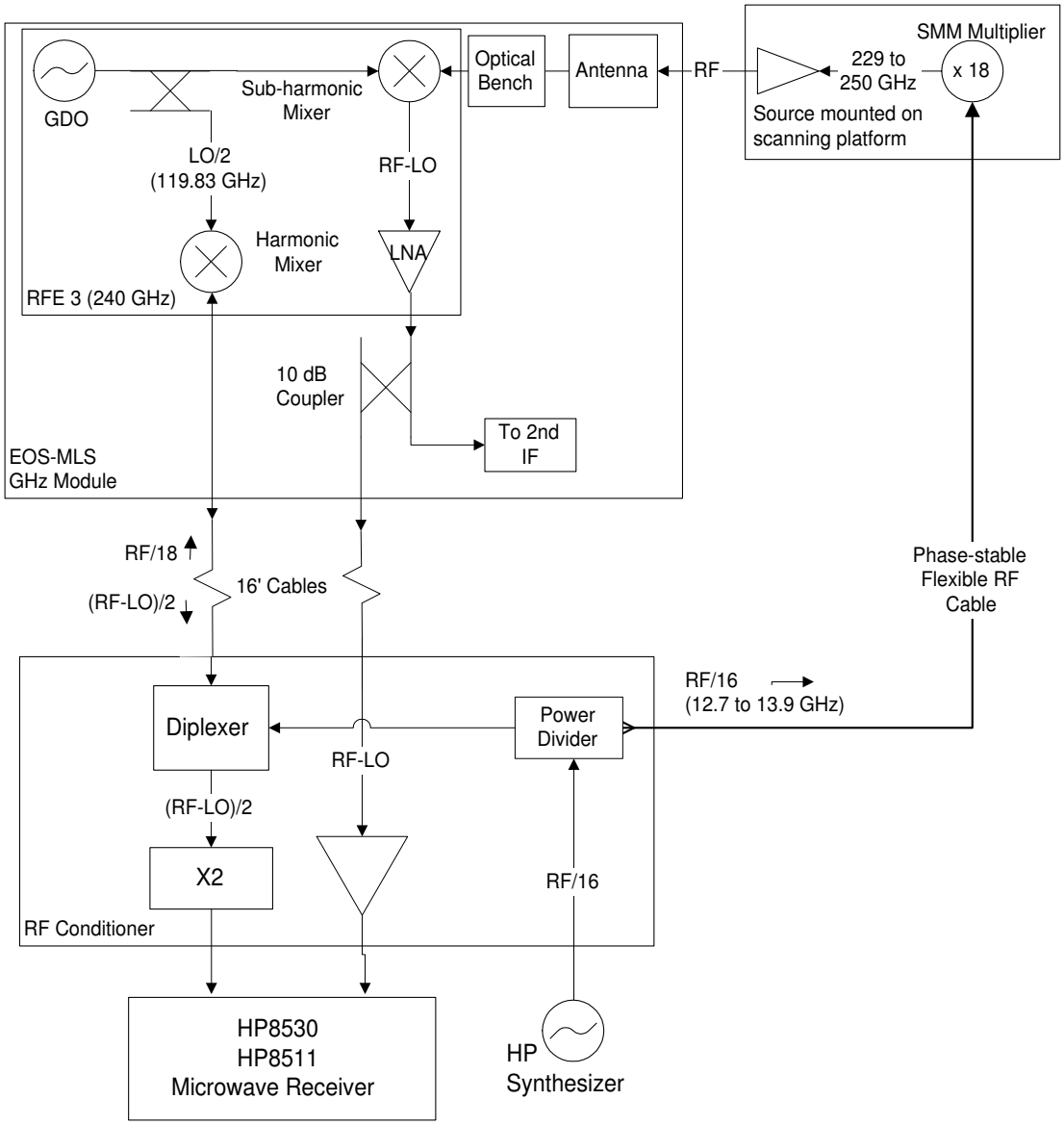

Figure D.5: Simplified design for the interferometer for R3 beam pattern measurements. See text for description of operation. Note figure needs updating. Multiplier was 18×, not 16× as shown.

in Figure D.6. This source was phase-locked through the GDO bias to the 9th harmonic of a synthesizer using a PLL manufactured by XL Microwave. The IF returned from the source harmonic mixer was 45 MHz. Multiplying this by 6 gives the frequency difference between the 54th harmonic of F_S and the source frequency and was used as the reference for the HP microwave receiver. Figure D.7 shows a simplified version of the R4 interferometer. The same synthesizer drives the detector being used as a harmonic mixer in the R4 RFE. This IF is then multiplied six to give the difference between the effective LO of the RFE and the 54th harmonic of F_S. The IF returned from the receiver was then downconverted by this difference to also give a 270 MHz signal carrying the phase and amplitude information for

the near field measurements.

Pickup or vibrations during operation often lead to temporary loss of phase-lock for the source, which in turn would lead to loss of phase-lock in the receiver, aborting the scan. This problem was primarily associated with vertical motion of the probe stage. For this reason most of the R4 measurements used horizontal scans rather than vertical ones so any loss of lock would occur outside of the measurement region. In addition a signal 10 dB lower than the reference signal, and a few MHz lower in frequency, was coupled into the reference for the receiver. In the event that the source PLL lost lock, the receiver PLL would lock to this signal, then relock to the reference when the PLL reacquired. No substantial change in the measured phase or amplitude was observed as a result of injecting this signal.

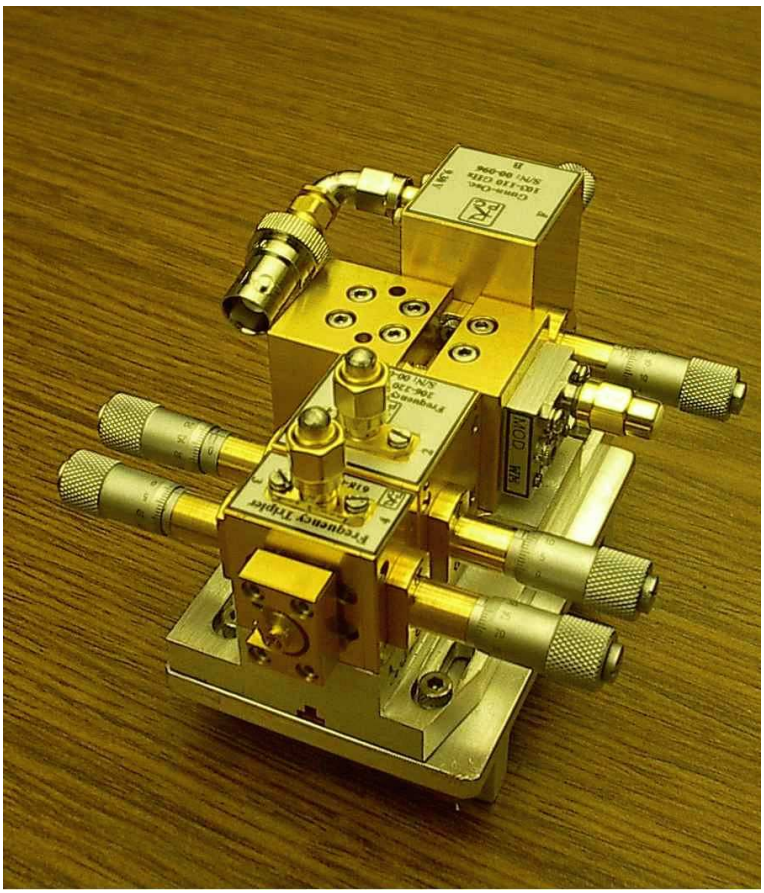

Figure D.6: Multiplied Gunn diode oscillator source for 640 GHz manufactured by RPG. There are 6 micrometers for tuning the frequency and peaking the power output of the source. The whisker-contacted multipliers are self biasing. GDO is phase-locked through the bias line. The bare aluminum finished component with an SMA termination is the harmonic mixer used to monitor the source frequency and phase. The antenna for the source is a Pickett-Potter horn. The aperture is visible at the center of the circular element attached to the multiplier with a 4 screw clamp.

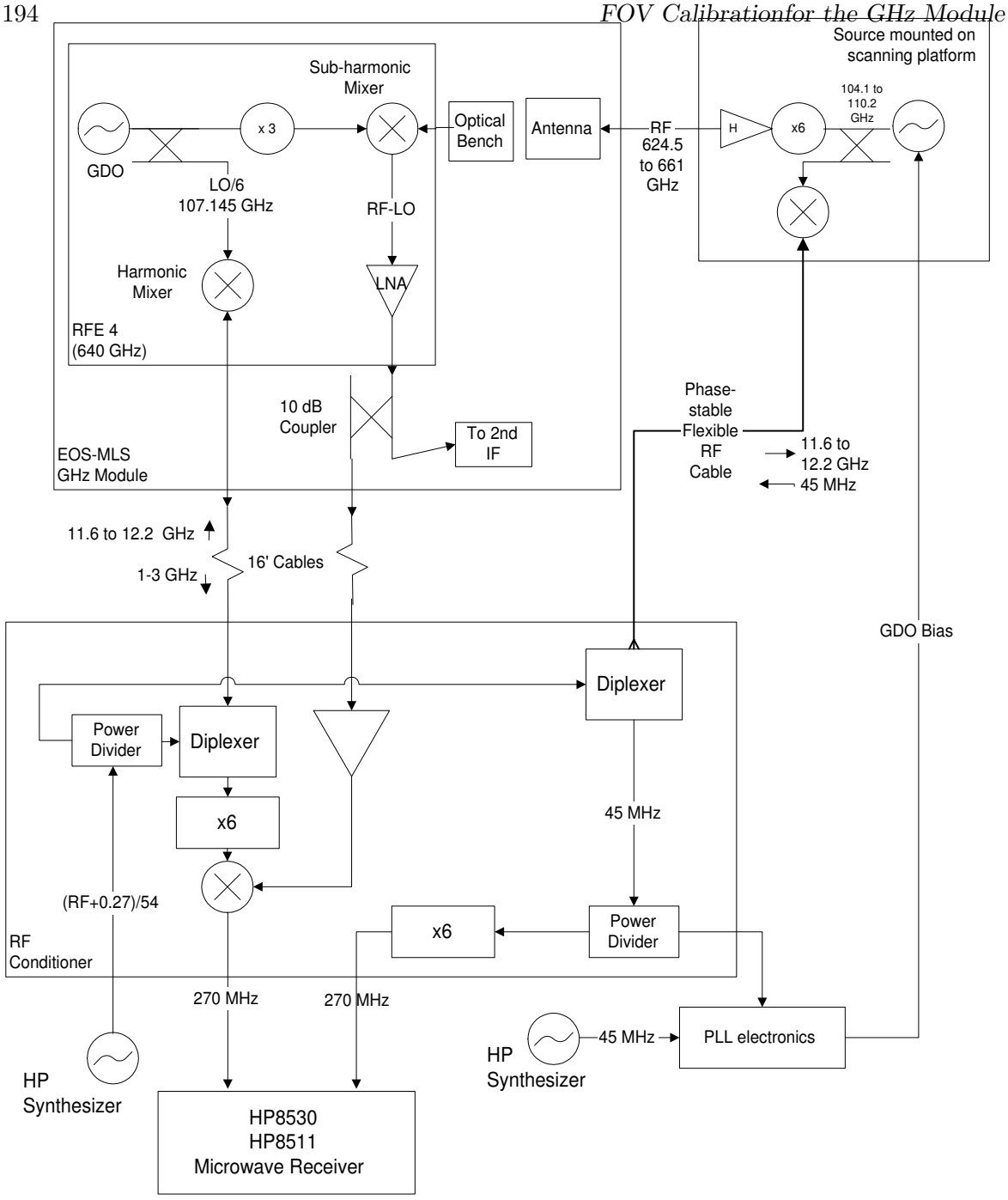

Figure D.7: We need a caption here.

D.3 Near Field Scanner

The mechanical scanner assembly, control electronics, and data acquisition software were procured from Near Field Systems, Inc. (NSI) of Carson California[4] [4]. Figure D.8 is a drawing of the NSI model 905V-8×8 scanner [3]. Figure D.8 is a photo of the scanner fully assembled in the MLS assembly and test facility, building 306 High Bay at JPL. The scanner consists of vertical granite rail that supports a vertical bearing track on which the probe rotation stage traveled. The entire assembly travels on two horizontal tracks supported by granite beams. The whole assembly is bolted to a $13' \times 13' \times 5'$ concrete seismic pad embedded in the floor. The rails are leveled and straightened through adjustable feet under the rails. The horizontal, vertical, and angular position of the stage is controlled through an interface box by a 486 PC running DOS that is itself a slave to a Pentium PC that runs the user interface and the NSI data analysis software. A blower delivers room temperature air to the motors to keep them from overheating. Air conditioners maintain the room temperature variations to 1 C or less, with temperature cycling on a 20 minute or longer time scale. The *rms* variation of the scanned surface was measured to be less than 5 μm.

[4]NSI had previously constructed the NFR for SWAS and MIRO, a $3' \times 3'$ scanner using a flat granite slab as a reference. We required an $8' \times 8'$ scan area making the previous design where the probe stage was referenced to a very flat granite table unworkable.

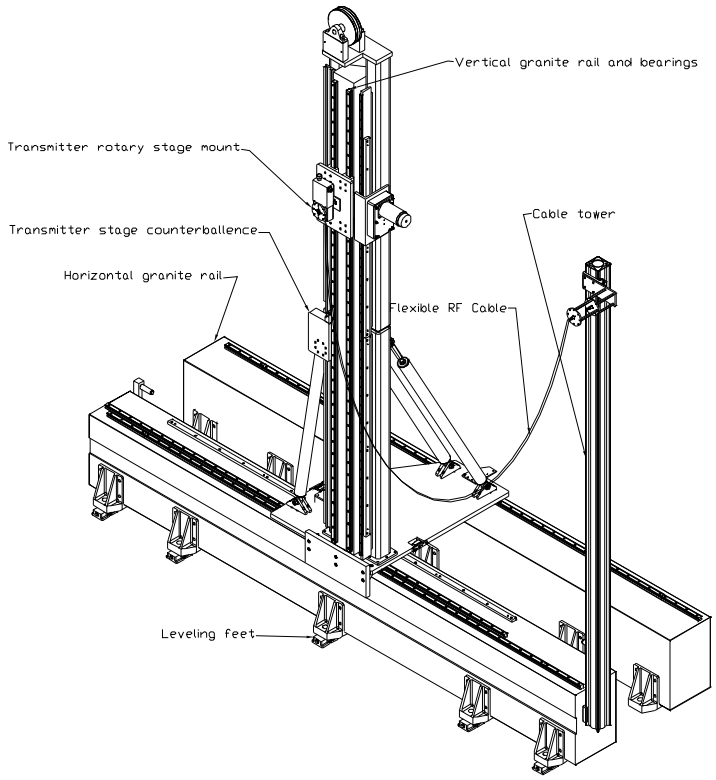

Figure D.8: NSI Model 905V-8x8 Near Field Scanner. The tower scans a total of eight feet horizontally. The probe mount on the tower scans eight feet vertically. Not shown are absorber panels on the tower and in front of the first horizontal granite support.

D.3.1 Planarity Verification

Discuss planarity of scan plane.
Discuss NSI technique.
Discuss Hamer level technique.
Discuss laser tracker technique.

D.3.2 Scan Pattern

Figure D.10 is a sketch of a vertical scan[5]. We used a raster scan pattern to measure the near field with MTI measurements every 5 minutes to correct for any thermal drifts in the system. Need to add stuff on how MTI works.

D.3.3 Cables

Come back to this.

D.4 Scan Plane/Instrument Angle Measurement

While our primary goal was to measure the alignment between the five receivers, we also need to know the pointing relative to the spacecraft. This is achieved by comparing a best fit to the plane of the scanner to the location of the alignment cube located near the encoder on the torque tube. Three theodolites were required for this. The first is located roughly in the plane of the scanner approximately 12 feet to the right of the scanner. A target was placed on the support for the probe stage. The probe is then moved to 9 positions on the extremes and center of the scan plane. The elevation and azimuth angles along with their position in the scan plane are recorded for each point. A best fit plane is later determined from these values. Two other theodolites were positioned to autocollimate with perpendicular faces of the alignment cube and cross collimate with themselves and the theodolite in the scan plane. At some antenna positions, we were not able to cross collimate between all three of the theodolites limiting our ability to demonstrate closure of the measured angles. During calibration periods, theodolite measurements were conducted once in the morning and again in the evening. Generally, any variations were less than the error on our measurements. Figure to follow.

D.5 Testing Procedure

Testing was conducted largely at night to limit the number of people in the test area during scanning, to limit the number of people exposed to the loud noises from the scanner motors, and to allow for spectral and sideband calibration along with final assembly efforts during regular work hours. The receiver front-end for the band being measured had to be on for at least one half hour before any measurements were made. If the instrument had been turned off, the antenna position encoder (APE) would have to be reset by rotating the antenna

[5]The orientation of the antenna is not optimal. The scanner moves much quicker in the vertical direction than in the horizontal. Since we are primarily interested in the vertical resolution of the instrument, the instrument should have been oriented with the primary axis of the primary reflector vertical.

through the zero point of the encoder and then to the position where the beam pattern was to be measured. For almost all of the measurements, the antenna actuator assembly (AAA) was not present and the position was set with a turnbuckle. After the antenna was set in position relative to the instrument, the instrument and its support stand were rotated so that the antenna was pointing close to perpendicular to the scan plane. The support structure was then jacked up and lowered onto aluminum blocks placed on the seismic pad. The angle of the scan plane relative to the alignment cube was then measured. Before each set of patterns, a quick pattern at 234 GHz was measured[6]. Then we would begin measuring the beam patterns for that antenna angle.

Insert chart of measurements and antenna angles.
Insert chart of scan angle and frequencies.

D.6 FOV Analysis Models

Polarization of FOV

Didn't get from Near Field range (nor RFE patterns); need to propagate analytic values from horn pattern spherical wave expansion through optics (esp. pol.grid) to far-field, to provide relative phase of co- and cross-pol patterns for `B22LD:PT` and `B26LD:PT` in polarized forward model. Analysis TBD spring 2004

D.6.1 Scattered Power Fraction

Scattering loss is estimated from the surface contour measurements made during the manufacture of the antenna reflectors. The theoretical basis is in [**?**, **?**, **?**].

Contours were measured with each reflector face up on a coordinate measuring machine, to a precision of 0.0002 inch. Deviations discussed here are residuals from the appropriate best-fit conic (paraboloid, hyperboloid, plane and plane for the Primary, Secondary, Tertiary and Switching Reflectors, respectively). The conic parameters, tilts and translations were used to size shims, placed during antenna assembly to collocate focal points. This placement, and its stability over time, were verified by metering rod measurements between reflectors and radiometer from assembly through integration with the Aura spacecraft. Misalignments within the observed range were analyzed for UARS MLS in [**?**]. Their effects on the FOV are confined to beam mis-pointing or (for quadratic aperture phase variation, such as results from *e.g.* feed defocus) changes in sidelobe level *near the main beam*. Because such effects will appear in the measured FOV (if their magnitude exceeds the measurement noise floor), surface errors whose correlation lengths exceed half the reflector diameter are excluded from this analysis.

continue as in UMLS cal.report...

The above scattering loss is an upper bound because no information about its angular distribution is included. For example, if the scattered power were all within the $\pm 6^\circ$ FOV measurement range, and exceeded the measurement noise floor, it would appear in the Level

[6]The alignment of the field of view to the instrument is of secondary importance to the alignment of the receivers relative to each other. The 234 GHz line of $O^{18}O$ is MLS's best line for measuring pressure and temperature, so all measurements were referenced to this line.

2 input pattern function as well as in the integrated loss, input to Level 1. This double bookkeeping is avoided by modeling the angular distribution of scattered power [**?**, **?**], which requires knowledge of the correlation length L of surface errors.

The 2-dimensional surface contour data cover the primary aperture at only 1/26%TBDEMLS? of its major diameter. We refer to the model for scattering based on these points as the *contour model*. For finer resolution of the correlation interval, we use the survey data from stylus traces over the Primary and Secondary Reflector semi-major axes, also shown in Figure %TBDFOV:fig:CMMgrids. For both reflectors, data were sampled at 0.01 inch = $0.5\lambda_{R4}$. The scattering model derived from these points is called the *trace model*.

The data were verified against the 2-dimensional contour points, and matched the best-fit conics within 0.0004 inch. The linear parts of these residuals were attributed to different setups, and were removed for this analysis by subtracting the best-fit line from each trace.

continue as in UMLS cal.report; difference for EMLS is that the reflector tolerance is 4 times better than for UMLS (hence we expect Ruze eqn. 8 to peak 16x lower), while pattern SNR is only moderately better, so that the Ruze bulge is not expected to show above the pattern noise floor.

D.6.2 Diffraction and Spillover

In the absence of blocking struts, the principal source of sidelobes far from the boresight is edge diffraction from the reflector outlines. A model for this radiation was developed, using the Geometrical Theory of Diffraction (GTD) [**?**, **?**]. This model treats the antenna as a transmitter, and considers only singly-diffracted rays from the Primary Reflector leading edge, using the appropriate wedge angle variation as the diffracting edge is traversed. The model accounts for both the electromagnetic field incident on the edge and its derivative; the latter contribution is referred to as *slope diffraction*. Edge diffraction from the Secondary and Tertiary Reflectors is ignored, since

1. these reflectors intercept the nominal beam at higher edge taper than does the Primary, *i.e.* $T_{\mathrm{Secondary}}/\mathrm{dB} = (40/30)T_{\mathrm{Primary}}/\mathrm{dB}$; and, more important,

2. outlines of the Tertiary and Secondary Reflectors nearly coincide with the reflection boundaries from the previous reflector or port; the corrections in the modern GTD for this involve the next level of calculation beyond slope diffraction, and are beyond the scope of this simple model. Hence the model at these edges is simply the Geometrical Optics (GO) spillover.

Although the extensions [**?**] to Keller's original GTD produce correct patterns in the transition regions about reflection and shadow boundaries, they are singular in the vicinity of GO caustics, such as the antenna boresight, our dFOV. When truncated at $\theta = 6°$, the GTD patterns match the FOV shape predicted by the aperture-field method [**?**].

Two sources for incident field are in the current model:

1. two-dimensional feed patterns measured on Receiver Front Ends (RFEs, §D.9), propagated through Tertiary and Secondary Reflectors by GO, and

2. theoretical feed patterns, calculated for all three radiometers with nominal edge taper.

Results using theoretical feed patterns are reconciled with those from the full RFE patterns by scaling both normal and slope-diffracted components from nominal to measured edge taper, to calculate diffracted power. Figure D.11 shows the pattern for the radiometer and cut angle in which the most diffracted power is produced: R1B, in the $-x_P$ half of the cradle $x_P y_P$ plane. The cusps in the region $\theta > 90°$ represent the Primary Reflector shadow boundary, and blockage by the cylindrical reflector edge; here the GTD and GO fields each contribute half of the total field. The plot subtitle shows integrated power (beam solid angle, in steradians). For each radiometer, these powers are summed over the 4 principal half-planes, to obtain diffracted beam solid angles tabulated in Table D.2 for the sensor FOVs. Using the solid angles of the measured definitive patterns ($\theta < 6°$) also shown, the diffraction efficiency is calculated in the last row.

D.7 Analysis of Measured Patterns

D.7.1 Definitive FOV direction (dFOV)

Figure D.12 shows the configuration of theodolites for the optical survey which relates the GHz alignment cube to scanner coordinates. Figure D.13 shows a view from behind theodolite station 2, the master station located approximately in the scan plane.

Scanner and theodolite master coordinate frames

In order to locate the scanner coordinate system with respect to a master reference frame centered in theodolite station 2, a square grid in the scan plane was established using that theodolite to observe an alignment target affixed to the probe in each of 9 known probe positions (scanner $dx = dy = 48$ inches). These 9 (x, y) pairs, with the corresponding theodolite (θ, ϕ) pairs, contain sufficient information to retrieve the 9 z displacements out of the scan plane, thus defining a best-fit scan plane's orientation in the master reference frame.

To assure consistent and rapid convergence, the parameters defining geometry were split into two groups and retrieved in two sets of iterations: the first set retrieved the 9 distances from master station to grid points by using three corner points expressed in both scanner coordinates (from reported x, y, assumed $z = 0$) and in the master frame (using theodolite angles with the retrieved distances). This set of iterations minimized the rss distance in the scanner $z = 0$ plane between nominal and retrieved points. Then, for the second set of iterations, 6 degrees of freedom (3 translations + 3 rotations) were appended to the first solution vector, representing a small correction to the coordinate transformation based on the three corner points. For these iterations the cost rss function included z out of the nominal scanner plane, so that the final solution gives the best-fit scanner plane in the master reference frame, with the 9 grid distances as Lagrange multipliers.

Convergence of the first set of iterations depended strongly on a good starting guess of the distance between scanner and master theodolite reference frames. Numbering the 9 scanner grid points as in Figure D.14, and assuming the grid is roughly vertical with height H,

$$s_{11} n_{z11} - s_{31} n_{z31} = H \quad \text{and} \quad s_{31} = s_{11}(n_{x11}/n_{x31});$$

so the starting guess of distance between the master theodolite and the origin of the 9-point scanner grid is

$$s_{11} = \frac{H}{n_{z11} - n_{z31}(n_{x11}/n_{x31})}$$

For other elements in the top row and left column,

$$s_{i1} = s_{11}(n_{x11}/n_{xi1}) \quad \text{for } i = 2, 3$$

$$s_{1j} = s_{11}(n_{z11}/n_{z1j}) \quad \text{for } j = 2, 3$$

and for the remaining elements.

$$s_{ij} = [s_{1j}(n_{x1j}/n_{xij}) + s_{i1}(n_{zi1}/n_{zij})]/2 \quad \text{for } i, j > 1$$

With these starting guesses, the algorithm was robust for both large buck-in errors (limited access in the high bay constrained the master station to be occasionally as much 30 inches out of the scan plane), and large angular differences (30° by simulation, in all 3 axes) between scanner and master frames.

Alignment referred to GHz module mounting interface

The orientation of the GHz module alignment cube in the master coordinate system was determined in each measurement set by observing two orthogonal cube faces with theodolites and cross-collimating these theodolites with the master station (Horizontal circle readings in cross-collimation relate theodolite azimuths to the master station, while vertical angles all have a common gravity reference). With both scanner and alignment cube orientations known in the master frame, we can derive the transformation between scanner and cube coordinate frames (called $x'y'z'$ here). Applying this to RF pointing data, from the near field patterns, yields the RF boresight directions in an opto-mechanical reference frame of the instrument.

The pair of cube faces observed by stations 1 and 3 in this procedure differs from the pair used when aligning MLS to Aura (The latter pair of faces also defines the definitive GHz module cube frame, in which the mounting features are known). Because adjacent cube faces are not perfectly orthogonal, a small 3-dimensional rotation matrix is applied to transform directions in the scanner frame through the interim cube frame $x'y'z'$ to the definitive frame. Elements of this matrix had been determined from a previous characterization of all visible cube face angles.

The transformation from GHz module alignment cube to the frame defined by instrument mounting interface was measured during the installation of the GHz module to the FOV fixture for calibration on the Near Field Range, and is recorded in the MLS Interface Control Document (ICD) [**?**, Table 3.5.5-1a]. This transformation is appended to the sequence described above.

Performance metrics

A closure check was made using the horizontal circle readings in cross-collimation of the three theodolites whose centers form the vertices of a triangle; this azimuth closure is the difference between the sum of interior angles and 180°. Similarly, the sum of vertical (zenith) angles read from two theodolites in cross-collimation should equal 180°. Departures from this elevation closure indicate that one or both theodolites are out of level. Finally, after cube face normals have been converted to the common master coordinate frame, a cube closure check results from comparing the angle between normal vectors to the inter-face angles measured in the laboratory characterization of the alignment cube. Automating these closure checks in the data analysis spreadsheet 1) validated the algorithm and first several measurement sets, 2) later revealed a very few instances of data dropout in the electronic recording of theodolite data, and 3) provided error estimates which were propagated to the ICD [**?**]. Ranges of the azimuth, elevation and cube closure during post-environmental tests were $[-6, +10], \pm 7$ and $[-6, +7]$ arcsec, respectively.

Quality metrics associated with the determination of scanner orientation in the master frame are shown in Figure D.15 and include: the rms deviation of probe x, y positions from nominal, the rms planarity of probe z, elevation angle of scanner z in the master frame (which should be constant and indicates how well the master station is leveled). The figure shows better rms planarity in the pre-environmental test activity, but in both sets the planarity is consistent with the canonical accuracy for a single point measurement of 0.0015 inch (38μm), corresponding to 1.4 arcsec at a mean distance of 250 inches from the master station. That is, this measurement has insufficient accuracy to confirm the 5 μm rms planarity measured by other methods. There is no correlation between buck-in error and the rms planarity, nor are the sag values, resulting from fitting a quadric surface to the z residuals, significant compared to the measurement error and to their own scatter of 18μm (1σ)

Combining optical alignment with RF dFOV

Euler angles ϕ, θ, ψ of the transformation from scanner to mount frames are assembled into a time series in `nfr_summary.xls`. After inspection of the test logs and engineering telemetry (GHz Antenna Position Encoder, Switching Mirror commanded position and, in some cases, selected filter bank counts), walls are inserted in the time series to isolate events when the configuration changed (*e.g.* fixture turned on the floor, switch to space view, antenna scanned or bumped through inadvertent contact). This allows a simple time-indexed lookup to find the appropriate pair of alignment datasets, from which to interpolate the scanner-mounts transformation to the time of a near-field scan.

Comparison of mechanical and RF boresights

On 2 occasions (once during pre- and once during post-environmental test FOV patterns) an additional station was used to determine directions of one face of the Secondary Reflector alignment prism in the cube frame. Directions of 2 faces of this prism, as well as prisms on the Primary and Tertiary Reflector, had been measured in the cradle frame, whose z_P axis was the best mechanical estimate of the antenna mechanical boresight, during antenna assembly. The other faces of this and the other prisms were all inaccessible (blocked or too steeply up or down) during FOV calibration, so the orientation of the prism frame, hence that of the

cradle frame, could not be determined with respect to the master frame. As a workaround, fictitious values for the pointing of the inaccessible face were determined by making 1) the angle between prism faces match that during antenna assembly; and 2) the azimuth angle ϕ of the z_P axis equal that of the RF boresight (analysis described below), both expressed in the mounts frame. The resulting zenith angles of the scan axis were 0.489° and 0.467°, whose bias and repeatability are plausible for removal and remount on the fixture. Moreover, the polar angle of cradle z_P (mechanical boresight) axis matched that of the RF boresight, again for both in the mounts frame, within %TBDPCS APE log? before and 0.002° after environmental tests.

Main-beam statistics

Describe best-fit Gaussian function to measured pattern peaks, resulting in HPBW and dFOV. Refined from UMLS to weight points correctly in dB space. Algorithm applies to RFE and NFR patterns; choice of dB cutoff is less critical for the latter, since all points in aperture field contribute to far-field pattern shape.

Reduction of Optical and RF Coincidence Data to Definitive dFOV

A model was developed and regressed for small misalignments, assumed to satisfy:

1. dFOV coincidence between radiometers can be attributed to small relative displacements in the phase centers for each radiometer, in the virtual focal plane seen by the antenna looking into the limb port, and

2. Direction of the reference dFOV (B8LF:PT), and its scan angle dependence, in the Instrument Mounts Frame (IMF), derived from the sensor alignment cube, arise from small misalignments of the coordinate systems which relate the scan axis and an equivalent surface normal vector, representing the nearly 90° rotation of the ray from virtual focus to limb port, into the antenna's RF boresight from the virtual focal plane through the antenna and to the IMF.

Neglecting its focusing properties, the antenna acts as a $\sim 90°$ folding mirror whose angle of incidence differs from 45° by δ_c radians. Thus we write the surface normal vector of that mirror as

$$\hat{n}_0 = \begin{pmatrix} \cos(\pi/4 - \delta_c) \\ \sin(\pi/4 - \delta_c) \\ 0 \end{pmatrix}$$

in an *unscanned* frame whose y axis is the scan axis and with $\hat{n}_0$ in the xy plane We express the misalignment of the scan axis from the y axis of the mounts frame with small components θ_x, θ_z, so that the transformation from *scanned* to mounts frame is

$$M = \begin{pmatrix} \cos\theta_z & -\sin\theta_z & 0 \\ \cos\theta_x \sin\theta_z & \cos\theta_x \cos\theta_z & -\sin\theta_x \\ \sin\theta_x \sin\theta_z & \sin\theta_x \cos\theta_z & \cos\theta_x \end{pmatrix}$$

M is an Euler 3–1–3 transformation with rotation angles $[0, \theta_x, \theta_z]$, and its center column is the scan axis expressed in the mounts frame.

Let $(\delta x_r, \delta z_r)$ represent the displacement of radiometer r's phase center from the boresight axis passing through the centers of tertiary and switching mirrors. $(\delta x_r, \delta z_r)$ are in units of radians obtained by dividing the offsets by the distance from the port center to the focal plane. Hence the chief ray from radiometer r's phase center (or image) to the tertiary, when transformed to the mounts frame, is given by

$$\hat{s}_1 = M \begin{pmatrix} \delta x_r \\ -\sqrt{1 - \delta x_r^2 - \delta z_r^2} \\ \delta z_r \end{pmatrix}$$

Finally, to relate the unscanned to scanned frames we calculate the elevation angle

$$\epsilon = (\epsilon_0 + \delta\epsilon + \texttt{APE})(\pi/180)$$

where `APE` is the GHz antenna encoder position, in degrees referred to the A side

ϵ_0 is the putative antenna elevation angle, determined *e.g.* from mechanical measurements

$\delta\epsilon$ is a small correction to ϵ_0 retrieved once for the entire calibration data set

so the transformation from unscanned to scanned frames is

$$S = \begin{pmatrix} \cos\epsilon & 0 & -\sin\epsilon \\ 0 & 1 & 0 \\ \sin\epsilon & 0 & \cos\epsilon \end{pmatrix}$$

and the effective surface normal, in the mounts frame, is

$$\hat{n} = MS\hat{n}_0$$

Both the image chief ray and the magnetic field unit vectors are reflected by the antenna according to Snell's reflection law:

$$\begin{aligned} \hat{s}_2 &= \hat{s}_1 - 2(\hat{n} \cdot \hat{s}_1)\hat{n} \\ \hat{H}_2 &= \hat{H}_1 - 2(\hat{n} \cdot \hat{H}_1)\hat{n} \end{aligned}$$

For each pattern measured, the spherical pointing angles θ, ϕ measured using theodolites are compared to angles resulting from the previous equations, in a spreadsheet summarizing all the FOV calibration pattern data. The unknown parameters are then δ_c, θ_x, θ_z and $\delta\epsilon$ (characteristics of the alignment of GHz antenna to radiometer, scan axis, and APE installation) and $(\delta x_r, \delta z_r)$ (2 values for each of the 5 GHz radiometers dependent on alignment of the multiplexer and receivers to the radiometer). These parameters are varied simultaneously to minimize the sum-squared differences of both angles, for all patterns. Although the spreadsheet was laid out to permit simultaneous solution of all $4 + 2 \times 5 = 14$ parameters in one operation, convergence was found to be much faster and more stable, with only slight penalty in the residual norm, by solving first for the R3 fiducials (B8LF:PT), then adding remaining R3, then R1A, R1B, R2 and R4.

$\delta\epsilon$ was separated from ϵ_0 to permit formulation of these equations as a linear function of parameters, which would readily yield *a posteriori* error estimates in a later version of this report. For now, the spreadsheet containing the data and equations retains the non-linear form shown above.

We construct the transformation **F** of Table 5.3 by defining the FOV frame to have $+z$ along the B8LF:PT boresight (average $\hat{s}_2$ over all fiducial patterns and x along the magnetic field vector $\hat{H}_2$, *i.e*

$$\begin{aligned} \hat{E}_2 &= \hat{H}_2 \times \hat{s}_2 \\ \mathbf{F} &= (\hat{E}_2 | \hat{H}_2 | \hat{s}_2) \end{aligned}$$

Since polarization was not measured in the THz FOV calibration, its FOV frame was defined using the boresight and scan axes determined above:

$$\begin{aligned} \hat{z} &= \hat{s}_2 \\ \hat{y} &= \frac{\hat{s}_2 \times \hat{n}}{||\hat{s}_2 \times \hat{n}||} \\ \hat{x} &= \hat{y} \times \hat{z} \end{aligned}$$

D.7.2 Definitive FOVs for L2PC

Errors introduced by Test Equipment

Text to flow from description of measurement system above. Figure D.16 shows the excellent repeatability of 640 GHz patterns measured on the near-field range before and after environmental tests. Add plots of convolved radiance differences and compare to calibration requirement.

Coverage of Scan Angle and Intermediate Frequency Spaces in Near-Field Range Patterns

Figure D.17 shows the scan angles of measured and interpolated patterns in the IF space of each GHz radiometer. Figures D.18–D.62 show the near and far field patterns at marked points in Figure D.17.

Figure D.9: Near Field Range in Building 306 High Bay Assembly and Test Facility. The black surfaces are composed of V groove absorber panels taped and tied to aluminum sheets. A probe horn is faintly visible in the gap between the 2 vertical absorber panels. This photo shows the UARS spare antenna mounted on the Field of View test fixture during initial testing of the range electronics. All of the electronics to run the testing are mounted in the gray racks behind the scanner. During flight calibrations, absorber panels cover the face of these racks. In addition, absorber panels are positioned between the scanner and the back wall of the test cell and covering portions of the FOV fixture that were observed to reflect signals back into the antenna.

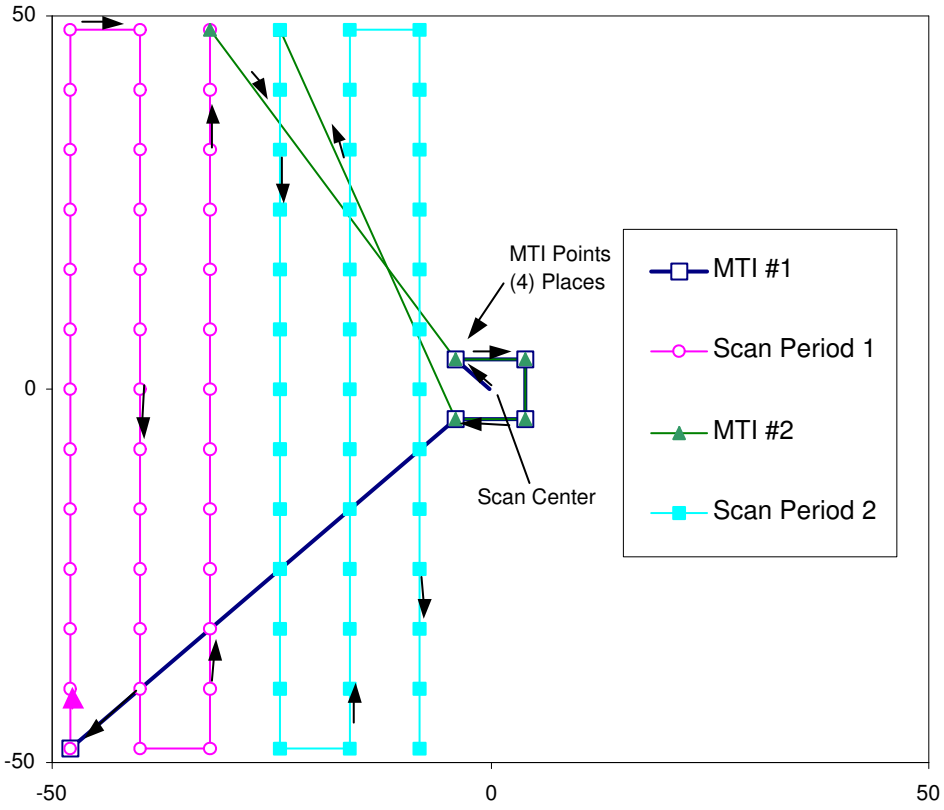

Figure D.10: Vertical Scan Pattern. Above is a sketch of a vertical scan pattern including two 4 point MTI scans. Amplitude and phase measurements are recorded in the HP 8530 during the vertical scan and transfered to the computer before moving on to the next vertical scan. An MTI measurement is made at the beginning and end of each scan, and approximately every 5 minutes during the scan.

Table D.1: Scattering Losses Calculated from Reflector Surface Errors

	R1A,B	R2	R3	R4
Scattering loss $1-\eta$	0.0003	0.0007	0.0012	0.0084

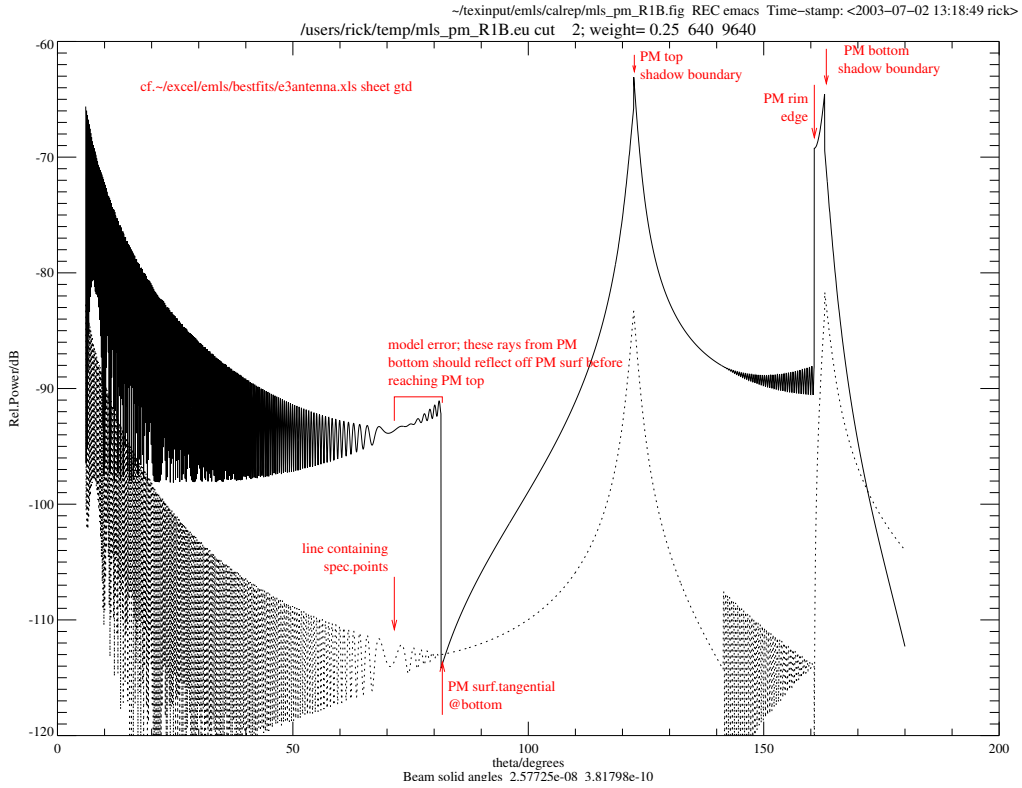

Figure D.11: Edge Diffracted Field in $-x_P, z_P$ half-plane of R1B FOV

Table D.2: Calculated from GTD Analysis Applied to Primary Reflector Edge

	R1A	R1B	R2	R3	R4
Ω_P/sr, beam solid angle of definitive FOV	8.9×10^{-6}	8.7×10^{-6}	4.3×10^{-6}	2.7×10^{-6}	5.2×10^{-7}
Ω_{GTD}/sr, beam solid angle of edge-diffracted pattern	8.5×10^{-9}	2.9×10^{-8}	6.2×10^{-10}	3.7×10^{-10}	1.4×10^{-11}
η_{diff}, edge diffraction efficiency	0.9990	0.9967	0.99986	0.99986	0.99997

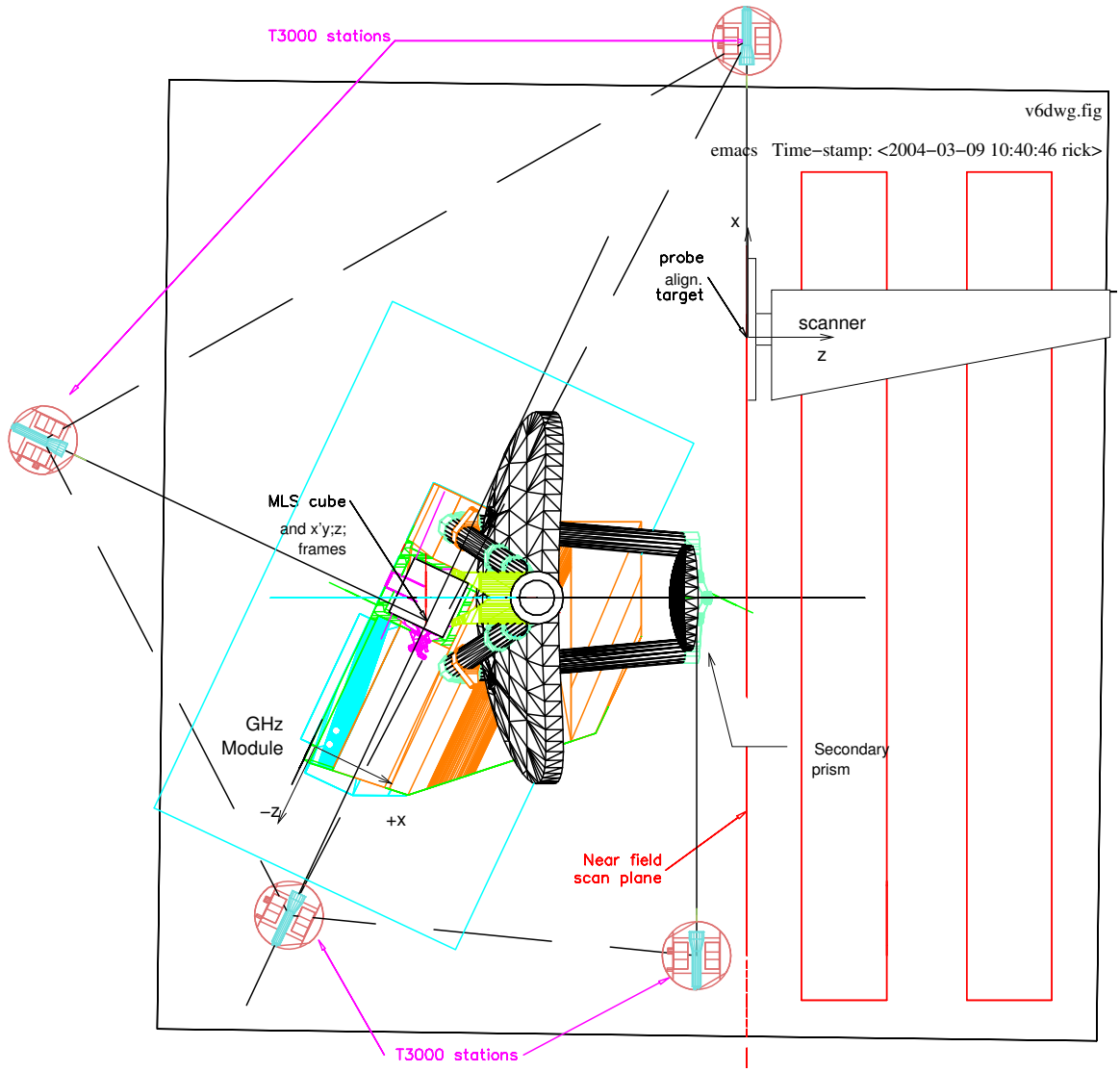

Figure D.12: Plan view of GHz module in Near Field Range, showing T3000 theodolite stations for measuring alignment of module cube and Secondary Reflector prism relative to scanner.

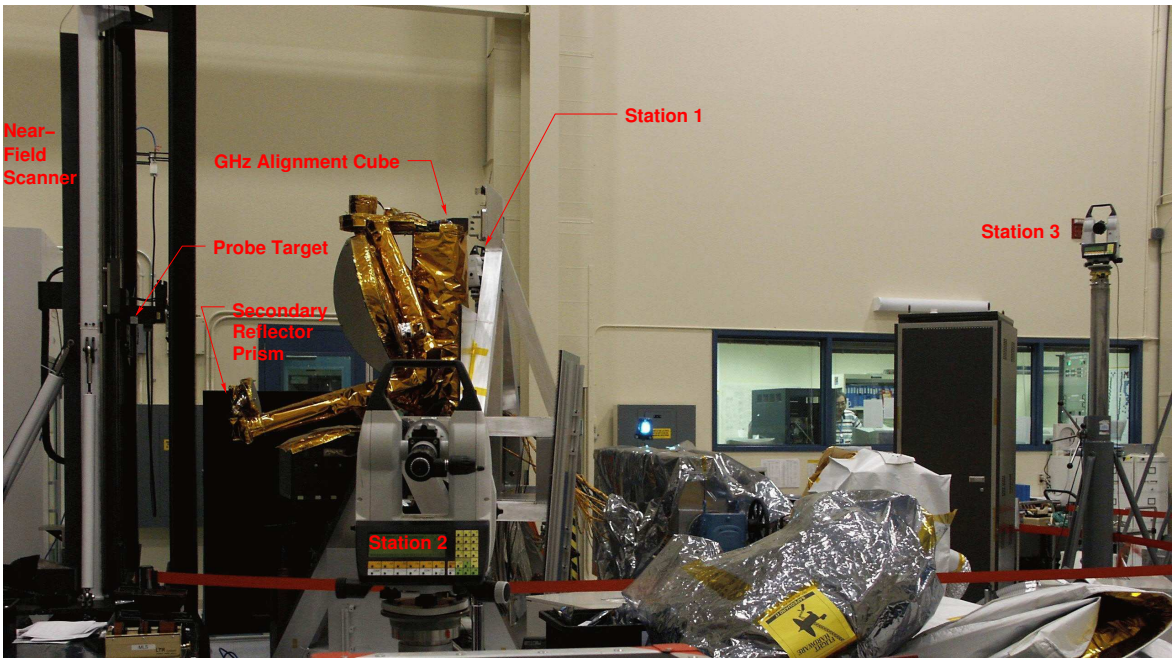

Figure D.13: Determination of FOV direction with respect to GHz Module alignment cube.

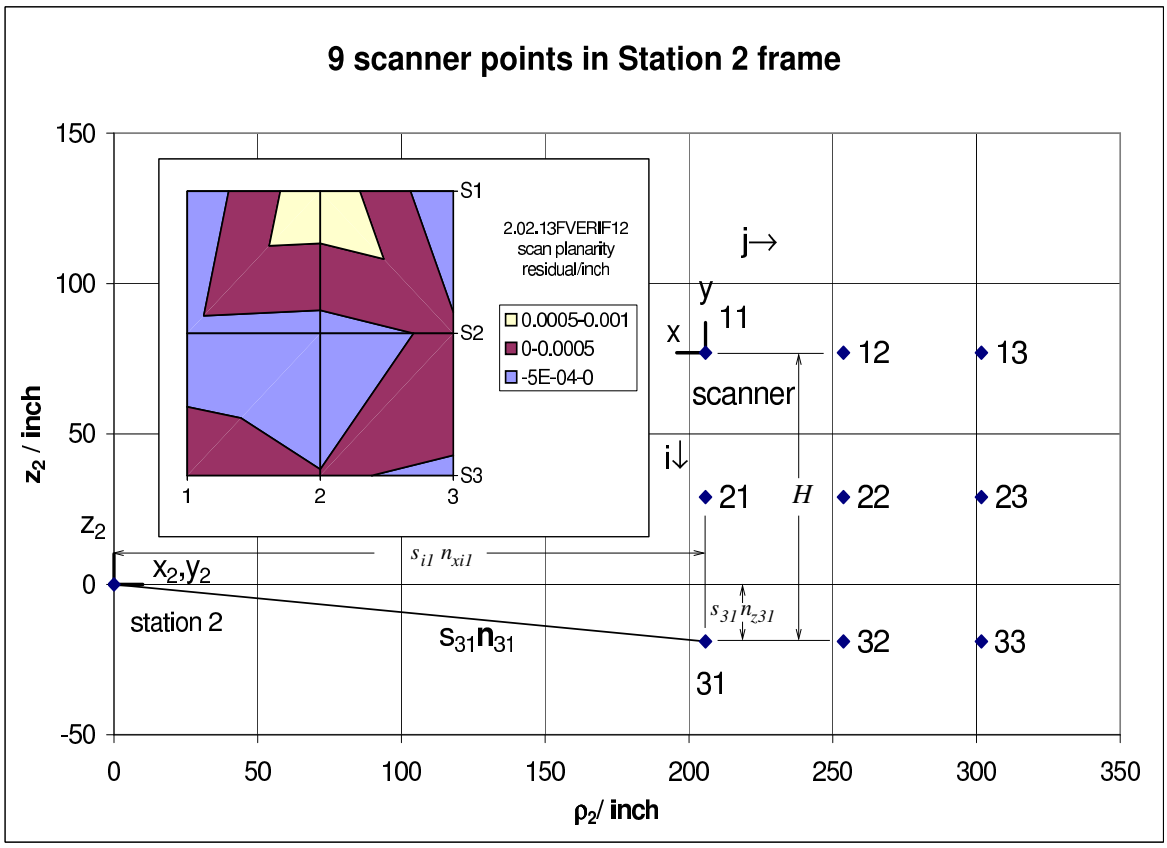

Figure D.14: Schematic view of scan plane for alignment measurements. The inset shows residuals from the best-fit scan plane.

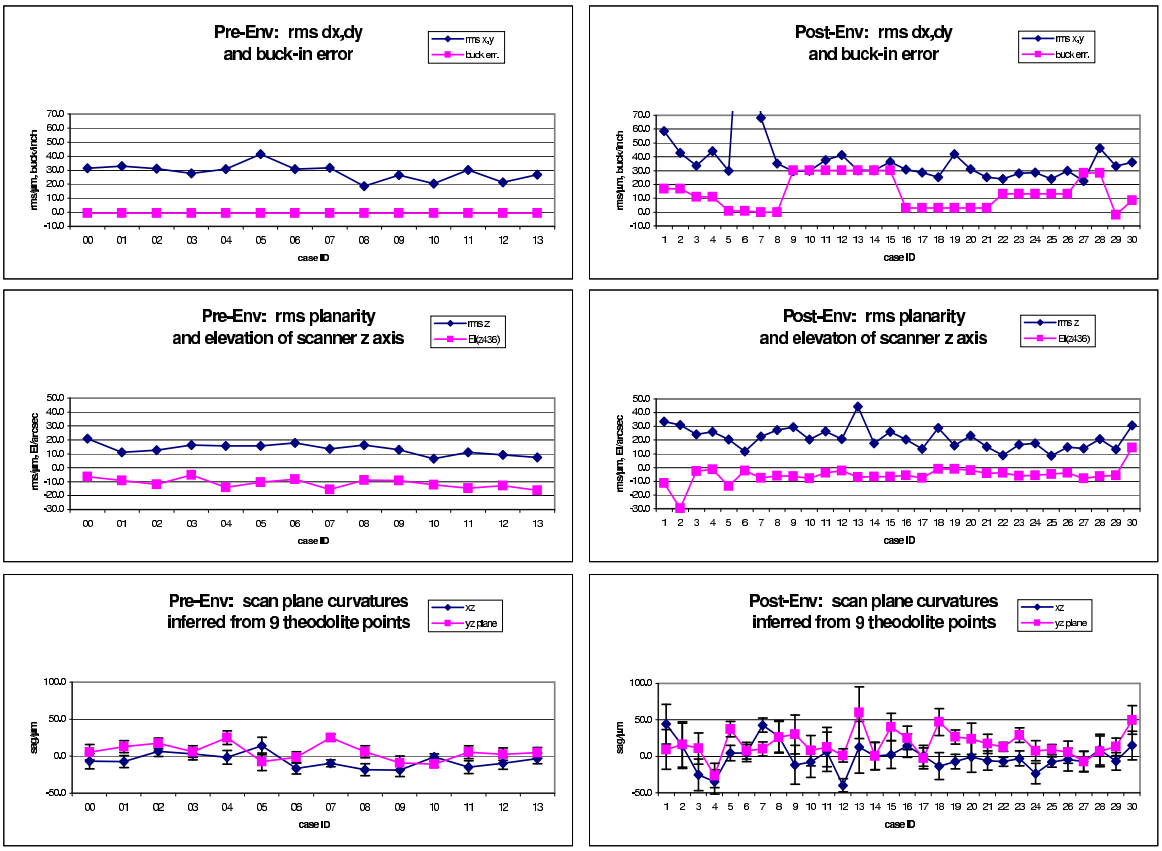

Figure D.15: Time series of optical alignment performance metrics.

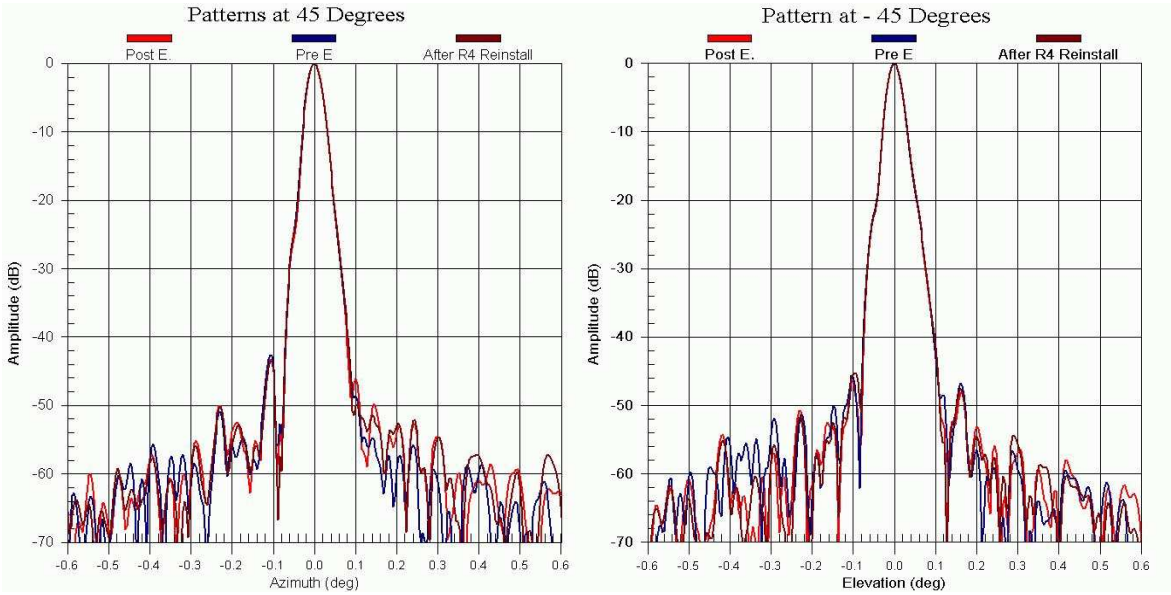

Figure D.16: Antenna pattern cuts in diagonal planes before and after environmental tests and removal/remount of the R4 RFE.

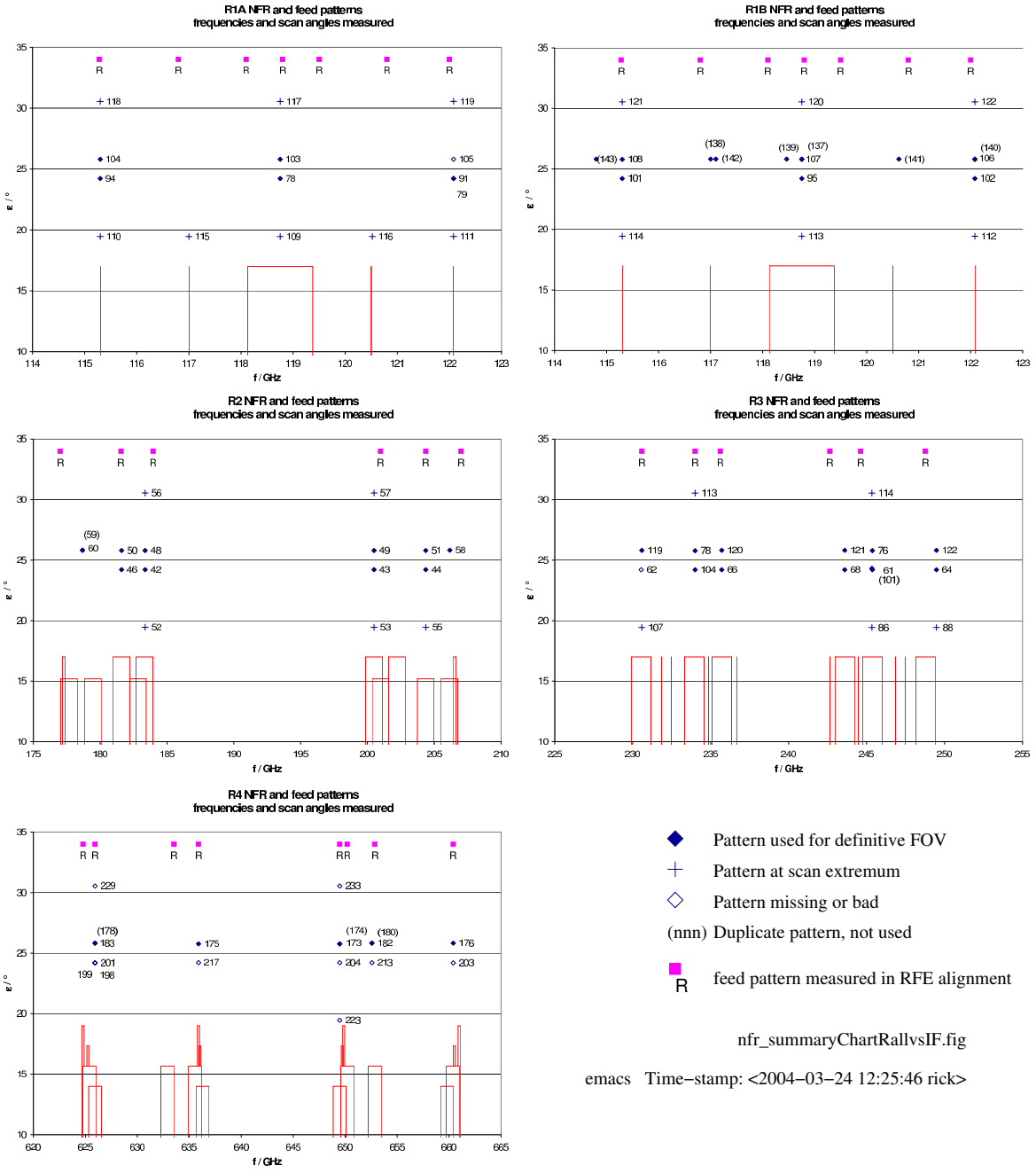

Figure D.17: Distribution of measured and interpolated patterns in IF spaces of GHz radiometers. Scan angle ϵ applies to antenna patterns measured on the Near Field Range, not feed patterns measured in receiver alignment.

Figure D.18: Near and Far-Field antenna patterns in the R1A radiometer TBR.

Figure D.19: Near and Far-Field antenna patterns in the R1A radiometer TBR.

Figure D.20: Near and Far-Field antenna patterns in the R1A radiometer TBR.

Figure D.21: Near and Far-Field antenna patterns in the R1A radiometer TBR.

Figure D.22: Near and Far-Field antenna patterns in the R1A radiometer TBR.

Figure D.23: Near and Far-Field antenna patterns in the R1A radiometer TBR.

Figure D.24: Near and Far-Field antenna patterns in the R1A radiometer TBR.

Figure D.25: Near and Far-Field antenna patterns in the R1B radiometer TBR.

Figure D.26: Near and Far-Field antenna patterns in the R1B radiometer TBR.

Figure D.27: Near and Far-Field antenna patterns in the R1B radiometer TBR.

Figure D.28: Near and Far-Field antenna patterns in the R1B radiometer TBR.

Figure D.29: Near and Far-Field antenna patterns in the R1B radiometer TBR.

Figure D.30: Near and Far-Field antenna patterns in the R1B radiometer TBR.

Figure D.31: Near and Far-Field antenna patterns in the R1B radiometer TBR.

Figure D.32: Near and Far-Field antenna patterns in the R1B radiometer TBR.

Figure D.33: Near and Far-Field antenna patterns in the R2 radiometer TBR.

Figure D.34: Near and Far-Field antenna patterns in the R2 radiometer TBR.

Figure D.35: Near and Far-Field antenna patterns in the R2 radiometer TBR.

Figure D.36: Near and Far-Field antenna patterns in the R2 radiometer TBR.

Figure D.37: Near and Far-Field antenna patterns in the R2 radiometer TBR.

Figure D.38: Near and Far-Field antenna patterns in the R2 radiometer TBR.

Figure D.39: Near and Far-Field antenna patterns in the R2 radiometer TBR.

Figure D.40: Near and Far-Field antenna patterns in the R2 radiometer TBR.

Figure D.41: Near and Far-Field antenna patterns in the R2 radiometer TBR.

Figure D.42: Near and Far-Field antenna patterns in the R2 radiometer TBR.

Figure D.43: Near and Far-Field antenna patterns in the R2 radiometer TBR.

Figure D.44: Near and Far-Field antenna patterns in the R2 radiometer TBR.

Figure D.45: Near and Far-Field antenna patterns in the R3 radiometer TBR.

Figure D.46: Near and Far-Field antenna patterns in the R3 radiometer TBR.

Figure D.47: Near and Far-Field antenna patterns in the R3 radiometer TBR.

Figure D.48: Near and Far-Field antenna patterns in the R3 radiometer TBR.

Figure D.49: Near and Far-Field antenna patterns in the R3 radiometer TBR.

Figure D.50: Near and Far-Field antenna patterns in the R3 radiometer TBR.

Figure D.51: Near and Far-Field antenna patterns in the R3 radiometer TBR.

Figure D.52: Near and Far-Field antenna patterns in the R3 radiometer TBR.

Figure D.53: Near and Far-Field antenna patterns in the R3 radiometer TBR.

Figure D.54: Near and Far-Field antenna patterns in the R3 radiometer TBR.

Figure D.55: Near and Far-Field antenna patterns in the R3 radiometer TBR.

Figure D.56: Near and Far-Field antenna patterns in the R3 radiometer TBR.

Figure D.57: Near and Far-Field antenna patterns in the R3 radiometer TBR.

Figure D.58: Near and Far-Field antenna patterns in the R4 radiometer TBR.

Figure D.59: Near and Far-Field antenna patterns in the R4 radiometer TBR.

D.7.3 FOV Variability due to Scan Angle and Frequency Dependence of FOVs

Scan Angle Dependence of FOVs

Figures in Chapter 4 show the collapsed FOV patterns at all frequencies measured on the NFR. The patterns are averages of collapsed patterns at $\epsilon = 24.2°$ and 25.8°, corresponding to tangent heights $h_T = 82$ km and 0 km respectively, except

```
B32LW:PT.C1  pattern #105 ($25.8^\circ$) N/A
B9LF:CO.coll4096     #62  (24.2       ) bad
B31LM:BRO            #199  24.2         N/A
B13LF:HCL            #198-201 #         N/A
B29LM:HOCL           #217  24.2
B10UF:CLO            #204  24.2
B12UF:N2O            #213  24.2
B14UF:O3             #203  24.2
```

The previous list shows R4 patterns only available at 25.8; Check in PSR, PER and with Paul whether we have any showing scan (in)dependence

The following note from ftp/.../emls/FOVcal/readme, explains why `R1B/B26LD:PTdualpol.coll4096`, made from 82km pattern only, differs at -52dB level from B21 pattern made from 0 and 82km patterns.

```
Thu Jun 12 10:51:36 PDT 2003
Posted DACS polarization-separated patterns made Jun 9 from hT=82km patterns
  R1A/B22LD:PTdualpol.coll4096
  R1B/B26LD:PTdualpol.coll4096

also replaced DACS patterns R1A/B22LD:PT.coll4096
                        and R1B/B26LD:PT.coll4096
These used to be averages over hT=0 and 82km patterns; replace by 82km only.
They now satisfy   g = g|| + gX   for all angles, within ~-70dB; viz.
  IDL> restore,'R1A/B22LD:PT.coll4096'
  IDL> restore,'R1A/B22LD:PTdualpol.coll4096'
  IDL> print,min(g1d-(g1dcopol+g1dXpol),max=temp),temp
   -5.96046e-08  5.96046e-08
and likewise for R1B/B26LD:PT.
```

Figure D.60: Near and Far-Field antenna patterns in the R4 radiometer TBR.

Figure D.61: Near and Far-Field antenna patterns in the R4 radiometer TBR.

Figure D.62: Near and Far-Field antenna patterns in the R4 radiometer TBR.

Frequency Dependence of FOVs

Collapsed patterns for bands not measured on the NFR are supplied by linear interpolation between patterns at the two nearest frequencies. To account for first-order frequency dependence, the horizontal (angle ϵ) axis of each neighboring pattern is scaled to the frequency of the interpolant before point-wise interpolation. Of the 25 patterns produced by interpolation, 8 are actually extrapolations; the most extreme of these is

`B33LW:O3.C1` 236.660 GHz ← `B7LF:O3` 235.715 GHz, `B8LF:PT` 233.951 GHz

and its USB image; these are 54% outside the range of available data, and show no ill effect due to extrapolation. When the interpolant lies within 5% of one available pattern, relative to the difference of available frequencies, it is obtained by frequency-scaling of its nearest neighbor, rather than interpolation.

Plots and discussion of convolved radiances here, to support assertion in next section that FOV calibration requirement is met for previously noted scan angle and IF dependences. Caption to Figure D.63 shows it may belong in §D.7.2.

D.7.4 Conclusions

D.8 Measured Reflectivity of Witness Specimens

Two witness specimens were provided from the fabrication of the GHz MLS Primary reflector. These were made of the same composite material and were given the same surface treatment (vacuum-deposited Aluminum and grit blast) as the Primary reflector throughout manufacture, except for the lay-up on a graphite mold to form curvature of the reflector.

An insertion loss measurement had been devised to measure reflectivity at the UARS MLS frequencies using its engineering model ([**?**]). Figure D.64 shows the schematic optical path for EOS MLS on the calibration fixture. The configuration is like that of Figure 3.8 but with SW1 and subsequent equipment replaced by a frame on which the witness sample and a silver reference plate can be clamped to view the cold load below. The sample size (12 inch × 13 inch to circumscribe the nominal beam contour at -75dB, and 0.010 inch flatness) covered > 0.9999 of the radiometer space-view beam off the LSC2 mirror, for viewing a cold load (foam absorber immersed in liquid nitrogen at the bottom of a metal vessel). The view was switched between the cold load and the internal ambient target (25°C) according to the

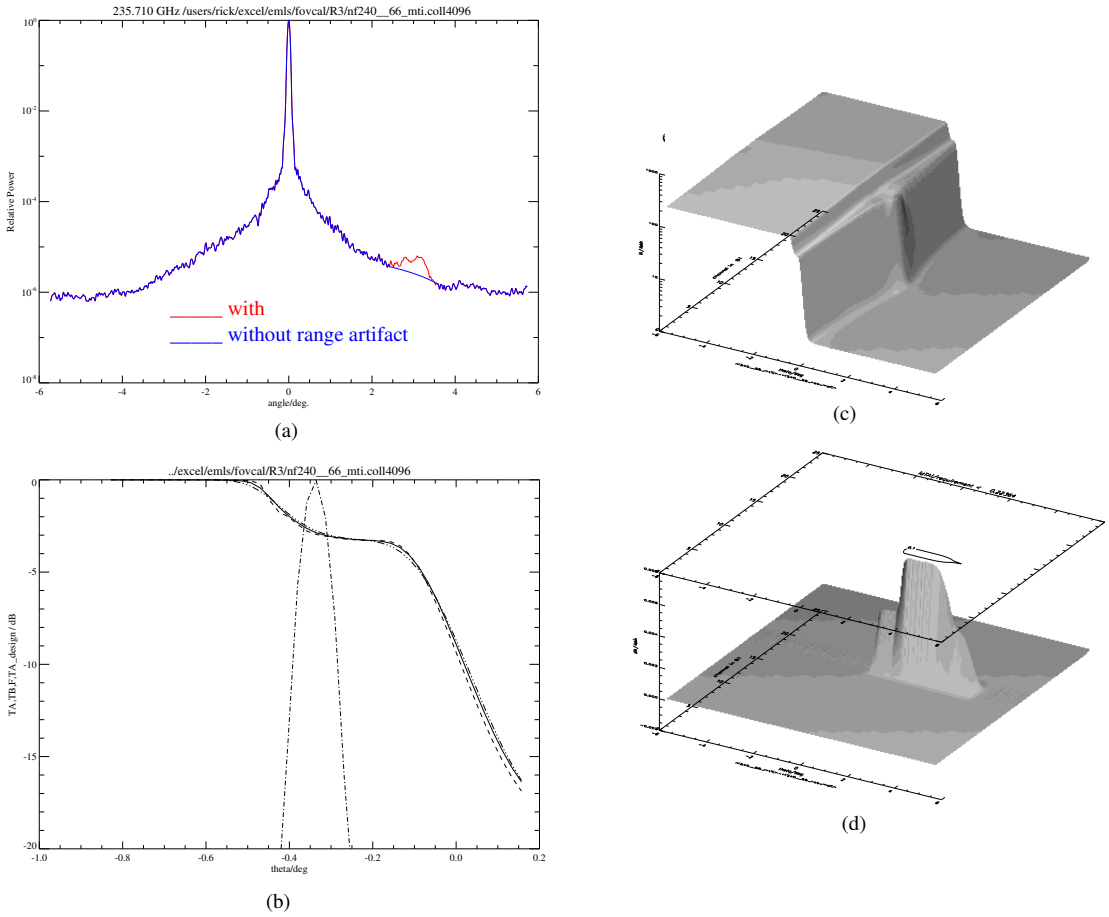

Figure D.63: Convolutions of measured FOVs to address calibration requirement: (a) collapsed patterns with and without range artifact, (b) T_A, T_B and $G(\epsilon)$, (c) spectrum of T_A *vs.* tangent height, and (d) spectrum of ΔT_A showing fraction of calibration budget consumed.

Table D.3: Measured Reflectivities of Witness Specimens. expand to separate 2 samples x 10 bands

		R1	R2	R3	R4
Reflectivity	ρ_r^1	0.9982	0.9974	0.9945	0.9882
uncertainty	1σ	0.0004	0.0001	0.0002	0.0007

following switching sequence:

<start MMAF> T S T I S S' <end MMAF>

where T = 4.5 second dwell at internal target followed by 0.5 second allowance for Switching Mirror motion.
S = 4.5 second dwell at space port followed by 0.5 second allowance for Switching Mirror motion.
S' = 4.7 second dwell at space port
I = Increment bus sniffer MMAF counter, to trigger LED indication every 4 MMAFs.

After 4 or more MAFs of this sequence, the test sample was replaced by a silver-plated standard of the same size, for the next 4 MAFs.

At the time of this test, the available standard filter banks provided data in bands B1 (R1), B2–5 (R2), B7 (R3) and B11–14 (R4). Figure D.65 shows a time series of band-averaged counts for filter bank 13 and sample PM#1. The colors show the filter bank data after removing MMIFs when the plates were being interchanged, and sorting into Target, sample or standard bins. Assuming the GHz mirror switching frequency is sufficiently high to capture drifts to LN_2 loss and thermal gradients in the high bay, the reflectivity relative to the standard is

$$I = \left\langle \frac{\langle C^{\text{ambient}} - C^{\text{sample}} \rangle_{\text{MMIF}}}{\langle C^{\text{ambient}} - C^{\text{standard}} \rangle_{\overline{\text{MMIF}}}} \right\rangle_{\substack{\text{channels,} \\ \text{filterbanks}}}$$

where C^X = Counts viewing source X, and
$\langle\rangle_E$ = average over ensemble E

Reflectivities relative to the standard are shown in Figure D.66 shows total ohmic losses calculated from the measurements combined with theoretical reflectivities of the standard plate (*e.g.* 0.9988 at 200 GHz[**?**]), and after averaging over filter bank channels and MMIFs. Table D.3 gives values and uncertainties after further averaging over radiometer bands and samples for input to the flight science software (Level 1 and forward model).

D.9 Radiometer FOV patterns

Receiver Front End (RFE) patterns were measured before delivery of the subsystems for integration into the MLS radiometer chassis, as part of RFE alignment [**?**]. The same interferometers developed for the sensor FOV tests were used to obtain amplitude and phase patterns of the RFEs at frequencies shown in Figure D.17. The same analysis was applied to these patterns as described above for the sensor FOVs, through calculation of beam efficiency.

Figure D.67 shows the Engineering model RFE 2 in the anechoic chamber for RFE patterns. Figure D.68 and Figure D.69 show pattern cuts from one frequency of the flight RFE

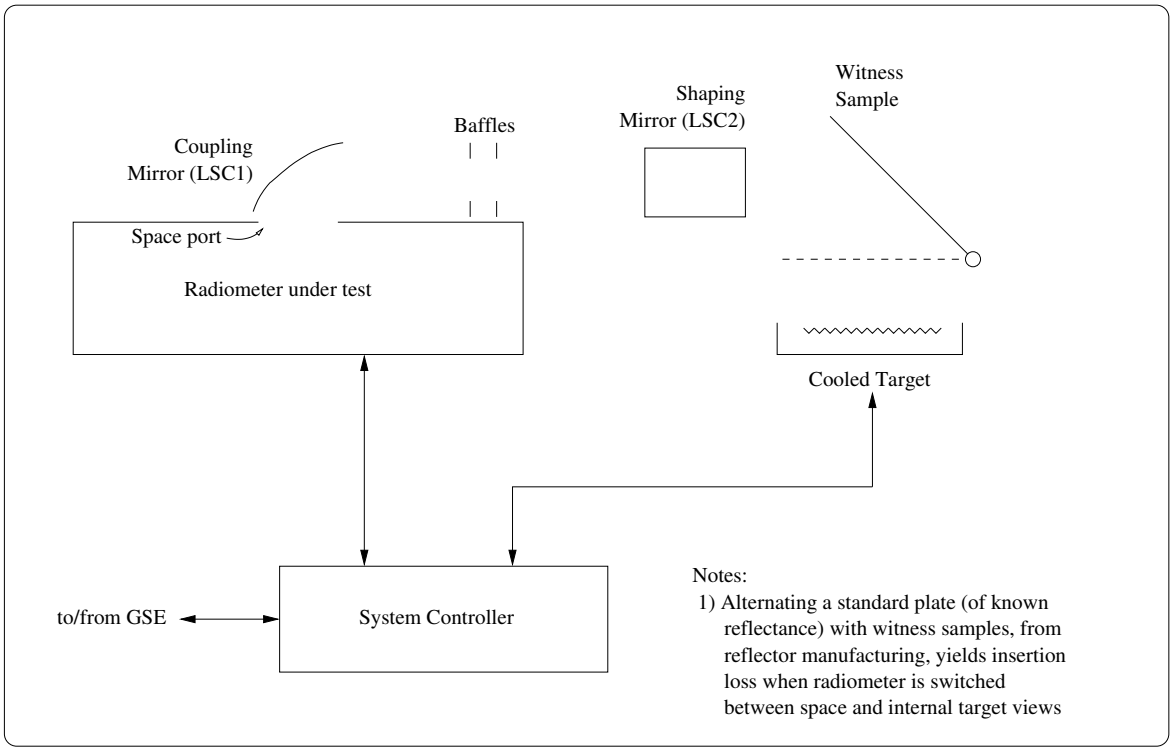

Figure D.64: Setup used to measure GHz antenna ohmic loss. The optics which focus the radiometer FOVs onto the reflector witness samples are described previously for spectral calibration.

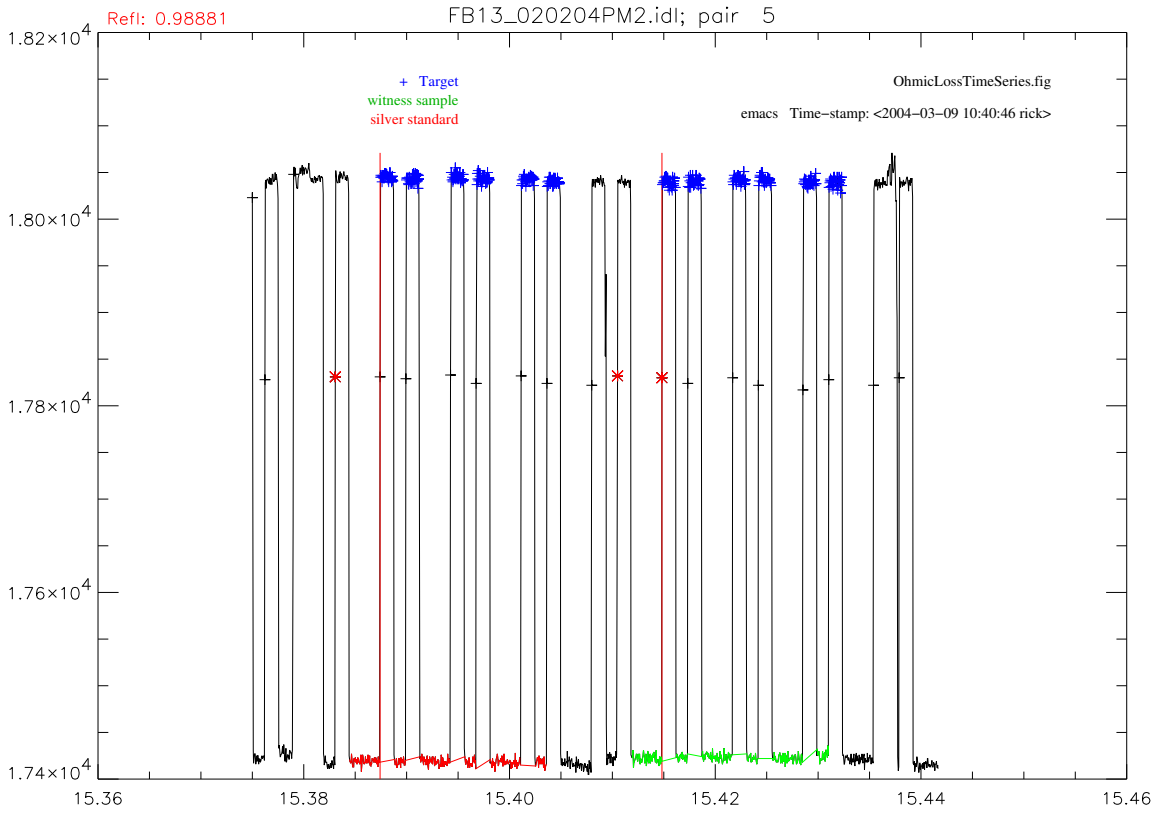

Figure D.65: Ohmic Loss Level 0 Time Series.

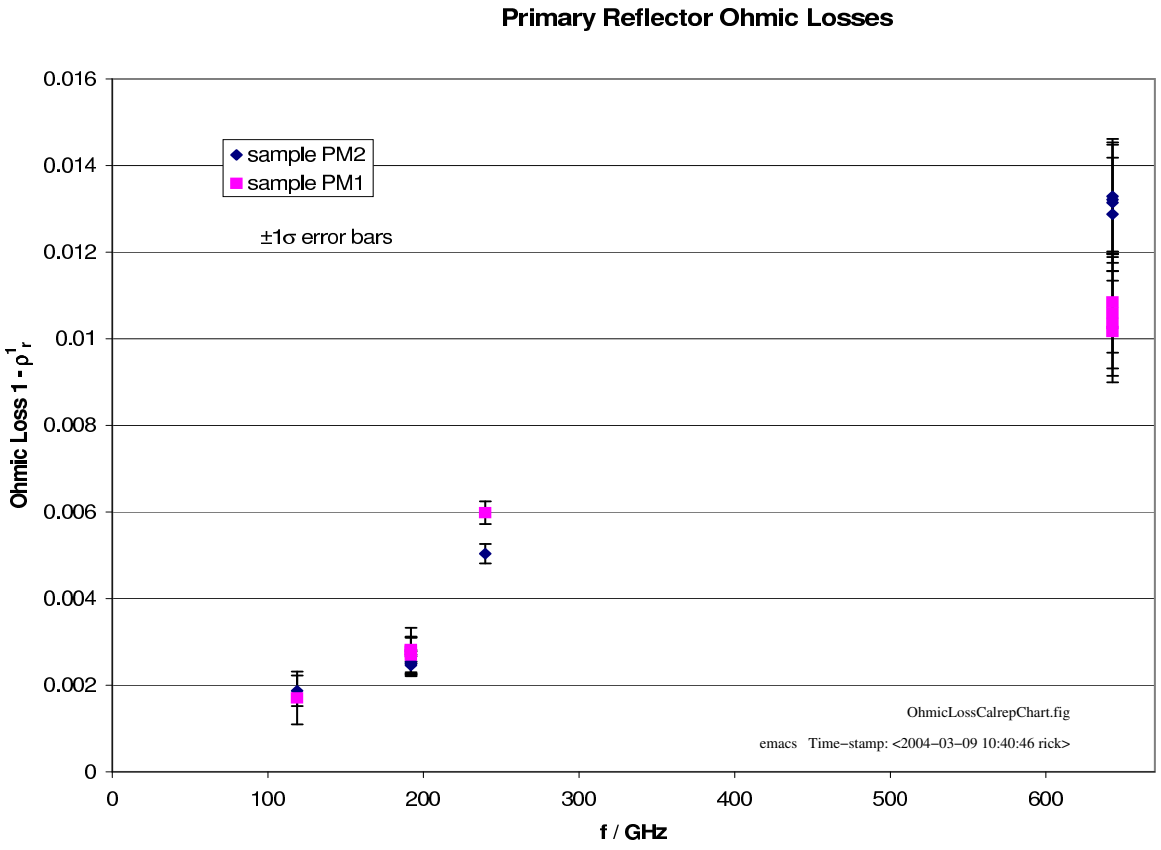

Figure D.66: Antenna Ohmic Losses. Results are displayed at the radiometer LO frequency, since the radiometric measurement combines upper and lower sideband reflectivities. 4 bands were measured in each of R2 and R4.

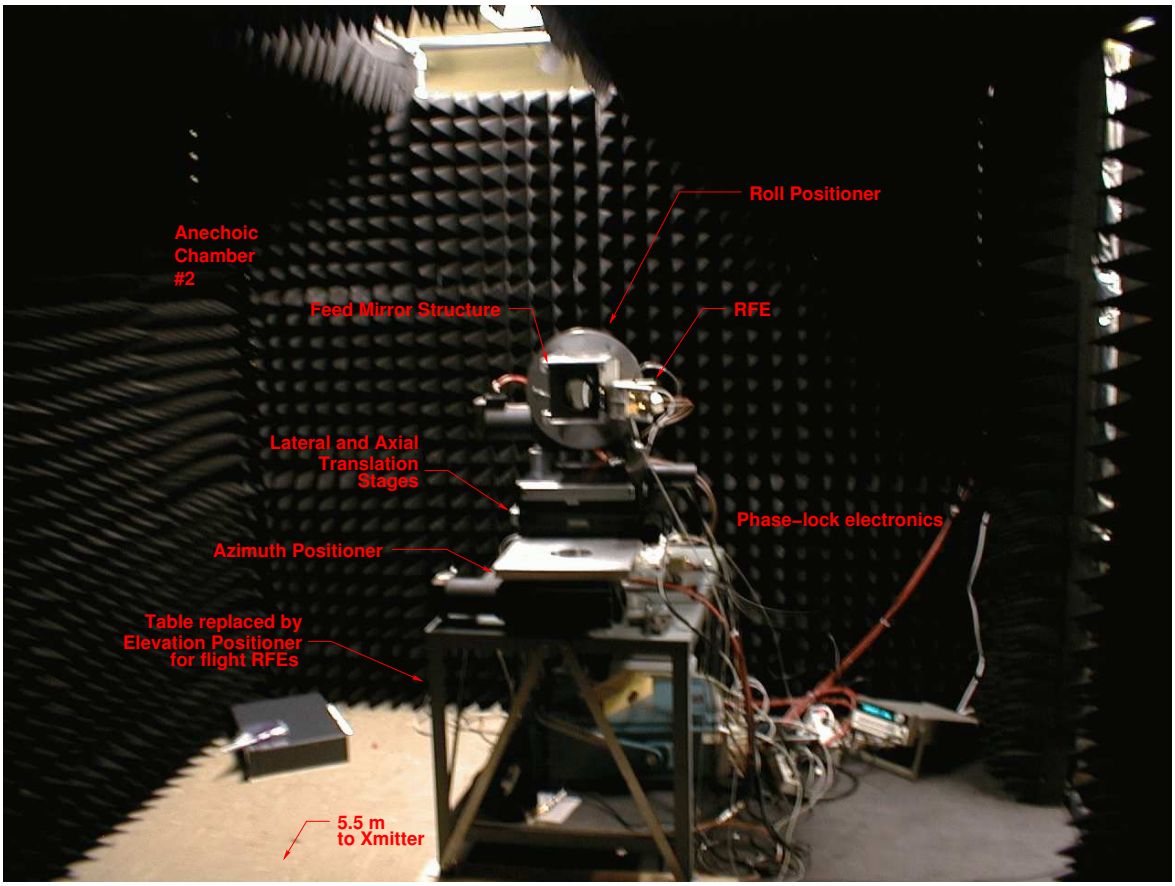

Figure D.67: Engineering Model RFE 2 in anechoic chamber for alignment and feed pattern measurement.

3 patterns, and Figure D.70 compares the aperture field projected from these patterns with that measured on the Near Field Range.

The FOV integration giving beam efficiencies was repeated, substituting for HPBW and 2.5×HPBW the angles subtended by limb, target and space port outlines, as well as the projected outlines of antenna reflectors. Integrated beam solid angles were normalized and delivered as Level 1 inputs for radiometric calibration (Chapter 2) and antenna radiance offsets (Chapter 4).

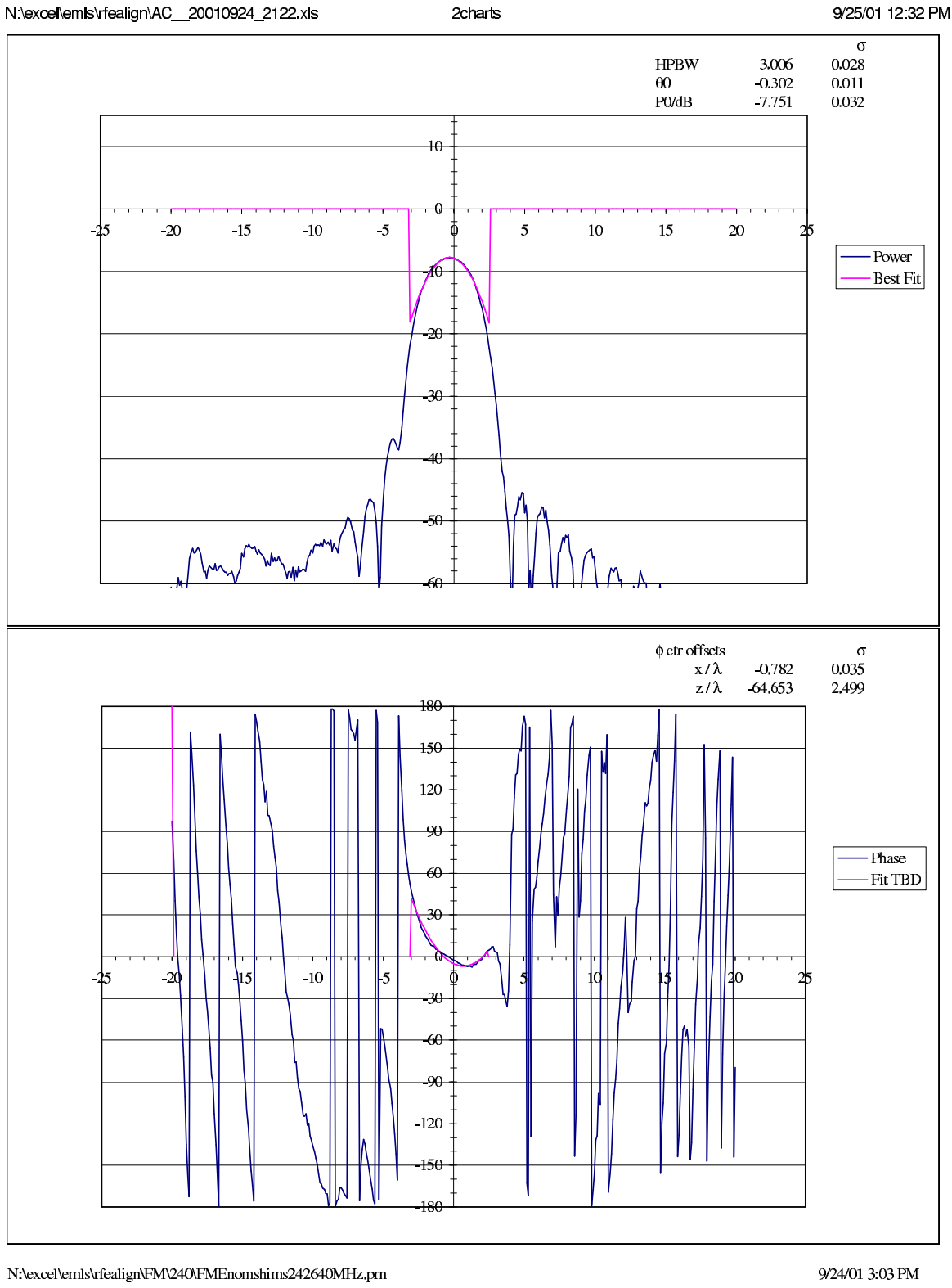

Figure D.68: amplitude/phase cut of an RFE pattern.

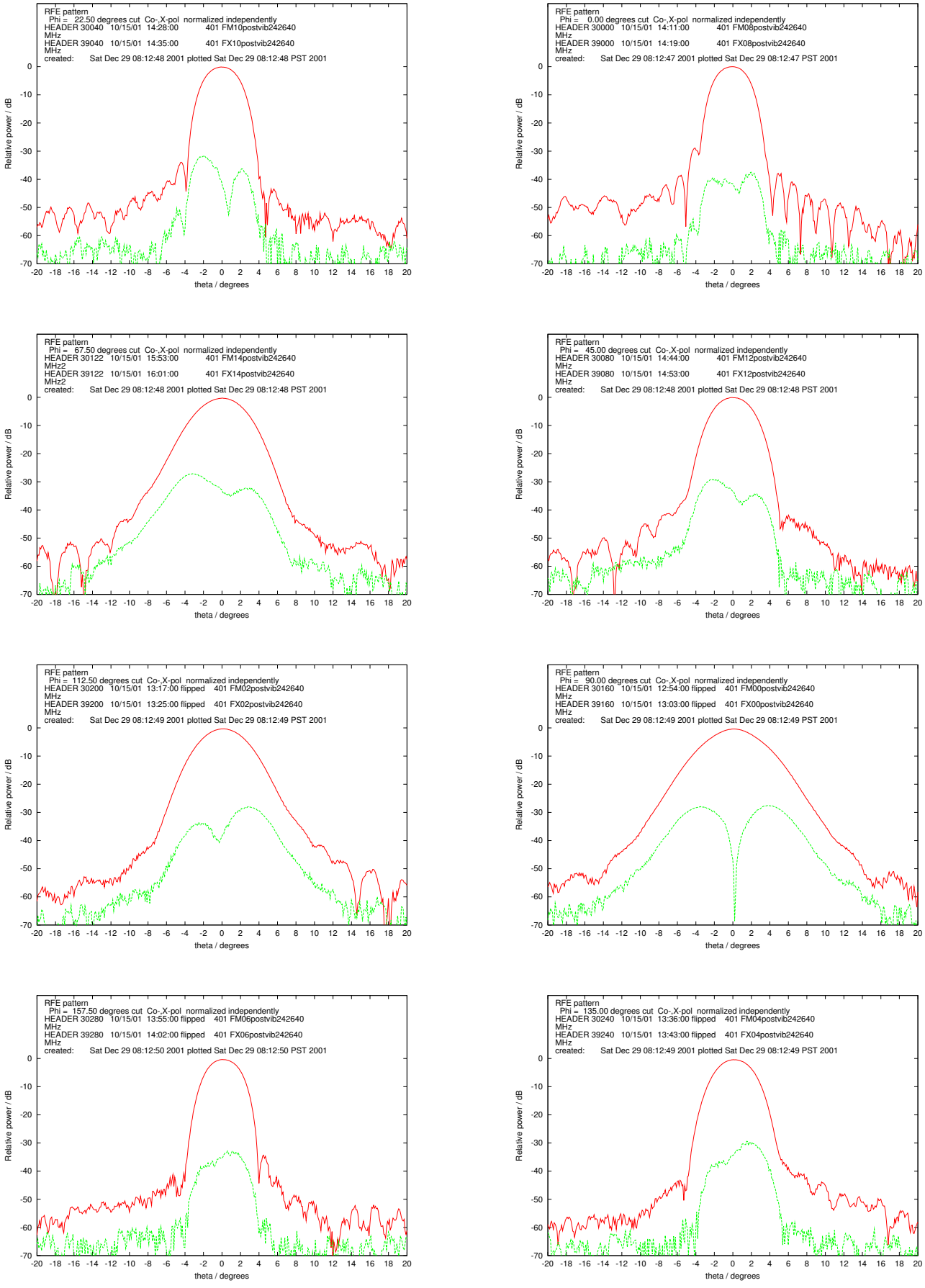

Figure D.69: Co- and cross-polarized amplitude cuts of an RFE pattern.

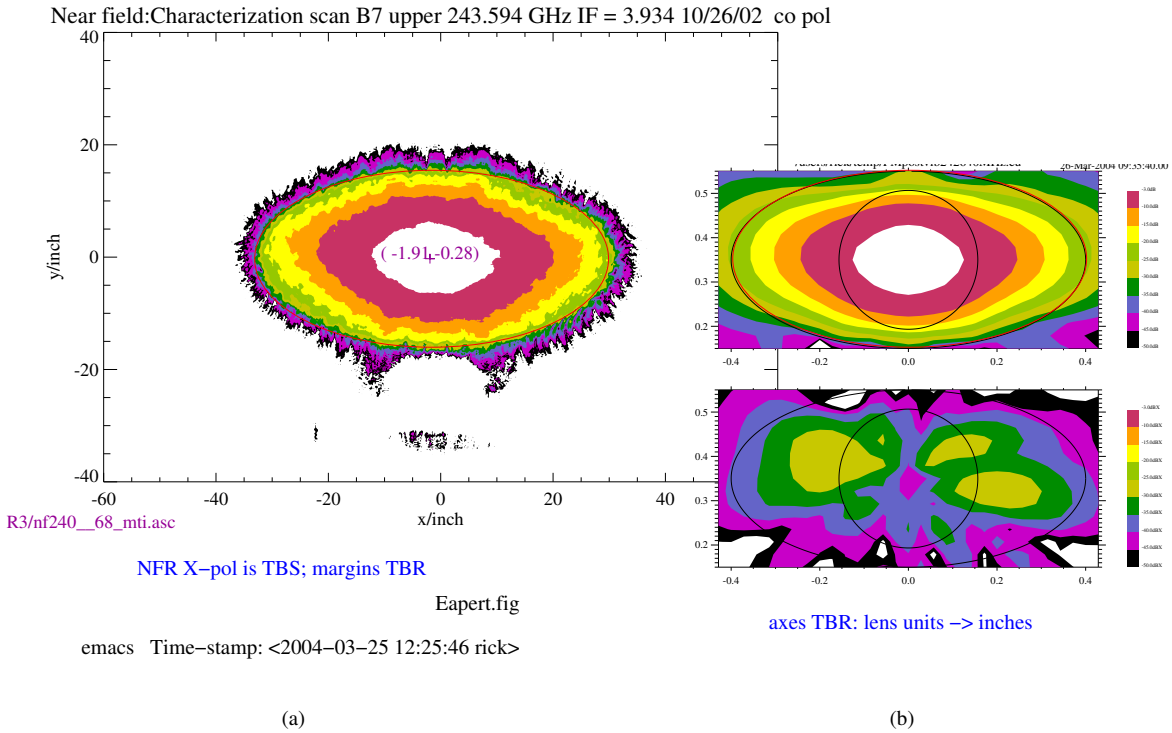

Figure D.70: 242.64 GHz Aperture Field: (a) Near Field measurement compared to (b) projection from RFE patterns (both polarizations).

Appendix E

Calibration Files and Programs

The numerous data tables plots and presented in this report were created with the use of application specific analysis and plotting code. Some data sets required pre-processing by Level 1 software with special overrides to redefine the radiometric calibration data measurements. A few Level 1 processing runs required slightly modified versions of the code to be created, to allow for such things as forcing some calibration views to be treated as views to fixed radiances, although later versions of the Level 1 code even allowed such details to be covered by overrides. Numerous programs (typically written in IDL) were used to further analyze both raw and Level 1 data. Given this enormous code base, we choose not to present it here, but details on specific analyses, including the code, can be obtained from the authors on request.

E.1 GHz Radiometric data files

The GHz radiometric calibration data are sufficiently compact that they have been reproduced in their entirety in this report.

E.2 GHz Spectral data files

The high resolution sweep files, used as channel position and shape data by the forward model software, are located in `/nas/gse/data/FESweep/`, with file names and contents as described in section 3.10 of Volume 1. Data files are provided for all filters and filterbanks, and for all signal paths that can be implemented by the GHz IF Switch Network.

The GHz relative sideband data used by Level 2 processing have been reproduced in full in the body of this document.

E.3 GHz FOV data files

E.4 THz data files

The high resolution sweep files for the THz bands are located in the same locations as the corresponding GHz data. For the THz data files the parameter `Zero_IF_frequency` assumes the *nominal* GLLO center frequency, and the user must be aware that this can wander by the

order of a MHz during each orbit. It is an additional task of the THz data analysis software to estimate the true frequency of the GLLO.

Appendix F

Bus Sniffing Calibration Controllers

A significant improvement in the calibration strategy over UARS MLS was that any calibrations that used instrument Science Data[1] had external calibration equipment operation synchronized tightly to instrument internal timing. In the UARS implementation, the GSE computer tracked instrument operation via the data stream generated by the Spacecraft Interface Simulator. This meant that the delay between a calibration configuration change, and the event being observed in the data stream, amounted to between ∼4 and ∼6 seconds (due to the MIF duration of 2.048 s, and the instrument and simulator data buffering). Until this change had been observed, and sufficient data accumulated, the GSE was unable to step the calibration equipment to its next setting. This resulted in high-resolution spectral sweeps taking 4 to 6 hours for a single 15-channel filterbank, and similar timescales for a minimal Fabry-Pérot sweep. Most of the 'wall clock' time for these calibrations was wasted in the sense that the majority of the data were not of value. The EOS instrument has almost an order of magnitude more filter channels than UARS, and the desire was to complete all of the calibrations in the same time or less, and to higher quality.

Three major contributors to achieving these goals were:

(1) Improved calibration approaches for some measurements,

(2) improved calibration equipment implementation, and

(3) tight synchronization between instrument operation and calibration equipment.

The improvements in calibration methods and equipment are discussed in Volume 1 of this document, and in the remainder of this chapter we discuss the method used to achieve tight calibration synchronization with the instrument operation.

F.1 Calibration Controller

Several interim calibration controllers were developed, but only the final version (used for high-resolution spectral and GHz relative sideband calibrations) will be discussed here. The EOS MLS instrument presents an optically-isolated copy of the internal RS-485 bus (read-only) on an external connector specifically to support calibrations. The bus carries all of the 500 kbps serial traffic between the master and slave RIUs, and also the Sync signal

[1] In this context, Instrument Science Data consists primarily of filterbank and DACS data.

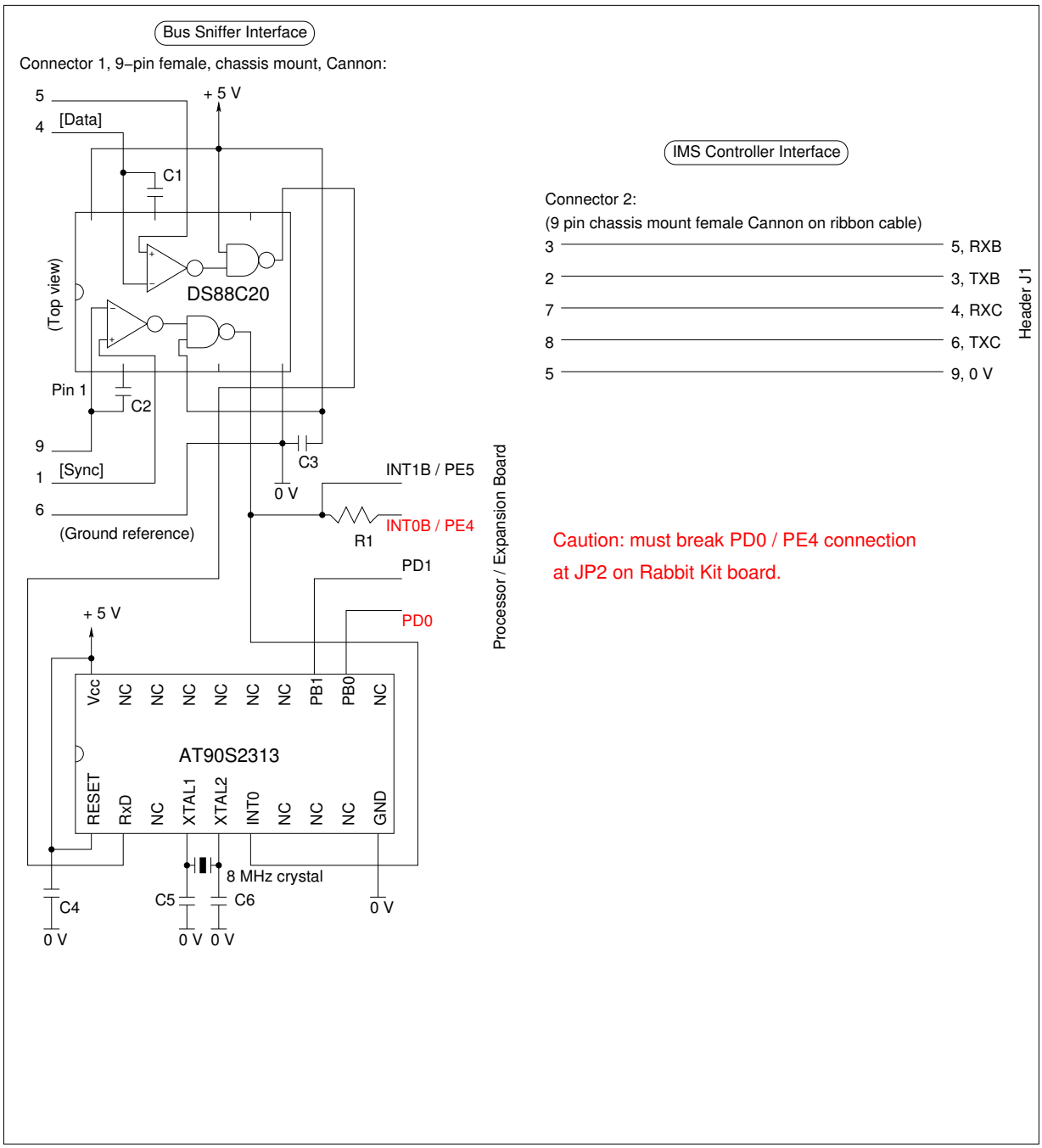

Connector 1: 9 pin Cannon, female

Connector 2: 9 pin Cannon, female (on ribbon cable)

Connector 3: 9 pin Cannon, male

C1, C2 = 0.01 uF ceramic; C3, C4 = 0.1 uF ceramic; C5, C6 = 20–33 pF ceramic (see resonator specs).

R1 = 1 kOhm

/users/jarnot/texinput/figures/Rabbit_AVR_Sniffer.fig

Figure F.1: Typical circuitry added to a Rabbitsemiconductor Rabbit 2000 Basic Development Kit to provide calibration equipment synchronization and control.

which marks the beginning and end of data integrations. The MLS switching and scanning mechanisms also use the Sync pulse to trigger mechanism movements. The task of the Calibration Controllers was to monitor and decode bus traffic to determine 'time' in MIF coordinates, and operate calibration equipment such as synthesizers, translation stages and switching mirrors in concert with internal instrument data collection and Switching Mirror operation.

The core of the Calibration Controllers consisted of a Rabbit Semiconductor[2] Rabbit 2000 Basic Development Kit with the circuitry shown in Figure F.1 included on the prototyping area of the motherboard. As an additional convenience, each Calibration Controller used a RabbitLink Card (EG2100) to provide ethernet connectivity between calibration controllers a PC used to program, control and monitor them. The AT90S2313 is an Atmel 8-bit RISC processor used to snoop and decode the internal instrument bus traffic, and determine 'time' in MIF coordinates. Both the Atmel and Rabbit processors use the Sync signal from the instrument as interrupts to coordinate the transfer of timing information from Atmel to Rabbit chips, and to trigger the output of commands strings from the Rabbit chips to the calibration equipment.

Each calibration setup typically used two of these calibration controllers, one to operate the external switching mirrors, the other to operate the remaining equipment (synthesizer, Fabry-Pérot translation stage, etc). Each Rabbit board had two standard RS-232 serial ports. These connected directly to such items as the motor controllers, or through a National Instruments Serial-to-GPIB converter module (National Instruments GPIB-232CT-A) to operate the frequency synthesizer (HP 83751A) and translation stage (Newport Research ESP300) controllers.

It can be seen that the controllers are cheap and simple to construct, consisting mainly of a few low-cost boards and components. An additional, and very useful, feature of these controllers is that they can be programmed in a manner that they start executing their code a few seconds after power is applied, without the need for any intervention. This mode of operation was used primarily for the controller used to operate the external calibration mirror(s), since, for example, the same switching sequence was used for all high-resolution and Fabry-Pérot sweeps. This meant that it was only necessary to bring up a remote interface to one controller to carry out such calibrations.

Some of the THz calibrations used a similar controller, but with an additional analog output (controlled by the Rabbit processor) to operate a piezo actuator in a calibration Fabry-Pérot.

F.2 Controller Software

By far the most important aspect of the Calibration Controllers was the internal software. Below we describe the software in the Atmel processor, used for instrument packet decoding, followed by an example of the Rabbit processor code used for some of the high-resolution spectral sweeps.

[2] www.RabbitSemiconductor.com

F.2.1 Atmel Software

The job of this processor was to read and decode the instrument bus traffic to determine instrument 'time,' and to convey this information to the companion Rabbit processor. A short interrupt-driven assembly program in the Atmel chip (AT90S2313) decoded the RIU packets on the RS-485 bus to determine instrument 'time' in MIF coordinates, updating the information on pins PD0 and PD1 of Figure F.1 to signal detection of MIFs 0, 48 and 96. Since the Atmel and Rabbit processor interrupts are triggered by opposite edges of the common Sync pulse from the instrument, this provides a robust signalling method with low overhead for keeping the Rabbit processor 'aware' of instrument time. Early versions of the Calibration Controllers used the Rabbit processor to monitor the RS-485 and operate all of the calibration equipment. This setup required changing the crystal on the Rabbit board to one that was a multiple of 8 MHz in order for the 500 kbaud bus traffic to be captured correctly by the UART. While this was found to be relatively easy with early versions of the Rabbit software, later versions started to incorporate more complex multi-level booting schemes that made the task more and more difficult. The inclusion of the cheap Atmel processor eliminated the need for any changes to clock speed of the Rabbit boards, ensuring that they remained compatible with the Rabbit development environment. A source code listing of the program in the flash memory of the Atmel processor is provided below. Note that *all* of the regular processing is performed by a short interrupt handler. The remainder of the code is initial setup, followed by an empty idle loop.

```
;*************************************************************************
;*
;* EOS MLS RS-485 Bus Sniffer * FM *  /users/jarnot/AtmelCode/AVR_Rabbit.txt
;*
;* Date                 : 24 April 2002
;* Target MCU           : AT90S2313
;*
;* DESCRIPTION
;*
;*   The objective is to extract the MIF count from the RIU data stream in
;* real time, and to present this information to an external device
;* (RabbitSemiconductor Kit Board) as a 2 bit code (00 = 'not a signalling
;* MIF', 0x01 == MIF 0, 0x10 == MIF 48, and 0x11 == MIF 96).  This information
;* is presented on bits 0 and 1 of PORT B by the SYNC interrupt handler,
;* triggered by the negative edge of the SYNC pulse.  The Rabbit processor
;* uses the positive edge triggered SYNC interrupt to access these data,
;* and hence runs 2 MIFs behind the current instrument MIF (if no software
;* corrections are applied).  The SYNC pulse interrupt is also responsible
;* for clearing the flag registers and character counter, and enabling the
;* UART receiver and interrupt.
;*
;* The RIU data format (a packet of 9-bit words) is assumed to be:
;*
;* First 'byte': RIU ID, 0x50..0x6f, with 9th bit set to zero.
;*             : packet size (9th bit is 1 for all subsequent 'bytes'
```

```
;*                              except for EOT).
;*             : packet type.
;*             : MIF count (this is what we are looking for).
;*             : etc, until
;*  Last 'byte': 0x02, EOT, with 9th bit set to zero.
;*
;* Note that in the code below, and in the equivalent Rabbit code, the
;* polarity of the 9th bit is reversed compared to the packet description
;* given above.  Since it is highly unlikely that both processors have
;* the same error in them, we must assume that the C&DH/RIU documentation
;* is incorrect.
;*
;*****************************************************************************

.include "2313def.inc"

;***** Global Register Variables
.def    DataFlag        =r16    ; flag byte.  Bit 0 == 1 = 'MIF updated'
.def    BCnt            =r17    ; byte count in current packet
.def    MIF             =r18    ; MIF read from RS-485 bus
.def    temp            =r19    ; scratch and temporary

;***** Main Program

        .cseg
        .org    $000
        RJMP    start           ; reset handler

        .org    $001
        RJMP    sync_intrpt     ; external interrupt 0 handler

        .org    $007
        RJMP    u_rcv_int       ; UART receive char interrupt handler

; initialization and idle loop:

start:
        CLI                     ; disable interrupts (global)
        LDI     temp, RAMEND    ; set up stack pointer
        OUT     SPL, temp

; set up Port D:
        LDI     temp, 0x00
        OUT     DDRD, temp      ; all PORTD pins are inputs, with pullups
        LDI     temp, 0x7A      ; on bits 1, 3, 4, 5 and 6.
        OUT     PORTD, temp
```

```
; set up Port B:
        LDI     temp, 0x03
        OUT     DDRB, temp      ; pins 0 and 1 are outputs, the rest are inputs
        LDI     temp, 0x03      ; with pullups.
        OUT     PORTB, temp

; set up UART:
        SBI     UCR, 2          ; enable 9th bit in character
        LDI     temp, 0x00      ; 500 kb/sec for an 8 MHz CPU clock
        OUT     UBRR, temp

; turn off analog comparator:
        SBI     ACSR, 7

; set up INT 0:
        LDI     temp, 0x02
        OUT     MCUCR, temp     ; INT0 falling edge triggered
        LDI     temp, 0x40      ; bit 6 = 1
        OUT     GIMSK, temp     ; enable INT0 (sync. pulse)

; initialise the 'data ready' flag:
        LDI     DataFlag, 0

        SEI                     ; enable global interrupts

; ***** Idle Loop:
IdleLoop:
        RJMP    IdleLoop        ; Nothing to do here.

; ***** INT0 handler:
sync_intrpt:
        SBRS    DataFlag, 0     ; Has MIF been updated?
        RJMP    NoData
        CPI     MIF, 0          ; MIF == 0?
        BRNE    NotZero
; continue here if MIF == 0:
        LDI     temp, 0x01
        OUT     PORTB, temp
        RJMP    BisSet
NotZero:
        CPI     MIF, 48         ; MIF == 48?
        BRNE    Not48
; continue here if MIF == 48:
        LDI     temp, 0x02
        OUT     PORTB, temp
```

```
        RJMP    BisSet
Not48:
        CPI     MIF, 96         ; MIF == 96?
        BRNE    NoData
; continue here if MIF == 96:
        LDI     temp, 0x03
        OUT     PORTB, temp
        RJMP    BisSet
NoData:
        LDI     temp, 0x00
        OUT     PORTB, temp
BisSet:
        CLR     DataFlag
        CLR     BCnt
        SBI     UCR,7           ; enable UART RCX interrupt
        SBI     UCR,4           ; enable UART receiver
        IN      MIF, UDR        ; clear data register and flags
        RETI                    ; return and enable global interrupts

;***** UART RCX interrupt handler:
u_rcv_int:
        TST     BCnt            ; compare ByteCount to 0
        BRNE    CntNot0
        SBIC    UCR, 1          ; 9th bit is zero?
        RJMP    EndUInt         ; jump if it's not

; If byte counter and 9th bit are both 0, then check RIU ID:
        INC     BCnt
        IN      MIF, UDR        ; read data from UART
        CPI     MIF, 0x50
        BRLO    WrongID
        CPI     MIF, 0x6f
        BRSH    WrongID
        RETI

; If byte counter is not zero:
CntNot0:
        INC     BCnt
        CPI     BCnt, 0x04      ; have we just read the MIF byte?
        BRLO    EndUInt
        LDI     DataFlag, 0x01
        IN      MIF, UDR
        CBI     UCR, 4
        CBI     UCR, 7          ; disable UART interrupt generation
        RETI
```

```
WrongID:
        CLR     BCnt
        RETI
EndUInt:
        IN      MIF, UDR
        RETI

; ------------------------------------------------------------------------
; Subroutines:

; None at this time. %% $ %% The dollar sign is just to return emacs
%%                          colorization back to sensible state.
```

F.2.2 Rabbit Software

The software in the Rabbit software consisted of two major elements:

(1) A small interrupt-driven routine to keep track of the timing information being passed on by the companion Atmel processor, and

(2) the main program which had the task of operating the switching mirrors, synthesizers, Fabry-Pérot grid separation micrometer, and any other external calibration mechanism.

The interrupt handler was written in assembler, and updated a global variable on each Sync interrupt to keep the main program aware of instrument MIF. An additional feature built into this handler was that it flagged its current state by means of the bank of user LEDs on the Rabbit motherboard. In nominal operation these LEDs indicated the last MIF number decoded, and when the processor was not synchronized to the instrument, patterns indicating 'loss of bus data,' 'loss of Sync pulse,' and so on, were displayed as a handy debugging and status indication. The main program, with its less stringent timing requirements, was always written in C. Because some of the computations in the main program were fairly complex (e.g., generating the ASCII control string for setting the synthesizer), a technique of software pipelining was employed where necessary. Simply put, this means that on detection of a MIF in which controller action was required, a pre-computed set of commands to the external equipment was sent via one or more RS-232 ports, and the processor then calculated the command strings to be sent at the next MIF requiring action. This provided short latency between a MIF change and a controller response, and maximized the time available for the Rabbit processor to perform the sometimes tedious calculations necessary to generate the next-required control string(s).

The Dynamic-C development environment provided for the Rabbit processors was found to be an excellent one for code development. For example, time could be simulated (at a user-controllable rate) using a coroutine to advance the variable that the main program used to monitor instrument MIF, eliminating the need for a connection to the instrument (or a simulator) when developing the main program. Controller output strings could be echoed to the console, and also directed to a file for subsequent review. It was also found to be advantageous to add `print` statements to ensure that the review file was self documenting.

The power of this technique is evidenced by the fact that the Rabbit code given below which was used to operate the synthesizer for the end-to-end high resolution 25-channel filterbank sweeps, as well as the related programs used to sweep the 11-channel filterbanks, Wide Filters, and baseband (IF) spectrometer sweeps, were all completely bug-free when run for the first time in the calibration environment.

```
/* sweepFB25.c                                              03 September 2002
   /users/jarnot/Rabbit/AVR/sweepFB25.c

   This program controls the synthesizer for all GHz FB25 front-end
   sweeps. When run, it prompts for the band/sideband to be swept, and
   the power level to be used during the sweep.  It then runs the
   synthesizer for the entire sweep.  Synchronization to the
   instrument is via an Atmel chip monitoring RS485 bus traffic.

   In this version we provide a 'flag' signal in the first channel to
   be swept to indicate that the next MAF is the first one of the
   sweep.  Also, the routine GPIB messages to the synthesizer are not
   echoed to STDOUT, but are replaced with once-per-MAF messages
   reporting the time remaining until the sweep has been completed.

   This program requires Sync signals and non-idle-mode RS485 data bus
   traffic in order to sequence the sweeper.  As a convenience, adding
   100 to the selected band (-100 to lower sideband sweeps) forces a
   costate to generate dummy MIFs at an (optionally) accelerated rate.
   When in this simulation mode, the signalling MAF actions are not
   executed.
*/

#define BINBUFSIZE 15
#define BOUTBUFSIZE 63
#define CINBUFSIZE 15
#define COUTBUFSIZE 31

// function prototype for external interrupt handler:
void _ext_ISR(); // Int 0 handler.

char MIF, SyncFlag, SyncLoss, Searching;  // byte vars used by INT0.

main() {
  unsigned int step, MIFindex, initializing, pli, sblen;
  unsigned long start_freq, fl;

  const char sfp[] = "wrt 10\nCW";  // synthesizer frequency string prefix
  const char sfs[] = "HZ\r\n";      // synthesizer frequency string suffix
  const char spp[] = "wrt 10\nPL";  // synthesizer O/P level string prefix
  const char sps[] = "DB\r\n";      // synthesizer O/P level string suffix
```

```
  char instring[36];   // This is used to store keyboard input.
  char synth_freq[36]; // String sent to synthesizer to set frequency.
  char synth_oobf[36]; // String sent to synthesizer to set out-of-band frequency.
  char synth_plvl[36]; // String sent to synthesizer to set O/P power level.
  char synth_sigf[36]; // String sent to synthesizer to set flag frequency.

  char sideband_string[15];
  char sa[12], sb[12], sc[12], sd[12], pls[12], sbb[10]; // string buffers.
  int i, OK, band, band_index, region, fh, testmode, mr;
  long int s_l, s_h, mult; // low and high portions of the synth start frequency,
                           // multiplication between synthesizer and final O/P.
  float level;             // This is the synth. O/P power level for the sweep.

/* Array of start frequencies (the bit below 1 GHz) for Bands -1..-14,
   14..1, in Hz.  These RF frequencies correspond to 0 Hz in the
   spectrometer IF for bands which run from channels 1..25 in
   increasing RF space, and 1.8 GHz for bands which run 'backwards' in
   RF space.  The downstream software is responsible for expanding any
   strings with less than 9 digits, as well as dealing with any
   overflows (i.e. expansion beyond 9 digits).
*/
 const long start_low[] =
                  {731666666,
                   201190476, 160000000,  58194444, 878611111, 730277778,
                    45277778, 947301587, 757962962,
                   127946429, 110619048,  47415000, 881740000, 868714286,
                   701285714, 688260073, 522585034, 459380952, 442053571,
                   770925926, 581587302, 483611111,
                   103055556, 954722223, 775138889, 673333333, 632142857,
                   743333334};

/* Array of the GHz portion of the synthesizer start frequencies (the
   portion above 1 GHz).
*/

 const int start_high[] = {14,
                           15, 15, 15, 14, 14,
                           13, 12, 12,
                           15, 15, 15, 14, 14,
                           15, 15, 15, 15, 15,
                           13, 13, 13,
                           17, 16, 16, 16, 16,
                           16};

 // Multipliers for the previous list of Band start frequencies:
```

```
const long int multiplier[] = {8,
                               12, 12, 12, 12, 12,
                               18, 18, 18,
                               42, 42, 42, 42, 42,
                               42, 42, 42, 42, 42,
                               18, 18, 18,
                               12, 12, 12, 12, 12,
                                8};

// IF frequency segment start frequencies, in Hz (with guard at end):

const long base_freq[] = {85000000, 181000000, 277000000, 373000000,
   469000000, 565000000, 629000000, 693000000, 757000000, 805000000,
   837000000, 861000000, 877000000, 889000000, 897000000, 903000000,
   911000000, 923000000, 939000000, 963000000, 995000000, 1043000000,
   1107000000, 1171000000, 1235000000, 1331000000, 1427000000,
   1523000000, 1619000000, 1715000000};

// RF frequency step sizes for each segment, in Hz, and indices to power levels:

const long freq_incr[] = {960000, 960000, 960000, 960000, 960000,
  640000, 640000, 640000, 480000, 320000, 240000, 160000, 120000,
   80000, 60000, 80000, 120000, 160000, 240000, 320000, 480000,
  640000, 640000, 640000, 960000, 960000, 960000, 960000, 960000, 96000};
// final entry is a guard.

// list of event MIFs, the MIFs at which this software has actions to perform:

const int eMIF[] = {6, 12, 18, 24, 30, 36, 42, 48, 54, 60, 66, 72, 78,
                    84, 90, 96, 102, 108, 114, 120, 130, 144};

const char sbzeros[][9] = {"0", "0", "00", "000", "0000", "00000", "000000",
                           "0000000", "00000000"};

 Searching = 0xEE;
 SyncFlag = 0;
 SyncLoss = 0;
 testmode = 0;

 // Set up the external (RTI) interrupts:
 WrPortI(PEDDR, &PEDDRShadow, 0x00); // port E pins are all inputs
 WrPortI(PEFR, &PEFRShadow, 0x00);   // with no I/O strobes.
 SetVectExtern2000(3, _ext_ISR);     // first clear out any pending interrupts.
 WrPortI(I0CR, &I0CRShadow, 0x23);   // enable PE4 as INT0B, rising edge
                                     //  triggered, priority 3.
```

```
  WrPortI(I1CR, &I1CRShadow, 0x23);   // enable PE5 as INT1B, rising edge
                                      //  triggered, priority 3.

  // Set up serial ports for interfacing with the GPIB and IMS controllers:
  serBopen(9600);             // This port is for the NI GPIB-232CT-A.
  WrPortI(SBCR, NULL, 0x22);  // port B: 8-bit, priority 2, input disabled.
  serCopen(9600);             // The port is for the IMS motor controller.
  WrPortI(SCCR, NULL, 0x22);  // port C: 8-bit, priority 2, input disabled.

  WrPortI(SPCR, &SPCRShadow, 0x84);  // LED port (A) initialized as output port.
  WrPortI(PADR, &PADRShadow, 0xff);  // write all 1's to port A (LEDs off).

  // Set up port D to read the 2 MIF status bits from the AVR -- the 2
  // lsbs as inputs (the rest as open drain outputs), no alternate
  // UART functionality.

  WrPortI(PDDDR, &PDDDRShadow, 0xfc);  // set up pin directions,
  WrPortI(PDDCR, &PDDCRShadow, 0xfc);  // pull-ups, and
  WrPortI(PDFR,   &PDFRShadow, 0x00);  // alternate functionality (none).

  // Send out first part of initialization string for IMS controller:
  //  printf("Space character to IMS\r\n");
  //  serCputs(" ");

  // Send out the initialization strings for the HP 83751A sweeper:
  printf("wrt 10\nCW15.0GZ\r\n");      // 15.0 GHz.
  serBputs("wrt 10\nCW15.0GZ\r\n");
  printf("wrt 10\nA1\r\n");            // Internal Leveling.
  serBputs("wrt 10\nA1\r\n");
  printf("wrt 10\nPL1DB\r\n");         // +1.0 dBm.
  serBputs("wrt 10\nPL1DB\r\n");

  // Next part of IMS initialization string:
  //  printf("f0\r\n");
  //  serCputs("f0\r");

  //  Next we request information as to which FB25 (and which sideband) we are
  // going to sweep, followed by the 3 power levels to be used during the sweep.

  OK = 0;
  printf("\n  Bands are in the range 1 to 14 (negative for lower sideband).");
  printf("\n  Synthesizer O/P power levels are in dBm.\n\n");

 while(!OK) {
   printf("\n  FB25 Band to sweep: ");
   band = atoi(gets(instring));
```

```
  if (band > 14) {
    band -= 100;
    testmode = 1;
  } // end if
  if (band < -14) {
    band += 100;
    testmode = 1;
  } // end if
  if ((band < -14) || (band > 14)) band = 1;
  (band < 0) ? strcpy(sideband_string, "lower sideband")
             : strcpy(sideband_string, "upper sideband") ;

  printf("  Synthesizer O/P level: ");
  level = atof(gets(instring));

  printf("\n  Band %d, %s\n", abs(band), sideband_string);
  printf("\n  Synthesizer O/P level is %5.1f dBm", level);

  printf("\n\n  If this is correct, enter 1, else 0: ");
  OK = atoi(gets(instring));
} // end while

 printf("\n\n");

 // Next part of IMS initialization string:
 //  printf("O\r\n");
 //  serCputs("O\r");

 band_index = (band > 0) ? (band - 1) : (band + 28);
 band_index = abs(band_index - 27);
 mult = multiplier[band_index];

 step = 0;
 region = 0;
 MIFindex = 24; // start with an out-of-range number so that the main
                // costate does not trigger prematurely.

 //  ************************************************************************

 fh = start_high[band_index];
 fl = start_low[band_index] + (base_freq[2] + freq_incr[2] * 50) / mult;
 itoa(fh, sa);
 ltoa(fl, sb);
 if (strlen(sb) > 9) { // first check for more than 9 digits in sb.
   fh += 1;            // The use of an IF statement allows for just
   fl -= 1000000000L;  // a unit overflow from fl into fh.
```

```
    itoa(fh, sa);
    ltoa(fl, sb);
  }
  sblen = 9 - strlen(sb); // Now ensure exactly 9 chars in sb.
  if (sblen != 0) {
    strcpy(sbb, sbzeros[sblen]);
    strcat(sbb, sb);
    strcpy(sb, sbb);
  } // end if
  strcpy(synth_freq, sfp);
  strcat(synth_freq, sa);
  strcat(synth_freq, sb);
  strcat(synth_freq, sfs);
  strcpy(synth_sigf, synth_freq); // set frequency to center of 1st. channel.

  fh = start_high[band_index];
  fl = start_low[band_index] + base_freq[region] / mult;
  itoa(fh, sa); // Need to reset sa in case it was modified above.
  ltoa(fl, sb);
  sblen = 9 - strlen(sb);
  if (sblen != 0) {
    strcpy(sbb, sbzeros[sblen]);
    strcat(sbb, sb);
    strcpy(sb, sbb);
  } // end if
  strcpy(synth_freq, sfp);
  strcat(synth_freq, sa);
  strcat(synth_freq, sb);
  strcat(synth_freq, sfs);
  strcpy(synth_oobf, synth_freq); // set out-of-band frequency to start frequency.

  printf(synth_oobf);             // set initial synthesizer frequency.
  serBputs(synth_oobf);

  sprintf(synth_plvl, "wrt 10\nPL%5.1fDB\r\n", level);

  printf(synth_plvl);             // set initial synthesizer O/P power level.
  serBputs(synth_plvl);

  if (!testmode) {
    // Now send the signal frequency at MIFs 20 and 60, out-of-band frequency at
    // MIFs 40 and 80, then start the sweep.
    printf("\nPreparing to send Level 1 sync. pattern ...\r\n");
    while (MIF != 20) {;}
    printf("synth_sigf\r\n");
    serBputs(synth_sigf);
```

```
  while (MIF != 40) {;}
  printf("synth_oobf\r\n");
  serBputs(synth_oobf);
  while (MIF != 60) {;}
  printf("synth_sigf\r\n");
  serBputs(synth_sigf);
  while (MIF != 80) {;}
  printf("synth_oobf\r\n");
  serBputs(synth_oobf);
  printf("Level 1 sync. pattern sent, preparing to sweep ...\r\n\n");
} // end if

MIFindex = 0;  // This allows the main costate to launch.

// Now the costates:

while(region < 29) {
  costate {  // This costate commands the synthesizer.
    if (MIF == eMIF[MIFindex]) {
      if (MIFindex < 19) { // update synthesizer frequency
        // printf("MIF %d, MIFindex %u, %s", MIF, MIFindex, synth_freq);
        // printf(synth_freq);
        serBputs(synth_freq);
      } // end if
      if (MIFindex == 19) {  // move SW mirror to LN2, synth out of band
// printf("R1000\r\n");
// serCputs("R1000\r"); // Move the switching mirror to LN2.
        // printf(synth_oobf);
        serBputs(synth_oobf);
      } // end if
      if (MIFindex == 20) { // view sweeper, synthesizer still out of band.
// printf("R500\r\n");
        // serCputs("R500\r"); // Move the switching mirror to LN2.
        // Report time remaining:
        mr = (29-region)*5-(step+1)/20;
        printf("MAFs remaining: %d (%.1f minutes)\n", mr, mr*25.666/60.0);
      } // end if
      if (MIFindex == 21) { // set next synthesizer frequency:
// printf(synth_freq);
        serBputs(synth_freq);
      } // end if

      // Check to see if MIFindex and step are in sync.:
      if ((MIFindex != 0) && (step == 0)) {
        printf("\nTiming error -- MIFindex and step are out of Sync.");
        printf("\nMIF = %d, MIFindex = %d, step = %d\n\n", MIF, MIFindex, step);
```

```
      }
      // We should eventually take other action on loss of sync.

      MIFindex += 1;
      MIFindex = (MIFindex == 22) ? 0 : MIFindex;

      if (MIFindex < 20) {
        step += 1;
        step = (step == 100) ? 0 : step;
        region = (step == 0) ? (region + 1) : region;

        // Set up the control strings for the next time through this loop.
        // We have almost 1 second to do this.

        fl = start_low[band_index];
        fl += (base_freq[region] + freq_incr[region] * step) / mult;
        fh = start_high[band_index];
        itoa(fh, sa);
        ltoa(fl, sb);
        while (strlen(sb) > 9) { // force less than 9 digits in sb.
          fh += 1;
          fl -= 1000000000L;
          itoa(fh, sa);
          ltoa(fl, sb);
        }
        // if necessary, pad sb with leading zeroes:
        sblen = 9 - strlen(sb);
        if (sblen != 0) {
          strcpy(sbb, sbzeros[sblen]);
          strcat(sbb, sb);
          strcpy(sb, sbb);
        } // end if
        strcpy(synth_freq, sfp);
        strcat(synth_freq, sa);
        strcat(synth_freq, sb);
        strcat(synth_freq, sfs);
        waitfor(DelayMs(200));
      } // end if
    } // end if
  } // end costate

  costate { // this costate looks for, and indicates, loss of Sync pulse.
    if (!testmode) {
      waitfor(DelayMs(1000));
      SyncLoss += 1;
      SyncLoss = (SyncLoss > 3) ? 3 : SyncLoss;
```

```
        if (SyncLoss == 3) {WrPortI(PADR, &PADRShadow, 0xaa);}
      } // end if
    } // end of 'presence of Sync interrupts' checking costate.

    costate { // this costate simulates interrupt updating of the variable MIF.
      if (testmode) {
        waitfor(DelayMs(66)); // Can change the simulated MIF rate here.
        MIF += 1;
        MIF = (MIF == 148 ? 0 : MIF);
        WrPortI(PADR, &PADRShadow, MIF ^ 0xff);
      } // end if
    } // end of MIF update costate

  }  // end 'while region' loop
} // end main


#asm

_ext_ISR::
; this is the handler for external interrupts, RTI signal (5 ms pulse at ~6 Hz)
     PUSH   AF
     PUSH   HL
     LD     HL, SyncLoss
     LD     (HL), 0    ; Clear SyncLoss at every interrupt.
;
     LD     A, (SyncFlag)
     OR     A
     JR     Z, NotSynced
;
; Continue here if we think we are in sync:
     LD    A, (MIF)
     INC   A
     CP    148
     JR    NZ, Not148
     XOR   A
Not148:
     LD    (MIF), A    ; MIF is now updated.
     CP    2           ; We now compare MIF to 2, 48+2 and 96+2.
     JR    NZ, notAVR1
ioi  LD    A, (PDDR)   ; Read AVR status.
     AND   0x03
     CP    1
     JR    NZ, BadSync
     JR    UpdMIF
;
```

```
notAVR1:
     CP    50
     JR    NZ, notAVR2
ioi  LD    A, (PDDR)   ; Read AVR status.
     AND   0x03
     CP    2
     JR    NZ, BadSync
     JR    UpdMIF
;
notAVR2:
     CP    98
     JR    NZ, UpdMIF
ioi  LD    A, (PDDR)   ; Read AVR status.
     AND   0x03
     CP    3
     JR    NZ, BadSync
     JR    UpdMIF
;
BadSync:               ; Come here if MIF and AVR flags disagree.
     LD    HL, SyncFlag
     LD    (HL), 0
NotYet:
     LD    HL, Searching
     LD    A, (HL)
ioi  LD    (PADR), A
     RLC   A
     LD    (HL), A
     JR    EndInt0
;
NotSynced:
ioi  LD    A, (PDDR)   ; Read AVR status.
     AND   3           ; Keep only the 2 lsbs.
     JR    Z, NotYet
;
; Continue here if we have Sync information from the AVR:
     LD    HL, MIF
     CP    1
     JR    NZ, not1
     LD    (HL), 2     ; MIF0 status from AVR, offset = 2
     JR    ISynced
;
not1:
     CP    2
     JR    NZ, Its3
AVR2:
     LD    (HL), 50    ; MIF48 status from AVR, offset = 2
```

```
     JR    ISynced
;
Its3:
     LD    (HL), 98    ; MIF96 status from AVR, offset = 2
     ;
ISynced:
     LD    HL, SyncFlag
     LD    (HL), 1     ; Indicate that we are in sync.
UpdMIF:
     LD    A, (MIF)
     XOR   0xFF
ioi  LD    (PADR), A   ; Update LEDs with current MIF
;
EndInt0:
     POP    HL
     POP    AF
     IPRES
     RET

#endasm
```

Bibliography

[1] Erickson, N., Tolls, V., Near-Field Measurements of the SWAS Antenna, *20th ESTEC Antenna Workshop on Millimetre Wave Antenna Technology and Antenna Measurements*, 18–20 June 1997, Noordwijk, The Netherlands.

[2] Slater,D., Near Field Antenna Measurements, 1991 Artech House, Inc. ISBN 0-89006-361-3.

[3] Slater,D., *et.al.*, A Large Aperture 650 GHz Near-Field Measurement System for the Earth Observing System Microwave Limb Sounder, *Antenna Measurement Techniques Association Conference*, October 2001.

[4] www.nearfield.com